FROM PEPTIDE AND PROTEIN TOXINS TO ION CHANNEL STRUCTURE/FUNCTION AND DRUG DESIGN

EDITED BY: Victor I. Tsetlin, Chris Ulens, Annette Nicke and Jean-Francois Rolland
PUBLISHED IN: Frontiers in Pharmacology

frontiers Research Topics

ISSN 1664-8714
ISBN 978-2-88966-186-2
DOI 10.3389/978-2-88966-186-2

About Frontiers

Frontiers is more than just an open-access publisher of scholarly articles: it is a pioneering approach to the world of academia, radically improving the way scholarly research is managed. The grand vision of Frontiers is a world where all people have an equal opportunity to seek, share and generate knowledge. Frontiers provides immediate and permanent online open access to all its publications, but this alone is not enough to realize our grand goals.

Frontiers Journal Series

The Frontiers Journal Series is a multi-tier and interdisciplinary set of open-access, online journals, promising a paradigm shift from the current review, selection and dissemination processes in academic publishing. All Frontiers journals are driven by researchers for researchers; therefore, they constitute a service to the scholarly community. At the same time, the Frontiers Journal Series operates on a revolutionary invention, the tiered publishing system, initially addressing specific communities of scholars, and gradually climbing up to broader public understanding, thus serving the interests of the lay society, too.

Dedication to Quality

Each Frontiers article is a landmark of the highest quality, thanks to genuinely collaborative interactions between authors and review editors, who include some of the world's best academicians. Research must be certified by peers before entering a stream of knowledge that may eventually reach the public - and shape society; therefore, Frontiers only applies the most rigorous and unbiased reviews.
Frontiers revolutionizes research publishing by freely delivering the most outstanding research, evaluated with no bias from both the academic and social point of view. By applying the most advanced information technologies, Frontiers is catapulting scholarly publishing into a new generation.

What are Frontiers Research Topics?

Frontiers Research Topics are very popular trademarks of the Frontiers Journals Series: they are collections of at least ten articles, all centered on a particular subject. With their unique mix of varied contributions from Original Research to Review Articles, Frontiers Research Topics unify the most influential researchers, the latest key findings and historical advances in a hot research area! Find out more on how to host your own Frontiers Research Topic or contribute to one as an author by contacting the Frontiers Editorial Office: researchtopics@frontiersin.org

FROM PEPTIDE AND PROTEIN TOXINS TO ION CHANNEL STRUCTURE/FUNCTION AND DRUG DESIGN

Topic Editors:
Victor I. Tsetlin, Institute of Bioorganic Chemistry (RAS), Russia
Chris Ulens, KU Leuven, Belgium
Annette Nicke, Ludwig Maximilian University of Munich, Germany
Jean-Francois Rolland, Axxam (Italy), Italy

Citation: Tsetlin, V. I., Ulens, C., Nicke, A., Rolland, J.-F., eds. (2020). From Peptide and Protein Toxins to Ion Channel Structure/Function and Drug Design. Lausanne: Frontiers Media SA. doi: 10.3389/978-2-88966-186-2

Table of Contents

frontiers in Pharmacology

EDITORIAL
published: 25 September 2020
doi: 10.3389/fphar.2020.548366

Editorial: From Peptide and Protein Toxins to Ion Channel Structure/Function and Drug Design

Annette Nicke[1], *Chris Ulens*[2], *Jean-Francois Rolland*[3] *and Victor I. Tsetlin*[4]*

[1] Walther Straub Institute of Pharmacology and Toxicology, Faculty of Medicine, Ludwig-Maximilians-Universität München, Munich, Germany, [2] Laboratory of Structural Neurobiology, Department of Cellular and Molecular Medicine, KU Leuven, Leuven, Belgium, [3] Axxam SpA, Milan, Italy, [4] Department of Molecular Neuroimmune Signaling, Shemyakin-Ovchinnikov Institute of Bioorganic Chemistry, Russian Academy of Sciences, Moscow, Russia

Keywords: α-conotoxins, Three-finger Ly6 proteins, nicotinic receptors, Cys-loop receptors, Voltage-gated ion channels, receptor complexes, drug design

Editorial on the Research Topic

From Peptide and Protein Toxins to Ion Channel Structure/Function and Drug Design

OPEN ACCESS

Edited by:
Domenico Tricarico,
University of Bari Aldo Moro, Italy

Reviewed by:
Hiroshi Hibino,
Niigata University, Japan

***Correspondence:**
Victor I. Tsetlin
victortsetlin3f@gmail.com

Specialty section:
This article was submitted to Pharmacology of Ion Channels and Channelopathies, a section of the journal Frontiers in Pharmacology

Received: *02 April 2020*
Accepted: *03 September 2020*
Published: *25 September 2020*

Citation:
Nicke A, Ulens C, Rolland J-F and Tsetlin VI (2020) Editorial: From Peptide and Protein Toxins to Ion Channel Structure/Function and Drug Design. Front. Pharmacol. 11:548366. doi: 10.3389/fphar.2020.548366

From the very beginning of receptor research, animal toxins have been crucial for the identification of ion channels and their subtype differentiation, biochemical investigation, and cloning. Today, they also serve as invaluable tools for the detailed structural characterization of receptors and might even have drug potential or serve as templates for drug development.

In this broadly planned topic, we included recent research and reviews on both three-fingered proteins with homology to neurotoxins from snakes and much smaller peptide toxins from cone snails, spiders, and scorpions. In line with the activity of the respective toxins, the articles describe their use as tools for research or potential therapeutic applications on ligand-gated nicotinic acetylcholine receptors (nAChRs), voltage-gated Na^+ and K^+ channels, and, last but not least, the effects of chlorotoxin fragments on cell migration via an unidentified target.

Two papers focus on endogenous prototoxins of the Ly6 family, a diverse family of three-fingered proteins with multiple physiological functions in mammals. J. M. Miwa who contributed to the discovery of this protein family together with her co-authors summarizes the current knowledge about these proteins, their structure, effects on nAChRs, and roles in cholinergic signaling (Miwa et al.). In a second publication on this topic, the first synthesis of water-soluble fragments of the central loop of Ly6 proteins and their binding to and effect on various nAChR subtypes are described, thereby identifying inhibition of the muscle type and therapeutically interesting α9α10 subtype by a Lynx1 fragment. Interestingly, the linear peptide and the disulfide bond-cyclized form had similar potency (Kryukova et al.). A third paper indirectly deals with three-finger folded proteins. Here, the soluble acetylcholine binding protein (AChBP), a valuable model for structural studies on nAChRs, was tested for its suitability as a potential treatment against snake bites. The authors describe efficient binding to and partial neutralization of long chain neurotoxins by an AChBP analog (Albulescu et al.).

Among the most selective tools in nAChRs research are α-conotoxins, comparably small peptides derived from the venom of marine predatory snails, and three papers in this issue are devoted to them. While several cryo-EM and X-ray structures of nicotine-bound nAChR exist, no full-length nAChR structure bound to a peptide or protein neurotoxin is known. Therefore, co-crystal structures of the AChBP or the ligand binding domains (LBD) of nAChRs provide important models. The paper by

Zouridakis et al. shows for the first time the X-ray structure of an α-conotoxin, the α9α10-selective RgIA, in complex with the LBD of the α9 nAChR. Despite the monomeric state of the α9 LBD, computer modeling enabled the construction of a pentameric α9α10 model and determination of the RgIA binding subunit interface in agreement with published functional data. The α9α10-selective conotoxin RgIA has previously been shown to have anti-inflammatory and anti-nociceptive action in neuropathic pain models. However, the exact physiological mechanisms are incompletely understood (Dutertre et al., 2017). The review by Grau et al. describes the development of α7 and human α9α10-selective analogs of conotoxins ArIB and RgIA, respectively, and their use in the characterization of nAChRs in immune cells. They summarize data that show that theses receptors via a metabotropic mechanism involving the purinergic P2X7 receptor modulate inflammation. Finally, in the paper by El Hamdaoui et al., a strategy for the production of α-conotoxin TxIA variants in *E. coli* was tested. Although it was demonstrated that this resulted predominantly in the so-called "ribbon" isomer in which disulfide bonds are misfolded (compared to the naturally occurring "globular" α-conotoxins), a weak antagonistic potency of these peptides was determined, and a binding mode at the α7 nAChR was proposed. Nevertheless, the study showed that careful structural analysis is a requirement if disulfide bond formation cannot be controlled.

Three papers were devoted to spider toxins targeting voltage-gated Na^+ and K^+ channels. The review by Cardoso and Lewis summarizes the current understanding of the structure-activity relationships of spider cysteine knot peptides, which are a highly diverse and chemically stable group of peptides that allosterically modulate voltage-gated sodium channels (Na_V) and have therapeutic potential for the treatment of pain. The study by Zhang Yunxiao et al. describes the identification and characterization of μ-TRTX-Ca2a, another spider toxin with activity at the Nav1.7 Na^+ channel subtype and analgesic properties. Another group (Zhang Yiya et al.) performed an alanine scan to determine the molecular mode of action of Jingzhaotoxin-V at the Kv4.2 potassium channels in rat cardiomyocytes.

Finally, Dastpeyman et al. investigated the structure, stability, and activity of chlorotoxin fragments to identify regions that determine its functions. This scorpion toxin binds selectively to tumor cells and has been shown to inhibit cell migration. While the target of the toxin is not known, two C-terminal fragments appeared to retain some activity in cellular assays for surface binding, internalization, and migration.

Taken together, this Research Topic provides topical examples how toxins have been modified to identify the principal determinants of their action or to develop improved tools for ion channel research.

AUTHOR CONTRIBUTIONS

VT was invited by Frontiers in Pharmacology, suggested the title of this special issue and invited AN, CU, and J-FR as co-editors. The Editorial was written by AN and VT with comments from CU and J-FR.

REFERENCE

Dutertre, S., Nicke, A., and Tsetlin, V. I. (2017). Nicotinic acetylcholine receptor inhibitors derived from snake and snail venoms. *Neuropharmacology* 127, 196–223. doi: 10.1016/j.neuropharm.2017.06.011

Conflict of Interest: The authors declare that the research was conducted in the absence of any commercial or financial relationships that could be construed as a potential conflict of interest.

frontiers in Pharmacology

ORIGINAL RESEARCH
published: 16 October 2018
doi: 10.3389/fphar.2018.01158

Discovery of a Novel $Na_v1.7$ Inhibitor From *Cyriopagopus albostriatus* Venom With Potent Analgesic Efficacy

Yunxiao Zhang†, Dezheng Peng†, Biao Huang†, Qiuchu Yang, Qingfeng Zhang, Minzhi Chen, Mingqiang Rong and Zhonghua Liu**

The National and Local Joint Engineering Laboratory of Animal Peptide Drug Development, College of Life Sciences, Hunan Normal University, Changsha, China

OPEN ACCESS

Edited by:
Annette Nicke, Ludwig-Maximilians-Universität München, Germany

Reviewed by:
David J. Adams, University of Wollongong, Australia
Roope Mannikko, University College London, United Kingdom

***Correspondence:**
Mingqiang Rong
rongmq@hunnu.edu.cn
Zhonghua Liu
liuzh@hunnu.edu.cn

†These authors have contributed equally to this work

Specialty section:
This article was submitted to Pharmacology of Ion Channels and Channelopathies, a section of the journal Frontiers in Pharmacology

Received: *12 July 2018*
Accepted: *24 September 2018*
Published: *16 October 2018*

Citation:
Zhang Y, Peng D, Huang B, Yang Q, Zhang Q, Chen M, Rong M and Liu Z (2018) Discovery of a Novel $Na_v1.7$ Inhibitor From Cyriopagopus albostriatus Venom With Potent Analgesic Efficacy. Front. Pharmacol. 9:1158. doi: 10.3389/fphar.2018.01158

Spider venoms contain a vast array of bioactive peptides targeting ion channels. A large number of peptides have high potency and selectivity toward sodium channels. $Na_v1.7$ contributes to action potential generation and propagation and participates in pain signaling pathway. In this study, we describe the identification of μ-TRTX-Ca2a (Ca2a), a novel 35-residue peptide from the venom of Vietnam spider *Cyriopagopus albostriatus* (*C. albostriatus*) that potently inhibits $Na_v1.7$ (IC_{50} = 98.1 ± 3.3 nM) with high selectivity against skeletal muscle isoform $Na_v1.4$ (IC_{50} > 10 μM) and cardiac muscle isoform $Na_v1.5$ (IC_{50} > 10 μM). Ca2a did not significantly alter the voltage-dependent activation or fast inactivation of $Na_v1.7$, but it hyperpolarized the slow inactivation. Site-directed mutagenesis analysis indicated that Ca2a bound with $Na_v1.7$ at the extracellular S3–S4 linker of domain II. Meanwhile, Ca2a dose-dependently attenuated pain behaviors in rodent models of formalin-induced paw licking, hot plate test, and acetic acid-induced writhing. This study indicates that Ca2a is a potential lead molecule for drug development of novel analgesics.

Keywords: sodium channel, electrophysiology, tarantula spider, peptide toxin, $Na_v1.7$, analgesic activity

INTRODUCTION

Voltage-gated sodium channels (VGSCs) are important integral membrane proteins expressed in electrically excitable cells. The opening of pore-forming α subunits causes an influx of sodium ions, which is essential for action potential generation and propagation. VGSCs are composed of α subunits in association with one or more auxiliary β subunits (Catterall, 2000, 2012, 2014). The α subunits are organized in four homologous domains (DI–DIV), each of which consists of six transmembrane α helices (S1–S6) connected by extracellular and intracellular loops. Up to now, nine distinct VGSC α subunits ($Na_v1.1$–1.9) and four β subunits have been cloned from mammals (Dib-Hajj et al., 2010). Compelling genetic studies and clinical evidence have revealed the importance of human $Na_v1.7$ ($hNa_v1.7$) as an analgesic target (Dib-Hajj et al., 2009; Wang et al., 2011; Gingras et al., 2014).

Loss-of-function mutations in *SCN9A*, the gene encoding $hNa_v1.7$, have been identified as a cause of congenital insensitivity to pain (CIP) (Mansouri et al., 2014; Shorer et al., 2014), while gain-of-function mutations of *SCN9A* are the cause of several pain disorders, including inherited

erythromelalgia (IEM) (Wu et al., 2017), paroxysmal extreme pain disorder (PEPD) (Fertleman et al., 2006) and small fiber neuropathy (Faber et al., 2012). Therefore, chemicals pharmacologically inhibiting $hNa_v1.7$ activity have the potential to treat chronic pain. Developing analgesics against $hNa_v1.7$ with Na_v subtype selectivity is essential, because α subunit shares high sequence similarity between each other, and off-target may cause serious side effects, especially $Na_v1.4$ expressed in skeletal muscle and $Na_v1.5$ expressed in cardiac muscle.

Spider venom is a highly complex mixture, mainly containing protein, polypeptide, and small molecules. Polypeptide toxins can specifically interact with ion channel proteins, membrane receptors, and transporters, and the spider venom-derived peptide toxins were used as a potential rich source of drug discovery (Escoubas and King, 2009; King, 2011). Most venom peptides have disulfide-rich architectures that provide extreme stability and a high level of resistance to proteases, which are necessary characteristics for drug discovery and design. The venom of spider *Cyriopagopus albostriatus* (C. *albostriatus*) has not been well investigated yet. Here we reported the isolation and characterization of μ-TRTX-Ca2a (Ca2a), a 35-residue peptide isolated from the venom of Vietnam Tarantula C. *albostriatus* with high potency and selectivity against $Na_v1.7$. Rodent pain models demonstrated that Ca2a had powerful analgesic effects.

MATERIALS AND METHODS

Purification of Peptide

The crude venom of *C. albostriatus* was obtained by electronic stimulation, and preserved at −80°C after lyophilization. The lyophilized venom was dissolved in ddH_2O to a final concentration of 5 mg/ml and subjected to the first round of semi-preparative RP-HPLC purification (C18 column, 10 mm × 250 mm, 5 μm, Welch, Shanghai, China) using linear acetonitrile gradient ranging from 10 to 55% with an increasing rate of 1% per minute (Waters e2695 Separations Module, Waters, CA, United States). The fraction containing Ca2a was then collected, lyophilized, and subjected to a second round of analytical RP-HPLC purification (C18 column, 4.6 mm × 250 mm, 5 μm, Welch, Shanghai, China). The acetonitrile gradient was increased ranging from 20 to 40% at an increasing rate of 1% per minute (Waters 2795 Separations Module, Waters, CA, United States). Fractions were lyophilized and stored at −20°C before use. The purity of the toxin was tested by MALDI-TOF MS analysis (AB SCIEX TOF/TOF^{TM} 5800 system, Applied Biosystems, United States).

Plasmid and Transfection

The cDNA genes encoding rat $Na_v1.4$ and human $Na_v1.7$ were subcloned into vectors pRGB4 and pcDNA3.1-mod, respectively. Mutations of $rNa_v1.4$ (N655D, Q657E, and N655D/Q657E) and $hNa_v1.7$ (D816N, E818Q, and D816N/E818Q) were constructed using the Gene Tailor Site-Directed Mutagenesis system (Invitrogen, Carlsbad, CA, United States), according to the manufacturer's instructions. $Na_v1.2$–$Na_v1.7$ and mutant plasmids together with eGFP were transiently transfected into HEK293T cells while $Na_v1.8$ together with eGFP was transiently transfected into ND7/23 cells by Lipofectamine 2000 (Invitrogen, Carlsbad, CA, United States). Additionally, plasmids β1- and β2-eGFP encoding the human β1 and β2 subunits, respectively, were co-transfected with those encoding WT $Na_v1.7$ and $Na_v1.7$ mutations in HEK293T cells. Human $Na_v1.9$ was transfected into ND7/23 cells according to a previous report (Zhou et al., 2017). HEK293T and ND7/23 cells were grown under standard tissue culture conditions (5% CO_2, 37°C) in Dulbecco's modified Eagle's medium (DMEM) supplemented with 10% fetal bovine serum (FBS). Cells with green fluorescent protein fluorescence were selected for whole-cell patch-clamp recordings 24 h after transfection.

Whole-Cell Patch-Clamp Recordings

Whole-cell patch-clamp recordings were performed at room temperature (20–25°C) using an EPC 10 USB Patch Clamp Amplifier (HEKA, Elektronik, Lambrecht, Germany). Suction pipettes with access resistance of 2.0–3.0 MΩ were made from borosilicate glass capillary tubes (thickness = 0.225 mm) using a two-step vertical microelectrode puller (PC-10; Narishige, Tokyo, Japan). The standard pipet solution contained (in mM): 140 CsCl, 10 NaCl, 1 EGTA, and 10 HEPES (pH 7.4). Bath solution contained (in mM): 140 NaCl, 2 $CaCl_2$, 1 $MgCl_2$, 5 KCl, 20 HEPES (pH 7.4), and 10 glucose. All chemicals were the products of Sigma-Aldrich (St. Louis, MO, United States) and dissolved in water. Data was acquired by PatchMaster software (HEKA Elektronik, Lambrecht, Germany). Data was analyzed by software Igo Pro 6.10A (WaveMetrics, Lake Oswego, OR, United States), SigmaPlot 10.0 (Sigma-Aldrich, St. Louis, MO, United States), OriginPro 8 (OriginLab Corp., Northampton, MA, United States), and GraphPad Prism 5 (GraphPad Software, San Diego, CA, United States). Membrane currents were filtered at 5 kHz and sampled at 20 kHz. To minimize voltage errors, 80–90% series resistance compensation was applied. Voltage-clamp recordings were acquired 5 min after establishing whole-cell configuration to allow adequate equilibration between the micropipette solution and the cell interior.

The $Na_v1.2$–$Na_v1.7$ channel currents were elicited by 50 ms depolarization potential to −10 mV from the holding voltage of −100 mV. The depolarization potential for $Na_v1.8$ was +20 mV. The $Na_v1.9$ current was elicited by 50 ms depolarization potential to −40 mV from the holding voltage of −120 mV in the presence of 1 μM TTX.

To measure current–voltage (I–V) relationships, a range of potentials from −100 mV to +80 mV in 5 mV increments were applied from the holding potential (−100 mV) for 50 ms at 5 s intervals. Peak values at each potential were plotted to form I–V curves. Activation curves were obtained by calculating the conductance G at each voltage. $G = I/(V - V_{rev})$, with V_{rev} being the reversal potential, determined for each cell individually. Steady-state fast inactivation was assessed with a 20-ms depolarizing test potential of −10 mV following a 500-ms prepulse at potentials that ranged from −110 to −30 mV with a 10-mV increment.

Fast inactivation time constants were calculated by fitting current decay traces with a single exponential function using the

I–V protocol described above. Recovery from fast-inactivation (repriming) was assessed by using a two-pulse protocol consisting of a depolarizing pulse to −10 mV for 50 ms to inactivate channels, followed by a step to −100 mV of variable duration (1 to 1024 ms) to promote recovery, and 50 ms test pulse to −10 mV to assess availability of channels. Voltage dependence of steady-state slow inactivation was measured using a series of 15 s pre-pulses, ranging from −120 to 0 mV in 10-mV increments, followed by a 50 ms step to −100 mV to remove fast inactivation, and a 50 ms test pulse to −10 mV to assess the available non-inactivated channels. The rate of toxin dissociation was determined by stepping to a depolarizing pulse of 100, 80, or 60 mV for various durations followed by a 500 ms hyperpolarization to −100 mV to allow recovery from fast inactivation, and then assessing the effect of the depolarizing pulse with a 50-ms test pulse to −10 mV. Very little re-binding takes place due to slow kinetics of the blocking of the channel during 500-ms hyperpolarization to −100 mV. Use/frequency-dependent inhibition of the channel was measured by applying repetitive pulses of different frequencies (1, 5, and 10 Hz) that mimic high firing frequency of DRG neurons expressing $Na_v1.7$.

Animals

The ICR mice (18–22 g) used in this study were purchased from the Experimental Animal Center of SLac-kinda (Changsha, China). The animals were maintained at 20–25°C and freely allowed to standard rodent chow and water *ad libitum*. Ethical approval for *in vivo* experiments in animals was approved by the Animal Care and Use Committee (ACUC) at the Hunan Province Animal Management Office (HPAMO).

Formalin-Induced Paw Licking

A formalin test was performed according to the previous method (Owoyele et al., 2005). Mice were intraperitoneally injected with saline, morphine or Ca2a 30 min before injection with 20 μL formalin (5%) solution under the plantar surface of the right hind paw. The time spent licking the injected paw by each mouse was recorded by a digital stopwatch during Phase I (0–15 min post-injection) and Phase II (15–40 min post-injection).

Hot Plate Test

According to a previous method (Meng et al., 2017), a hot plate apparatus (model YLS-21A, Jinan, China) maintained at 55 ± 1°C, was used to measure the pain threshold of mice subjected to a thermal stimulus. Each female mouse was placed on hot plate to observe its pain response (hind-paw-licking or jumping) acted as its own control. The mice whose latent response times were shorter than 5 s or longer than 30 s were excluded from the test. The saline, morphine, and Ca2a were intraperitoneally injected to mice and the latent response time was recorded at 0.5, 1, 1.5, and 2 h.

Abdominal Writhing Induced by Acetic Acid

According to the method previously described (Liu et al., 2014), mice were injected intraperitoneally with a saline, morphine, or Ca2a for 15 min prior to injection with 200 μL of 0.8% (*v/v*) acetic acid solution, which induced abdominal contraction and hind limb stretching. The abdominal writhing responses were counted for 30 min continuously.

Data Analysis

Concentration-response curves were fitted using the following Hill logistic equation: $y = f_{max} - (f_{max} - f_{min})/(1 + (x/IC_{50})^n)$, where f_{max} and f_{min}, respectively, represent the channel's maximum and minimum responses to toxins, f_{min} was set to 0, x represents toxin concentration and n is an empirical Hill coefficient. Activation curves were fitted with the Boltzmann equation: $y = 1/(1 + \exp(V - V_{1/2}/k))$, in which V is the test potential, $V_{1/2}$ is the midpoint voltage of kinetics, and k is the slope factor. Peak inward currents from steady-state inactivation were normalized by the maximum current amplitude and fit with a Boltzmann equation $I = I_{min} + 1/(1 + \exp[V_m - V_{1/2}/k])$ where I is the current amplitude measured during the test depolarization, $V_{1/2}$ is the midpoint of inaction, and k is the slope factor. The currents recovery from inactivation were fitted using a single exponential equation $f(t) = Ae^{-t/T} + C$, where A represents the amplitude of the current, t is the time, τ is the time constant, and C is the steady-state asymptote. Statistical analyses were performed using paired student's t-test or ANOVA with paired comparisons. Results with $p < 0.05$ were considered significant. All data are presented as mean ± SEM.

RESULTS

Isolation of Ca2a From *C. albostriatus*

The venom of spider *C. albostriatus* was purified by C18 RP-HPLC. The eluted fractions were lyophilized and tested on pain-related ion channel $hNa_v1.7$ heterologously expressed in HEK293T cells. The peak labeled with the red asterisk showed inhibition activity against $Na_v1.7$ (**Figure 1A**). This fraction was further purified by analytical RP-HPLC (**Figure 1B**, asterisk labeled peak). MALDI-TOF MS analysis revealed that this peak represented a peptide toxin with a molecular weight of 3905.08 Da (**Figure 1C**). N-terminal Edman sequencing disclosed that the novel peptide toxin contained 35 amino acid residues (**Figure 1D**) and was named μ-TRTX-Ca2a (Ca2a). Ca2a contained six cysteines and belonged to the Family 1 of NaSpTx conforming to a conserved cysteine pattern of ICK motif. This family is comprised by spider venom-derived Na_v channel toxins with 33–35 residues forming a hyper-stable ICK motif (Klint et al., 2012).

Selectivity of Ca2a for Sodium Channel Subtypes

The biological function of Ca2a was investigated on HEK293T cells transiently transfected with VGSCs. A total of 1 μM Ca2a showed 87.3 ± 4.4% inhibition on $Na_v1.7$ currents, and decreased the $Na_v1.2$, $Na_v1.3$, and $Na_v1.6$ current amplitude by 82.6 ± 2.7%, 67.7 ± 3.8%, and 78.7 ± 2.9%, respectively. However, no inhibitory effects were observed against $Na_v1.4$,

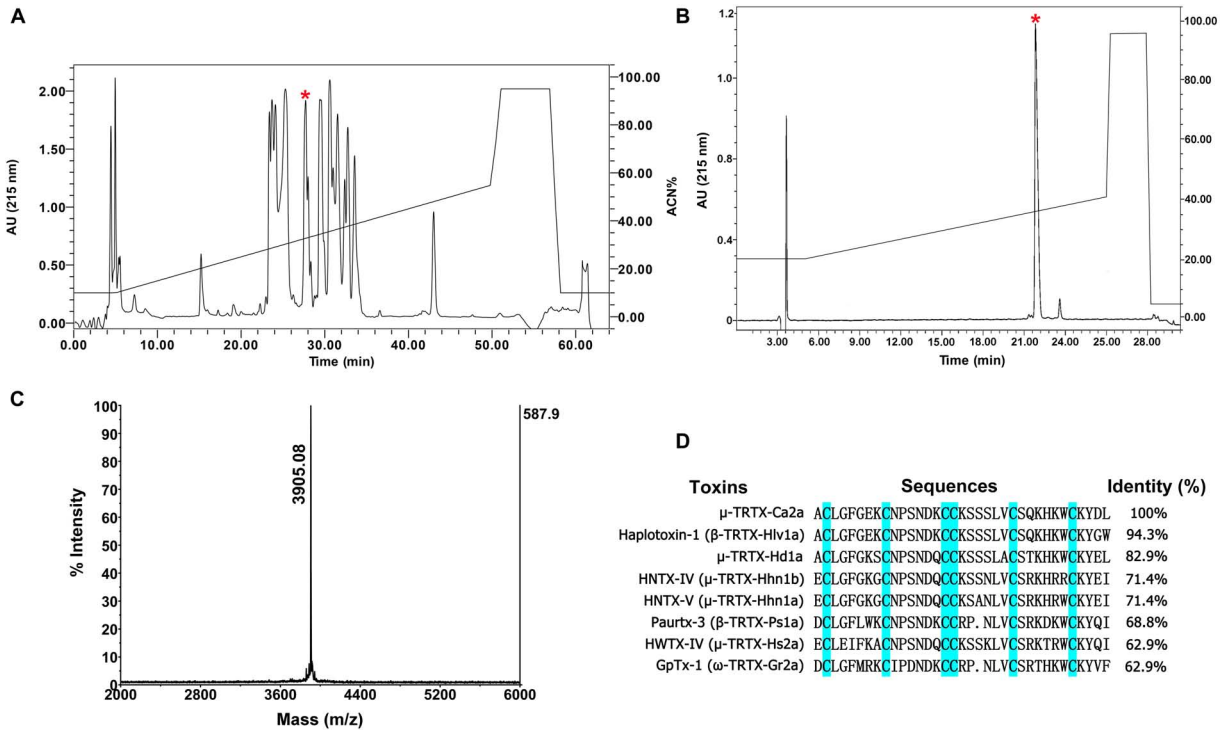

FIGURE 1 | Identification of μ-TRTX-Ca2a from the venom of spider *C. albostriatus*. **(A)** Isolation of native Ca2a from the pooled protein fraction by a C18 RP-HPLC column. **(B)** Ca2a was purified to homogeneity by analytical RP-HPLC. **(C)** MALDI-TOF MS analysis showing a single predominant mass of 3905.08 Da. **(D)** Cysteines shaded in *cyan* formed disulfide bonds. Sequence alignment of Ca2a with related toxins. N-terminal sequencing analysis revealed a peptide with 35 residues containing 6 cysteines.

$Na_v1.5$, $Na_v1.8$, or $Na_v1.9$ currents even at high concentrations of up to 10 μM Ca2a (**Figures 2A–H**). Currents of $Na_v1.1$ were not detected in heterogeneously expressed HEK293T cells, and the effect of Ca2a on $Na_v1.1$ could not be examined in the present study. Thus, Ca2a had highest potency for $Na_v1.7$ (IC_{50} of 98.1 ± 3.3 nM), followed by $Na_v1.2$ (IC_{50} of 216.3 ± 9.1 nM), $Na_v1.6$ (IC_{50} of 313.6 ± 6.3 nM), and $Na_v1.3$ (IC_{50} of 491.3 ± 3.9 nM) (**Figure 2I**).

Effect of Ca2a on $Na_v1.7$ Activation and Inactivation Properties

Many spider peptide toxins are regarded as gating modifiers because these toxins bind to the voltage-sensing domains of Na_v channels and alter voltage dependence of activation and/or inactivation (Catterall et al., 2007). Ca2a inhibited 64.5 ± 2.1% of the $Na_v1.7$ current at the concentration of 0.2 μM (**Figure 3A**), so we chose this subsaturation concentration to analyze the effects of Ca2a on the activation and inactivation of $Na_v1.7$. Ca2a decreased the currents at all tested voltages, but it did not change the threshold of initial activation voltage, the active voltage of peak current, or the reversal potential of the $Na_v1.7$ current (**Figure 3B**). In addition, the half-activation voltage and half-inactivation voltage of $Na_v1.7$ after treatment with 0.2 μM Ca2a were −18.9 ± 1.3 and −70.7 ± 1.1 mV, respectively. In the control group, the half-activation voltage and the half-inactivation voltage of $Na_v1.7$ were −20.1 ± 1.1 and −70.2 ± 0.8 mV, respectively. These results indicated that Ca2a inhibited the peak currents without affecting the voltage-dependent activation and fast inactivation (**Figures 3C,D**).

Kinetics of Ca2a Inhibition and Dissociation in $Na_v1.7$

Spider toxins usually modulate the gating behaviors of VGSCs and can influence voltage sensor movement (Yamaji et al., 2009; Bosmans and Swartz, 2010). To investigate the effects of Ca2a on the kinetics of fast inactivation and repriming, we measured the time constants of fast inactivation and recovery from fast inactivation. Fast inactivation time constants were calculated by fitting current decay traces with a single exponential function. Ca2a only inhibited the peak current, but it did not alter the inactivation time constants between −15 and 10 mV ($P > 0.05$; two-way ANOVA; **Figure 4A**). However, Ca2a significantly but modestly slowed recovery from fast inactivation at $Na_v1.7$ (control, τ = 6.42 ± 0.85 ms; Ca2a, τ = 8.93 ± 1.62 ms; $P < 0.05$; paired *t*-test; **Figure 4B**). Moreover, Ca2a significantly shifted steady-state slow inactivation to more hyperpolarized membrane potentials (control, −52.62 ± 3.79 mV; Ca2a, −72.00 ± 2.76 mV; $P < 0.01$; paired *t*-test; **Figure 4C**). Slow inactivation is a process that occurs under a high-frequency stimulation or a prolonged depolarizing pulse. This process is most likely to involve a rearrangement of the channel pore, which results in a different conformational state and directly regulates

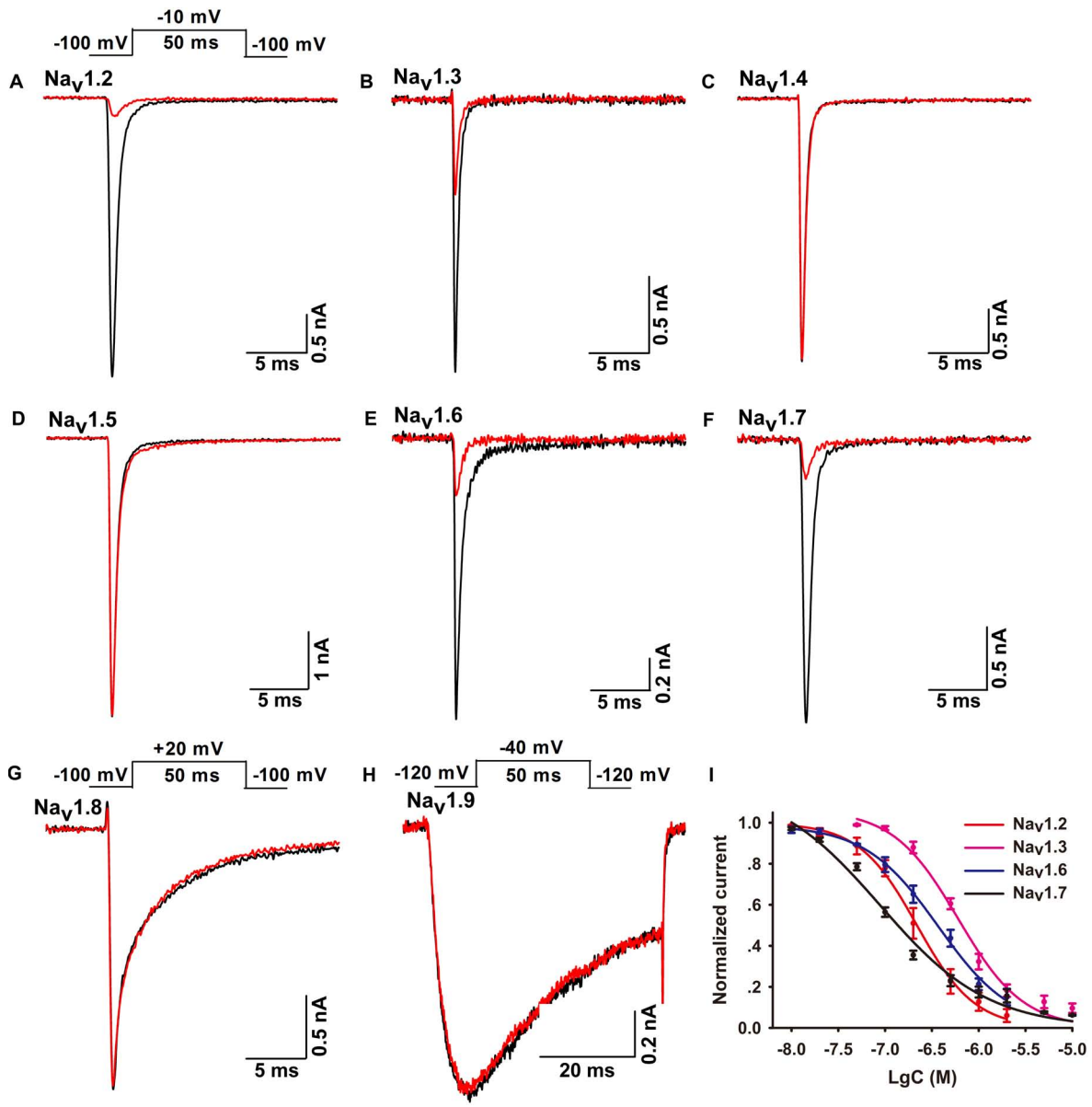

FIGURE 2 | Effects of μ-TRTX-Ca2a on $Na_v1.2$–$Na_v1.9$ channels. **(A–H)** Representative $Na_v1.2$–$Na_v1.9$ current traces before (black) and after (red) addition of Ca2a. Ca2a at 1 μM inhibited $Na_v1.2$–$Na_v1.3$, $Na_v1.6$, and $Na_v1.7$. 10 μM Ca2a showed no obvious effect on $Na_v1.4$–$Na_v1.5$ or $Na_v1.8$–$Na_v1.9$ current. Inset above panel **(A)** shows the pulse protocol for recording $Na_v1.2$–$Na_v1.7$ channel currents. Inset above panel **(G)** shows the pulse protocol for recording $Na_v1.8$ channel current. Inset above panel **(H)** shows the pulse protocol for recording $Na_v1.9$ channel current. **(I)** Concentration-response curves of Ca2a at $Na_v1.2$–$Na_v1.3$, $Na_v1.6$, and $Na_v1.7$ assessed by whole-cell patch-clamp experiments. Data are mean ± SEM, with n = 4–7 cells per data point.

cellular excitability (Chatterjee et al., 2018). The dissociation time constants were calculated to be 169.8 ± 25.6 ms at 100 mV, 347.9 ± 29.2 ms at 80 mV, and 547.2 ± 24.3 ms at 60 mV in the presence of 1 μM Ca2a (**Figure 4D**). This indicated that Ca2a dissociated quickly from $Na_v1.7$ in a voltage-dependent manner. In addition, Ca2a did not show obvious use/frequency dependence of inhibition for $Na_v1.7$, and the IC_{50} values of 1, 5, and 10 Hz were 229.3 ± 34.8, 243.8 ± 30.7, and 184.9 ± 23.8 nM, respectively (**Supplementary Figure S1**).

Ca2a Binds to the DIIS3–S4 Linker of $Na_v1.7$

The mechanism of Ca2a acting on $Na_v1.7$ is similar to that of HWTX-IV and HNTX-III, and it might be a site 4 toxin acting on the DIIS3–S4 linker of the sodium channel (Xiao et al., 2008; Liu et al., 2013). As Ca2a showed no activity on $Na_v1.4$, we constructed chimeric channels of $Na_v1.4$ and $Na_v1.7$ to validate this hypothesis. As shown in **Figure 5A**, only two amino acids are different in DIIS3–S4 linkers of $Na_v1.4$ and

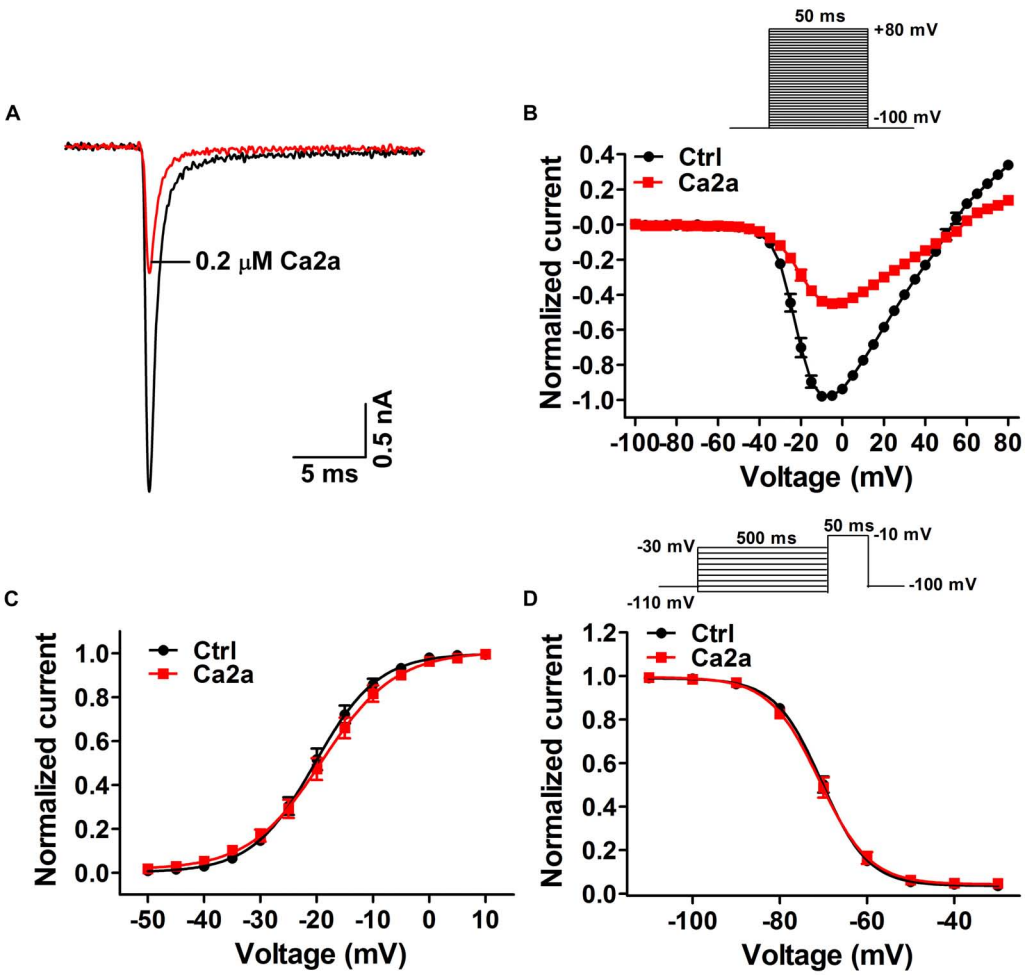

FIGURE 3 | Effects of μ-TRTX-Ca2a on the voltage dependence of $Na_v1.7$ activation and inactivation gating. **(A)** Representative current traces of $Na_v1.7$ channel inhibited by 0.2 μM Ca2a. **(B)** I–V curves before (black) and after (red) treatment of Ca2a (n = 10). Inset shows the pulse protocol for measuring current–voltage (I–V) relationships. **(C)** G–V curves before (black) and after (red) treatment of Ca2a (n = 10). **(D)** Voltage-dependence of steady-state fast inactivation curves before (black) and (red) after treatment of Ca2a (n = 10). Inset shows the pulse protocol for measuring steady-state fast inactivation.

$Na_v1.7$. To investigate the role of these two acidic residues, we mutated their compartments in $Na_v1.4$ (N655D, Q657E, and N655D/Q657E). The results showed that 1 μM Ca2a had no inhibitory effect on WT $Na_v1.4$ and $Na_v1.4$/N655D, but it significantly inhibited the peak current of $Na_v1.4$/Q657E and $Na_v1.4$/N655D/Q657E (**Figures 5C–F**). The IC_{50} values of $Na_v1.4$/Q657E and Nav1.4/N655D/Q657E were 268.9 ± 14.9 and 237.9 ± 26.1 nM, respectively (**Figure 5B**). These results indicate that the residue Q657 plays an important role in resistance to Ca2a rather than N655 located in DIIS3–S4 linker of $Na_v1.4$.

To validate the role of Q657 in Ca2a inhibition, we constructed reverse mutations in $Na_v1.7$ (D816N, E818Q, and D816N/E818Q). A total of 1 μM Ca2a significantly inhibited $Na_v1.7$/D816N current amplitude with IC_{50} value (172.0 ± 11.4 nM) twofold higher than the wild type. This validates the hypothesis that D816 plays a negligible role in Ca2a interacting with $Na_v1.7$ (**Figures 6B,E**). The time course of 1 μM Ca2a inhibiting the Nav1.7/D816N current was characterized by a slow onset of action (τ_{on} = 18.4 ± 1.3 s) similar to that of WT $Na_v1.7$ (τ_{on} = 18.0 ± 2.5 s) while the current did not recover during the extended washout in contrast to that of WT $Na_v1.7$ (τ_{off} = 295.6 ± 27.5 s) (**Supplementary Figures S2A,B**). In contrast to complete inhibition on WT $Na_v1.7$ (**Figure 6A**), 1 μM Ca2a showed no activity on $Na_v1.7$/E818Q or $Na_v1.7$/D816N/E818Q, implying that E818 plays an important role in Ca2a inhibition (**Figures 6C,D**). These results demonstrate that the DIIS3–S4 linker is critical for Ca2a binding to the sodium channel.

Effects of Ca2a on Pain

To assess the analgesic potential of Ca2a *in vivo*, we examined the effects of Ca2a in animal models of pain including formalin-induced paw licking, hot plate test and acetic acid-induced writhing.

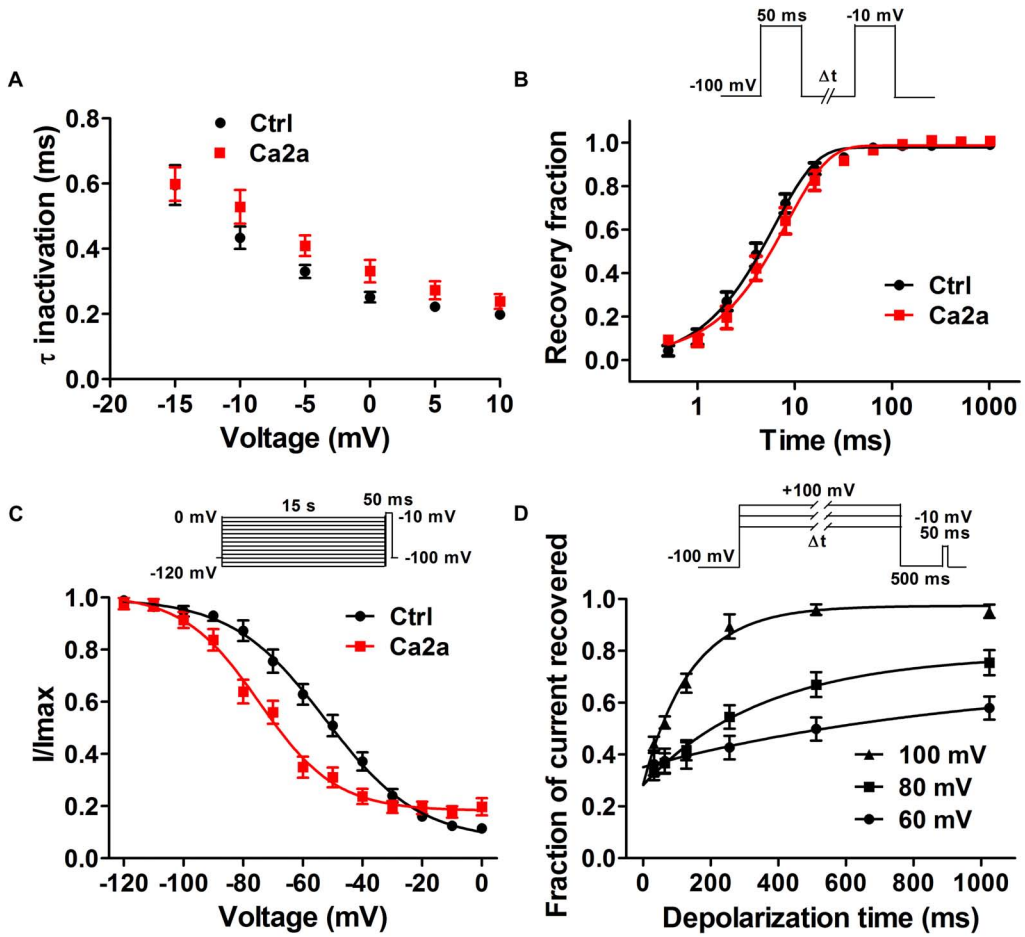

FIGURE 4 | $Na_v1.7$ kinetic parameters affected by the addition of μ-TRTX-Ca2a. **(A)** Voltage-dependence of fast inactivation time constants of $Na_v1.7$ before (black) and after (red) addition of 0.2 μM Ca2a. **(B)** Kinetics of current recovery from fast inactivation of $Na_v1.7$ before (black) and after (red) addition of 0.2 μM Ca2a at −100 mV. Inset shows the pulse protocol for measuring recovery from fast-inactivation. **(C)** Voltage-dependence of steady-state slow inactivation of $Na_v1.7$ before (black) and after (red) addition of 0.2 μM Ca2a. Inset shows the pulse protocol for measuring steady-state slow inactivation. **(D)** Time course of dissociation of 1 μM Ca2a from $Na_v1.7$ at 100, 80, and 60 mV. Data are mean ± SEM, with n = 6–11 cells per data point. Inset shows the pulse protocol for measuring the rate of toxin dissociation.

The paw licking time of the control was 90.3 ± 6.6 s on Phase I (0–15 min) and 197.7 ± 20.7 s on Phase II (15–40 min) (**Figure 7A**). The paw licking time in Phase I was 80.1 ± 4.6 s, 79.4 ± 9.5 s and 75.6 ± 7.7 s for 50, 100, and 200 μg/kg Ca2a, respectively, while the paw licking time of 100 μg/kg morphine was 64.1 ± 8.5 s on Phase I (**Figure 7A**). Ca2a (50, 100, and 200 μg/kg) produced no analgesic effect on Phase I compared to the control while morphine (100 μg/kg) showed modest analgesia (**Figure 7B**). However, Ca2a produced a significant analgesic effect in a dose-dependent manner on Phase II. The paw licking time was significantly reduced to 100.9 ± 16.2 s, 67.2 ± 20.2 s, and 40.5 ± 7.1 s for 50, 100, and 200 μg/kg Ca2a, respectively. The paw licking time of 100 μg/kg morphine was 126.1 ± 19.8 s in Phase II (**Figure 7C**). In the hot plate test, Ca2a also showed a strong analgesic effect (**Figure 7D**). The latency time of the control was 10.6 ± 1.1 s, while the latency time of Ca2a at each dose (50, 100, and 200 μg/kg) was increased to 12.9 ± 0.8 s, 15.4 ± 1.2 s, and 18.1 ± 1.6 s, respectively. As a positive control, the latency time of morphine at a concentration of 2 mg/kg increased to 15.2 ± 1.9 s (**Figure 7E**). In the acetic acid-induced writhing test, Ca2a dose-dependently reduced the writhing numbers. Intraperitoneal injection of 50, 100, and 200 μg/kg Ca2a reduced the duration of writhing from 27.3 ± 3.3 of the control to 15.8 ± 2.4, 10.5 ± 2.8, and 5.4 ± 2.2, respectively, while morphine at 100 μg/kg caused a reduction to 11 ± 3.7 (**Figure 7F**).

DISCUSSION

In this study, we described the identification and characterization of a novel peptide μ-TRTX-Ca2a, which is a 35-residue peptide toxin isolated from the venom of tarantula spider *C. albostriatus* with six cysteines and belongs to the ICK motif. It has been thought that ICK toxins typically owned tremendous chemical,

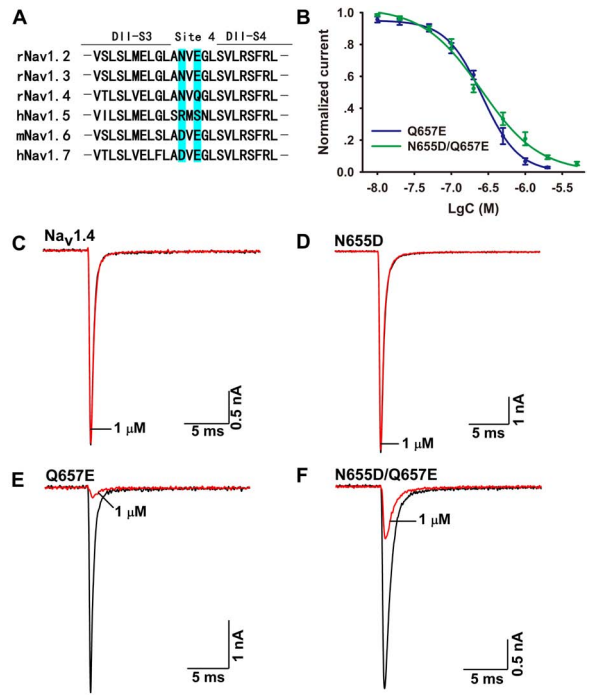

FIGURE 5 | Effect of Ca2a on WT and mutant $Na_v1.4$ expressed in HEK293T cells. **(A)** Amino acids of potential binding sites in the sequence were shaded in *cyan*. Sequence alignment of DIIS3-S4 of $Na_v1.2$–$Na_v1.7$. **(B)** Dose-response curves of Q657E and N655D/Q657E. **(C–F)** Representative current traces for WT and mutant channels (N655D, Q657E, and N655D/Q657E) inhibited by 1 μM Ca2a. Data are mean ± SEM, with n = 4–5 cells per data point.

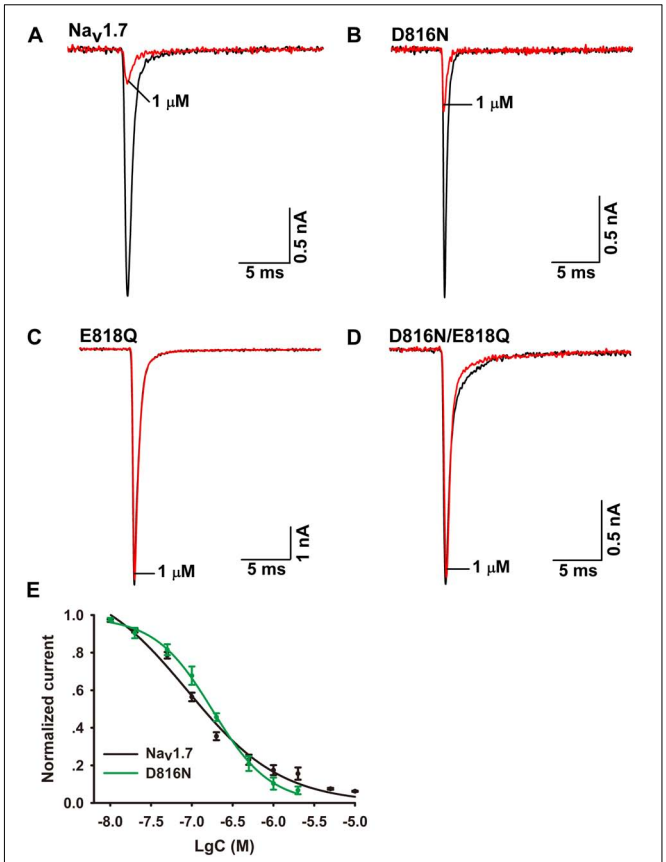

FIGURE 6 | Effect of Ca2a on WT and mutant $Na_v1.7$ expressed in HEK293T cells. **(A)** Representative current traces for WT inhibited by 1 μM Ca2a. **(B–D)** Representative current traces for mutant channels (D816N, E818Q, and D816N/E818Q) inhibited by 1 μM Ca2a. **(E)** Dose-response curves of $Na_v1.7$ and D816N. Data are mean ± SEM, with n = 5 cells per data point.

thermal, and biological stability and provided a variety of delivery options for therapeutic administration (Colgrave and Craik, 2004; Saez et al., 2010). Ca2a inhibited $Na_v1.2$, $Na_v1.3$, $Na_v1.6$, and $Na_v1.7$ channels but had negligible effect on $Na_v1.4$, $Na_v1.5$, $Na_v1.8$, and $Na_v1.9$ channels, suggesting that Ca2a is a selective antagonist of neuronal TTX-S VGSCs. Meanwhile, Ca2a ought to have an effect on neurons where $Na_v1.7$ accounts for a majority of TTX-S Na^+ current, and peptide toxins inhibiting $Na_v1.7$ usually have inhibitory activity on DRG neurons (Deuis et al., 2017; Kornecook et al., 2017; Moyer et al., 2018).

Ca2a belongs to NaSpTx family 1 and shares identity to some known spider toxins. β-TRTX-Hlv1a from *Haplopelma lividum* exhibits 94.3% identity to Ca2a (Meir et al., 2011). Although β-TRTX-Hlv1a was thought to be a Na_v channel inhibitor, it only inhibited $Na_v1.3$ with IC_{50} of 1 μM. Moreover, β-TRTX-Ps1a (Pautx-3) and ω-TRTX-Gr2a (GpTx-1) with an identity of 68.8 and 62.9% to Ca2a, respectively, were potent VGSC blockers (Bosmans et al., 2006; Cherki et al., 2014). β-TRTX-Ps1a was an inhibitor of $Na_v1.2$, but it had no effect on $Na_v1.7$. ω-TRTX-Gr2a exhibited activity against all sodium channel subtypes ($Na_v1.1$–$Na_v1.8$) without any selectivity. Similar to μ-TRTX-Hhn1b (HWTX-IV), Ca2a showed preferred affinity to $Na_v1.7$ without inhibitory activity against $Na_v1.5$ or $Na_v1.4$ while HWTX-IV inhibited skeletal isoform $Na_v1.4$ with an IC_{50} value of 400 nM (Xiao et al., 2008; Goncalves et al., 2018). Therefore, Ca2a shows stronger activity or higher selectivity to $Na_v1.7$ than other similar toxins.

Consistent with the molecular mechanism of μ-TRTX-Hd1a, μ-TRTX-Hhn1b (HNTX-IV), and μ-TRTX-Hs2a (HWTX-IV) interacting with $Na_v1.7$, Ca2a caused no change of I–V curve, G–V curve, and steady-state fast inactivation. The critical residue of Ca2a binding to $Na_v1.7$ channel is E818 in the S3–S4 linker of DII. E818 also plays an important role in HWTX-IV's binding, but another residue D816 critical for HWTX-IV binding does not (Xiao et al., 2008; Cai et al., 2015; Klint et al., 2015). However, E818 is a critical residue for Ca2a binding to $Na_v1.7$, and $Na_v1.7$/E818Q greatly reduces the binding affinity of Ca2a. The IC_{50} value of $Na_v1.7$/D816N is similar to that of wild-type $Na_v1.7$, implying that D816 does not play an important role in binding affinity. Asn ($Na_v1.7$/D816N) residue may strengthen the binding energy and make the binding a more compact. The irreversible washout of Ca2a inhibition of $Na_v1.7$/D816N may be attributed to the higher binding energy and more compact structure. Ca2a did not affect channel inactivation progress, which was validated by a similar inactivation process

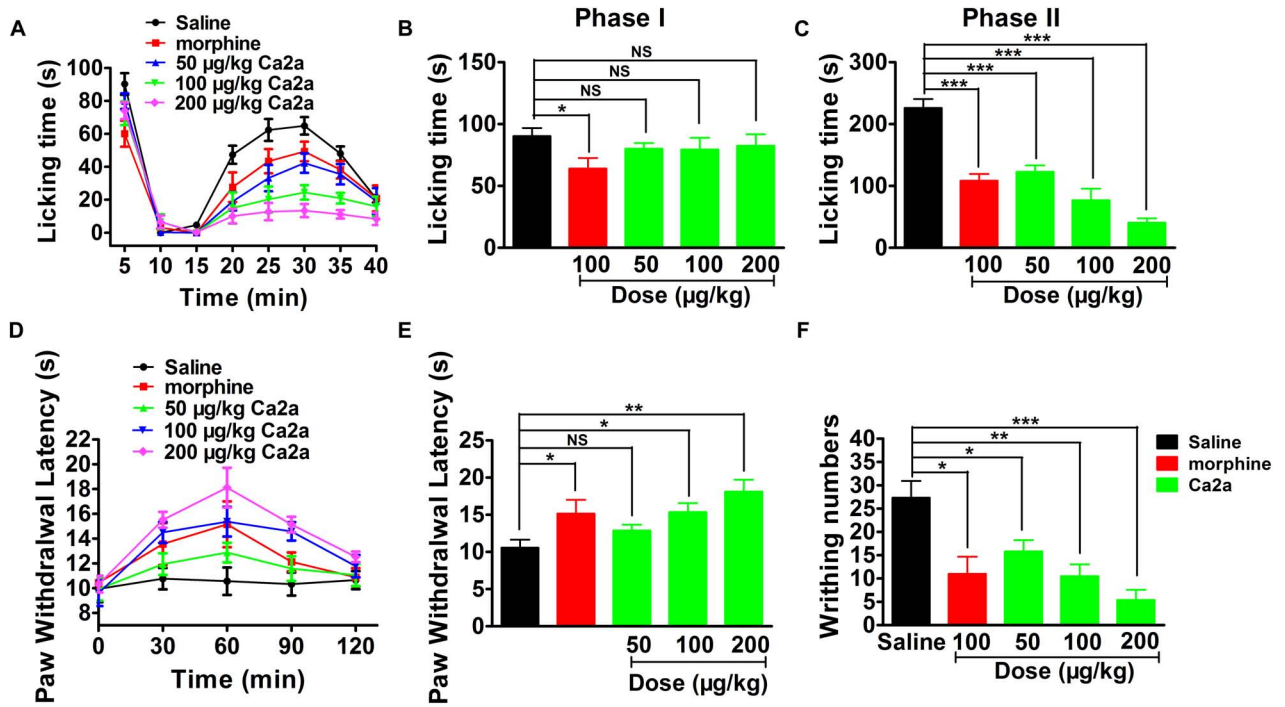

FIGURE 7 | Analgesic effect of Ca2a. **(A)** Time course of the antinociceptive effect of Ca2a in the formalin test. Evaluation of the antinociceptive effect of Ca2a on phase I **(B)** or phase II **(C)**. **(D)** Time course of the antinociceptive effect of Ca2a in hot plate test. **(E)** Analgesic effect was assessed after 30 min of Ca2a injection. **(F)** The antinociceptive effect of Ca2a in the abdominal constriction test. The data are shown as mean ± SEM, with $n = 6–8$; $^{*}P < 0.05$, $^{**}P < 0.01$, $^{***}P < 0.001$ vs. vehicle.

observed in $Na_v1.7$/D816N channel (**Supplementary Figure S3**). Nevertheless, Ca2a significantly but modestly slowed recovery from fast inactivation. In addition, the large hyperpolarized shift in slow inactivation suggests that Ca2a binds tightly to the slow inactivated state of the channel. These results suggest Ca2a may also interact with DIV because toxins affect channel inactivation by interacting with DIV (Xiao et al., 2010; Tao et al., 2016), and activation is affected by toxins binding to any of DI–III (Klint et al., 2015). This is similar with ProTx-II in which DII and DIV voltage sensors are involved in interaction by the dual modulatory effect (Bosmans et al., 2008) and a recently reported peptide Pn3a interacting with DII and DIV voltage sensors (Deuis et al., 2017). The mechanism of Ca2a acting on $Na_v1.7$ is similar to that of HWTX-IV, but it also exhibits a little difference.

In formalin-induced paw licking, hot plate test and abdominal writhing, Ca2a showed dose-dependently equipotent or stronger analgesia than morphine (100 μg/kg Ca2a equals to the concentration of 25.6 nmol/kg Ca2a, and 100 μg/kg morphine refers to 350.9 nmol/kg morphine). As a selective antagonist of neuronal TTX-S VGSCs, Ca2a preferentially inhibited $Na_v1.7$ with more than 100-fold selectivity against off-targets skeletal isoform $Na_v1.4$ and cardiac isoform $Na_v1.5$. Of the nine mammalian sodium channels, $Na_v1.3$, $Na_v1.7$, $Na_v1.8$, and $Na_v1.9$ channel subtypes are widely regarded as "pain channels" associated with nociception and chronic pain disorders that play essential roles in pain pathway (Dib-Hajj et al., 2010; Liu and Wood, 2011). In addition, $Na_v1.2$, distributed in the central nervous system, is unlikely to contribute to analgesia because it is associated with epilepsy (Sugawara et al., 2001). $Na_v1.6$, mainly distributed in the central nervous system and mature nodes of Ranvier in the peripheral nervous system (Habib et al., 2015), has been previously shown to be related with infantile epileptic encephalopathy (Veeramah et al., 2012; Estacion et al., 2014; Blanchard et al., 2015). However, recent studies have reported that the gain-of-function mutation of $Na_v1.6$ increased trigeminal ganglia (TRG) neuron excitability in trigeminal neuralgia (Tanaka et al., 2016) while $Na_v1.6$ knockdown ameliorated mechanical pain behavior in models of local inflammation and neuropathic pain (Xie et al., 2013, 2015). The exact role of $Na_v1.6$ in the pain pathway currently remains unclear currently. Inhibition of $Na_v1.6$ was also previously regarded to cause movement disorders and hind limb paralysis (Meisler et al., 2001). The dose of Ca2a used in this study does not cause significant adverse effects, indicating that the peptide dose not target $Na_v1.6$ *in vivo*. Meanwhile, the expression of $Na_v1.7$ is higher than other TTX-S VGSCs in DRG neurons (Fukuoka et al., 2008; Ho and O'Leary, 2011). $Na_v1.3$ is not expressed in adult rat DRG except for upregulated expression after nerve injury (Abe et al., 2002). Meanwhile, the effective analgesic doses of Ca2a used in the studies are very low. These results suggest that the analgesic effect of Ca2a is due to the inhibition of $Na_v1.7$ and not affected by blocking other Na_v channels. The effect of Ca2a on motor functions remains to be elucidated, and further study is required

to improve the selectivity and potency of Ca2a, making Ca2a a clinical potential peptide for the treatment of pain.

In summary, a new spider peptide toxin named μ-TRTX-Ca2a was identified. Ca2a binds to the DIIS3–S4 linker to inhibit channel current and may interact with DIVS3–S4 to affect channel inactivation. Moreover, *in vivo* analgesic efficacy suggests Ca2a may be a lead molecule for the development of analgesics targeting $Na_v1.7$ channel.

AUTHOR CONTRIBUTIONS

YZ, MR, and ZL conceived and designed the experiments. YZ, DP, BH, QY, QZ, and MC performed the experiments. YZ, DP, BH, and MR analyzed the data. YZ and MR wrote the manuscript. All authors have read and approved the manuscript.

FUNDING

This work was supported by NSFC (31670783 and 81573320).

SUPPLEMENTARY MATERIAL

The Supplementary Material for this article can be found online at: https://www.frontiersin.org/articles/10.3389/fphar.2018.01158/full#supplementary-material

REFERENCES

Abe, M., Kurihara, T., Han, W., Shinomiya, K., and Tanabe, T. (2002). Changes in expression of voltage-dependent ion channel subunits in dorsal root ganglia of rats with radicular injury and pain. *Spine* 27, 1517–1524; discussion 1525.

Blanchard, M. G., Willemsen, M. H., Walker, J. B., Dib-Hajj, S. D., Waxman, S. G., Jongmans, M. C., et al. (2015). De novo gain-of-function and loss-of-function mutations of SCN8A in patients with intellectual disabilities and epilepsy. *J. Med. Genet.* 52, 330–337. doi: 10.1136/jmedgenet-2014-102813

Bosmans, F., Martin-Eauclaire, M. F., and Swartz, K. J. (2008). Deconstructing voltage sensor function and pharmacology in sodium channels. *Nature* 456, 202–208. doi: 10.1038/nature07473

Bosmans, F., Rash, L., Zhu, S., Diochot, S., Lazdunski, M., Escoubas, P., et al. (2006). Four novel tarantula toxins as selective modulators of voltage-gated sodium channel subtypes. *Mol. Pharmacol.* 69, 419–429. doi: 10.1124/mol.105.015941

Bosmans, F., and Swartz, K. J. (2010). Targeting voltage sensors in sodium channels with spider toxins. *Trends Pharmacol. Sci.* 31, 175–182. doi: 10.1016/j.tips.2009.12.007

Cai, T., Luo, J., Meng, E., Ding, J., Liang, S., Wang, S., et al. (2015). Mapping the interaction site for the tarantula toxin hainantoxin-IV (beta-TRTX-Hn2a) in the voltage sensor module of domain II of voltage-gated sodium channels. *Peptides* 68, 148–156. doi: 10.1016/j.peptides.2014.09.005

Catterall, W. A. (2000). From ionic currents to molecular mechanisms: the structure and function of voltage-gated sodium channels. *Neuron* 26, 13–25. doi: 10.1016/S0896-6273(00)81133-2

Catterall, W. A. (2012). Voltage-gated sodium channels at 60: structure, function and pathophysiology. *J. Physiol.* 590, 2577–2589. doi: 10.1113/jphysiol.2011.224204

Catterall, W. A. (2014). Structure and function of voltage-gated sodium channels at atomic resolution. *Exp. Physiol.* 99, 35–51. doi: 10.1113/expphysiol.2013.071969

Catterall, W. A., Cestele, S., Yarov-Yarovoy, V., Yu, F. H., Konoki, K., and Scheuer, T. (2007). Voltage-gated ion channels and gating modifier toxins. *Toxicon* 49, 124–141. doi: 10.1016/j.toxicon.2006.09.022

Chatterjee, S., Vyas, R., Chalamalasetti, S. V., Sahu, I. D., Clatot, J., Wan, X., et al. (2018). The voltage-gated sodium channel pore exhibits conformational flexibility during slow inactivation. *J. Gen. Physiol.* 150, 1333–1347. doi: 10.1085/jgp.201812118

Cherki, R. S., Kolb, E., Langut, Y., Tsveyer, L., Bajayo, N., and Meir, A. (2014). Two tarantula venom peptides as potent and differential Na(V) channels blockers. *Toxicon* 77, 58–67. doi: 10.1016/j.toxicon.2013.10.029

Colgrave, M. L., and Craik, D. J. (2004). Thermal, chemical, and enzymatic stability of the cyclotide kalata B1: the importance of the cyclic cystine knot. *Biochemistry* 43, 5965–5975. doi: 10.1021/bi049711q

Deuis, J. R., Dekan, Z., Wingerd, J. S., Smith, J. J., Munasinghe, N. R., Bhola, R. F., et al. (2017). Pharmacological characterisation of the highly NaV1.7 selective spider venom peptide Pn3a. *Sci. Rep.* 7:40883. doi: 10.1038/srep40883

Dib-Hajj, S. D., Black, J. A., and Waxman, S. G. (2009). Voltage-gated sodium channels: therapeutic targets for pain. *Pain Med.* 10, 1260–1269. doi: 10.1111/j.1526-4637.2009.00719.x

Dib-Hajj, S. D., Cummins, T. R., Black, J. A., and Waxman, S. G. (2010). Sodium channels in normal and pathological pain. *Annu. Rev. Neurosci.* 33, 325–347. doi: 10.1146/annurev-neuro-060909-153234

Escoubas, P., and King, G. F. (2009). Venomics as a drug discovery platform. *Expert Rev. Proteomics* 6, 221–224. doi: 10.1586/epr.09.45

Estacion, M., O'Brien, J. E., Conravey, A., Hammer, M. F., Waxman, S. G., Dib-Hajj, S. D., et al. (2014). A novel de novo mutation of SCN8A (Nav1.6) with enhanced channel activation in a child with epileptic encephalopathy. *Neurobiol. Dis.* 69, 117–123. doi: 10.1016/j.nbd.2014.05.017

Faber, C. G., Hoeijmakers, J. G., Ahn, H. S., Cheng, X., Han, C., Choi, J. S., et al. (2012). Gain of function Nav1. 7 mutations in idiopathic small fiber neuropathy. *Ann. Neurol.* 71, 26–39. doi: 10.1002/ana.22485

Fertleman, C. R., Baker, M. D., Parker, K. A., Moffatt, S., Elmslie, F. V., Abrahamsen, B., et al. (2006). SCN9A mutations in paroxysmal extreme pain disorder: allelic variants underlie distinct channel defects and phenotypes. *Neuron* 52, 767–774. doi: 10.1016/j.neuron.2006.10.006

Fukuoka, T., Kobayashi, K., Yamanaka, H., Obata, K., Dai, Y., and Noguchi, K. (2008). Comparative study of the distribution of the alpha-subunits of voltage-gated sodium channels in normal and axotomized rat dorsal root ganglion neurons. *J. Comp. Neurol.* 510, 188–206. doi: 10.1002/cne.21786

Gingras, J., Smith, S., Matson, D. J., Johnson, D., Nye, K., Couture, L., et al. (2014). Global Nav1. 7 knockout mice recapitulate the phenotype of human congenital indifference to pain. *PLoS One* 9:e105895. doi: 10.1371/journal.pone.0105895

Goncalves, T. C., Boukaiba, R., Molgo, J., Amar, M., Partiseti, M., Servent, D., et al. (2018). Direct evidence for high affinity blockade of NaV1.6 channel subtype by huwentoxin-IV spider peptide, using multiscale functional approaches. *Neuropharmacology* 133, 404–414. doi: 10.1016/j.neuropharm.2018.02.016

Habib, A. M., Wood, J. N., and Cox, J. J. (2015). Sodium channels and pain. *Handb. Exp. Pharmacol.* 227, 39–56. doi: 10.1007/978-3-662-46450-2-3

Ho, C., and O'Leary, M. E. (2011). Single-cell analysis of sodium channel expression in dorsal root ganglion neurons. *Mol. Cell. Neurosci.* 46, 159–166. doi: 10.1016/j.mcn.2010.08.017

King, G. F. (2011). Venoms as a platform for human drugs: translating toxins into therapeutics. *Expert Opin. Biol. Ther.* 11, 1469–1484. doi: 10.1517/14712598.2011.621940

Klint, J. K., Senff, S., Rupasinghe, D. B., Er, S. Y., Herzig, V., Nicholson, G. M., et al. (2012). Spider-venom peptides that target voltage-gated sodium channels: pharmacological tools and potential therapeutic leads. *Toxicon* 60, 478–491. doi: 10.1016/j.toxicon.2012.04.337

Klint, J. K., Smith, J. J., Vetter, I., Rupasinghe, D. B., Er, S. Y., Senff, S., et al. (2015). Seven novel modulators of the analgesic target NaV 1.7 uncovered using a high-throughput venom-based discovery approach. *Br. J. Pharmacol.* 172, 2445–2458. doi: 10.1111/bph.13081

Kornecook, T. J., Yin, R., Altmann, S., Be, X., Berry, V., Ilch, C. P., et al. (2017). Pharmacologic characterization of AMG8379, a potent and selective small

molecule sulfonamide antagonist of the voltage-gated sodium channel NaV1.7. *J. Pharmacol. Exp. Ther.* 362, 146–160. doi: 10.1124/jpet.116.239590

Liu, M., and Wood, J. N. (2011). The roles of sodium channels in nociception: implications for mechanisms of neuropathic pain. *Pain Med.* 12(Suppl. 3), S93–S99. doi: 10.1111/j.1526-4637.2011.01158.x

Liu, Y., Tang, J., Zhang, Y., Xun, X., Tang, D., Peng, D., et al. (2014). Synthesis and analgesic effects of mu-TRTX-Hhn1b on models of inflammatory and neuropathic pain. *Toxins* 6, 2363–2378. doi: 10.3390/toxins6082363

Liu, Z., Cai, T., Zhu, Q., Deng, M., Li, J., Zhou, X., et al. (2013). Structure and function of hainantoxin-III, a selective antagonist of neuronal tetrodotoxin-sensitive voltage-gated sodium channels isolated from the Chinese bird spider *Ornithoctonus hainana*. *J. Biol. Chem.* 288, 20392–20403. doi: 10.1074/jbc.M112.426627

Mansouri, M., Elalaoui, S. C., Bencheikh, B. O. A., El Alloussi, M., Dion, P. A., Sefiani, A., et al. (2014). A novel nonsense mutation in SCN9A in a moroccan child with congenital insensitivity to pain. *Pediatr. Neurol.* 51, 741–744. doi: 10.1016/j.pediatrneurol.2014.06.009

Meir, A., Cherki, R. S., Kolb, E., Langut, Y., and Bajayo, N. (2011). Novel peptides isolated from spider venom, and uses thereof. U. S. Patent No US 2011/0065647A1. Washington, DC: U. S. Patent and Trademark Office.

Meisler, M. H., Kearney, J., Escayg, A., MacDonald, B. T., and Sprunger, L. K. (2001). Sodium channels and neurological disease: insights from Scn8a mutations in the mouse. *Neuroscientist* 7, 136–145. doi: 10.1177/107385840100700208

Meng, D., Wang, L., Du, J., Chen, J., Chen, C., Xu, W., et al. (2017). The analgesic activities of *Stauntonia brachyanthera* and YM 11 through regulating inflammatory mediators and directly controlling the sodium channel prompt. *Sci. Rep.* 7:7574. doi: 10.1038/s41598-017-07095-x

Moyer, B. D., Murray, J. K., Ligutti, J., Andrews, K., Favreau, P., Jordan, J. B., et al. (2018). Pharmacological characterization of potent and selective NaV1.7 inhibitors engineered from *Chilobrachys jingzhao* tarantula venom peptide JzTx-V. *PLoS One* 13:e0196791. doi: 10.1371/journal.pone.0196791

Owoyele, V. B., Adediji, J. O., and Soladoye, A. O. (2005). Anti-inflammatory activity of aqueous leaf extract of *Chromolaena odorata*. *Inflammopharmacology* 13, 479–484. doi: 10.1163/156856005774649386

Saez, N. J., Senff, S., Jensen, J. E., Er, S. Y., Herzig, V., Rash, L. D., et al. (2010). Spider-venom peptides as therapeutics. *Toxins* 2, 2851–2871. doi: 10.3390/toxins2122851

Shorer, Z., Wajsbrot, E., Liran, T.-H., Levy, J., and Parvari, R. (2014). A novel mutation in SCN9A in a child with congenital insensitivity to pain. *Pediatr. Neurol.* 50, 73–76. doi: 10.1016/j.pediatrneurol.2013.09.007

Sugawara, T., Tsurubuchi, Y., Agarwala, K. L., Ito, M., Fukuma, G., Mazaki-Miyazaki, E., et al. (2001). A missense mutation of the Na + channel alpha II subunit gene Na(v)1.2 in a patient with febrile and afebrile seizures causes channel dysfunction. *Proc. Natl. Acad. Sci. U.S.A.* 98, 6384–6389. doi: 10.1073/pnas.111065098

Tanaka, B. S., Zhao, P., Dib-Hajj, F. B., Morisset, V., Tate, S., Waxman, S. G., et al. (2016). A gain-of-function mutation in Nav1.6 in a case of trigeminal neuralgia. *Mol. Med.* 22, 338–348. doi: 10.2119/molmed.2016.00131

Tao, H., Chen, X., Lu, M., Wu, Y., Deng, M., Zeng, X., et al. (2016). Molecular determinant for the tarantula toxin Jingzhaotoxin-I slowing the fast inactivation of voltage-gated sodium channels. *Toxicon* 111, 13–21. doi: 10.1016/j.toxicon.2015.12.009

Veeramah, K. R., O'Brien, J. E., Meisler, M. H., Cheng, X., Dib-Hajj, S. D., Waxman, S. G., et al. (2012). De novo pathogenic SCN8A mutation identified by whole-genome sequencing of a family quartet affected by infantile epileptic encephalopathy and SUDEP. *Am. J. Hum. Genet.* 90, 502–510. doi: 10.1016/j.ajhg.2012.01.006

Wang, W., Gu, J., Li, Y.-Q., and Tao, Y.-X. (2011). Are voltage-gated sodium channels on the dorsal root ganglion involved in the development of neuropathic pain? *Mol. Pain* 7:16. doi: 10.1186/1744-8069-7-16

Wu, B., Zhang, Y., Tang, H., Yang, M., Long, H., Shi, G., et al. (2017). A novel SCN9A mutation (F826Y) in primary erythromelalgia alters the excitability of Nav1. 7. *Curr. Mol. Med.* 17, 450–457. doi: 10.2174/1566524017666171009105029

Xiao, Y., Bingham, J. P., Zhu, W., Moczydlowski, E., Liang, S., and Cummins, T. R. (2008). Tarantula huwentoxin-IV inhibits neuronal sodium channels by binding to receptor site 4 and trapping the domain ii voltage sensor in the closed configuration. *J. Biol. Chem.* 283, 27300–27313. doi: 10.1074/jbc.M708447200

Xiao, Y., Blumenthal, K., Jackson, J. O. II, Liang, S., and Cummins, T. R. (2010). The tarantula toxins ProTx-II and huwentoxin-IV differentially interact with human Nav1.7 voltage sensors to inhibit channel activation and inactivation. *Mol. Pharmacol.* 78, 1124–1134. doi: 10.1124/mol.110.066332

Xie, W., Strong, J. A., Ye, L., Mao, J. X., and Zhang, J. M. (2013). Knockdown of sodium channel NaV1.6 blocks mechanical pain and abnormal bursting activity of afferent neurons in inflamed sensory ganglia. *Pain* 154, 1170–1180. doi: 10.1016/j.pain.2013.02.027

Xie, W., Strong, J. A., and Zhang, J. M. (2015). Local knockdown of the NaV1.6 sodium channel reduces pain behaviors, sensory neuron excitability, and sympathetic sprouting in rat models of neuropathic pain. *Neuroscience* 291, 317–330. doi: 10.1016/j.neuroscience.2015.02.010

Yamaji, N., Little, M. J., Nishio, H., Billen, B., Villegas, E., Nishiuchi, Y., et al. (2009). Synthesis, solution structure, and phylum selectivity of a spider delta-toxin that slows inactivation of specific voltage-gated sodium channel subtypes. *J. Biol. Chem.* 284, 24568–24582. doi: 10.1074/jbc.M109.030841

Zhou, X., Xiao, Z., Xu, Y., Zhang, Y., Tang, D., Wu, X., et al. (2017). Electrophysiological and pharmacological analyses of Nav1.9 voltage-gated sodium channel by establishing a heterologous expression system. *Front. Pharmacol.* 8:852. doi: 10.3389/fphar.2017.00852

Conflict of Interest Statement: The authors declare that the research was conducted in the absence of any commercial or financial relationships that could be construed as a potential conflict of interest.

frontiers in Pharmacology

MINI REVIEW
published: 07 January 2019
doi: 10.3389/fphar.2018.01499

Conopeptides [V11L;V16D]ArIB and RgIA4: Powerful Tools for the Identification of Novel Nicotinic Acetylcholine Receptors in Monocytes

*Veronika Grau[1], Katrin Richter[1], Arik J. Hone[2] and J. Michael McIntosh[2,3,4]**

[1] Laboratory of Experimental Surgery, Department of General and Thoracic Surgery, German Centre for Lung Research (DZL), Giessen University, Giessen, Germany, [2] Department of Biology, University of Utah, Salt Lake City, UT, United States, [3] George E. Wahlen Department of Veterans Affairs Medical Center, Salt Lake City, UT, United States, [4] Department of Psychiatry, University of Utah, Salt Lake City, UT, United States

OPEN ACCESS

Edited by:
Annette Nicke, Ludwig Maximilian University of Munich, Germany

Reviewed by:
Sebastien Dutertre, Center for the National Scientific Research (CNRS), France
Hai Minh Nguyen, University of California, Davis, United States

***Correspondence:**
J. Michael McIntosh
mcintosh.mike@gmail.com

Specialty section:
This article was submitted to Pharmacology of Ion Channels and Channelopathies, a section of the journal Frontiers in Pharmacology

Received: *26 October 2018*
Accepted: *07 December 2018*
Published: *07 January 2019*

Citation:
Grau V, Richter K, Hone AJ and McIntosh JM (2019) Conopeptides [V11L;V16D]ArIB and RgIA4: Powerful Tools for the Identification of Novel Nicotinic Acetylcholine Receptors in Monocytes. Front. Pharmacol. 9:1499. doi: 10.3389/fphar.2018.01499

Venomous marine snails of the genus *Conus* employ small peptides to capture prey, mainly osteichthyes, mollusks, and worms. A subset of these peptides known as α-conotoxins, are antagonists of nicotinic acetylcholine receptors (nAChRs). These disulfide-rich peptides provide a large number of evolutionarily refined templates that can be used to develop conopeptides that are highly selective for the various nAChR subtypes. Two such conopeptides, namely [V11L;V16D]ArIB and RgIA4, have been engineered to selectively target mammalian α7* and α9* nAChRs, respectively, and have been used to study the functional roles of these subtypes in immune cells. Unlike in neurons and cochlear hair cells, where α7* and α9* nAChRs, respectively, function as ligand-gated ion channels, in immune cells ligand-evoked ion currents have not been demonstrated. Instead, different metabotropic functions of α7* and α9* nAChRs have been described in monocytic cells including the inhibition of ATP-induced ion currents, inflammasome activation, and interleukin-1β (IL-1β) release. In addition to conventional nAChR agonists, diverse compounds containing a phosphocholine group inhibit monocytic IL-1β release and include dipalmitoyl phosphatidylcholine, palmitoyl lysophosphatidylcholine, glycerophosphocholine, phosphocholine, phosphocholine-decorated lipooligosaccharides from *Haemophilus influenzae*, synthetic phosphocholine-modified bovine serum albumin, and the phosphocholine-binding C-reactive protein. In monocytic cells, the effects of [V11L;V16D]ArIB and RgIA4 suggested that activation of nAChRs containing α9, α7, and/or α10 subunits inhibits ATP-induced IL-1β release. These results have been corroborated utilizing gene-deficient mice and small interfering RNA. Targeted re-engineering of native α-conotoxins has resulted in excellent tools for nAChR research as well as potential therapeutics. *indicates possible presence of additional subunits.

Keywords: α-conotoxin, CHRNA7, CHRNA9, CHRNA10, immunomodulation, interleukin-1β, P2X7 receptor

INTRODUCTION

Nicotinic acetylcholine (ACh) receptors (nAChRs) are present at the neuromuscular junction in a wide variety of animal species. Venomous predators have evolved toxins targeted to neuromuscular nAChRs to facilitate prey capture and to defend against predators (Dutertre et al., 2014). Elapid snakes produce toxins characterized by a three finger protein domain (Fry et al., 2003; Utkin, 2013). These proteins are 60–80 amino acids in length, contain four disulfide bonds, and when injected produce paralysis in marine and terrestrial vertebrata. The vertebrate muscle nAChR subtype composed of α1, β1, δ, and ε/γ subunits has been intensively studied and extensive structure and function information has been obtained by examining the muscle nAChR in complex with three finger toxins, most notably α-bungarotoxin (Dellisanti et al., 2007).

Cone snails are among the dominant marine predators in coral reefs. Although their prey types include vertebrate fish, the predominant prey types of *Conus* species are invertebrates that include mollusks, polychaete, and hemichordate worms. Cone snails produce numerous types of conopeptides which are named, in part, according to their disulfide bond framework. Highly prevalent peptides include those that belong to the α-conotoxin family which target nAChRs (Abraham and Lewis, 2018; Giribaldi and Dutertre, 2018). Compared to elapid snake toxins, α-conotoxins are much smaller, usually 13–25 amino acids in length, and have only two disulfide bonds. Their small size facilitates *de novo* peptide synthesis of the native toxin as well synthesis of α-conotoxin-derived peptide analogs.

In addition to neurons, ACh is secreted and sensed by a broad range of non-neuronal cells including immune cells (Kawashima and Fujii, 2003, 2004; Wessler and Kirkpatrick, 2008; Beckmann and Lips, 2013; Kummer and Krasteva-Christ, 2014; Fujii et al., 2017a,b). The cholinergic system of immunity is a highly complex, regulated network that is capable of sending and receiving signals and can be modulated by other organ systems such as the central nervous system. We are only beginning to understand the cholinergic control of immunity that encompasses innate and adaptive immunity and can be pro- and anti-inflammatory (Fujii et al., 2017a,b). Essential components of the cholinergic system are expressed by immune cells in a regulated fashion, including transporters and enzymes involved in ACh synthesis, nAChRs, muscarinic ACh receptors, endogenous modulators of receptor function, and ACh-degrading esterases (Kawashima and Fujii, 2003, 2004; Fujii et al., 2017b). Immune cells express all five muscarinic ACh receptor subtypes (M1–M5) as well as nAChR subunits α2, α5, α6, α7, α9, α10, and β2 (Fujii et al., 2017b).

Similar to ACh, ATP can be released by nerve endings and function as a neurotransmitter (Burnstock, 2014). In addition, activated or damaged cells release cytoplasmic ATP into the extracellular space (Bortolotti et al., 2018). The most recognized and presumably most important function of extracellular ATP is that of a danger signal for monocytes/macrophages that leads to ion-channel functions of the ATP-receptor P2X7 (P2X7R) resulting in NLRP3 (NACHT, LRR, and PYD domains-containing protein 3) inflammasome assembly, activation of caspase-1, interleukin-1β (IL-1β) maturation, and release (Broz and Dixit, 2016; Bortolotti et al., 2018). IL-1β is a potent pro-inflammatory cytokine involved in host defense against infections (Broz and Dixit, 2016). However, IL-1β contributes to the pathogenesis of numerous debilitating diseases including autoimmune diseases and the life-threatening systemic inflammatory response syndrome (Dinarello et al., 2012; Bortolotti et al., 2018).

In this mini review, we summarize the strategies used to develop highly selective nAChR antagonists using native α-conotoxins as starting templates as well as their use in the discovery of an unexpected interaction of nAChR subunits α7, α9, and α10 in monocytic and epithelial cells. These unusual nAChRs efficiently control P2X7R activation, inflammasome assembly and, hence, release of IL-1β.

Conopeptide Structure, Function and Development

There are ca. 700 species of *Conus*. Proteomic and transcriptomic analyses of *Conus* have demonstrated that there are likely thousands of unique α-conotoxins synthesized in the cone snail venom ducts (Lebbe et al., 2014; Robinson and Norton, 2014; Giribaldi and Dutertre, 2018). *Conus* thus represent an abundant source of lead compounds for conopeptide-based development. Peptide synthesis and pharmacological testing of α-conotoxins has shown that toxins from mollusk- and worm-hunting *Conus* lack potent activity at mammalian neuromuscular nAChRs and therefore are non-paralytic when injected into rodents. In contrast, some of these same α-conotoxins are potent antagonists of the nAChR subtypes expressed by neurons and non-neuronal cells (Azam and McIntosh, 2012) including those of immune cells as described in this review.

Development of the α7 nAChR-Selective [V11L;V16D]ArIB

Conus arenatus is a vermivore that hunts throughout the Indo-Pacific from East Africa to French Polynesia. Native ArIB was identified by genomic cloning from *C. arenatus* hepatopancreas and the predicted peptide synthesized (Whiteaker et al., 2007). Testing of ArIB on cloned nAChRs revealed potent activity on homomeric α7 (1.8 nM IC_{50}) but also had substantial potency on α3β2 nAChRs (60 nM IC_{50}). Structure-activity information from previously characterized α-conotoxins that have activity at α7 and α3β2 nAChRs was used to improve the selectivity of ArIB. Serial substitutions of the primary sequence of ArIB were made based on structure-activity studies of α-conotoxins PnIA and MII. PnIA inhibits both α7 and α3β2 nAChRs, but a single amino acid substitution of Leu for Val in position 10 of PnIA shifts activity in favor of α7 (Hogg et al., 1999; Luo et al., 1999). Substitution of Ala for Leu in position 15 of MII reduces activity for α3β2 nAChRs (McIntosh et al., 2004). We inserted both of these amino acids into the homologous position of ArIB to make [V11L;V16A]ArIB and determined that this analog had increased activity for α7 and decreased activity for α3β2 compared to native ArIB. Subsequent mutation of position 15 to Asp further lessened activity for α3β2. The final analog, [V11L;V16D]ArIB, had IC_{50} values of 1.1 nM for

α7 and >10,000 nM IC_{50} for α3β2. [V11L;V16D]ArIB (**Table 1**) is the most selective α7 antagonist yet reported and is the basis for the generation of selective conopeptides with radioactive and fluorescent reporter groups (Whiteaker et al., 2008; Hone et al., 2009, 2010).

Development of the α9α10 nAChR-Selective RgIA4

Conus regius, known as the crown cone, is found in the Caribbean Sea and in coastal waters of Brazil. *C. regius* preys on amphinomid worms and employs a small, 13 amino acid α-conotoxin known as RgIA. RgIA was shown to potently and selectively block rat α9α10 nAChRs (Ellison et al., 2006, 2008). In addition, RgIA was shown to treat and prevent the development neuropathic pain, suggesting a range of potential human therapeutic applications (Vincler et al., 2006; Di Cesare Mannelli et al., 2014; Pacini et al., 2016). Unfortunately, RgIA has low potency for human α9α10 nAChRs due to a Thr to Ile difference in the (-) binding face of the α9 subunit of the human α9α10 nAChR (Azam and McIntosh, 2012). In an attempt to overcome the low potency at the human nAChRs, non-Cys residues of RgIA were systematically substituted and the resulting analogs tested for activity. Residues in both the first and second disulfide loops of RgIA could be substituted to create analogs with increased potency for human α9α10 nAChRs. Four favorable substitutions were combined into one analog to create RgIA4 (**Table 1**). RgIA4 has low nM potency and high selectivity for human, mouse and rat α9α10 nAChRs (Christensen et al., 2017; Romero et al., 2017). Like RgIA, RgIA4 is effective at preventing and treating neuropathic pain in mice and rats (Christensen et al., 2017; Romero et al., 2017).

The α7 and α9 nAChR subunits have a close evolutionary relationship. Their similar sequences have made distinguishing among these subtypes difficult. α-Bungarotoxin and the plant norditerpenoid alkyloid methyllycaconitine both potently block α7 nAChRs but also have substantial potency for α9* nAChRs (Elgoyhen et al., 2001; Baker et al., 2004). With the advent of [V11L;V16D]ArIB and RgIA4, molecular dissection of α7 and α9* nAChR functions was enabled.

Ion-Current Versus Metabotropic Functions of α7* NACHR and α9* NACHR

In most cases, nAChRs including α7* and α9* nAChRs function as ionotropic receptors that are permeable to the cations Na^+, K^+, and Ca^{2+} (Ullian et al., 1997; Katz et al., 2000; Verbitsky et al., 2000). α7* nAChRs are highly permeable to Ca^{2+} and display rapid desensitization characteristics which means a channel conformation state with high agonist affinity at the same time being impermeable to ions (Corradi and Bouzat, 2016).

Increasing evidence supports the existence of non-canonical signaling pathway(s) used by ligand-gated ion channels like nAChRs (Valbuena and Lerma, 2016). This metabotropic mode of action of nAChRs was first shown for the α7* nAChR in leukocytes. In T cells, activation of α7* nAChRs induced metabotropic signaling that resulted in an increase of intracellular Ca^{2+} concentrations independent of obvious ionotropic receptor functions (De Jonge and Ulloa, 2007; Razani-Boroujerdi et al., 2007). Similar channel-independent functions have also been shown in microglial cells (Suzuki et al., 2006; King et al., 2017) and in neurons (Zhong et al., 2008, 2013).

Proteomic analyses identified 55 intracellular interaction partners of α7* nAChR in the central nervous system and some of them may potentially mediate metabotropic signaling (Paulo et al., 2009). In addition, studies on neuronal cells indicate that α7* nAChRs are directly coupled to G-proteins and regulate axon growth at the growth cone (Kabbani et al., 2013; Kabbani and Nichols, 2018). G-protein mediated signaling in neuronal cells enables activation of growth-associated protein 43, as well as activation of phospholipase C, leading to inositol triphosphate-mediated release of Ca^{2+} from intracellular stores (Kabbani and Nichols, 2018).

In innate immune cells, various classical metabotropic signal transduction pathways and micro RNAs are involved in α7 nAChR-mediated down-regulation of pro-inflammatory cytokines and up-regulation of anti-inflammatory molecules at the transcriptional and translational level (Corradi and Bouzat, 2016; Fujii et al., 2017a; Hoover, 2017; Pavlov et al., 2018). In addition, one study suggests that extracellular ACh enters the cytoplasm, activates mitochondrial α7 nAChR and inhibits the release of mitochondrial DNA (Lu et al., 2014).

Whether stimulation of immune cells with nAChR agonists induces ion-channel functions is unclear. In most studies, no ion-currents have been detected in response to nAChR agonists (Peng et al., 2004; Razani-Boroujerdi et al., 2007; Hecker et al., 2009, 2015; Mikulski et al., 2010; Richter et al., 2016, 2018a; Zakrzewicz et al., 2017). However, stimulation of murine intestinal macrophages with agonists of α7 nAChR evoked small Ca^{2+} transients (Matteoli et al., 2014). It remains to be determined if these Ca^{2+} signals are due to ion-channel activity of nAChRs.

It has been suggested that metabotropic signal transduction through α7* nAChRs is associated with the desensitized conformation of the channel (Stokes et al., 2015; Corradi and Bouzat, 2016; Kabbani and Nichols, 2018). This suggestion is supported by the findings that some of the most effective modulators of α7* nAChR-mediated anti-inflammatory responses are compounds termed nAChR silent agonists, potent agonists of metabotropic functions in innate immune cells but do not evoke ionotropic functions (Thomsen and Mikkelsen, 2012; Chojnacka et al., 2013; Papke et al., 2014; Stokes et al., 2015; Horenstein and Papke, 2017).

TABLE 1 | Conopeptide Sequences.

Peptide	Sequence
ArIB[1]	DECCSNPACRVNNPHVCRRR
[V11L;V16D]ArIB[1]	DECCSNPACRLNNPHDCRRR
[A10L]PnIA[2]	GCCSLPPCALNNPDYC
[15A]MII[3]	GCCSNPVCHLEHSNAC
RgIA[4]	GCCSDPRCRYRCR
RgIA4[5]	GCCTDPRCX1X2QCY

[1]*Whiteaker et al., 2007;* [2]*Luo et al., 1999;* [3]*McIntosh et al., 2004;* [4]*Ellison et al., 2006;* [5]*Romero et al., 2017. X1, citrulline; X2, monoiodotyrosine; underlining indicates amino acid change from native peptide.*

Cholinergic Control of Innate Immunity

Control of Gene Expression via α7* nAChR and α9* nAChR

A role of nAChRs in the regulation of innate immunity was first suggested by Tracey and colleagues, who reported that vagal nerve stimulation attenuates the release of the pro-inflammatory tumor necrosis factor in a model of endotoxin shock and coined the term "cholinergic anti-inflammatory pathway" (Borovikova et al., 2000). The anti-inflammatory effects were sensitive to an unspecified "α-conotoxin," suggesting that signaling involves nAChRs (Borovikova et al., 2000). Subsequently, an essential role of α7 nAChR for the vagal control of inflammation was demonstrated (Wang et al., 2003). The current knowledge on cholinergic neuro-immune interactions involving α7 nAChR has recently been summarized in excellent reviews (e.g., Fujii et al., 2017a; Hoover, 2017; Pavlov et al., 2018). In addition to the nAChR α7 subunit, α9 and β2 subunits contribute to anti-inflammatory effects of nAChR agonists (Simard et al., 2013; Jiang et al., 2016; St-Pierre et al., 2016; Liu et al., 2017). It is, however, unclear if these nAChR subunits interact or if they independently trigger anti-inflammatory mechanisms.

Inhibition of P2X7R Ion-Channel Function by Conventional nAChR Agonists

ATP-dependent IL-1β release by lipopolysaccharide-primed human monocytic U937 cells, primary human blood monocytes as well as human and mouse peripheral blood mononuclear cells (PBMCs) is efficiently inhibited by the nAChR agonists nicotine and ACh, but also by choline, a selective agonist of α7* and α9* nAChRs (Hecker et al., 2015; Richter et al., 2016; **Figure 1**). In line with an involvement of α7* and α9* nAChRs, inhibition of IL-1β release is sensitive to mecamylamine, α-bungarotoxin and strychnine (Hecker et al., 2015; Richter et al., 2016; Zakrzewicz et al., 2017). As these nAChR antagonists do not differentiate between α7* or α9* nAChRs, the conopeptides [V11L;V16D]ArIB and RgIA4 have turned out to be invaluable tools. Surprisingly, both conopeptides reversed the inhibitory effects of nicotine and ACh (Hecker et al., 2015; Zakrzewicz et al., 2017), suggesting an involvement of nAChR subunits α7, α9, and/or α10. Gene knock-down in U937 cells and knock-out mice revealed an obligate role of nAChR subunits α7, α9, and α10 in signaling (Hecker et al., 2015; Zakrzewicz et al., 2017).

Of note, nAChR agonists do not provoke obvious ion-channel functions in U937 cells as measured by whole-cell patch-clamp recordings, but completely abolish the ion-currents induced by P2X7R activation (Hecker et al., 2015; Richter et al., 2016). This is of eminent clinical importance, because nAChR agonists control sterile, trauma-associated inflammation without completely inhibiting host defense against pathogens that stimulate numerous ATP-independent pathways of IL-1β maturation (Broz and Dixit, 2016). The mechanism down-stream of nAChR activation controlling P2X7R ion-channel function is currently under investigation.

Phosphocholine Is an Agonist of Monocytic nAChR

Apart from conventional nAChR agonists, phosphocholine stimulates monocytic nAChRs and inhibits ATP-induced IL-1β release (Hecker et al., 2015; Richter et al., 2016, 2018a,b; **Figure 1**). The response of monocytic cells to free phosphocholine resembles that of choline: IC_{50} values are in the range of 10 μM, signaling involves nAChR subunits α7, α9, and α10, both compounds do not elicit ion-currents at U937 cells, but inhibit the ion-channel function of the P2X7R (Hecker et al., 2015; Richter et al., 2016). In sharp contrast to choline, phosphocholine does not induce ion-current responses in *Xenopus laevis* oocytes that heterologously express human nAChR α9 subunits, alone or co-injected with α7 and/or α10 (Richter et al., 2016; Zakrzewicz et al., 2017). Remarkably, choline-gated currents in *Xenopus* oocytes expressing human α9α10 nAChR are strongly but reversibly inhibited by phosphocholine, resembling silent agonist or antagonist functions (Richter et al., 2016). Hence, metabotropic functions of monocytic nAChRs can be elicited by endogenous agonists that do not induce ion-currents at conventional receptors. Whether phosphocholine functions as silent agonist of canonical α9* nAChR *in vivo*, remains to be investigated.

C-Reactive Protein (CRP) Potentiates the nAChR Agonist Function of Phosphocholine

The pentameric acute-phase protein CRP is mainly synthesized in the liver in response to increased circulating levels of IL-1β and IL-6. Under physiological conditions, CRP forms Ca^{2+}-dependent complexes with phosphocholine and other compounds with a phosphocholine head-group at a stoichiometric proportion of 1:1 per monomer (Pepys and Hirschfield, 2003; Mantovani et al., 2008). Native CRP-ligand complexes are potent nAChR agonists at human monocytic cells that inhibit the ATP-dependent inflammasome assembly (**Figure 1**) and IL-1β release, whereas CRP devoid of ligands is ineffective (Richter et al., 2018a). The IC_{50} of CRP isolated from human bodily fluids is about 40 nM, far below that of phosphocholine (10 μM), suggesting that CRP potentiates the effect of free phosphocholine (Richter et al., 2018a). The effects of CRP-phosphocholine complexes on monocytic cells are sensitive to [V11L;V16D]ArIB and RgIA4, depend on interaction of nAChR subunits α7, α9, α10, and resemble silent agonists or partial antagonists at canonical α9α10 nAChR (Richter et al., 2018a). A prospective clinical study on patients suffering from multiple traumata was in line with a protective anti-inflammatory function of CRP *in vivo*, suggesting that endogenous CRP is a negative feed-back regulator of IL-1β-mediated inflammation (Richter et al., 2018a).

Phosphocholine-Modified Macromolecules Function as nAChR Agonists

Some eukaryotic parasites and bacterial pathogens conjugate phosphocholine moieties to proteins or cell wall glycolipids (Grabitzki and Lochnit, 2009; Clark and Weiser, 2013). Two opposing but not necessarily mutually exclusive views on the biological relevance of these PC-modified molecules prevail. First, CRP and highly prevalent phosphocholine-specific antibodies bind to phosphocholine-modified surfaces and activate mechanisms of pathogen elimination

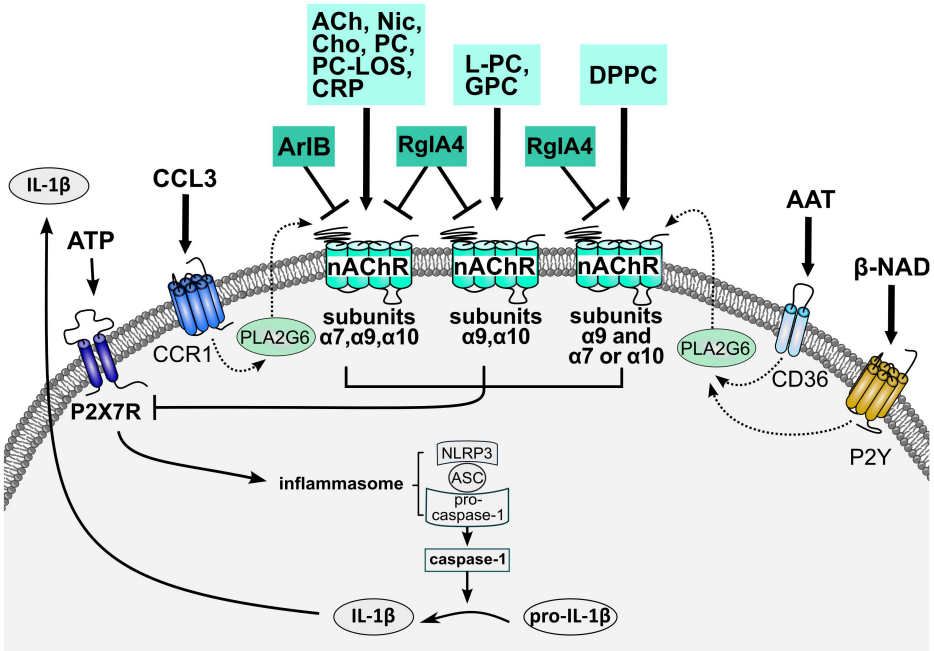

FIGURE 1 | Working hypothesis of the cholinergic control of ATP-dependent release of monocytic IL-1β. Stimulation of the ATP-gated P2X7R results in the assembly of the NLRP3 inflammasome and activation of capspase-1 that cleaves pro-IL-β and enables its swift release. Agonists of monocytic nAChRs metabotropically inhibit the ionotropic function of P2X7R and, hence, eventually IL-1β release. Different nAChR subunits interact, depending on the respective nicotinic agonist. Conventional nAChR agonists (ACh, Cho, and Nic) as well as PC, PC/CRP complexes and PC-LOS require nAChR subunits α7, α9, and α10 for signaling. LPC and G-PC depend on the interaction of nAChR subunits α9 and α10, whereas only nAChR subunit α9 is essential for signaling of DPPC. In the latter case, nAChR subunit α9 interacts with either subunit α7 or α10. Accordingly, signaling of ACh, Cho, Nic, PC, PC/CRP complexes, and PC-LOS is sensitive to both conopeptides, [V11L;V16D]ArIB and RgIA4, whereas signaling of L-PC, GPC and DPPC is only sensitive to RgIA4. These cholinergic control mechanisms are also triggered by the chemokine CCL3 that signals via chemokine receptor CCR1, activates PLA2G6, and induces the release of a yet unknown agonist of nAChRs composed of subunits α7, α9, and α10. In a similar way, AAT and β-NAD signal via CD36 and P2Y receptors and trigger the secretion of a nAChR agonist that activates nAChRs similar to DPPC. The structure of the nAChRs involved in the control of IL-1β release remains to be elucidated as well as the signaling cascade resulting in P2X7R inhibition. AAT, α1-antitrypsin; ACh, acetylcholine; ASC, apoptosis-associated speck like protein containing a caspase recruitment domain; Cho, choline; CRP, C-reactive protein; DPPC, dipalmitoyl phosphatidylcholine; GPC, nAChR, nicotinic acetylcholine receptor; Nic, nicotine; NLRP3, NACHT, LRR and PYD domains-containing protein 3; P2X7R, ATP receptor P2X7; PC, phosphocholine; PC-LOS, PC-modified lipooligosaccharides; PLA2G6, calcium-independent phospholipase A2β.

(Scott et al., 1987; Nishinarita et al., 1990; Shaw et al., 2000; Pepys and Hirschfield, 2003; Mantovani et al., 2008; De Faire and Frostegård, 2009; Frostegård, 2010; Fiskesund et al., 2014). Second, PC-modified products exert strong anti-inflammatory effects and serve the immune evasion of pathogens (Grabitzki and Lochnit, 2009; Clark and Weiser, 2013). We recently demonstrated that phosphocholine-modified lipooligosaccharides from wildtype *Haemophilus influenzae* are potent nAChR agonists inhibiting the ATP-induced release of IL-1β in monocytic U937 cells (25 nM IC_{50}), in pulmonary epithelial cell lines and in living lung slices (Hecker et al., 2015; Richter et al., 2018b; **Figure 1**). Similarly, phosphocholine synthetically conjugated to bovine serum albumin, a compound that mimics the properties of secreted phosphocholine-modified helminth proteins, is a functional agonist of monocytic nAChR (Hecker et al., 2015).

Phosphatidylcholines and Their Metabolites Are Agonists at Monocytic α9* nAChRs

Phosphatidylcholines, common constituents of biomembranes and surfactant, are amphiphilic neutral lipids composed of a phosphocholine head-group linked to glycerol with two variable fatty acid chains. Dipalmitoyl phosphatidylcholine, the dominating lipid component of pulmonary surfactant (Lang et al., 2005; Lopez-Rodriguez and Pérez-Gil, 2014), inhibits ATP-induced IL-1β release (10 μM IC_{50}) (Backhaus et al., 2017; **Figure 1**). This function is sensitive to RgIA4 but remarkably not to [V11L;V16D]ArIB (Backhaus et al., 2017). Accordingly, knock-down of nAChR subunit α9 blunts the effect of dipalmitoyl phosphatidylcholine, whereas single knock-down of nACh subunits α7 and α10 does not. However, concomitant knock-down of nAChR subunits α7 and α10 abolishes the effect of dipalmitoyl phosphatidylcholine suggesting that nAChR subunit α9 is mandatory for signaling, whereas α7 and α10 can replace each other (Backhaus et al., 2017).

Phosphatidylcholine metabolites palmitoyl lysophosphatidylcholine and glycerophosphocholine, are also efficient inhibitors of ATP-mediated IL-1β release (1 μM IC_{50}), their effects are sensitive to RgIA4 but not to [V11L;V16D]ArIB and they function as silent agonists or partial antagonists at canonical α9α10 nAChR (Zakrzewicz et al., 2017; **Figure 1**). In contrast to dipalmitoyl phosphatidylcholine, however, nAChR

subunits α9 and α10 are mandatory for signaling of palmitoyl lysophosphatidylcholine and glycerophosphocholine, whereas α7 is dispensable (Zakrzewicz et al., 2017). It remains to be investigated, if these findings apply to all phosphatidylcholines and lysophosphatidylcholines or if the structure of the fatty acid remnants is of functional importance.

Signaling of Chemokines, β-NAD and α1-Antitrypsin Induce the Secretion of Agonists of Monocytic nAChR

Chemokines, β-NAD and α1-antitrypsin surprisingly inhibit the ATP-induced release of IL-1β via mechanisms that join the above described cholinergic pathways (Amati et al., 2017; Hiller et al., 2018; Siebers et al., 2018; **Figure 1**). CCL3 signals via chemokine receptor CCR1, activates the Ca^{2+}-independent phospholipase A2β (PLA2G6) and induces the release of low molecular mass factors that function as agonists of monocytic nAChR. Signaling is sensitive to [V11L;V16D]ArIB and RgIA4 suggesting that subunits α7, α9, and/or α10 are required (Amati et al., 2017). β-NAD activates purinergic receptors P2Y1 and P2Y11, whereas α1-antitrypsin signals via CD36 to activate PLA2G6 and to induce the release of nAChR agonists (Hiller et al., 2018; Siebers et al., 2018). Surprisingly, these factors are different from those secreted in response to CCL3, as they are sensitive to RgIA4 but insensitive to [V11L;V16D]ArIB. Results from gene silencing experiments are in line with the assumption that β-NAD and α1-antitrypsin signal via nAChR subunits α9 and either α7 or α10 (Hiller et al., 2018; Siebers et al., 2018). The structure of these secreted factors remains to be determined. As the preferred substrates of PLA2G6 are phosphatidylcholines (Ramanadham et al., 2015), their above described metabolites are possible candidates. This novel triple-membrane passing signaling pathway involving PLA2G6 activation and nAChRs might be of general importance, far beyond the control of inflammasome activation.

Do Monocytic nAChRs Structurally Differ From Canonical nAChRs?

It is an open question as to how monocytic nAChRs inhibit ion-channel function of P2X7Rs. There are, however, several hints that monocytic nAChRs differ from classical pentameric channels. As they induce metabotropic functions (Hecker et al., 2009, 2015; Mikulski et al., 2010; Richter et al., 2016), there may be no need for the activatable state of a classical pentameric ion channel. In this instance, binding of agonist to the nAChR promotes a receptor state that allows G-protein coupling but not fast ionotropic conduction. Whereas nicotine acts as an agonist that induces ion-channel function at α7 nAChRs, for α9* nAChRS expressed in cochlear hair cells and those heterologously expressed in *Xenopus* oocytes, nicotine acts as an antagonist (Lustig et al., 2001; Sgard et al., 2002). In contrast, nicotine functions as an agonist at monocytic α9*nAChRs. This might be due to the addition of an α7 subunit to the α9-containing receptor complex. Alternatively, pentameric nAChRs can exist in a state that is 'uncoupled' from ion-conducting function, yet might maintain metabotropic properties (Drenan et al., 2008; Baenziger et al., 2015). It is also possible that α9 subunits form non-pentameric oligomers together with subunits α7 and/or α10 that lack ionotropic function but possess metabotropic function.

Structural modeling revealed an accumulation of charged amino acids at the α9 (-) side that seems to interfere with loop-C closure and might hinder nicotine engulfment by the ligand binding pocket (Giastas et al., 2018). Because nicotine and bulky molecules such as palmitoyl lysophosphatidylcholine, dipalmitoyl phosphatidylcholine, CRP-phosphocholine complexes, phosphocholine-modified lipooligosaccharides, and phosphocholine-modified bovine serum albumin function as agonists (Hecker et al., 2015; Backhaus et al., 2017; Zakrzewicz et al., 2017), we speculate that binding sites of monocytic nAChR do not necessarily close upon ligand binding. May be, they even do not involve the (-) side of an adjacent subunit.

CONCLUSION

Conus produce a vast array of toxins some of which have been systematically modified to produce peptides highly selective for mammalian nAChR subtypes. These conopeptides have been used to help demonstrate that monocytes express novel unexpected nAChRs that contain α9, α7, and/or α10 subunits, inhibit the ionotropic function of P2X7R and modulate ATP-induced IL-1β release. A diverse set of key compounds, some of them already known to modulate immune responses, act as agonists of these nAChRs suggesting a pivotal role in health and disease processes.

AUTHOR CONTRIBUTIONS

VG, KR, AH, and JMM wrote the article. VG and KR designed the figure.

FUNDING

VG was funded by the German Research Foundation (GR 1094/7-1) and by the German Center for Lung Research (DZL). KR obtained a grant from the Fritz-Thyssen-Stiftung, Germany (Grant No. 50.18.0.004MN). JMM received funding from the National Institutes of Health (GM48677 and GM103801) and from the Office of the Assistant Secretary of Defense for Health Affairs under Award No. W81XWH-17-1-0413.

REFERENCES

Abraham, N., and Lewis, R. J. (2018). Neuronal nicotinic acetylcholine receptor modulators from cone snails. *Mar. Drugs* 16:E208. doi: 10.3390/md16060208

Amati, A. L., Zakrzewicz, A., Siebers, K., Wilker, S., Heldmann, S., Zakrzewicz, D., et al. (2017). Chemokines (CCL3, CCL4, and CCL5) inhibit ATP-induced release of IL-1β by monocytic cells. *Med. Inflamm.* 2017:434872. doi: 10.1155/2017/1434872

Azam, L., and McIntosh, J. M. (2012). Molecular basis for the differential sensitivity of rat and human α9α10 nAChRs to α-conotoxin RgIA. *J. Neurochem.* 122, 1137–1144. doi: 10.1111/j.1471-4159.2012.07867.x

Backhaus, S., Zakrzewicz, A., Richter, K., Damm, J., Wilker, S., Fuchs-Moll, G., et al. (2017). Surfactant inhibits ATP-induced release of interleukin-1β via nicotinic acetylcholine receptors. *J. Lipid Res.* 58, 1055–1066. doi: 10.1194/jlr.M071506

Baenziger, J. E., Hénault, C. M., Therien, J. P., and Sun, J. (2015). Nicotinic acetylcholine receptor-lipid interactions: mechanistic insight and biological function. *Biochim. Biophys. Acta* 1848, 1806–1817. doi: 10.1016/j.bbamem.2015.03.010

Baker, E. R., Zwart, R., Sher, E., and Millar, N. S. (2004). Pharmacological properties of α 9 α 10 nicotinic acetylcholine receptors revealed by heterologous expression of subunit chimeras. *Mol. Pharmacol.* 65, 453–460. doi: 10.1124/mol.65.2.453

Beckmann, J., and Lips, K. S. (2013). The non-neuronal cholinergic system in health and disease. *Pharmacology* 92, 286–302. doi: 10.1159/000355835

Borovikova, L. V., Ivanova, S., Zhang, M., Yang, H., Botchkina, G. I., Watkins, L. R., et al. (2000). Vagus nerve stimulation attenuates the systemic inflammatory response to endotoxin. *Nature* 405, 458–462. doi: 10.1038/35013070

Bortolotti, P., Faure, E., and Kipnis, E. (2018). Inflammasomes in tissue damages and immune disorders after trauma. *Front. Immunol.* 9:1900. doi: 10.3389/fimmu.2018.01900

Broz, P., and Dixit, V. M. (2016). Inflammasomes: mechanism of assembly, regulation and signalling. *Nat. Rev. Immunol.* 16, 407–420. doi: 10.1038/nri.2016.58

Burnstock, G. (2014). Purinergic signalling: from discovery to current developments. *Exp. Physiol.* 99, 16–34. doi: 10.1113/expphysiol.2013.071951

Chojnacka, K., Papke, R. L., and Horenstein, N. A. (2013). Synthesis and evaluation of a conditionally-silent agonist for the α7 nicotinic acetylcholine receptor. *Bioorg. Med. Chem. Lett.* 23, 4145–4149. doi: 10.1016/j.bmcl.2013.05.039

Christensen, S., Hone, A. J., Roux, I., Kniazeff, J., Pin, J. P., Upert, G., et al. (2017). RgIA4 potently blocks mouse α9α10 nAChRs and provides long lasting protection against oxaliplatin-induced cold allodynia. *Front. Cell. Neurosci.* 11:219. doi: 10.3389/fncel.2017.00219

Clark, S. E., and Weiser, J. N. (2013). Microbial modulation of host immunity with the small molecule phosphorylcholine. *Infect. Immun.* 81, 392–401. doi: 10.1128/IAI.01168-12

Corradi, J., and Bouzat, C. (2016). Understanding the bases of function and modulation of α7 nicotinic receptors: implications for drug discovery. *Mol. Pharmacol.* 90, 288–299. doi: 10.1124/mol.116.104240

De Faire, U., and Frostegård, J. (2009). Natural antibodies against phosphorylcholine in cardiovascular disease. *Ann. N. Y. Acad. Sci.* 1173, 292–300. doi: 10.1111/j.1749-6632.2009.04748.x

De Jonge, W. J., and Ulloa, L. (2007). The α7 nicotinic acetylcholine receptor as a pharmacological target for inflammation. *Br. J. Pharmacol.* 151, 915–929. doi: 10.1038/sj.bjp.0707264

Dellisanti, C. D., Yao, Y., Stroud, J. C., Wang, Z. Z., and Chen, L. (2007). Crystal structure of the extracellular domain of nAChR α1 bound to α-bungarotoxin at 1.94 A resolution. *Nat. Neurosci.* 10, 953–962. doi: 10.1038/nn1942

Di Cesare Mannelli, L., Cinci, L., Micheli, L., Zanardelli, M., Pacini, A., McIntosh, J. M., et al. (2014). α-conotoxin RgIA protects against the development of nerve injury-induced chronic pain and prevents both neuronal and glial derangement. *Pain* 155, 1986–1995. doi: 10.1016/j.pain.2014.06.023

Dinarello, C. A., Simon, A., and van der Meer, J. W. (2012). Treating inflammation by blocking interleukin-1 in a broad spectrum of diseases. *Nat. Rev. Drug Discov.* 11, 633–652. doi: 10.1038/nrd3800

Drenan, R. M., Nashmi, R., Imoukhuede, P., Just, H., McKinney, S., and Lester, H. A. (2008). Subcellular trafficking, pentameric assembly, and subunit stoichiometry of neuronal nicotinic acetylcholine receptors containing fluorescently labeled α6 and β3 subunits. *Mol. Pharmacol.* 73, 27–41. doi: 10.1124/mol.107.039180

Dutertre, S., Jin, A. H., Vetter, I., Hamilton, B., Sunagar, K., Lavergne, V., et al. (2014). Evolution of separate predadtion-and defence-evoked venoms in carnivorous cone snails. *Nat. Commun.* 5:352. doi: 10.1038/ncomms4521

Elgoyhen, A. B., Vetter, D. E., Katz, E., Rothlin, C. V., Heinemann, S. F., and Boulter, J. (2001). α10: a determinant of nicotinic cholinergic receptor function in mammalian vestibular and cochlear mechanosensory hair cells. *Proc. Natl. Acad. Sci. U.S.A.* 98, 3501–3506. doi: 10.1073/pnas.051622798

Ellison, M., Feng, Z. P., Park, A. J., Zhang, X., Olivera, B. M., McIntosh, J. M., et al. (2008). α-RgIA, a novel conotoxin that blocks the α9α10 nAChR: structure and identification of key receptor-binding residues. *J. Mol. Biol.* 377, 1216–1227. doi: 10.1016/j.jmb.2008.01.082

Ellison, M., Haberlandt, C., Gomez-Casati, M. E., Watkins, M., Elgoyhen, A., McIntosh, J. M., et al. (2006). α-RgIA: a novel conotoxin that specifically and potently blocks the α9α10 nAChR. *Biochemistry* 45, 1511–1517. doi: 10.1021/bi0520129

Fiskesund, R., Steen, J., Amara, K., Murray, F., Szwajda, A., Liu, A., et al. (2014). Naturally occurring human phosphorylcholine antibodies are predominantly products of affinity-matured B cells in the adult. *J. Immunol.* 192, 4551–4559. doi: 10.4049/jimmunol.1303035

Frostegård, J. (2010). Low level natural antibodies against phosphorylcholine: a novel risk marker and potential mechanism in atherosclerosis and cardiovascular disease. *Clin. Immunol.* 134, 47–54. doi: 10.1016/j.clim.2009.08.013

Fry, B. G., Wuster, W., Kini, R. M., Brusic, V., Khan, A., Venkataraman, D., et al. (2003). Molecular evolution and phylogeny of elapid snake venom three-finger toxins. *J. Mol. Evol.* 57, 110–129. doi: 10.1007/s00239-003-2461-2

Fujii, T., Mashimo, M., Moriwaki, Y., Misawa, H., Ono, S., Horiguchi, K., et al. (2017a). Expression and function of the cholinergic system in immune cells. *Front. Immunol.* 8:1085. doi: 10.3389/fimmu.2017.01085

Fujii, T., Mashimo, M., Moriwaki, Y., Misawa, H., Ono, S., Horiguchi, K., et al. (2017b). Physiological functions of the cholinergic system in immune cells. *J. Pharmacol. Sci.* 134, 1–21. doi: 10.1016/j.jphs.2017.05.002

Giastas, P., Zouridakis, M., and Tzartos, S. J. (2018). Understanding structure-function relationships of the human neuronal acetylcholine receptor: insights from the first crystal structures of neuronal subunits. *Br. J. Pharmacol.* 175, 1880–1891. doi: 10.1111/bph.13838

Giribaldi, J., and Dutertre, S. (2018). α-conotoxins to explore the molecular, physiological and pathophysiological functions of neuronal nicotinic acetylcholine receptors. *Neurosci. Lett.* 679, 24–34. doi: 10.1016/j.neulet.2017.11.063

Grabitzki, J., and Lochnit, G. (2009). Immunomodulation by phosphocholine—biosynthesis, structures and immunological implications of parasitic PC-epitopes. *Mol. Immunol.* 47, 149–163. doi: 10.1016/j.molimm.2009.09.035

Hecker, A., Küllmar, M., Wilker, S., Richter, K., Zakrzewicz, A., Atanasova, S., et al. (2015). Phosphocholine-modified macromolecules and canonical nicotinic agonists inhibit ATP-induced IL-1β release. *J. Immunol.* 195, 2325–2334. doi: 10.4049/jimmunol.1400974

Hecker, A., Lips, K. S., Pfeil, U., Zakrzewicz, A., Wilker, S., Padberg, W., et al. (2009). Pivotal advance: upregulation of acetylcholine synthesis in intravascular transplant leukocytes during rejection of rat renal allografts. *J. Leukoc. Biol.* 86, 13–22. doi: 10.1189/jlb.1107722

Hiller, S. D., Heldmann, S., Richter, K., Jurastow, I., Küllmar, M., Hecker, A., et al. (2018). β-nicotinamide adenine dinucleotide (β-NAD) inhibits ATP-dependent inflammasome activation in human monocytic cells. *Int. J. Mol. Sci.* 19:E1126. doi: 10.3390/ijms19041126

Hogg, R. C., Miranda, L. P., Craik, D. J., Lewis, R. J., Alewood, P. F., and Adams, D. J. (1999). Single amino acid substitutions in α-conotoxin PnIA shift selectivity for subtypes of the mammalian neuronal nicotinic acetylcholine receptor. *J. Biol. Chem.* 274, 36559–36564.

Hone, A. J., Whiteaker, P., Christensen, S., Xiao, Y., Meyer, E. L., and McIntosh, J. M. (2009). A novel fluorescent α-conotoxin for the study of α7 nicotinic acetylcholine receptors. *J. Neurochem.* 111, 80–89. doi: 10.1111/j.1471-4159.2009.06299.x

Hone, A. J., Whiteaker, P., Mohn, J. L., Jacob, M. H., and McIntosh, J. M. (2010). Alexa Fluor 546-ArIB[V11L;V16A] is a potent ligand for selectively labeling α7 nicotinic acetylcholine receptors. *J. Neurochem.* 114, 994–1006. doi: 10.1111/j.1471-4159.2010.06819.x

Hoover, D. B. (2017). Cholinergic modulation of the immune system presents new approaches for treating inflammation. *Pharmacol. Ther.* 179, 1–16. doi: 10.1016/j.pharmthera.2017.05.002

Horenstein, N. A., and Papke, R. L. (2017). Anti-inflammatory silent agonists. *ACS Med. Chem. Lett.* 8, 989–991. doi: 10.1021/acsmedchemlett.7b00368

Jiang, W., St-Pierre, S., Roy, P., Morley, B. J., Hao, J., and Simard, A. R. (2016). Infiltration of CCR2+Ly6Chigh proinflammatory monocytes and neutrophils

into the central nervous system is modulated by nicotinic acetylcholine receptors in a model of multiple sclerosis. *J. Immunol.* 196, 2095–2108. doi: 10.4049/jimmunol.1501613

Kabbani, N., and Nichols, R. A. (2018). Beyond the channel: metabotropic signaling by nicotinic receptors. *Trends Pharmacol. Sci.* 39, 354–366. doi: 10.1016/j.tips.2018.01.002

Kabbani, N., Nordman, J. C., Corgiat, B. A., Veltri, D. P., Shehu, A., Seymour, V. A., et al. (2013). Are nicotinic acetylcholine receptors coupled to G proteins? *BioEssays* 35, 1025–1034. doi: 10.1002/bies.201300082

Katz, E., Verbitsky, M., Rothlin, C. V., Vetter, D. E., Heinemann, S. F., and Elgoyhen, A. B. (2000). High calcium permeability and calcium block of the α9 nicotinic acetylcholine receptor. *Hear. Res.* 141, 117–128. doi: 10.1016/S0378-5955(99)00214-2

Kawashima, K., and Fujii, T. (2003). The lymphocytic cholinergic system and its contribution to the regulation of immune activity. *Life Sci.* 74, 675–696.

Kawashima, K., and Fujii, T. (2004). Expression of non-neuronal acetylcholine in lymphocytes and its contribution to the regulation of immune function. *Front. Biosci.* 9, 2063–2085.

King, J. R., Gillevet, T. C., and Kabbani, N. (2017). A G protein-coupled α7 nicotinic receptor regulates signaling and TNF-α release in microglia. *FEBS Open Bio.* 7, 1350–1361. doi: 10.1002/2211-5463.12270

Kummer, W., and Krasteva-Christ, G. (2014). Non-neuronal cholinergic airway epithelium biology. *Curr. Opin. Pharmacol.* 16, 43–49. doi: 10.1016/j.coph.2014.03.001

Lang, C. J., Postle, A. D., Orgeig, S., Possmayer, F., Bernhard, W., Panda, A. K., et al. (2005). Dipalmitoylphosphatidylcholine is not the major surfactant phospholipid species in all mammals. *Am. J. Physiol. Regul. Integr. Comp. Physiol.* 289, R1426–R1439. doi: 10.1152/ajpregu.00496.2004

Lebbe, E. K., Peigneur, S., Wijesekara, I., and Tytgat, J. (2014). Conotoxins targeting nicotinic acetylcholine receptors: an overview. *Mar. Drugs* 12, 2970–3004. doi: 10.3390/md12052970

Liu, Q., Whiteaker, P., Morley, B. J., Shi, F.-D., and Lukas, R. J. (2017). Distinctive roles for α7*- and α9*-nicotinic acetylcholine receptors in inflammatory and autoimmune responses in the murine experimental autoimmune encephalomyelitis model of multiple sclerosis. *Front. Cell. Neurosci.* 11:287. doi: 10.3389/fncel.2017.00287

Lopez-Rodriguez, E., and Pérez-Gil, J. (2014). Structure-function relationships in pulmonary surfactant membranes: from biophysics to therapy. *Biochim. Biophys. Acta* 1838, 1568–1585. doi: 10.1016/j.bbamem.2014.01.028

Lu, B., Kwan, K., Levine, Y. A., Olofsson, P. S., Yang, H., Li, J., et al. (2014). α7 nicotinic acetylcholine receptor signaling inhibits inflammasome activation by preventing mitochondrial DNA release. *Mol. Med.* 20, 350–358. doi: 10.2119/molmed.2013.00117

Luo, S., Nguyen, T. A., Cartier, G. E., Olivera, B. M., Yoshikami, D., and McIntosh, J. M. (1999). Single-residue alteration in α-conotoxin PnIA switches its nAChR subtype selectivity. *Biochemistry* 38, 14542–14548.

Lustig, L. R., Peng, H., Hiel, H., Yamamoto, T., and Fuchs, P. A. (2001). Molecular cloning and mapping of the human nicotinic acetylcholine receptor α10 (CHRNA10). *Genomics* 73, 272–283. doi: 10.1006/geno.2000.6503

Mantovani, A., Garlanda, C., Doni, A., and Bottazzi, B. (2008). Pentraxins in innate immunity: from C-reactive protein to the long pentraxin PTX3. *J. Clin. Immunol.* 28, 1–13. doi: 10.1007/s10875-007-9126-7

Matteoli, G., Gomez-Pinilla, P. J., Nemethova, A., Di Giovangiulio, M., Cailotto, C., van Bree, S. H., et al. (2014). A distinct vagal anti-inflammatory pathway modulates intestinal muscularis resident macrophages independent of the spleen. *Gut* 63, 938–948. doi: 10.1136/gutjnl-2013-304676

McIntosh, J. M., Azam, L., Staheli, S., Dowell, C., Lindstrom, J. M., Kuryatov, A., et al. (2004). Analogs of α-conotoxin MII are selective for α6-containing nicotinic acetylcholine receptors. *Mol. Pharmacol.* 65, 944–952. doi: 10.1124/mol.65.4.944

Mikulski, Z., Hartmann, P., Jositsch, G., Zasłona, Z., Lips, K. S., Pfeil, U., et al. (2010). Nicotinic receptors on rat alveolar macrophages dampen ATP-induced increase in cytosolic calcium concentration. *Respir. Res.* 11:133. doi: 10.1186/1465-9921-11-133

Nishinarita, S., Sawada, S., and Horie, T. (1990). Phosphorylcholine antibodies in pulmonary infection. *Med. Microbiol. Immunol.* 179, 205–214.

Pacini, A., Micheli, L., Maresca, M., Branca, J. J., McIntosh, J. M., Ghelardini, C., et al. (2016). The α9α10 nicotinic receptor antagonist α-conotoxin RgIA prevents neuropathic pain induced by oxaliplatin treatment. *Exp. Neurol.* 282, 37–48. doi: 10.1016/j.expneurol.2016.04.022

Papke, R. L., Chojnacka, K., and Horenstein, N. A. (2014). The minimal pharmacophore for silent agonism of the α7 nicotinic acetylcholine receptor. *J. Pharmacol. Exp. Therap.* 350, 665–680. doi: 10.1124/jpet.114.215236

Paulo, J. A., Brucker, W. J., and Hawrot, E. (2009). Proteomic analysis of an α7 nicotinic acetylcholine receptor interactome. *J. Proteome Res.* 8, 1849–1858. doi: 10.1021/pr800731z

Pavlov, V. A., Chavan, S. S., and Tracey, K. J. (2018). Molecular and functional neuroscience in immunity. *Annu. Rev. Immunol.* 36, 783–812. doi: 10.1146/annurev-immunol-042617-053158

Peng, H., Ferris, R. L., Matthews, T., Hiel, H., Lopez-Albaitero, A., and Lustig, L. R. (2004). Characterization of the human nicotinic acetylcholine receptor subunit alpha (α) 9 (CHRNA9) and alpha (α) 10 (CHRNA10) in lymphocytes. *Life Sci.* 76, 263–280. doi: 10.1016/j.lfs.2004.05.031

Pepys, M. B., and Hirschfield, G. M. (2003). C-reactive protein: a critical update. *J. Clin. Invest.* 111, 1805–1812. doi: 10.1172/JCI18921

Ramanadham, S., Ali, T., Ashley, J. W., Bone, R. N., Hancock, W. D., and Lei, X. (2015). Calcium-independent phospholipases A2 and their roles in biological processes and diseases. *J. Lipid Res.* 56, 1643–1668. doi: 10.1194/jlr.R058701

Razani-Boroujerdi, S., Boyd, R. T., Dávila-García, M. I., Nandi, J. S., Mishra, N. C., Sing, S. P., et al. (2007). T cells express α7-nicotinic acetylcholine receptor subunits that require a functional TCR and leukocyte-specific protein tyrosine kinase for nicotine-induced Ca2+ response. *J. Immunol.* 17, 2889–2898. doi: 10.4049/jimmunol.179.5.2889

Richter, K., Koch, C., Perniss, A., Wolf, P. M., Schweda, E. K. H., Wichmann, S., et al. (2018a). Phosphocholine-modified lipooligosaccharides of *Haemophilus influenzae* inhibit ATP-induced IL-1β release by pulmonary epithelial cells. *Molecules* 23:E1979. doi: 10.3390/molecules23081979

Richter, K., Sagawe, S., Hecker, A., Küllmar, M., Askevold, I., Damm, J., et al. (2018b). C-reactive protein stimulates nicotinic acetylcholine receptors to control ATP-mediated monocytic inflammasome activation. *Front. Immunol.* 9:1604. doi: 10.3389/fimmu.2018.01604

Richter, K., Mathes, V., Fronius, M., Althaus, M., Hecker, A., Krasteva-Christ, G., et al. (2016). Phosphocholine – an agonist of metabotropic but not of ionotropic functions of α9-containing nicotinic acetylcholine receptors. *Sci. Rep.* 6:28660. doi: 10.1038/srep28660

Robinson, S. D., and Norton, R. S. (2014). Conotoxin gene superfamilies. *Mar. Drugs* 12, 6058–6101. doi: 10.3390/md12126058

Romero, H. K., Christensen, S. B., Di Cesare Mannelli, L., Gajewiak, J., Ramachandra, R., Elmslie, K. S., et al. (2017). Inhibition of α9α10 nicotinic acetylcholine receptors prevents chemotherapy-induced neuropathic pain. *Proc. Natl. Acad. Sci. U.S.A.* 114, E1825–E1832. doi: 10.1073/pnas.1621433114

Scott, M. G., Briles, D. E., Shackelford, P. G., Smith, D. S., and Nahm, M. H. (1987). Human antibodies to phosphocholine. IgG anti-PC antibodies express restricted numbers of V and C regions. *J. Immunol.* 138, 3325–3331.

Sgard, F., Charpantier, E., Bertrand, S., Walker, N., Caput, D., Graham, D., et al. (2002). A novel human nicotinic receptor subunit, α10, that confers functionality to the α9-subunit. *Mol. Pharmacol.* 61, 150–159. doi: 10.1124/mol.61.1.150

Shaw, P. X., Hörkkö, S., Chang, M. K., Curtiss, L. K., Palinski, W., Silverman, G. J., et al. (2000). Natural antibodies with the T15 idiotype may act in atherosclerosis, apoptotic clearance, and protective immunity. *J. Clin. Invest.* 105, 1731–1740. doi: 10.1172/JCI8472

Siebers, K., Fink, B., Zakrzewicz, A., Agné, A., Richter, K., Konzok, S., et al. (2018). α-1 antitrypsin inhibits ATP-mediated release of interleukin-1β via CD36 and nicotinic acetylcholine receptors. *Front. Immunol.* 9:877. doi: 10.3389/fimmu.2018.00877

Simard, A. R., Gan, Y., St-Pierre, S., Kousari, A., Patel, V., Whiteaker, P., et al. (2013). Differential modulation of EAE by α9*- and β2*-nicotinic acetylcholine receptors. *Immunol. Cell Biol.* 91, 195–200. doi: 10.1038/icb.2013.1

Stokes, C., Treinin, M., and Papke, R. L. (2015). Looking below the surface of nicotinic acetylcholine receptors. *Trends Pharmacol. Sci.* 36, 514–523. doi: 10.1016/j.tips.2015.05.002

St-Pierre, S., Jiang, W., Roy, P., Champigny, C., LeBlanc, É, Morley, B. J., et al. (2016). Nicotinic acetylcholine receptors modulate bone marrow-derived pro-inflammatory monocyte production and survival. *PLoS One* 11:e0150230. doi: 10.1371/journal.pone.0150230

Suzuki, T., Hide, I., Matsubara, A., Hama, C., Harada, K., Miyano, K., et al. (2006). Microglial α7 nicotinic acetylcholine receptors drive a phospholipase C/IP3 pathway and modulate the cell activation toward a neuroprotective role. *J. Neurosci. Res.* 83, 1461–1470. doi: 10.1002/jnr.20850

Thomsen, M. S., and Mikkelsen, J. D. (2012). The α7 nicotinic acetylcholine receptor ligands methyllycaconitine, NS6740 and GTS-21 reduce lipopolysaccharide-induced TNF-α release from microglia. *J. Neuroimmunol.* 251, 65–72. doi: 10.1016/j.jneuroim.2012.07.006

Ullian, E. M., McIntosh, J. M., and Sargent, P. B. (1997). Rapid synaptic transmission in the avian ciliary ganglion is mediated by two distinct classes of nicotinic receptors. *J. Neurosci.* 17, 7210–7219.

Utkin, Y. N. (2013). Three-finger toxins, a deadly weapon of elapid venom–milestones of discovery. *Toxicon* 62, 50–55. doi: 10.1016/j.toxicon.2012.09.007

Valbuena, S., and Lerma, J. (2016). Non-canonical signaling, the hidden life of ligand-gated ion channels. *Neuron* 92, 316–329. doi: 10.1016/j.neuron.2016.10.016

Verbitsky, M., Rothlin, C. V., Katz, E., and Elgoyhen, A. B. (2000). Mixed nicotinic-muscarinic properties of the α9 nicotinic cholinergic receptor. *Neuropharmacology* 39, 2515–2524.

Vincler, M., Wittenauer, S., Parker, R., Ellison, M., Olivera, B. M., and McIntosh, J. M. (2006). Molecular mechanism for analgesia involving specific antagonism of α9α10 nicotinic acetylcholine receptors. *Proc. Natl. Acad. Sci. U.S.A.* 103, 17880–17884. doi: 10.1073/pnas.0608715103

Wang, H., Yu, M., Ochani, M., Amella, C. A., Tanovic, M., Susarla, S., et al. (2003). Nicotinic acetylcholine receptor α7 subunit is an essential regulator of inflammation. *Nature* 421, 384–388. doi: 10.1038/nature01339

Wessler, I., and Kirkpatrick, C. J. (2008). Acetylcholine beyond neurons: the non-neuronal cholinergic system in humans. *Br. J. Pharmacol.* 154, 1558–1571. doi: 10.1038/bjp.2008.185

Whiteaker, P., Christensen, S., Yoshikami, D., Dowell, C., Watkins, M., Gulyas, J., et al. (2007). Discovery, synthesis, and structure activity of a highly selective α7 nicotinic acetylcholine receptor antagonist. *Biochemistry* 46, 6628–6638. doi: 10.1021/bi7004202

Whiteaker, P., Marks, M. J., Christensen, S., Dowell, C., Collins, A. C., and McIntosh, J. M. (2008). Synthesis and characterization of ^{125}I-α-conotoxin ArIB[V11L;V16A], a selective α7 nicotinic acetylcholine receptor antagonist. *J. Pharmacol. Exp. Ther.* 325, 910–919. doi: 10.1124/jpet.108.136895

Zakrzewicz, A., Richter, K., Agné, A., Wilker, S., Siebers, K., Fink, B., et al. (2017). Canonical and novel non-canonical cholinergic agonists inhibit ATP-induced release of monocytic interleukin-1β via different combinations of nicotinic acetylcholine receptor subunits α7, α9 and α10. *Front. Cell. Neurosci.* 11:189. doi: 10.3389/fncel.2017.00189

Zhong, C., Du, C., Hancock, M., Mertz, M., Talmage, D. A., and Role, L. W. (2008). Presynaptic type III neuregulin 1 is required for sustained enhancement of hippocampal transmission by nicotine and for axonal targeting of α7 nicotinic acetylcholine receptors. *J. Neurosci.* 28, 9111–9116. doi: 10.1523/JNEUROSCI.0381-08.2008

Zhong, C., Talmage, D. A., and Role, L. W. (2013). Nicotine elicits prolonged calcium signaling along ventral hippocampal axons. *PLoS One* 8:e82719. doi: 10.1371/journal.pone.0082719

Conflict of Interest Statement: Certain conopeptides, including RgIA4 have been patented by the University of Utah; JMM is an inventor on these patents.

The remaining authors declare that the research was conducted in the absence of any commercial or financial relationships that could be construed as a potential conflict of interest.

frontiers in Pharmacology

ORIGINAL RESEARCH
published: 20 March 2019
doi: 10.3389/fphar.2019.00250

A C-Terminal Fragment of Chlorotoxin Retains Bioactivity and Inhibits Cell Migration

*Mohadeseh Dastpeyman, Paul Giacomin, David Wilson, Matthew J. Nolan, Paramjit S. Bansal and Norelle L. Daly**

Centre for Molecular Therapeutics, Australian Institute of Tropical Health and Medicine, James Cook University, Cairns, QLD, Australia

Chlorotoxin was originally isolated from the venom of the Israeli scorpion *Leiurus quinquestriatus*, and has potential as a tumor imaging agent based on its selective binding to tumor cells. Several targets have been suggested for chlorotoxin including voltage-gated chloride channels, and it has been shown to have anti-angiogenic activity and inhibit cell migration. The structure of chlorotoxin is stabilized by four disulfide bonds and contains β-sheet and helical structure. Interestingly, the reduced form has previously been shown to inhibit cell migration to the same extent as the wild type, but structural analysis indicates that the reduced form of the peptide does not maintain the native secondary structure and appears unstructured in solution. This lack of structure suggests that a short stretch of amino acids might be responsible for the bioactivity. To explore this hypothesis, we have synthesized fragments of chlorotoxin without disulfide bonds. As expected for such small peptides, NMR analysis indicated that the peptides were unstructured in solution. However, the peptide corresponding to the eight C-terminal residues inhibited cell migration, in contrast to the other fragments. Our results suggest that the C-terminal region plays a critical role in the bioactivity of chlorotoxin.

Keywords: chlorotoxin, tumor-imaging agent, metastasis, migration, invasion, disulfide-rich peptide

OPEN ACCESS

Edited by:
Annette Nicke, Ludwig Maximilian University of Munich, Germany

Reviewed by:
Hai Minh Nguyen, University of California, Davis, United States
Conan Wang, University of Queensland, Australia
Hilmar Ebersbach, Novartis Pharma AG, Australia

***Correspondence:**
Norelle L. Daly
norelle.daly@jcu.edu.au

Specialty section:
This article was submitted to Pharmacology of Ion Channels and Channelopathies, a section of the journal Frontiers in Pharmacology

Received: *24 October 2018*
Accepted: *26 February 2019*
Published: *20 March 2019*

Citation:
Dastpeyman M, Giacomin P, Wilson D, Nolan MJ, Bansal PS and Daly NL (2019) A C-Terminal Fragment of Chlorotoxin Retains Bioactivity and Inhibits Cell Migration. Front. Pharmacol. 10:250. doi: 10.3389/fphar.2019.00250

INTRODUCTION

One of the most well-studied scorpion venom peptides is chlorotoxin (CTX), which was originally purified from the venom of the Israeli scorpion *Leiurus quinquestriatus* (DeBin et al., 1993). CTX contains 36 amino acids with 4 disulfide bonds at the core of its well-defined structure. The tertiary structure, as shown in **Figure 1**, comprises a β-hairpin and an α-helix (Lippens et al., 1995; Correnti et al., 2018). The disulfide connectivity is C_I–C_{IV}, C_{II}–C_{VI}, C_{III}–C_{VII}, and C_V–C_{VIII} (**Figure 1**).

CTX selectively binds to glioma cells and other embryologically related cells and derived tumors of neuroectodermal origin (Soroceanu et al., 1998; Lyons et al., 2002). By contrast, more than 15 normal human tissues have been shown to be negative for CTX binding (Lyons et al., 2002). The selective binding of CTX to tumor cells bodes well for its application in cancer therapy as a tumor optical imaging contrast agent, particularly for brain cancer (Albert et al., 1994; Kieran et al., 2010; Wiranowska et al., 2011; Kovar et al., 2013;

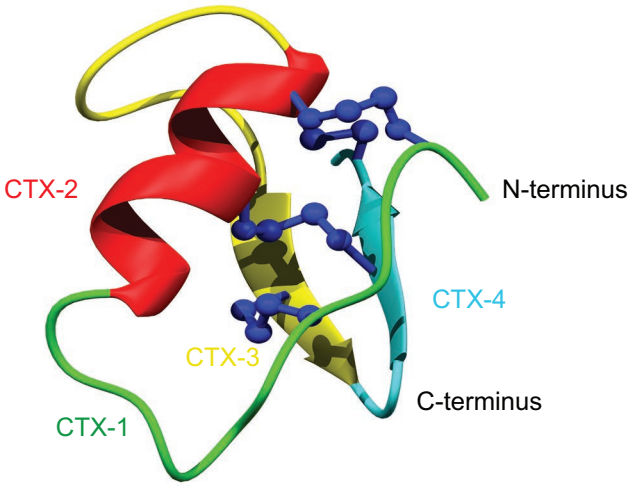

Peptide	Sequence
	1 10 20 30
Chlorotoxin	MCMPCFTTDHQMARKCDDCCGGKGRGKCYGPQCLCR
CTX-1	MAMPAFTTDH
CTX-2	QMARKADDAAG
CTX-3	GKGRGKA
CTX-4	YGPQALAR

FIGURE 1 | Schematic three-dimensional structure of chlorotoxin (PDB code 5L1C). Each structural element represents the four fragments and is color coded. The sequences for the fragments are given below the structure.

Ojeda et al., 2014). Radiolabeled CTX successfully passed human clinical trial phases I and II (Mamelak et al., 2006; Mamelak and Jacoby, 2007; Gribbin et al., 2009) and FDA approval has been granted to progress to phase III, under the name TM-601 (Lefranc et al., 2018).

CTX is known to inhibit migration and invasion of tumor cells through mechanisms that potentially involve multiple pathways (Soroceanu et al., 1998; Lyons et al., 2002; Ojeda et al., 2014; Dardevet et al., 2015). The molecular targets identified for CTX are all involved in malignant cell migration and invasion, including voltage-gated chloride channels (ClC-3), annexin-2, and matrix metalloproteinase-2 (MMP-2) (Ullrich and Sontheimer, 1996; Deshane et al., 2003; Olsen et al., 2003; Kesavan et al., 2010). It has been shown CTX can effectively block the ClC-3 voltage-gated chloride channel (DeBin and Strichartz, 1991; DeBin et al., 1993), which is selectively expressed in glioma cells (Ullrich et al., 1998; Olsen et al., 2003; Jentsch, 2008). ClC-3 is involved in cell cytoskeleton rearrangements and consequently cell shape and movements during cell migration (Soroceanu et al., 1998; Soroceanu et al., 1999; Mcferrin and Sontheimer, 2006). Furthermore, it has been shown that CTX also interacts with a cell surface protein complex composed of MMP-2, membrane type-I MMP (MT1-MMP), a transmembrane inhibitor of metalloproteinase-2, $\alpha_v\beta_3$ integrin, and other proteins (Hofmann et al., 2000; Deshane et al., 2003; Jacoby et al., 2010).

Direct binding of CTX with molecular targets has not been experimentally characterized but a recent computational study predicted the binding of CTX with MMP-2 (Othman et al., 2017). The model proposed in this study suggests that the β-sheet of CTX interacts in a region between the collagen binding domain and catalytic domain of the MMP-2, whereas the α-helix of CTX does not appear to be involved in the interaction (Othman et al., 2017).

The three-dimensional structure of disulfide-rich toxins, such as the scorpion venom peptides leiurotoxin-I and

Non-Standard Abbreviations: ANOVA, Analysis of variance; APC, Allophycocyanin; BSA, Bovine serum albumin; CTX, Chlorotoxin; DIPEA, Ethyldiisopropylamine; DMSO, dimethyl sulfoxide; DSS, 4,4-dimethyl-4-silapentane-1-sulfonic acid; ECACC, European Collection of Authenticated Cell Cultures; FBS, Fetal bovine serum; HCTU, 2-(6-chloro-1-H-benzotriazole-1-yl)-1,1,3,3-tetramethylaminium hexafluorophosphate; HEPES, 4-(2-hydroxyethyl)-1-piperazineethanesulfonic acid; HSQC, Heteronuclear single quantum correlation experiment; HUVEC, Human umbilical vein endothelial cells; ITS-G, Insulin-transferrin-selenium; MALDI TOF/TOF MS, Matrix-assisted laser desorption/ionization-time of flight mass spectrometry; MEM, Minimum essential medium; MMP-2, MMP matrix metalloproteinase-2; NHS, N-hydroxy-succinimide; NMR, Nuclear magnetic resonance; NOESY, Nuclear overhauser spectroscopy; PBS, Phosphate-buffered saline; QTOF, Time-of-flight mass spectrometry; RP-HPLC, Reversed-phase HPLC; TCA, Trichloroacetic acid; TFA, Trifluoroacetic acid; TOCSY, Total correlated spectroscopy; XTT, 2,3-Bis(2-methoxy-4-nitro-5-sulfophenyl)-2*H*-tetrazolium-5-carboxanilide inner salt.

charybdotoxin (Drakopoulou et al., 1998; Zhu et al., 2002), is generally critical for bioactivity. However, a recent study suggests this is not the case for CTX. A reduced form of CTX, with the cysteine residues mutated to aminobutyric acid, maintains inhibitory effects on HUVEC cell migration compared to the wild-type peptide, but does not have regular secondary structure (Ojeda et al., 2014). This lack of structure suggests that a short stretch of amino acids might be responsible for the bioactivity. Determining the minimal sequence of CTX with bioactivity is likely to enhance the understanding of the structure/function relationships. We have synthesized four fragments of CTX, containing 7–11 residues, with the cysteine residues replaced with alanine residues to prevent disulfide bond formation, and analyzed the structure, *in vitro* binding, and bioactivity.

MATERIALS AND METHODS

Mammalian Cell Culture

The U-87 MG (ATCC® HTB-14), human primary glioblastoma astrocytoma cell line was grown and maintained in modified Minimum Essential Medium (MEM) (Life Technologies) at 37°C and 5% CO_2. The growth medium was supplemented to a final concentration of 10% fetal bovine serum (FBS) (Gibco, Scotland), 15 mM HEPES, 1× penicillin-streptomycin solution, 1 mM sodium pyruvate, and 2 mM L-glutamine.

The 1BR.3.GN (ECACC 90020509), human skin normal fibroblast cell line was purchased from the European Collection of Authenticated Cell Cultures (ECACC). 1BR.3.GN cells were grown and maintained in DMEM/F12 (Life Technologies, Australia) containing 1× GlutaMAX, 1× penicillin-streptomycin solution, and supplemented with FBS at 37°C and 5% CO_2.

Peptide Synthesis, Purification, and Characterization

Chlorotoxin (CTX) was purchased from Iris Biotech GmbH (Marktredwitz, Germany). CTX fragments were chemically synthesized using standard stepwise Fmoc solid-phase peptide synthesis methods on the rink amide resin (Anaspec, Fremont, CA, USA) using an automated PS3 bench top peptide synthesizer (Protein Technologies, Tuscon, AZ, USA). Peptides were deprotected and cleaved from the resin using the following cleavage cocktail: 95% TFA: 2.5% TIPS: 2.5% H_2O (v/v/v). The peptide was then precipitated and washed several times with cold diethyl ether, dissolved in 50% acetonitrile:50% H_2O, lyophilized, and stored as lyophilized powder. Crude peptide mixtures were purified by reversed-phase HPLC (RP-HPLC) on a C_{18} preparative column (Phenomenex Jupiter 250 × 21.2 mm, 10 µm, 300 Å). The peptides were eluted with a 1% gradient from 1 to 60% of solvent B in solvent A over 60 min at the flow rate of 5 ml/min (Solvent A: 0.05% TFA/water, Solvent B: 0.05% TFA in 90% acetonitrile/water). The purified fractions were characterized by a SCIEX 5800 MALDI TOF/TOF mass spectrometer (SCIEX, Foster city, CA, USA).

NMR Spectroscopy and Structure Analysis

Samples were prepared from lyophilized peptides at a concentration of 0.2 mM in 90% H_2O:10% D_2O with 4,4-dimethyl-4-silapentane-1-sulfonic acid (DSS) as a reference. All NMR spectra were recorded on a 600-MHz AVANCE III NMR spectrometer (Bruker, Karlsruhe, Germany). 2D ^{1}H-^{1}H TOCSY, ^{1}H-^{1}H NOESY, ^{1}H-^{15}N HSQC, and ^{1}H-^{13}C HSQC spectra were collected at 290 K and used for amino acid assignment. All spectra were recorded with an interscan delay of 1 s. NOESY spectra were acquired with mixing times of 200 ms, and TOCSY spectra were acquired with isotropic mixing periods of 80 ms. All spectra were assigned using CCPNMR (Vranken et al., 2005) based on the approach described by Wüthrich (2003).

Serum Stability Assay

The serum stability of the peptides was tested using human male serum (Sigma, USA), as previously described (Chan et al., 2011). All peptides were tested at a final concentration of 6.6 µM after dilution from a stock solution at 200 µM. The serum was centrifuged at 17,000*g* for 10 min to remove the lipid component, and the supernatant incubated at 37°C for 15 min, prior to conducting the assay. The peptides were incubated in serum or phosphate-buffered saline (PBS) at 37°C, and aliquots were taken at 0, 3, 8, and 24 h (40-µl aliquots were taken in triplicate). The aliquots of serum were quenched with 40 µl of 6 M urea and incubated for 10 min at 4°C. The aliquots were then quenched with 40 µl of 20% trichloroacetic acid (TCA) and incubated for another 10 min at 4°C to precipitate serum proteins. Finally, samples were centrifuged at 17,000*g* for 10 min, and 90 µl of the supernatant was analyzed on reversed-phase HPLC using a Phenomenex Jupiter Proteo C_{12} analytical column (150 mm × 2.00 mm, 4 µm, 90 Å, Phenomenex, Torrance, CA, USA) and a linear gradient of solvent B [90% acetonitrile/10% H_2O, 0.045% trifluoroacetic acid (TFA)] at a flow rate of 0.4 ml/min using an Agilent 1260 Infinity system (Agilent Technologies, Hanover, Germany). The control samples contained equivalent amounts of the peptides in PBS and were subjected to the same treatment procedure. The stability at each time point was calculated based on the area of the RP-HPLC peaks following incubation with serum at 214 nm as a percentage of the area of 0-h serum-treated peptides (Chan et al., 2013).

Cytotoxicity Assay

The 2,3-bis-(2-methoxy-4-nitro-5-sulfophenyl)2*H*-tetrazolium-5-carboxanilide (XTT) colorimetry assay was performed to determine whether CTX at the applied concentration was toxic to the U-87 cell line (Page et al., 1993). Cells were seeded in 96-well microplates (7.5×10^3 cells/well) and incubated at 37°C for 24 h. The culture media were then replaced with 150 µl of treatment at two final concentrations of 5 and 60 µM. The treatment was in either media supplemented with 10% FBS or media supplemented with 0.5% FBS, 1× ITS-G, and 1% BSA. DMSO (50% v/v) was used as a control for cell death (Diaz-Perlas et al., 2018). Cells then were incubated at

37°C for 24 h. The media was removed after 24 h and the cells were incubated with 50 µl XTT [1.0 mg/ml in media without phenol red and 0.025 mM phenazine methosulfate (Sigma, USA)] for 3.5 h. Absorbance (A) was measured at 450 nm wavelength, 650 nm used as reference wavelength in a plate reader (Polarstar Optima, Germany). Cell viability was calculated as percentage of control cells using the equation: $(A_{450} - A_{650})$ of treated cells $\times$ 100/$(A_{450} - A_{650})$ of control cells.

The experiments were repeated three times in pentaplicates and statistical significance of the observed difference was determined using one-way ANOVA with Dunnett's multiple comparison tests using the GraphPad Prism v7 software (GraphPad Software Inc., USA).

Peptide Biotinylation

CTX fragments were biotinylated on the resin to be detected by streptavidin-APC for the binding assay according to the following protocol. The assembled peptide on the resin (0.1 mmol) was washed with DMF. Biotin (Sigma, USA) was coupled to the N-terminal amide using HCTU/DIPEA activation in DMSO:DMF (1:1), overnight. The resin was washed with DMSO:DMF (1:1) twice to remove excess biotin and washed further with DMF (2×) and DCM (2×) and allowed to dry before proceeding to cleavage step. The biotinylated peptide was cleaved from the resin as previously mentioned. The mono-labeled peptides were then purified using preparative RP-HPLC and characterized using a SCIEX 5800 MALDI TOF/TOF mass spectrometer (SCIEX, Foster City, CA, USA) and analytical RP-HPLC.

The CTX biotinylation was performed as described previously (Selo et al., 1996). Briefly, 1 mg/ml CTX (Iris, Germany) solution was prepared in phosphate buffer (pH 8.0) and incubated with 27.5 µl of 10 mM NHS-Biotin (Sigma, USA) in DMSO (10 molar excess). The final concentration of the organic solvent was kept <20% in the reaction buffer. After 6 h of incubation at room temperature, excess biotin was removed by passing the reaction solution through Phenomenex Strata C_8 unit (55 µm, 70 Å). The collected sample was characterized using TripleTOF® 6,600 Quadrupole Time-Of-Flight (QTOF) mass analyzer (SCIEX, Foster City, CA, USA) and analytical RP-HPLC.

Cell Surface Binding and Internalization Assay

Flow cytometric analysis was performed to investigate binding of CTX and fragments to U-87 MG and 1BR.3.GN cells. For cell surface binding analysis, cells were detached from adherent culture using StemPro™ Accutase™ Cell Dissociation reagents (Gibco, USA), washed and resuspended in media supplemented with 0.5% FBS, 1× ITS-G, and 0.1% BSA. After adjusting the cell density to 10^6 cells per ml, 100 µl of the cell suspension was placed in round-bottom 96-well plate. For each concentration of CTX and fragments, duplicate wells received treatments of either 5 or 50 µM CTX or CTX fragments for 30 min at 4°C. Biotinylated anti-mouse/human CD44 antibody (BioLegend) was used as control positive in all sets of experiments (Knupfer et al., 1999).

Following the incubation, cells were washed 3 times with PBS and centrifuged at 400 g for 3 min to remove the unbound peptides. APC-conjugated streptavidin (BD Pharmingen, USA) was added at a concentration of 6.5 µg/ml to each well and incubated for further 30 min on ice. Incubation was followed by two further washes in PBS and stained cells were then analyzed on a BD FACS Canto II flow cytometer (BD Bioscience, USA). Data analysis was performed using FlowJo software (Tree Star, v. 8.8.4.).

To investigate whether CTX fragments internalize into cells *via* the same thermodynamic pathway as CTX, cells were incubated with CTX fragments at a concentration of 50 µM in 0.5% media supplemented with 1× ITS-G and 0.1% BSA for 30 min at 37°C, with 5% CO_2. Then cells were washed with PBS and fixed using 1× fixation/permeabilization buffer (eBioscience, USA). Cells were washed and permeabilized using 1× permeabilization buffer (eBioscience, USA) for 10 min. Cells then were stained with APC-streptavidin at 4°C for 30 min. Samples were washed twice with PBS and subsequently analyzed on BD FACS Canto II flow cytometer (BD Bioscience, USA) and data were analyzed as described above.

Cell Migration/Invasion Assay

Migration assays were performed using CytoSelect cell migration assay kit (8 µm, Fluorometric format, Cell Biolabs, USA) according to the manufacturer's instructions. Briefly, cells were serum-starved overnight, then harvested using StemPro™ Accutase™ Cell Dissociation reagents and resuspended in media supplemented with 1× ITS-G and 1% BSA at 10^6 cells/ml. Aliquots of 100 µl of cells were then pre-incubated with CTX or fragments (at two concentrations of 5 and 50 µM) for 30 min at room temperature. Then cells were added to each insert (upper chamber), and 150-µl media supplemented with or without 10% FBS (chemoattractants) was added to each well (lower chamber). The plate was incubated at 37°C for 16 h to allow cell migration through the polycarbonate membrane pores in response to chemoattractant (10% FBS) and subsequently lysed and detected by CyQuant® GR dye. Fluorescence measurement was performed using a fluorescence plate reader (Polarstar Optima, Germany) with a 485/520-nm filter (at an extinction of 480 nm and an emission of 520 nm). The percentage inhibition of migration in each treatment was calculated relative to that of the untreated cells. Statistical analyses using one-way ANOVA were performed for comparing treatments against control cells followed by Dunnett's test using the GraphPad Prism software.

The invasion assay was performed using CytoSelect cell invasion assay kit (8 µm, Fluorometric format, Cell Biolabs, USA) using the same protocol. The cells were allowed to pass through a polycarbonate membrane bearing 8-µm-sized pores with a thin layer of basement membrane for 24 h. Cells that had invaded to the other side of the inserts were lysed and detected by CyQuant® GR dye. The percentage inhibition of invasion in each treatment was calculated relative to that of the untreated cells. Statistical analyses using one-way ANOVA were performed for comparing

treatments against control cells followed by Dunnett's test using the GraphPad Prism software.

Protein Array Analysis of CTX

CTX used for the protein array analysis was chemically synthesized using Fmoc chemistry with 2-chlorotrityl resin and oxidized using 0.1 M ammonium bicarbonate pH 8 and 1 mM reduced glutathione, with stirring overnight at room temperature. The peptide was biotinylated using a 20-fold excess of EZ-Link® Sulfo-NHS-LC-biotin (ThermoFisher Scientific), according to the manufacturer's instructions. The biotinylated sample was analyzed utilizing an SCIEX 5800 MALDI TOF/TOF mass spectrometer (SCIEX, Foster city, CA, USA), followed by purification of labeled CTX (to remove excess non-reacted and hydrolyzed biotin reagent from the solution) *via* HPLC. The purified sample was dried and resuspended in 100 µl of 1.0% PBS (pH 7.2) to give a final concentration of 10 µg. Protein-protein interactions among biotinylated CTX and more than 9,000 human proteins were then investigated employing a ProtoArray® Human Protein Microarray v5.0 Protein-Protein Interaction (PPI) kit (Invitrogen™) and significant interactions detected employing a GenePix® microarray scanner (Molecular Devices), according to the manufacturer's instructions.

RESULTS

Design and Synthesis of Chlorotoxin Fragments

To determine the minimal sequence requirements of CTX to elicit cellular effects, four CTX fragments (CTX-1, -2, -3, -4) were chemically synthesized using Fmoc solid-phase peptide synthesis. The sequences of the full-length CTX and synthetic fragments, and the location of the fragments in the CTX structure are shown in **Figure 1**. The crude peptides were purified using RP-HPLC and mass analysis carried out using MALDI TOF/TOF mass spectrometry.

Structural Analysis With NMR Spectroscopy

The structures of the purified peptides were analyzed using NMR spectroscopy. The one-dimensional spectra of the CTX fragments did not have significant dispersion in the amide region. Further analysis of the TOCSY and NOESY spectra for the individual fragments allowed assignment of the resonances and analysis of the secondary shifts, which indicated that the peptides had shifts close to random coil, consistent with the peptides being unstructured in solution **(Supplementary Figure S1)**.

Serum Stability Assay

The stability of the CTX peptide fragments in human serum was assessed using RP-HPLC, and the degradation profiles are shown in **Figure 2**. CTX-1 and -2 degraded more slowly than CTX-4. The latter peptide had less than 10% peptide remaining after 3 h, whereas CTX-1 had more than 18% remaining at the 8-h time point and could be detected up to 24 h. The serum stability could not be measured accurately for CTX-3 peptide, using the same column as that used for the other fragments, because of the hydrophilic nature of this peptide. CTX has been previously shown to be highly stable in serum with only 10% degradation after 24-h incubation with human serum at 37°C using the same protocol (Akcan et al., 2011; Diaz-Perlas et al., 2018).

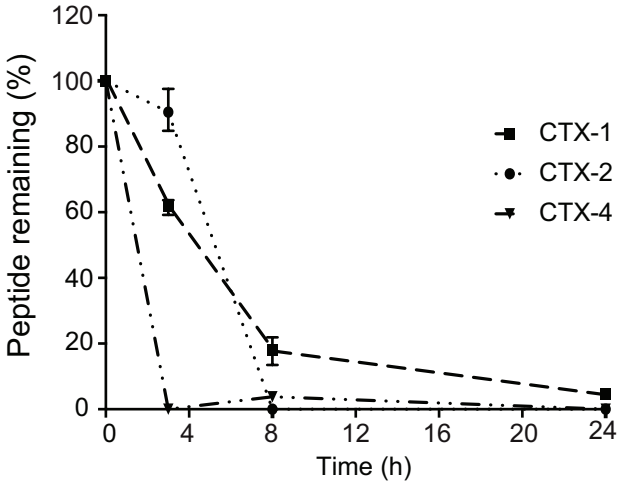

FIGURE 2 | Stability of the peptides in human serum. The amount of peptide remaining was calculated by comparing the area of the elution peak of peptides incubated in human serum and that of peptides that had not been incubated. The experiments were performed in triplicate. All data are represented as mean ± SEM.

Due to low serum stability of CTX fragments, the cell assays were designed to minimize the exposure of the peptides to serum media (FBS). Prior to the cell assays, cells were pre-treated with CTX or CTX fragments in 0.5–1% media supplemented with 1× ITS-G and 0.1% BSA which were used to ensure cells remain healthy and viable over the course of the 30-min treatment (Gstraunthaler, 2003). It has been previously shown that CTX achieves the maximum cellular level at a concentration of 10 µM within 30 min of incubation with cells under physiological conditions (37°C, 5% CO_2) (Wiranowska et al., 2011). CTX has been shown to significantly label cells (Kesavan et al., 2010), block chloride channel (Mcferrin and Sontheimer, 2006), inhibit endothelial cell migration (Ojeda et al., 2014), and induce biochemical changes in U87-MG cells (Falahat et al., 2016) over 30-min incubation with cells. Thus, 30 min of pre-treatment appears to be the optimum treatment time for CTX and fragments, in this study.

Cytotoxicity Assay

The cytotoxicity of CTX and the CTX fragments was investigated using an XTT assay on the U-87 MG cell line. Cells were incubated with either 5 or 60 µM peptide. These concentrations are comparable to those used in the subsequent cell assays. The XTT assays were carried out in media (10%), and also in media supplemented with 0.5% FBS,

1× ITS-G, and 1% BSA. The CTX fragments were not cytotoxic to U87-MG cells under either media condition or peptide concentration, with cell viability after a 24-h incubation period higher than 90% for all peptides tested (**Supplementary Figure S2**).

These results are consistent with previous study that showed CTX is not toxic to U87-MG cells and HUVECs at concentrations up to 10 and 200 μM, respectively (Ojeda et al., 2014; Park et al., 2018).

Peptide Biotinylation

Peptides were labeled with biotin to allow detection using flow cytometry. The CTX fragments were biotinylated on resin, resulting in a single biotin moiety attached to the N-terminus. Following incubation with biotin, the peptides were purified using RP-HPLC to remove excess biotin. By contrast, CTX was biotinylated in solution. The mass spectrometry analysis indicated the presence of CTX species with one, two, three, and four biotin moieties attached, consistent with the four biotinylation sites. Excess biotin was removed from the sample using RP-HPLC but it was not possible to purify the individual species, and therefore, the mixture was used in the subsequent experiments.

Cell Surface Binding/Endocytosis Assay

To evaluate the interaction of CTX fragments with U87-MG cells, a cell line previously shown to bind to CTX, *in vitro* binding assays were carried out with the biotinylated peptides and binding detected by flow cytometry using APC-conjugated streptavidin as shown in **Figure 3A**. As expected, native CTX demonstrated a significant level of APC fluorescence and surface binding to cells when compared to control-treated cells (**Figure 3A**). Further analysis of the relative binding efficiency of the four fragments revealed that while CTX-1, CTX-2, and CTX-4 did not display any significant binding to the surface of cells, CTX-3 did significantly bind to the surface of both U87-MG and 1BR.3.GN cell lines in a dose-dependent manner (**Figures 3A,B**). These studies were done at 4°C. A direct comparison of the peptides with CTX is difficult, given the differences in the number of biotin moieties present in the full-length peptide and the fragments, which will affect the signal intensity.

We next assessed whether the peptide fragments were being internalized and interacting with a target within the cell. Analysis of the internalization of the fragments into the U87-MG cells at 37°C indicated that while CTX-1 and CTX-2 do not appear to be internalized into either the tumor cell line (U87-MG) or normal cell line (1BR.3.GN), CTX-3 and CTX-4 appeared to be binding internally to U87-MG cells (**Figures 4A,B**). Interestingly, only CTX-3 showed any evidence of fluorescence signal when exposed to 1BR.3.GN cells; however, it is not clear whether this binding was on the surface of the cell or internal (**Figure 4B**). Given that CTX-4 appeared to bind internally to U87-MG cells but not 1BR.3.GN cells suggests that this intracellular interaction may be specific to the glioblastoma cell line. Chlorotoxin has been previously shown not to bind to human fibroblasts (Lyons et al., 2002).

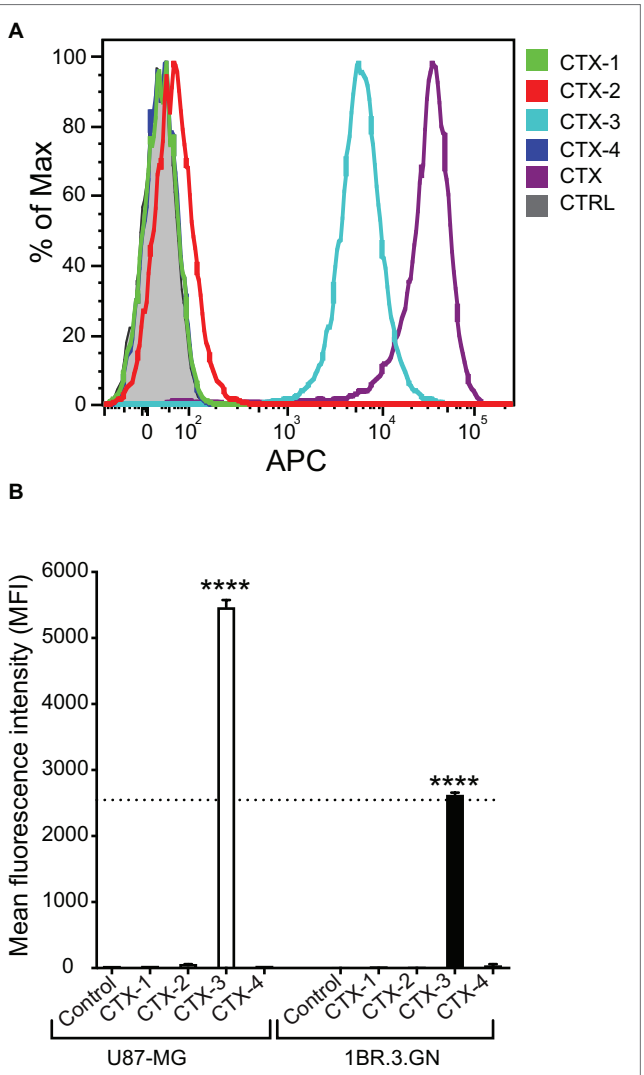

FIGURE 3 | *In vitro* cell surface binding of CTX fragments. **(A)** Representative flow cytometric histogram of *in vitro* U87-MG cell surface binding of biotinylated CTX fragments detected by APC-labeled streptavidin. Cells were treated with 50 μM CTX or fragments at 4°C for 30 min. Gray shaded histograms represent cells treated with APC-streptavidin alone. **(B)** Mean fluorescence intensity (MFI) of *in vitro* cell surface binding of CTX fragments (50 μM) to U87-MG and 1BR.3.GN cell line. The experiments were performed three times in duplicate. Data are presented as mean ± SEM. The statistical analysis was performed using an ANOVA Dunnett's multiple comparison test by comparison of CTX fragments with control cells (****$p < 0.0001$). The data were normalized to account for differences in cell number and expressed as percent of maximum cell number for each sample (% of Max).

Migration and Invasion Assay

The inhibitory effects of CTX and the CTX fragments on migration and invasion of U87-MG cells were analyzed and the results summarized in **Figure 5**. CTX significantly inhibited U87-MG cell migration with inhibitory effects of 32.9% ($p < 0.01$) and 34.6% ($p < 0.001$) compared to control cells at 5 and 50 μM, respectively (**Figure 5A**). Only CTX-4 inhibited U87-MG cell migration at a concentration of 50 μM (20.4%, $p < 0.05$).

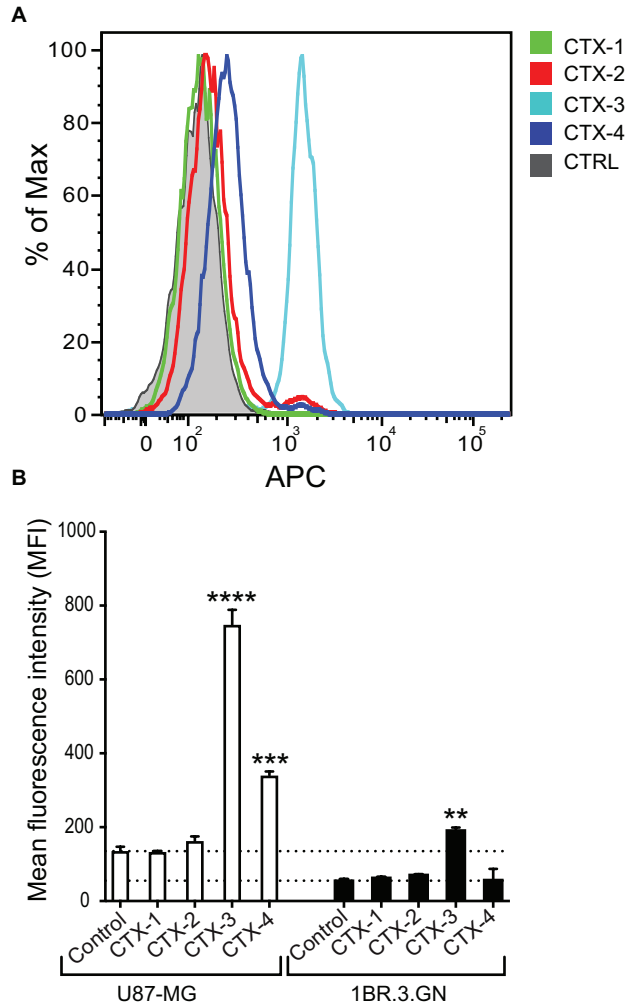

FIGURE 4 | *In vitro* cell internalization of CTX fragments. **(A)** Representative flow cytometric histogram of *in vitro* U87-MG cell internalization of biotinylated CTX fragments detected by APC-labeled streptavidin. Cells were treated with 50 μM CTX fragments at 37°C for 30 min. Gray shaded histograms represent cells treated with APC-streptavidin alone. **(B)** Mean fluorescence intensity (MFI) of *in vitro* cell internalization of CTX fragments (50 μM) to U87-MG and 1BR.3.GN cell line. The experiments were performed three times in duplicate. Data are presented as mean ± SEM. The statistical analysis was performed using an ANOVA Dunnett's multiple comparison test by comparison of CTX fragments with control cells (**$p < 0.01$, ***$p < 0.001$, ****$p < 0.0001$).

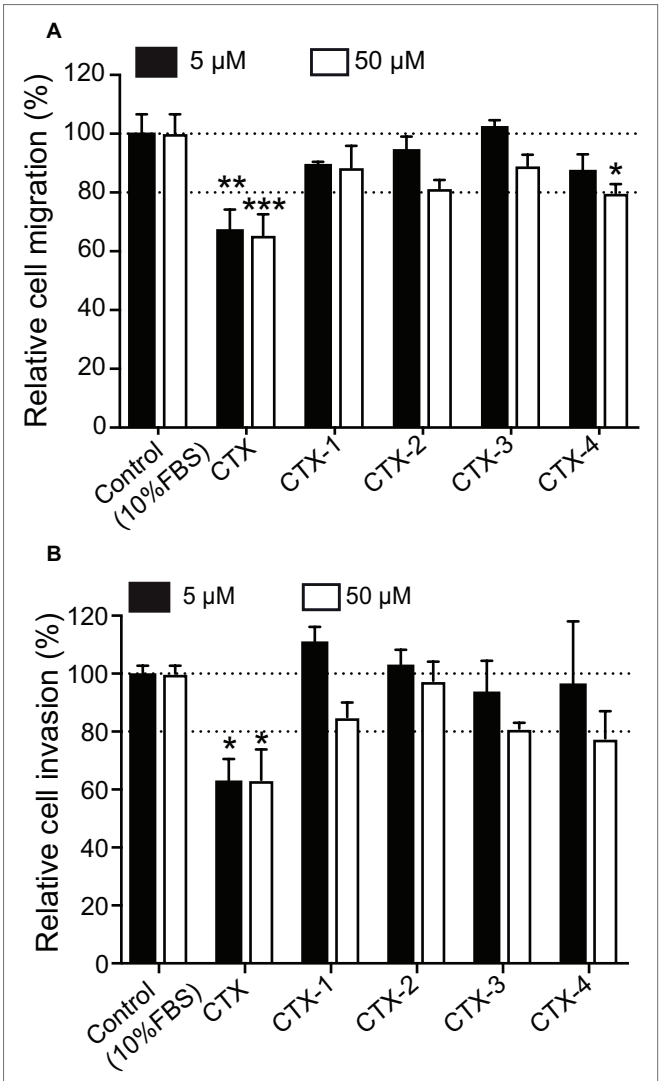

FIGURE 5 | The migration and invasion assay. Cells were pre-incubated with CTX and fragments at 5 and 50 μM and then were used for migration/invasion assay. **(A)** The effect of CTX and fragments on U87-MG cell migration. **(B)** The effect of CTX and fragments on U87-MG cell invasion. The percentage inhibition of migration/invasion in each treatment was calculated relative to that of the untreated well. The experiments were performed two times in quadruplicate. The data were expressed as mean ± SEM. Data were analyzed by one-way ANOVA against peptide control. *$p < 0.05$, **$p < 0.01$, ***$p < 0.001$.

CTX also significantly inhibited U87-MG cell invasion by 37% ($p < 0.05$) and 36.7% ($p < 0.05$) at 5 and 50 μM (**Figure 5B**), respectively, consistent with previous studies (Deshane et al., 2003; Mcferrin and Sontheimer, 2006; Kesavan et al., 2010). None of the CTX fragments significantly inhibited U87-MG cell invasion even at the highest concentration tested (50 μM).

Protein Array Analysis of CTX

Protein-protein interactions among biotinylated CTX and more than 9,000 human proteins were investigated employing a ProtoArray® Human Protein Microarray v5.0 Protein-Protein Interaction (PPI) kit (Invitrogen™) and monitored with a GenePix® microarray scanner (Molecular Devices). Of the more than 9,000 possible interactions tested herein, 104 (ca. 1.0%) were significant (*Z*-score of >3), while 4 of the top 9, including interactions between CTX and cortactin (CTTN; Z-score 32.27), polo-like kinase 1 (PLK1; Z-score 11.20), homeobox protein HOXB6 (Z-score 10.47), and XTP3-transactivated protein A (XTP3TPA; *Z*-score 6.21825), are relevant to the present investigation as these proteins have been shown to be involved in cancer.

DISCUSSION

Given the potential of CTX as a therapeutic, it is of significant interest to understand the structural features important for function, as this information is likely to facilitate the development of CTX as a therapeutic. Numerous studies have analyzed the binding of CTX and conjugates to cells but there is still limited information on the structure-function relationships and target interaction.

The CTX fragments synthesized in the current study showed limited stability in human serum and did not display regular secondary structure in solution. Interestingly, CTX-2 was the most stable of the peptides tested in human serum and is also the longest peptide, which might explain the enhanced stability. The lack of structure in solution is expected for such small peptides and is consistent with the previous study, which showed that the disulfide bonds in CTX are critical for the three-dimensional structure (Ojeda et al., 2014).

The C-terminal fragments of CTX (CTX-3 and CTX-4) displayed interesting properties in the cellular assays. CTX-3 showed cell surface binding and cell internalization, whereas CTX-4 was internalized into cells and was the only fragment to inhibit U87-MG cell migration at the highest concentration tested (50 μM). Despite the effect of CTX-4 on cell migration, it did not inhibit cell invasion.

The cell surface binding and internalization of CTX is critical to its potential as a tumor imaging agent and our current results suggest that residues 22–28, present in CTX-3, might be involved with this process. However, given that CTX-3 binds to both a tumor cell line and a normal cell line, in contrast to previous studies on CTX, it appears likely that this region is not sufficient by itself to account for the selective binding to tumor cells. It is possible the cell surface binding observed for CTX-3 is non-specific membrane binding mediated by the presence of the high proportion of positively charged (two lysine and one arginine) residues within a seven-residue peptide as reported for other highly charged peptides (Futaki et al., 2007; Ojeda et al., 2017). Although no cell surface binding was observed for CTX-4, it was the only fragment that appeared to be specifically internalized into the glioma cells at 37°C. The differences between CTX-3 and CTX-4 suggest they might have different internalization mechanisms.

Our results, whereby CTX-4 only inhibits migration and not invasion, indicate that it might inhibit the ClC-3 channel, which is involved in cell migration, independently from the MMP2 macromolecular complex, which is involved in cell invasion. The other possibility is that CTX-4 inhibits U87-MG cell migration through another pathway, which does not necessarily involve the macromolecular complex. Annexin A2, which is identified as another CTX target, is involved in cell migration in a series of glioma cells including U87-MG cells (Tatenhorst et al., 2006; Kesavan et al., 2010). Therefore, it is possible that CTX-4 inhibits U87-MG cell migration through an annexin A2 interaction. However, more research, including mutagenesis studies, are required to investigate CTX-4 binding to the targets previously suggested for CTX. Additional studies involving the synthesis of over-lapping peptide fragments might also provide further insight into the structure/function relationships.

The recently proposed model of MMP-2 interacting with CTX (Othman et al., 2017) shows that residues 29–36 (which correspond to CTX-4) are directly involved in the interaction with MMP-2 (Othman et al., 2017). Neither of the cysteine residues (C33 and C35) in this region interact with MMP-2, therefore it is highly likely that replacing cysteines with alanine in our study would not make a significant difference in CTX-4 binding and bioactivity. Furthermore, a recent study has used CTX as inspiration to design blood-brain barrier shuttles. MiniCTX3 contains residues 28–32 of CTX and a lactam bridge, and was able to transport nanoparticles across endothelial cells (Diaz-Perlas et al., 2018). These studies highlight the potential importance of the C-terminal region of CTX in cellular interactions and support our current findings.

Although several biological targets for CTX have been proposed, direct binding has not been reported. Here, we used protein array technology to identify another possible target for CTX. CTX bound most strongly to cortactin, a substrate of the Src nonreceptor tyrosine kinase. Overexpression of cortactin is linked to invasive cancers, including melanoma, colorectal cancer, and glioblastoma, making it an important biomarker for invasive cancers (MacGrath and Koleske, 2012). Cortactin localizes to invasive protrusions in cells including invadopodia and has been shown to associate with MMP-2 using co-immunoprecipitation studies (Banon-Rodriguez et al., 2011). Similar to annexin A2, it has been suggested that a transient interaction between cortactin and complexes containing MMPs might exist (Banon-Rodriguez et al., 2011). Given CTX can penetrate cells *via* clathrin-mediated endocytosis, it is possible that it can interact with cortactin intracellularly, or alternatively as part of a MMP-2 complex that is subsequently internalized (Wiranowska et al., 2011). The importance of intracellular targeting of cortactin has been shown with a cell-permeable peptide that binds cortactin, and inhibits the invasion of a range of cancers including glioblastomas (Hashimoto et al., 2006). Our cell internalization assay provides support for the possibility that CTX-4 can bind an intracellular target that is specific to tumor cells compared to normal cells. It would be of interest to determine if CTX-4 can also bind to cortactin.

Overall, this study provides insight into understanding the important sequence requirements for CTX bioactivity, and indicates that a small region of CTX, which is not structured in solution, can have an influence on cell migration, albeit at relatively high concentrations. This result might explain the bioactivity previously observed for the reduced form of CTX (Ojeda et al., 2014). We also provide evidence that fragments of CTX are involved in cell binding and/or internalization. Further study is required to determine if these fragments can bind to the biological targets previously suggested for CTX.

DATA AVAILABILITY

The datasets generated for this study are available on request to the corresponding author.

AUTHOR CONTRIBUTIONS

ND and MD contributed to study conception. MD, MN, and PB performed experiments. MD, ND, PG, and MN contributed to data analysis. MD, ND, and PG contributed to data presentation. MD and ND contributed to manuscript preparation. MD, ND, DW, and PG contributed to manuscript editing. ND, DW, and PG contributed to supervision. ND contributed to funding acquisition.

FUNDING

This work was supported by a Future Fellowship to NLD (110100226). PG is supported by an Advance Queensland Mid-Career Fellowship. The James Cook University NMR facility was partially funded by the Australian Research Council (LE120100015, LE160100218).

ACKNOWLEDGMENTS

MD would like to thank James Cook University for a PhD scholarship. The authors would like to thank Dr. Roland Ruscher for his valuable comments on analyzing the flow cytometry data.

SUPPLEMENTARY MATERIAL

The Supplementary Material for this article can be found online at: https://www.frontiersin.org/articles/10.3389/fphar.2019.00250/full#supplementary-material

REFERENCES

Akcan, M., Stroud, M. R., Hansen, S. J., Clark, R. J., Daly, N. L., Craik, D. J., et al. (2011). Chemical re-engineering of chlorotoxin improves bioconjugation properties for tumor imaging and targeted therapy. *J. Med. Chem.* 54, 782–787. doi: 10.1021/jm101018r

Albert, F. K., Forsting, M., Sartor, K., Adams, H. P., and Kunze, S. (1994). Early postoperative magnetic resonance imaging after resection of malignant glioma: objective evaluation of residual tumor and its influence on regrowth and prognosis. *Neurosurgery* 34, 45–60. discussion 60–61.

Banon-Rodriguez, I., Monypenny, J., Ragazzini, C., Franco, A., Calle, Y., Jones, G. E., et al. (2011). The cortactin-binding domain of WIP is essential for podosome formation and extracellular matrix degradation by murine dendritic cells. *Eur. J. Cell Biol.* 90, 213–223. doi: 10.1016/j.ejcb.2010.09.001

Chan, L. Y., Gunasekera, S., Henriques, S. T., Worth, N. F., Le, S. J., Clark, R. J., et al. (2011). Engineering pro-angiogenic peptides using stable, disulfide-rich cyclic scaffolds. *Blood* 118, 6709–6717. doi: 10.1182/blood-2011-06-359141

Chan, L. Y., Zhang, V. M., Huang, Y. H., Waters, N. C., Bansal, P. S., Craik, D. J., et al. (2013). Cyclization of the antimicrobial peptide gomesin with native chemical ligation: influences on stability and bioactivity. *ChemBioChem* 14, 617–624. doi: 10.1002/cbic.201300034

Correnti, C. E., Gewe, M. M., Mehlin, C., Bandaranayake, A. D., Johnsen, W. A., Rupert, P. B., et al. (2018). Screening, large-scale production and structure-based classification of cystine-dense peptides. *Nat. Struct. Mol. Biol.* 25, 270–278. doi: 10.1038/s41594-018-0033-9

Dardevet, L., Rani, D., Abd El Aziz, T., Bazin, I., Sabatier, J. M., Fadl, M., et al. (2015). Chlorotoxin: a helpful natural scorpion peptide to diagnose glioma and fight tumor invasion. *Toxins* 7, 1079–1101. doi: 10.3390/toxins7041079

DeBin, J. A., Maggio, J. E., and Strichartz, G. R. (1993). Purification and characterization of chlorotoxin, a chloride channel ligand from the venom of the scorpion. *Am. J. Phys.* 264, 361–369.

DeBin, J., and Strichartz, G. (1991). Chloride channel inhibition by the venom of the scorpion *Leiurus quinquestriatus*. *Toxicon* 29, 1403–1408. doi: 10.1016/0041-0101(91)90128-E

Deshane, J., Garner, C. C., and Sontheimer, H. (2003). Chlorotoxin inhibits glioma cell invasion via matrix metalloproteinase-2. *J. Biol. Chem.* 278, 4135–4144. doi: 10.1074/jbc.M205662200

Diaz-Perlas, C., Varese, M., Guardiola, S., Garcia, J., Sanchez-Navarro, M., Giralt, E., et al. (2018). From venoms to BBB-shuttles. Mini CTX3: a molecular vector derived from scorpion venom. *Chem. Commun.* 54, 12738–12741. doi: 10.1039/C8CC06725B

Drakopoulou, E., Vizzavona, J., Neyton, J., Aniort, V., Bouet, F., Virelizier, H., et al. (1998). Consequence of the removal of evolutionary conserved disulfide bridges on the structure and function of charybdotoxin and evidence that particular cysteine spacings govern specific disulfide bond formation. *Biochemistry* 37, 1292–1301. doi: 10.1021/bi9721086

Falahat, R., Wiranowska, M., Toomey, R., and Alcantar, N. (2016). ATR-FTIR analysis of spectral and biochemical changes in glioma cells induced by chlorotoxin. *Vib. Spectrosc.* 87, 164–172. doi: 10.1016/j.vibspec.2016.10.004

Futaki, S., Nakase, I., Tadokoro, A., Takeuchi, T., and Jones, A. T. (2007). Arginine-rich peptides and their internalization mechanisms. *Biochem. Soc. Trans.* 35, 784–787. doi: 10.1042/BST0350784

Gribbin, T. E., Senzer, N., Raizer, J. J., Shen, S., Nabors, L. B., Wiranowska, M., et al. (2009). A phase I evaluation of intravenous (IV) ^{131}I-chlorotoxin delivery to solid peripheral and intracranial tumors. *J. Clin. Oncol.* 27:14507. doi: 10.1200/jco.2009.27.15s.e14507

Gstraunthaler, G. (2003). Alternatives to the use of fetal bovine serum: serum-free cell culture. *ALTEX* 20, 275–281.

Hashimoto, S., Hirose, M., Hashimoto, A., Morishige, M., Yamada, A., Hosaka, H., et al. (2006). Targeting AMAP1 and cortactin binding bearing an atypical src homology 3/proline interface for prevention of breast cancer invasion and metastasis. *Proc. Natl. Acad. Sci. USA* 103, 7036–7041. doi: 10.1073/pnas.0509166103

Hofmann, U. B., Westphal, J. R., Waas, E. T., Becker, J. C., Ruiter, D. J., and van Muijen, G. N. (2000). Coexpression of integrin αvβ3 and matrix metalloproteinase-2 (MMP-2) coincides with MMP-2 activation: correlation with melanoma progression. *J. Invest. Dermatol.* 115, 625–632. doi: 10.1046/j.1523-1747.2000.00114.x

Jacoby, D. B., Dyskin, E., Yalcin, M., Kesavan, K., Dahlberg, W., Ratliff, J., et al. (2010). Potent pleiotropic anti-angiogenic effects of TM601, a synthetic chlorotoxin peptide. *Anticancer Res.* 30, 39–46.

Jentsch, T. J. (2008). CLC chloride channels and transporters: from genes to protein structure, pathology and physiology. *Crit. Rev. Biochem. Mol. Biol.* 43, 3–36. doi: 10.1080/10409230701829110

Kesavan, K., Ratliff, J., Johnson, E. W., Dahlberg, W., Asara, J. M., Misra, P., et al. (2010). Annexin A2 is a molecular target for TM601, a peptide with tumor-targeting and anti-angiogenic effects. *J. Biol. Chem.* 285, 4366–4374. doi: 10.1074/jbc.M109.066092

Kieran, M. W., Walker, D., Frappaz, D., and Prados, M. (2010). Brain tumors: from childhood through adolescence into adulthood. *J. Clin. Oncol.* 28, 4783–4789. doi: 10.1200/JCO.2010.28.3481

Knupfer, M. M., Poppenborg, H., Hotfilder, M., Kuhnel, K., Wolff, J. E., and Domula, M. (1999). CD44 expression and hyaluronic acid binding of malignant glioma cells. *Clin. Exp. Metastasis* 17, 71–76.

Kovar, J. L., Curtis, E., Othman, S. F., Simpson, M. A., and Olive, D. M. (2013). Characterization of IRDye 800CW chlorotoxin as a targeting agent for brain tumors. *Anal. Biochem.* 440, 212–219. doi: 10.1016/j.ab.2013.05.013

Lefranc, F., Le Rhun, E., Kiss, R., and Weller, M. (2018). Glioblastoma quo vadis: will migration and invasiveness reemerge as therapeutic targets? *Cancer Treat. Rev.* 68, 145–154. doi: 10.1016/j.ctrv.2018.06.017

Lippens, G., Najib, J., Wodak, S. J., and Tartar, A. (1995). NMR sequential assignments and solution structure of chlorotoxin, a small scorpion toxin that blocks chloride channels. *Biochemistry* 34, 13–21.

Lyons, S. A., O'Neal, J., and Sontheimer, H. (2002). Chlorotoxin, a scorpion-derived peptide, specifically binds to gliomas and tumors of neuroectodermal origin. *Glia* 39, 162–173. doi: 10.1002/glia.10083

MacGrath, S. M., and Koleske, A. J. (2012). Cortactin in cell migration and cancer at a glance. *J. Cell Sci.* 125, 1621–1626. doi: 10.1242/jcs.093781

Mamelak, A. N., and Jacoby, D. B. (2007). Targeted delivery of antitumoral therapy to glioma and other malignancies with synthetic chlorotoxin (TM-601). *Expert Opin. Drug Deliv.* 4, 175–186. doi: 10.1517/17425247.4.2.175

Mamelak, A. N., Rosenfeld, S., Bucholz, R., Raubitschek, A., Nabors, L. B., Fiveash, J. B., et al. (2006). Phase I single-dose study of intracavitary-administered iodine-131-TM-601 in adults with recurrent high-grade glioma. *J. Clin. Oncol.* 24, 3644–3650. doi: 10.1200/JCO.2005.05.4569

Mcferrin, M. B., and Sontheimer, H. (2006). A role for ion channels in glioma cell invasion. *Neuron Glia Biol.* 2, 39–49. doi: 10.1017/S17440925X06000044

Ojeda, P. G., Chan, L. Y., Poth, A. G., Wang, C. K., and Craik, D. J. (2014). The role of disulfide bonds in structure and activity of chlorotoxin. *Future Med. Chem.* 6, 1617–1628. doi: 10.4155/fmc.14.93

Ojeda, P. G., Henriques, S. T., Pan, Y., Nicolazzo, J. A., Craik, D. J., and Wang, C. K. (2017). Lysine to arginine mutagenesis of chlorotoxin enhances its cellular uptake. *Biopolymers* 108:e23025. doi: 10.1002/bip.23025

Olsen, M., Schade, S., Lyons, S., Amaral, M., and Sontheimer, H. (2003). Expression of voltage-gated chloride channels in human glioma cells. *J. Neurosci.* 23, 5572–5582. doi: 10.1523/JNEUROSCI.23-13-05572.2003

Othman, H., Wieninger, S. A., ElAyeb, M., Nilges, M., and Srairi-Abid, N. (2017). In silico prediction of the molecular basis of ClTx and AaCTx interaction with matrix metalloproteinase-2 (MMP-2) to inhibit glioma cell invasion. *J. Biomol. Struct. Dyn.* 35, 2815–2829. doi: 10.1080/07391102.2016.1231633

Page, B., Page, M., and Noel, C. (1993). A new fluorometric assay for cytotoxicity measurements in-vitro. *Int. J. Oncol.* 3, 473–476.

Park, T., Min, K. A., Cheong, H., Moon, C., and Shin, M. C. (2018). Genetic engineering and characterisation of chlorotoxin-fused gelonin for enhanced glioblastoma therapy. *J. Drug Target.* 11, 1–9. doi: 10.1080/1061186X.2018.1516221

Selo, I., Negroni, L., Creminon, C., Grassi, J., and Wal, J. M. (1996). Preferential labeling of alpha-amino N-terminal groups in peptides by biotin: application to the detection of specific anti-peptide antibodies by enzyme immunoassays. *J. Immunol. Methods* 199, 127–138. doi: 10.1016/S0022-1759(96)00173-1

Soroceanu, L., Gillespie, Y., Khazaeli, M., and Sontheimer, H. (1998). Use of chlorotoxin for targeting of primary brain tumors. *Cancer Res.* 58, 4871–4879.

Soroceanu, L., Manning, T. J., and Sontheimer, H. (1999). Modulation of glioma cell migration and invasion using Cl^- and K^+ ion channel blockers. *J. Neurosci.* 19, 5942–5954. doi: 10.1523/JNEUROSCI.19-14-05942.1999

Tatenhorst, L., Rescher, U., Gerke, V., and Paulus, W. (2006). Knockdown of annexin 2 decreases migration of human glioma cells in vitro. *Neuropathol. Appl. Neurobiol.* 32, 271–277. doi: 10.1111/j.1365-2990.2006.00720.x

Ullrich, N., Bordey, A., Gillespie, G., and Sontheimer, H. (1998). Expression of voltage-activated chloride currents in acute slices of human gliomas. *Neuroscience* 83, 1161–1173. doi: 10.1016/S0306-4522(97)00456-9

Ullrich, N., and Sontheimer, H. (1996). Biophysical and pharmacological characterization of chloride currents in human astrocytoma cells. *Am. J. Phys.* 270, C1511–C1521.

Vranken, W. F., Boucher, W., Stevens, T. J., Fogh, R. H., Pajon, A., Llinas, M., et al. (2005). The CCPN data model for NMR spectroscopy: development of a software pipeline. *Proteins* 59, 687–696. doi: 10.1002/prot.20449

Wiranowska, M., Colina, L. O., and Johnson, J. O. (2011). Clathrin-mediated entry and cellular localization of chlorotoxin in human glioma. *Cancer Cell Int.* 11:27. doi: 10.1186/1475-2867-11-27

Wüthrich, K. (2003). NMR studies of structure and function of biological macromolecules. *Biosci. Rep.* 23, 119–168. doi: 10.1023/B:BIRE.0000007689.27614.7c

Zhu, Q., Liang, S., Martin, L., Gasparini, S., Menez, A., and Vita, C. (2002). Role of disulfide bonds in folding and activity of leiurotoxin I: just two disulfides suffice. *Biochemistry* 41, 11488–11494. doi: 10.1021/bi026136m

Conflict of Interest Statement: The authors declare that the research was conducted in the absence of any commercial or financial relationships that could be construed as a potential conflict of interest.

frontiers in Pharmacology

REVIEW
published: 11 April 2019
doi: 10.3389/fphar.2019.00366

Structure–Function and Therapeutic Potential of Spider Venom-Derived Cysteine Knot Peptides Targeting Sodium Channels

Fernanda C. Cardoso and Richard J. Lewis**

Centre for Pain Research, Institute for Molecular Bioscience, The University of Queensland, St Lucia, QLD, Australia

Spider venom-derived cysteine knot peptides are a mega-diverse class of molecules that exhibit unique pharmacological properties to modulate key membrane protein targets. Voltage-gated sodium channels (Na_V) are often targeted by these peptides to allosterically promote opening or closing of the channel by binding to structural domains outside the channel pore. These effects can result in modified pain responses, muscle paralysis, cardiac arrest, priapism, and numbness. Although such effects are often deleterious, subtype selective spider venom peptides are showing potential to treat a range of neurological disorders, including chronic pain and epilepsy. This review examines the structure–activity relationships of cysteine knot peptides from spider venoms that modulate Na_V and discusses their potential as leads to novel therapies for neurological disorders.

Keywords: spider venoms, ICK peptides, voltage-gated ion channels, structure–activity relationship, novel drugs

OPEN ACCESS

Edited by:
Jean-Francois Rolland, AXXAM, Italy

Reviewed by:
Roope Mannikko, University College London, United Kingdom
Heike Wulff, University of California, Davis, United States

****Correspondence:***
Fernanda C. Cardoso
f.caldascardoso@uq.edu.au
Richard J. Lewis
r.lewis@uq.edu.au;
r.lewis@imb.uq.edu.au

Specialty section:
This article was submitted to Pharmacology of Ion Channels and Channelopathies, a section of the journal Frontiers in Pharmacology

Received: *08 February 2019*
Accepted: *25 March 2019*
Published: *11 April 2019*

Citation:
Cardoso FC and Lewis RJ (2019) Structure–Function and Therapeutic Potential of Spider Venom-Derived Cysteine Knot Peptides Targeting Sodium Channels. Front. Pharmacol. 10:366. doi: 10.3389/fphar.2019.00366

INTRODUCTION

Animal venoms are an extraordinary source of bio-active peptides that modulate membrane proteins to facilitate prey capture and defense. Venomous spiders, cone snails, fish, sea anemones, wasps, scorpions, snakes and dinoflagellates produce small molecules and/or peptides exhibiting pharmacological properties of singular value for the research in pharmacological tools and novel drugs (Ziegman and Alewood, 2015; Dongol et al., 2016; Cardoso and Lewis, 2017; Kessler et al., 2017; Abraham and Lewis, 2018; Cardoso et al., 2018). These toxins modulate a range of receptors and channels, including VGIC, TRP, muscarinic and nicotinic acetylcholine receptors (mAChR and nAChR), ASIC, NET and G protein coupled receptors (GPCRs). Based on the number of species and venom complexity, spider venoms provide a mega-diverse source of bio-active cysteine knot peptides, many of which modulate Na_V with high potency and selectivity (Cardoso and Lewis, 2017).

Voltage-gated sodium channels ($Na_V1.1$–1.9), in particular, are key players in the transmission of electrical signals in excitable cells and also involved in the pathophysiology of neurological disorders, including poorly treated conditions as chronic pain and epilepsy (Luiz and Wood, 2016; Klein-Weigel et al., 2018; Sloan et al., 2018; Szepetowski, 2018). The Na_V channels

Abbreviations: ASIC, acid sensing channels; Ca_V, voltage-gated calcium channel; CyA, β-cyanoalanine; DRG, dorsal root ganglion; ICK, inhibitory cysteine knot; K_V, voltage-gated potassium channel; mAChR, muscarinic acetylcholine receptor; nAchR, nicotinic acetylcholine receptor; Na_V, voltage-gated sodium channels; Na_VPaS, insect Na_V channel; NET, norepinephrine transporter; Pra, propargylglycine; PyroE, pyroglutamate; SAR, structure-activity relationship; TRP, transient receptor potential channels; TTX-R, tetrodotoxin-resistant; TTX-S, tetrodotoxin-sensitive; VGIC, voltage-gated ion channels; VSD, voltage-sensor domain.

α-subunit comprises four domains (DI–DIV), each formed by six transmembrane segments (S1–S6), including S4 which contributes transmembrane voltage sensitivity, the tip of S5–S6 which contributes to sodium ion selectivity, and the intracellular loop connecting S6 of DIII and S1 of DIV which contributes to fast inactivation (**Figure 1**). The co-associated auxiliary β-subunits (β1–β4) are positioned above the VSD explaining their ability to influence channel gating (**Figures 1A,B**). Interestingly, human genetic studies disclosed mutations in $Na_V1.7$ and $Na_V1.9$ channels leading to congenital insensitivity to pain, a rare condition characterized by lack of physical pain (Cox et al., 2006; Phatarakijnirund et al., 2016), while gain-of-function mutations in $Na_V1.6$, $Na_V1.7$, $Na_V1.8$, and $Na_V1.9$ lead to painful neuropathies such as trigeminal neuralgia and erythromelalgia (Drenth and Waxman, 2007; Faber et al., 2012; Huang et al., 2014; Grasso et al., 2016). Genetic mutations in the $Na_V1.1$ and $Na_V1.2$ channels result in functional defects linked to epileptic syndromes (Meisler and Kearney, 2005; Thompson et al., 2011). Furthermore, altered Na_V channels function and expression are prominent in chronic inflammatory and neuropathic pains, with localization remodeling, altered expression and sensitization often observed in the subtypes $Na_V1.3$, $Na_V1.6$, $Na_V1.7$, $Na_V1.8$, and $Na_V1.9$ (Cardoso and Lewis, 2017). $Na_V1.4$ and $Na_V1.5$ have restricted expression in the skeletal and cardiac muscle, respectively, which are important off-target pharmacologies to be considered when developing Na_V channel therapeutics.

The role of Na_V channels in both health and pathological pain have been further elucidated with the support of potent and selective Na_V channels modulators isolated from spider venoms. By using a subtype selective $Na_V1.1$ activator isolated from the tarantula *Heteroscodra maculata*, the key role played by $Na_V1.1$ in physiological mechanical pain (Osteen et al., 2016) and chronic visceral pain (Salvatierra et al., 2018) was established. More interestingly, pain relief is achieved in pre-clinical models of inflammatory and neuropathic pain administrated with Na_V channels inhibitors isolated from other spiders venoms, as for the ICK peptides ProTx-II (Tanaka et al., 2015; Flinspach et al., 2017), HnTX-IV (Liu et al., 2014a), Hl1a (Meng et al., 2016), HwTx-IV (Liu et al., 2014b), and Pn3a (Deuis et al., 2017).

The unique properties of spider ICK peptides in modulating ion channels give rise to opportunities for developing better and safer therapies targeting Na_V channels. This, in association to the current need for effective drugs to treat challenging neurological disorders and to overcome severe side-effects by opioid analgesic drugs foster the use of these bio-active spider peptides in therapeutics development. In this review, we examine recent advances in the SAR of cysteine knot peptides from spider venoms that inhibit Na_V and discuss their potential for the development of novel therapies.

STRUCTURE–ACTIVITY RELATIONSHIPS OF SPIDER ICK PEPTIDES

Spiders are the largest group of venomous animals, with more the 40,000 species described to date (Platnick, 2014). Their venoms are rich in peptides that inhibit or activate Na_V channels by binding to domains outside the channel pore to allosterically promote opening or closing of the channel (**Figures 1A–C**) (Cardoso and Lewis, 2017). These binding sites include the VSD associated with domains II and IV that bind site 4 and 3 Na_V channel toxins, respectively. Interestingly, these peptides have a conserved ICK scaffold that confers high stability and resistance to high temperatures, low pH and digestion by proteases. A typical spider peptide ICK scaffold, with few exceptions, comprises three disulphide bridges C1–C4, C2–C5, and C3–C6 that fold these peptides into a globular structure with four distinct loops and an extended C-terminal tail (**Figure 1D**). These peptides were classified into distinct families of Na_V modulators named NaSpTx 1–12 based on their amino acids sequence and cysteine position (Klint et al., 2012), with extensive SAR studies reported for NaSpTx 1 and 3, and to a lesser extent for NaSpTx 7. Modern high throughput screening technologies using fluorescence-imaging and automated patch-clamp cell-based assays have facilitated the identification of peptides that display high potency and selectivity to modulate Na_V subtypes (Cardoso et al., 2015; Klint et al., 2015b). These peptides have been the focus of studies to unravel their pharmacological properties and potential for the development of novel and more effective drugs, studies which have been considerably advanced through investigations of the SAR of spider ICK peptides over Na_V channel subtypes. By using state-of-art methods for peptide production and detailed pharmacology characterization through patch-clamp electrophysiology in primary isolated neurons (e.g., DRG) or mammalian cells expressing Na_V channels subtypes, and X-ray and nuclear magnetic resonance (NMR) for determination of three-dimensional structure, these SAR studies have unraveled key features associated to modulation Na_V channels. Our current understanding of the SAR of each of the main ICK family peptides at Na_V channels are outlined below.

NaSpTx 1

GpTx-1

The ICK peptide GpTx-1 (μ/ω-TRTX-Gr2a) isolated from the tarantula *Grammostola rosea* was first described as a nanomolar inhibitor of Ca_V (Ono et al., 2011) and later as a nanomolar Na_V inhibitor from *Grammostola porter* (Murray et al., 2015). Its high potency for the sodium channel subtype $Na_V1.7$ (IC_{50} of 10 nM) made it an attractive lead for SAR studies (Murray et al., 2015, 2016) (**Table 1**). Alanine scanning revealed the residues W29, K31 and F34 are essential for the $Na_V1.7$ inhibition (Murray et al., 2015). In its native form, GpTx-1 is 20-fold and 1000-fold selective over $Na_V1.4$ and $Na_V1.5$, respectively, with the F5A mutant enhancing to 300-fold selectivity over $Na_V1.4$. In the same study, additional positional substitutions using natural and non-natural amino acids other than alanine in the positions 5, 6, 26, and 28 put forward the rational design of an optimized GpTx-1 containing the substitutions F5A, M6F, T26L, K28R. This new GpTx-1 analog displayed 6-fold enhanced potency for $Na_V1.7$ and 1000-fold selectivity over $Na_V1.4$ and $Na_V1.5$.

Later, another positional scan using glutamic acid, arginine, lysin, tryptophan and 1-naphthylalanine substitutions supported

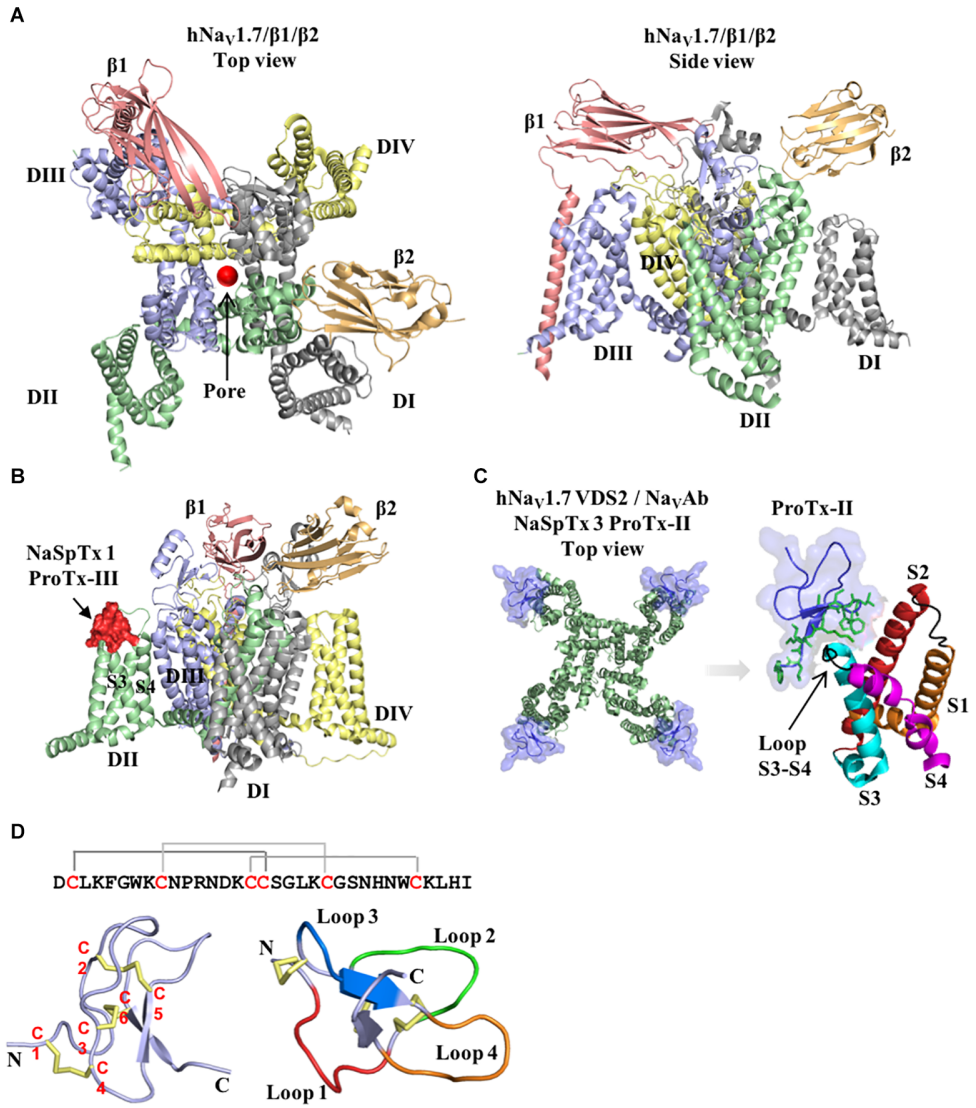

FIGURE 1 | Structure of the voltage-gated sodium channel and the inhibitory cysteine knot (ICK) spider peptide. **(A)** Three-dimensional structure of the human $Na_V1.7$ in the presence of the auxiliary subunits β1 and β2 determined by cryo-EM (PDB 6J8J) (Shen et al., 2019). Top and side views are presented. The domain I (DI) is colored in gray, domain II (DII) is colored in green, domain III (DIII) is colored in blue and domain IV (DIV) is colored in yellow. The auxiliary subunits β1 and β2 are colored in salmon and orange, respectively. **(B)** Representative binding site of a NaSpTx 1 in the DII S3-S4 loop of the $hNa_V1.7$ channel (PDB 6J8J) (Shen et al., 2019). Domains and auxiliary subunits are colored as in **(A)**, and the NaSpTx1 peptide ProTx-III (PDB 2MXM) (Cardoso et al., 2015) is colored in red. **(C)** Detailed binding site of the NaSpTx 3 ProTx-II over the $hNa_V1.7$ voltage–sensor domain 2 (VSD2)-Na_VAb chimeric channel (PBD 6N4I) (Xu et al., 2019). Top view of the $hNa_V1.7$ VSD2-Na_VAb chimeric channel colored in green showing ProTx-II colored in blue bound to the voltage sensor domain 2 in close proximity with the S3–S4 loop. In the structure on the left, the segments S1 to S4 are colored in orange, red, cyan and magenta, respectively. The loops S1–S2 and S3–S4 are colored in black and the residues in the loop 4 and C-terminal of ProTx-II are represented by green sticks. **(D)** Typical structure of an inhibitory cysteine knot (ICK) peptide from spider. Primary and three-dimensional structure of ProTx-III (PDB 2MXM) (Cardoso et al., 2015) showing cysteine connectivity (C1 – C4, C2 – C5, and C3 – C6) and loops 1–4 colored in red, green, blue and orange, respectively.

previous alanine scanning observations and revealed a number of new positions in GpTx-1 essential for the $Na_V1.7$ activity, all together these key residues are F5, M6, S24, H27, W29, K31, Y32, and F34 (Murray et al., 2016). Contrary to alanine substitutions, most of the substitutions with 1-naphthylalanine didn't produce folded peptides, with few similar cases for substitutions with tryptophan, followed by lysine, arginine and glutamic acid. Furthermore, the importance of S24 was observed only in the S24E mutant, being all other substitutions at position 24 unable to produce folded peptides. In the three-dimensional structure of GpTx-1, these identified active residues form a cluster on the surface allowing a direct interaction with $Na_V1.7$ (Murray et al., 2016). These potential interactions were further investigated using a homology model of the $hNa_V1.7$ channel docked with the NMR structure of GpTx-1, which predicted interactions of the residues F5 and K31 of GpTx-1 with I767 and E811 located in

the domain II voltage sensor region, respectively. Other potential electrostatic interactions were predicted between R25 and R7 of GpTx-1 and E759 and E818 of the ion channel, respectively. Overall, the optimization of GpTx-1 toward an increase in potency for $Na_V1.7$ and selectivity over $Na_V1.4$ and $Na_V1.5$ was possible with the addition of a hydrophobic aromatic residue at position 6 (substitution M6F), and a hydrophobic residue at position 26 (substitution T26L). A summary of the SAR for GpTx-1 is shown in **Table 1**.

HwTx-IV

Huwentoxin-IV (μ-TRTX-Hs2a), isolated from the venom of the Chinese bird spider *Selenocosmia huwena*, was first identified as a potent (IC_{50} of 30 nM) Na_V inhibitor of TTX-S currents in DRG neurons (Peng et al., 2002). This inhibitor has been the subject of extensive SAR studies (**Table 1** and **Figure 2**). Initial SAR observations for HwTx-IV described a naturally occurring toxin variant with an N-terminal pyroglutamate instead of glutamate that had unchanged potency despite its irreversibility at strong depolarizing potentials (e.g., +200 mV) in DRG neurons and in $Na_V1.7$ expressed in HEK293 cells (Rong et al., 2013). More detailed SAR studies of HwTx-IV revealed that C-terminal mutations T28D, R29A or Q34D reduced Na_V potency in DRG neurons (Deng et al., 2013), while an alanine scan of HwTX-IV additionally revealed W30 and K32 also critical for high affinity interactions at $Na_V1.2$ and $Na_V1.7$ (Minassian et al., 2013) (**Figure 2A**). In this latter study, molecular dynamics simulations revealed substitutions displaying loss of potency for $Na_V1.2$ and $Na_V1.7$ also led to an increase in the flexibility of the loops 2 (substitutions P11A and D14A), in loop 3 (substitutions F6A, L22A, W30A, and Y33A) and in loop 4 (substitutions R26A and K27A), while the substitutions S25A, K32A, and I35A reduced HwTx-IV potency for $Na_V1.2$ and $Na_V1.7$ without affecting its structure and loops flexibility (Minassian et al., 2013).

Further alanine scanning of HwTx-IV identified E1, E4, F6, and Y33 as important contributors for $Na_V1.7$ affinity (Revell et al., 2013). These findings afforded the rational design and optimization of HwTx-IV with increased potency for $Na_V1.7$ and maintaining low affinity for the off-target $Na_V1.5$ (**Figure 3**). Among these new HwTx-IV analogs, the mutant HwTx-IV-G1/G4/W33 demonstrated the highest increase in activity, with 42-fold enhanced potency for $Na_V1.7$ inhibition, followed by HwTx-G1/G4 and HwTx-IV-A1/A4/W33 (Revell et al., 2013). More recently, the activity of HwTx-IV-G1/G4/W33 was tested over other members of the Na_V family, showing an increase in inhibition of 12-fold for $Na_V1.2$ and 47-fold for $Na_V1.3$ compared to wild-type HwTx-IV, but maintained the low potency for the off-target $Na_V1.4$ and $Na_V1.5$ (Xiao et al., 2008a; Rahnama et al., 2017). Altogether, the residues F6, P11, D14, L22, T28, R29, W30, K32, Y33, and Q34, when mutated, led to a loss of affinity of HwTx-IV for Na_V channels (**Table 1** and **Figure 3A**). Furthermore, the optimization of HwTx-IV activity for $Na_V1.7$ was possible with the removal of acid negative residues at the N-terminal (substitutions E1 to A or G), and increase in hydrophobicity at the C-terminal (substitution Y33W) (**Table 1** and **Figure 3A**). These produced a new surface in the HwTx-IV three-dimensional structure with increased polarity and hydrophobicity.

CcoTx1

CcoTx1 (β-TRTX-Cm1a) is a potent Na_V inhibitor isolated from the tarantula *Ceratogyrus cornuatus* (Bosmans et al., 2006). It has strong preference for the subtype $Na_V1.2$ and lower affinity for the off-targets $Na_V1.4$ and $Na_V1.5$ (**Table 1**). The SAR of CcoTx1 was investigated using a combination of direct evolution, saturation mutagenesis, chemical modifications and rational drug design to unravel key residues involved in potency and selectivity of this peptide over the Na_V family (Shcherbatko et al., 2016). Using direct evolution, CcoTx1 was optimized to improve its potency for the subtype $Na_V1.7$, and off-target selectivity for $Na_V1.2$ and $Na_V1.6$, producing the variant named 2670. This mutant contained the substitutions W5M, K12E, N19R, Y20L, T21V, R25S, D26H, Y31W, and D32K (**Table 1** and **Figure 3B**).

Further SAR investigations aiming to improve selectivity and potency for $Na_V1.7$ were performed using saturation mutagenesis, revealing that substitutions at the N- and C-terminal regions, along with positions 20 and 21 of 2670, were not well tolerated. Combining this SAR information, the $Na_V1.7$ pharmacophore of 2670 was defined by the hydrophobic residues M5, F6, W28, W31, and L33, and polar or positively charged residues R19, H26, K30, and K32. Saturation mutagenesis substitutions that conferred improved selectivity over off-targets and didn't alter the $Na_V1.7$ inhibitory potency were K18Y, R24K, and R27N. Still using this approach, a new mutant was identified with one single substitution D1I that conferred improved activity and selectivity (**Table 1**). C-terminal amidation of 2670 (2670a) and D1I (D1Ia) improved potency for $Na_V1.7$ which was accompanied by an increase in potency for $Na_V1.6$, but not for $Na_V1.2$. In addition, a D1Ia variant containing a terminal pyroglutamate (D1Za) improved binding to $Na_V1.7$ by 27% at strong depolarizing potentials, and maintained the same potency as D1Ia. This observation resembles the SAR properties of HwTx-IV (Rong et al., 2013). Overall, the optimization of CcoTx-1 activity toward $Na_V1.7$ was possible with the replacement of acid negative residues at both N- and C-terminal to residues with increased hydrophobicity and positive charges, and with modifications toward the C-terminal that included substitutions for aromatic residues H and W. This led to a considerable change in the CcoTx-1 surface to include more hydrophobic and positively charged residues (**Figure 3B**).

Hainantoxin

Hainantoxins (HNTXs) are ICK peptides comprised in the venom of the Chinese bird spider *Selenocosmia hainana*. Among these, the HNTX-I (μ-TRTX-Hhn2b) has weak to no activity over Na_V channels. SAR studies to restore the Na_V inhibitory activity of HNTX-I were performed using rational design based on other members of the NaSpTx 1 (Klint et al., 2015a; Zhang et al., 2018b) (**Table 1** and **Figure 3C**). The substitutions G6W/N23S/W28F and G6W/N23S produced analogs with IC_{50} values of 1 and 0.44 μM for $Na_V1.7$, respectively (Klint et al., 2015a). Later, the analogs N23S/D26H, N23S/D26H/L32W and E1G/N23S/D26H/L32W showed IC_{50} values of 79, 71, and 36 nM

TABLE 1 | Structure–activity relationship of spider ICK peptides and Na_V channels.

Peptide	Amino acids sequences	*In vitro* properties	References
NaSpTx 1			
GpTX-I	wt-DCLGFMRKCIPDNDKCCRPNLVCSRTHKWCKYVF	IC_{50} value of 4 nM for $Na_V1.7$ and 68- and 950-fold selective over $Na_V1.4$ and $Na_V1.5$, respectively.	Murray et al., 2015
	DCLGAMRKCIPDNDKCCRPNLVCSRTHKWCKYVF	Improved 300-fold selectivity over $Na_V1.4$.	
	DCLGFFRKCIPDNDKCCRPNLVCSRLHRWCKYVF	Improved 6-fold potency for $Na_V1.7$ and 1000-fold selective over $Na_V1.4$ and $Na_V1.5$.	Murray et al., 2016
HwTx-IV	wt-ECLEIFKACNPSNDQCCKSSKLVCSRKTRWCKYQI*	IC_{50} value of 26 nM for $Na_V1.7$ and 6-, 13- and 15-fold selective over $Na_V1.2$, $Na_V1.3$, and $Na_V1.4$, respectively.	Xiao et al., 2008b; Deng et al., 2013; Minassian et al., 2013
	(Pyro)ECLEIFKACNPSNDQCCKSSKLVCSRKTRWCKYQI*	Confer irreversible inhibition for TTX-S Na_V currents in DRG.	Rong et al., 2013
	ACLEIFKACNPSNDQCCKSSKLVCSRKTRWCKYQI	Improved 2 to 4-fold potency for $Na_V1.7$ and $Na_V1.2$.	Minassian et al., 2013
	ECLAIFKACNPSNDQCCKSSKLVCSRKTRWCKYQI		
	GCLGIFKACNPSNDQCCKSSKLVCSRKTRWCKWQI*	Improved potency at 42-fold for $Na_V1.7$.	Revell et al., 2013
	GCLGIFKACNPSNDQCCKSSKLVCSRKTRWCKWQI	Improved potency at 15-fold for $Na_V1.7$ and 4-fold for $Na_V1.2^{\#}$.	Rahnama et al., 2017
	ECLEIFKACNPSNDQCCKSSKLVCSRKTRWCKYQI*	Altered lipid binding in the cell membrane.	Henriques et al., 2016
CcoTx1	wt-DCLGWFKSCDPKNDKCCKNYTCSRRDRWCKYDL	IC_{50} value of 3 nM for $Na_V1.2$, 75 nM for Nav1.7 and >300 nM for other Na_V subtypes ($Na_V1.6$ was not tested).	Bosmans et al., 2006; Shcherbatko et al., 2016
	DCLGMFKSCDPENDKCCKRLVCSRSHRWCKWKL	IC_{50} value of 25 nM for $Na_V1.7$ and selectivity of 6-fold over $Na_V1.2$ and 4-fold over $Na_V1.6$.	Shcherbatko et al., 2016
	ICLGMFKSCDPENDKCCKRLVCSRSHRWCKWKL	IC_{50} value of 11 (C-terminal carboxi) and 2 nM (C-terminal amide) for $Na_V1.7$, and selectivity of 15-fold over $Na_V1.2$ and 6-fold over $Na_V1.6$.	
	ICLGMFKSCDPENDKCCKRLVCSRSHRWCKWKL*		
	(Pyro)ECLGIFKSCDPENDKCCYRLVCSKSHRWCKWKL*	IC_{50} value of 2.5 nM for $Na_V1.7$, and selectivity of 80-fold over $Na_V1.2$ and 20-fold over Nav1.6, and extra 1.5-fold of irreversible binding for $Na_V1.7$.	
HNTX-I	wt-ECKGFGKSCVPGKNECCSGYACNSRDKWCKVLL	No activity over Na_V channels	Klint et al., 2015a; Zhang et al., 2018b
	ECKGFWKSCVPGKNECCSGYACSSRDKWCKVLL	IC_{50} value of 440 nM for $Na_V1.7$	Klint et al., 2015a
	GCKGFGKSCVPGKNECCSGYACSSRHKWCKVWL	IC_{50} value of 36 nM for $Na_V1.7$	Zhang et al., 2018b
HNTX-III	wt-GCKGFGDSCTPGKNECCPNYACSSKHKWCKVYL	IC_{50} value of 150 nM for $Na_V1.7$	Zhang et al., 2015
HNTX-IV	wt-ECLGFGKGCNPSNDQCCKSSNLVCSRKHRWCKYEI*	IC_{50} value of 34 nM for $Na_V1.7$	Li et al., 2004
NaSpTx 3			
ProTx-II	wt-YCQKWMWTCDSERKCCEGMVCRLWCKKKLW	IC_{50} value of 0.3–1 nM for $Na_V1.7$ and 26-146 nM for the other Na_V subtypes ($Na_V1.1$ was not tested).	Priest et al., 2007; Smith et al., 2007; Schmalhofer et al., 2008; Park et al., 2014

(Continued)

TABLE 1 | Continued

Peptide	Amino acids sequences	*In vitro* properties	References
	YCQKWMWTCDSERKCCEGMVCRLWCKKKLW–$NHCH_3$	IC_{50} value of 42 pMol for $Na_V1.7$, selectivity of 83-fold over $Na_V1.2$.	Park et al., 2014
	GPYCQKWMQTCDSERKCCEGMVCRLWCKKKLL	Improved selectivity over $Na_V1.4$ and $Na_V1.5$.	Flinspach et al., 2017
	YCQKWMWTCDSERKCCEGMVCRLWCKKKLW	Altered lipid binding in the cell membrane.	Agwa et al., 2017
JZTX-V	wt–YCQKWMWTCDSKRACCEGLRCKLWCRKII*	IC_{50} value of 0.6 nM for $Na_V1.7$, and selectivity of 4- and 4000-fold over $Na_V1.4$ and $Na_V1.5$, respectively.	Moyer et al., 2018
	YCQKWMWTCDSKRACCEGLRCKLWCRKEI*	Improved selectivity over $Na_V1.4$ to 500-fold (AM-8145).	
	(Pra)YCQKWMWTCDSKRACCEGLRCKLWCRKEI*	Improved selectivity to 300- and 6000-fold over $Na_V1.4$ and $Na_V1.5$, respectively.	
	(CyA)YCQKWMWTCDSKRACCEGLRCKLWCRKEI* (Pra)	Improved selectivity to 128- and 1200-fold over $Na_V1.4$ and $Na_V1.5$, respectively.	
NaSpTx 7			
JZTX-III	wt–DGECGGFWWKCGRGKPPCCKGYACSKTWGWCAVEAP	IC_{50} value of 348 nM for $Na_V1.5$, not active over other Na_V subtypes	Rong et al., 2011
	DGECGGFWWKCGEGKPPCCKGYACSKTWGWCAVEAP	Improved potency by 11-fold for $Na_V1.5$.	

Key amino acids residues identified in SAR studies of GpTx-1, HwTx-IV, CcoTx1, ProTx-II, JZTX-V, and JZTX-III which are involved in the potency and/or selectivity of ICK peptides for the Na_V channels family are described, along with the NaSpTx family of these peptides. Cysteines are colored in gray. Amino acids residues colored in red play a key role in potency over Na_V channels. Amino acids substitutions colored in blue lead to improvement in potency over key Na_V channels subtypes, and colored in green lead to improvement in selectivity over key Na_V off-targets. Amino acids residues colored in orange play a key role in lipid cell membrane binding. Asterisk (*) denotes C-terminal amidation. #Compared to Minassian et al. (2013). wt, wild-type.

for $Na_V1.7$, respectively. In this study, the motif $X_1X_2SWCKX_3$ was identified as critical for the inhibitory activity for $Na_V1.7$. Altogether, the HNTX-I activity for $Na_V1.7$ was restored by removal of acid negative residues at both N- and C-terminal, and the addition of residues with increased hydrophobicity and positive charges, including the aromatic residues H and W.

Another hainantoxin, HNTX-III (μ-TRTX-Hhn2a), is an inhibitor of $Na_V1.7$ with IC_{50} value of 232 nM (Liu et al., 2013). The SAR of this peptide was performed consequent to the discovery of several isoforms variants present in the transcriptome of the venom gland of this spider (Zhang et al., 2015) (**Table 1**). The pharmacological properties of these variants were tested, revealing that the substitutions Y20H, S24N, H26D and Y20H/S24N were all detrimental to the $Na_V1.7$ activity (**Figure 2B**). The last hainantoxin discussed is HNTX-IV (μ-TRTX-Hhn1b), a potent inhibitor of TTX-S currents in DRG neurons (IC_{50} of 34 nM; Li et al., 2004). In this study, the SAR of HNTX-IV revealed K27 and R29 residues positions involved in the Na_V activity (**Table 1** and **Figure 2C**). More specifically, the mutants S12A and R26A produced IC_{50} values of 58 and 96 nM, respectively, while K27A and R29A produced IC_{50} values of 3.2 and 7 μM, respectively. This work reinforces the essential role of positively charged residues located in the surface of spider ICK peptides for $Na_V1.7$ inhibition.

NaSpTx 3

ProTx-II

ProTx-II (β/ω-TRTX-Tp2a) is amongst the most potent Na_V inhibitors described to date, with reported IC_{50} value of 0.3 nM for inhibition of $Na_V1.7$ (Schmalhofer et al., 2008). This toxin was isolated from the spider *Thrixopelma pruriens* using rNav1.8 assay guided fraction that evaluated the inhibitory properties for the $Na_V1.8$ channel of individual venom fractions separated by cation exchange liquid chromatography (Middleton et al., 2002). Despite of its exquisite inhibitory potency for $Na_V1.7$, it also potently inhibits other members of the Na_V family, including the off-targets $Na_V1.4$ and $Na_V1.5$. The SAR of ProTx-II was initially investigated over the $Na_V1.5$ channel (**Table 1** and **Figure 2D**). Analogs of ProTx-II produced by recombinant expression and chemical synthesis containing alanine or glutamine substitutions revealed a peptide active face composed of hydrophobic and cationic residues (Smith et al., 2007). More specifically, ten of these analogs showed losses in potency from 10- to 125-fold, with major losses associated with W5A and K26A substitutions. The positively charged residues substitutions K27Q, R13Q, and R22A led a significant loss in potency, while neutralization of negatively charged residues didn't affect the $Na_V1.5$ inhibition. Furthermore, the substitutions M6A, W7A, M19L, V20A, W24L, L29A, and W30A each produced a > 10-fold loss in potency. Similarly, another SAR study of ProTx-II identified the residues in the hydrophobic face essential for $Na_V1.5$ activity, including W5, M6, W7, W24, while residues identified as not critical for inhibitory activity included Y1, Q3, T8, N10, S11, E12, E17, and L23 (Priest et al., 2007).

SAR of ProTx-II has also been investigated over the channels $Na_V1.2$ and $Na_V1.7$ (Park et al., 2014) (**Table 1** and **Figure 2D**). In this study, besides the identification of residues mutations detrimental to Na_V activity such as substitution of C-terminal KLW to II, an optimized analog ProTx-II-$NHCH_3$ with ∼23-fold greater potency for $Na_V1.7$ was identified. In this same work, the

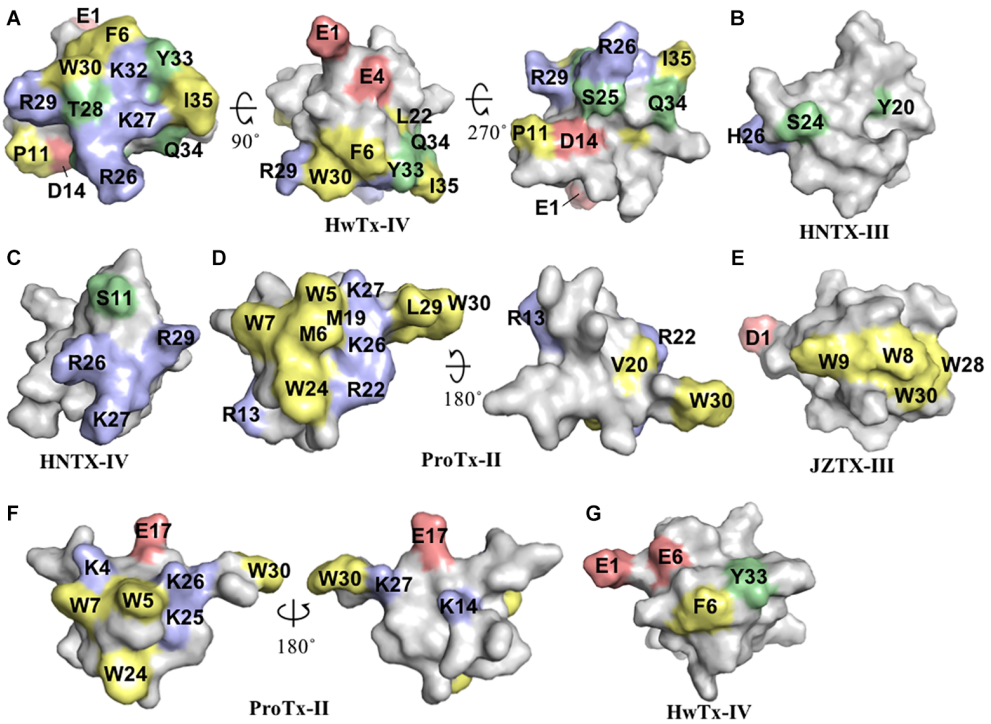

FIGURE 2 | Three-dimensional structure of spider ICK peptides displaying key residues involved in the inhibition of Na_V channels and cell membrane binding. **(A)** Three-dimensional structure of HwTx-IV determined by NMR (PBD 2m4x) (Minassian et al., 2013), **(B)** HNTX-III determined by NMR (PBD 2jtb), **(C)** HNTX-IV determined by NMR (PBD 1niy) (Li et al., 2004), **(D)** ProTx-II determined by X-Ray (PBD 5o0u) (Wright et al., 2017), and **(E)** JZTX-III determined by NMR (PBD 2i1t). The labeled amino acids residues have key role in potency over Na_V channels and lead to loss in activity as described in the text and **Table 1**. **(F)** Structure of ProTx-II determined by X-Ray (PDB 5o0u) (Wright et al., 2017) and **(G)** Structure of HwTx-IV (PDB 2m4x) (Minassian et al., 2013) determined by NMR. The labeled amino acids residues have key role in cell membrane binding as described in the text and **Table 1**. Amino acids residues are colored as follow: yellow for hydrophobic, red for acid, blue for basic and green for neutral. All three-dimensional structures were prepared in PyMOL (DeLano, 2002).

ICK peptide Phrixotoxin I, also known as PaTx I, isolated from the tarantula *Phrixotrichus auratus*, and a potent K_V inhibitor with IC_{50} value of 28 nM was submitted to a SAR study over Na_V channels (Diochot et al., 1999). It differs from ProTx-II by only 4 amino acids residues, and has moderate potency for Na_V channels, with IC_{50} value of 423 nM for $Na_V1.7$, and no activity for $Na_V1.2$ (Park et al., 2014). These naturally occurring differences were useful for the understand of the ProTx-II SAR over Na_V channels. The PaTx I C-terminal substitutions I28K and I29K, and addition of L30 and W31 (actual ProTx-II C-terminal) lead to an increase of 85-fold in the $Na_V1.7$ potency, and an IC_{50} value of 45 nM for $Na_V1.2$. This work unraveled a key role of the C-terminal for activity of NaSpTx 3 peptides, and describes interesting approaches for the improvement of Na_V activity through C-terminal modifications.

More recently, a detailed SAR of ProTx-II over Nav channels was investigated by 1500 toxin-derived peptides to identify a double mutant with extended N-terminal that maintained the inhibitory properties for $Na_V1.7$ but lost affinity for $Na_V1.4$ and $Na_V1.5$ (Flinspach et al., 2017) (**Table 1** and **Figure 3D**). This mutant, named JNJ63955918, contained additional G-2 and P-1 at the N-terminal and the substitutions W7Q and W30L. The interactions of ProTx-II with lipid membranes as well as with the hNav1.7 channels were investigated, revealing ProTx-II does interact with the cell membrane as part of its strategy to inhibit the $Na_V1.7$ channel (Henriques et al., 2016) (**Figure 3**). In this study, substitutions of residues K to R and W to Y lead to a reduction in the potency of ProTx-II for $hNa_V1.7$. The ProTx-II lipid interactions will be discussed in more details later in this review. Altogether, the residues W5, M6, W7, R13, M19, V20, R22, W24, K26, K27, L29, and W30, when mutated, led to a loss of affinity of ProTx-II for Na_V channels (**Table 1** and **Figure 2D**). Interestingly, the optimization of ProTx-II toward a potent and selective $Na_V1.7$ inhibitor was possible through the extension of the N-terminal with neutral and positively charged residues, and introduction of a positively charged group in the C-terminal.

JZTX-V

Isolated from the tarantula *Chilobrachys jingzhao*, JZTX-V (β-TRTX-Cg2a) is a potent $Na_V1.7$ inhibitor with IC_{50} value of 0.6 nM (Moyer et al., 2018). The SAR of JZTX-V over the subtypes $Na_V1.4$, $Na_V1.5$, and $Na_V1.7$ was investigated using alanine or glutamic acid positional scanning to unravel key residues involved in Na_V inhibition, and to produce new mutants with improved potency and selectivity (**Table 1** and **Figure 3E**). Substitutions that contribute to loss of the $Na_V1.7$ inhibitory activity observed by alanine substitutions were W5, L19, W24, and R26, and by glutamic acid substitutions were M6, T8, D10,

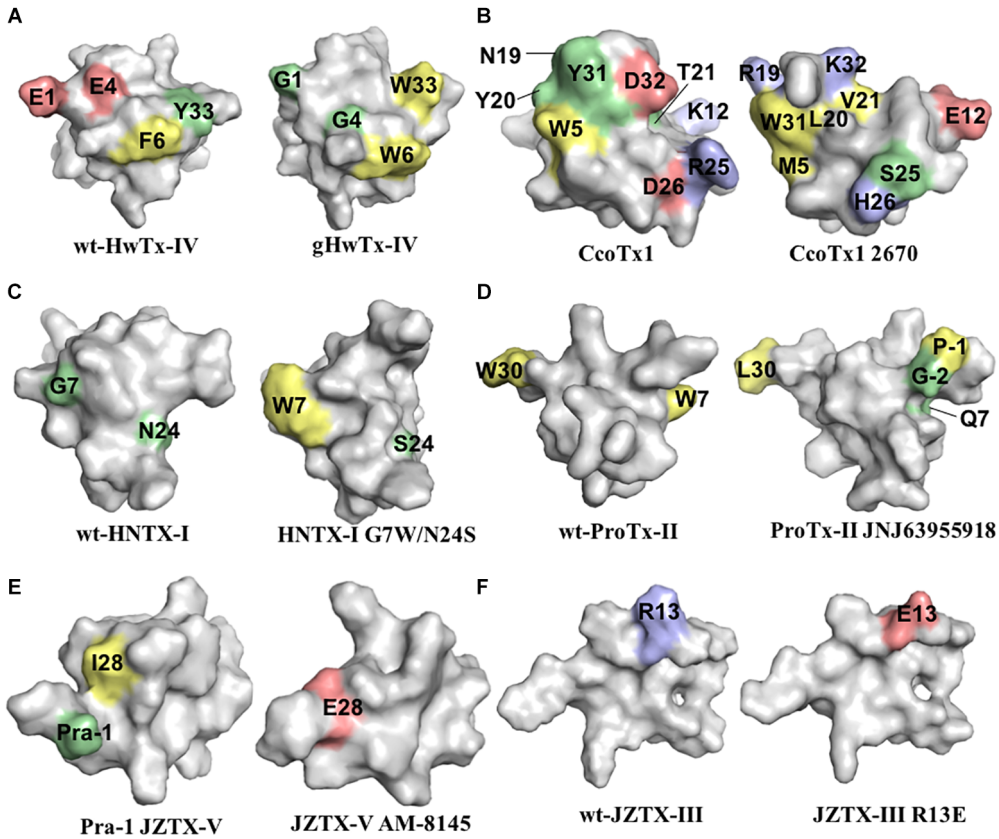

FIGURE 3 | Three-dimensional structure of spider ICK peptides displaying key residues involved in the enhancement of activity for Na_V channels, or enhancement of selectivity for Na_V channels off-targets. **(A)** Structures of HwTx-IV (PDB 2m4x) (Minassian et al., 2013) and gHwTx-IV (PDB 5tlr) (Agwa et al., 2017) determined by NMR. **(B)** Structures of CcoTx1 determined by NMR (PDB 6br0) (Agwa et al., 2018) and the derived analog 2670 determined by X-ray (PDB 5epm) (Shcherbatko et al., 2016). **(C)** Structures of HNTX-I (PDB 2mqf) and the derived analog G7W/N24S (PDB 2mxo) determined by NMR (Klint et al., 2015a). **(D)** Structures of ProTx-II determined by X-Ray (PDB 5o0u) (Wright et al., 2017) and derived analog JNJ63955918 determined by NMR (PDB 5tcz) (Flinspach et al., 2017). **(E)** Structure of analogs Pra-1 JZTX-V (PDB 6chc) and AM-8145 (6cgw) determined by NMR (Moyer et al., 2018). **(F)** Structure of JZTX-III determined by NMR (PDB 2i1t) (Liao et al., 2006) and modeling of the derived analog R13A using SWISS-MODEL (Arnold et al., 2006). Amino acids residues are colored as follow: yellow for hydrophobic, red for acid, blue for basic and green for neutral. Amino acids substitutions or additions labeled in the respective analogs are involved in the improvement of Na_V inhibitory activity or selectivity as described in the text and **Table 1**. All three-dimensional structures alignments were prepared in PyMOL (DeLano, 2002).

R13, and L23. Interestingly, a key substitution that improved off-target selectivity of JZTX-V over $Na_V1.4$ was I28E. This mutation was able to induce a change in the conformation of JZTX-V to produce 500-fold selectivity and maintain the potency for $Na_V1.7$.

In the same study, further investigation of the SAR of JZTX-V was performed through the introduction of side-chains containing residues such as Pra and β-cyanoalanine (CyA). Positions showing minimum involvement in $Na_V1.7$ inhibitory activity disclosed by the glutamic acid scanning were Y1, S11, A14, and E17, and therefore selected to test this approach. The addition of Pra at the N-terminus of I28E created a new analog named AM-8145 with improved selectivity for $Na_V1.4$ (300-fold) and $Na_V1.5$ (6000-fold) and maintained potency for $Na_V1.7$. Similar results were found for the addition of CyA at the N-terminus of I28E (analog AM-0422) and substitutions in the other selected positions. These properties were not present in the wild-type JZTX-V containing the Pra additions, but only in the I28E mutant. In summary, the optimization of JZTX-V toward a more selective $Na_V1.7$ inhibitor was possible through the extension of the N-terminal with neutral or hydrophobic residues containing side-chains and addition of negative charge at the C-terminal. Interestingly, JZTX-V share similar key residues with ProTx-II essential for the inhibition of $Na_V1.7$, as for W5, M6, R26, and W24 in JZTX-V, and selectivity optimization for $Na_V1.4$ and $Na_V1.5$ through N-terminal extensions.

NaSpTx 7

JZTX-III

The spider peptide JZTX-III (β/κ-TRTX-Cg1a), also isolated from the tarantula *Chilobrachys jingzhao*, was first characterized as a potent inhibitor of TTX-R currents in rat cardiac myocytes with IC_{50} value of 380 nM (Xiao et al., 2004), and later found to

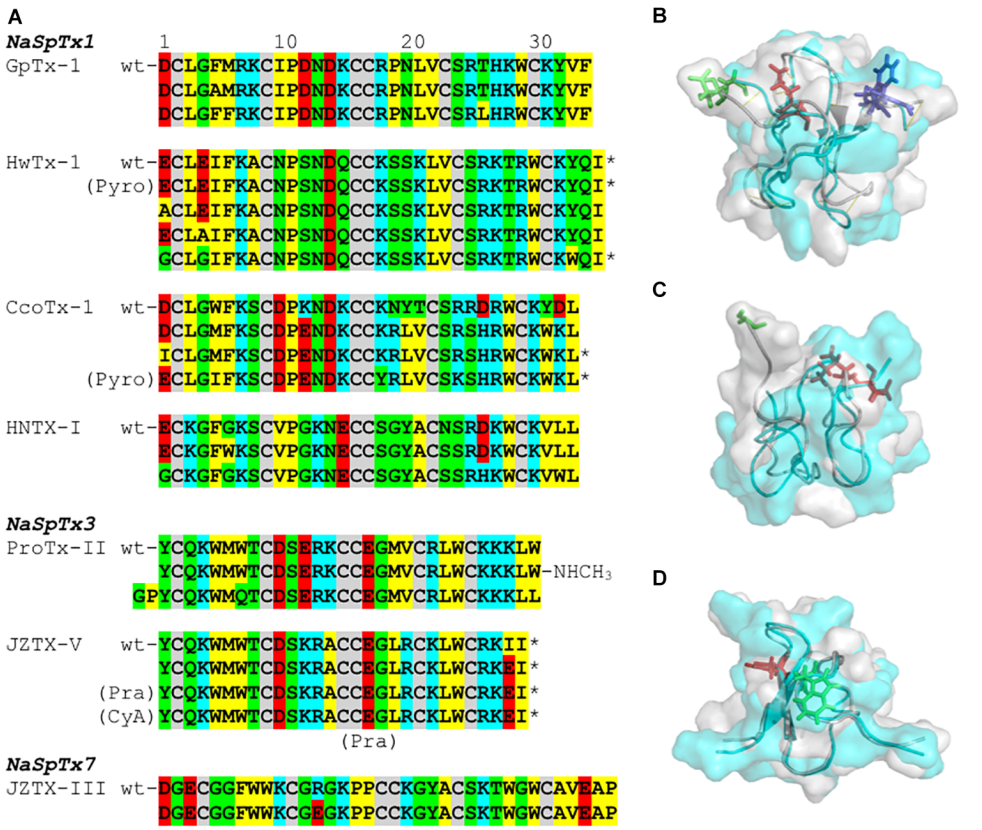

FIGURE 4 | SAR integration of spider ICK peptides. Primary and three-dimensional structures comparison of spider ICK peptides belonging to NaSpTx families 1, 3, and 7. **(A)** Primary structure alignment of wild-type peptides and respective optimized analogs showing enhancement of activity and/or selectivity of Na_V channels. The amino acids residues are highlighted as follow: yellow for hydrophobic, red for acid, blue for basic, green for neutral, and gray for the cysteines. **(B)** Alignment of the three-dimensional structures of HwTx-IV (PDB 2m4x) (Minassian et al., 2013) colored in gray and gHwTx-IV (PDB 5tlr) (Agwa et al., 2017) colored in cyan. Structures are represented by cartoon and surface, and substitutions E1G, E4G and Y32W are represented by sticks colored in green, red, and blue, respectively. **(C)** Alignment of the three-dimensional structures of Pra-1 JZTX-V (PDB 6chc) colored in gray and AM-8145 (6cgw) colored in cyan (Moyer et al., 2018). Structures are represented by cartoon and surface, and the Pra-1 addition and substitution I28E are represented by sticks colored in green and red, respectively. **(D)** Alignment of the three-dimensional structures of HNTX-I (PDB 2mqf) colored in gray and the derived analog G7W/N24S (PDB 2mxo) colored in cyan (Klint et al., 2015a). Structures are represented by cartoon and surface, and substitutions G7W and N24S are represented by sticks colored in green and red, respectively. All three-dimensional structures alignments were performed in PyMOL (DeLano, 2002). Asterisk (*) denotes C-terminal amidation.

also inhibit $K_V2.1$ channels (Yuan et al., 2007). The SAR of JZTX-III with $Na_V1.5$ channels using alanine substitutions revealed residues D1, E3 and W8, W9, W28, and W30 as key players for its $Na_V1.5$ inhibition (Rong et al., 2011) (**Table 1** and **Figure 2E**). In addition, the substitution R13E enhanced the $Na_V1.5$ inhibition by 11-fold (**Figure 3F**). Interestingly, JZTX-III does not inhibit the $Na_V1.7$ channel, and this lack of affinity was associated to the residue D816 in the $Na_V1.7$. The substitution D816R (corresponding to the R800 in the $Na_V1.5$ channel) enhanced significantly the inhibitory properties of JZTX-III for $Na_V1.7$.

INTERACTIONS WITH THE CELL MEMBRANE

Spider ICK peptides are known to interact with the lipids in the cell membrane. Early studies showed these peptides are water-soluble and bind to the aqueous-exposed extracellular surface of ion channels, and surprisingly reach the target by partitioning into the lipid membrane (Lee and MacKinnon, 2004). This strategy allows the peptide to reach the voltage-sensor and enhance high-affinity inhibition. The ability to bind to lipids seems exclusive of gating modifiers ICK peptides binding to site 4 of Na_V channels (Smith et al., 2005). Furthermore, the Na_V VSD s are affected by the cell membrane lipid composition, with changes from native lipids to sphingomyelin altering G-V relations and affinity of ProTx-I for the domain II and domain IV S3-S4 loops (Milescu et al., 2009).

Detailed studies of these interactions using NMR revealed that ICK peptides can interact with the headgroup region of lipid membrane to induce a thinning of the bilayer (Mihailescu et al., 2014). In this interaction, many basic residues are positioned toward the aqueous phase, the W residues adopt an interfacial position and hydrophobic residues are in direct contact with the membrane. The SAR of ProTx-II, membrane lipids and $Na_V1.7$ confirmed the previous observations, and revealed the ProTx-II

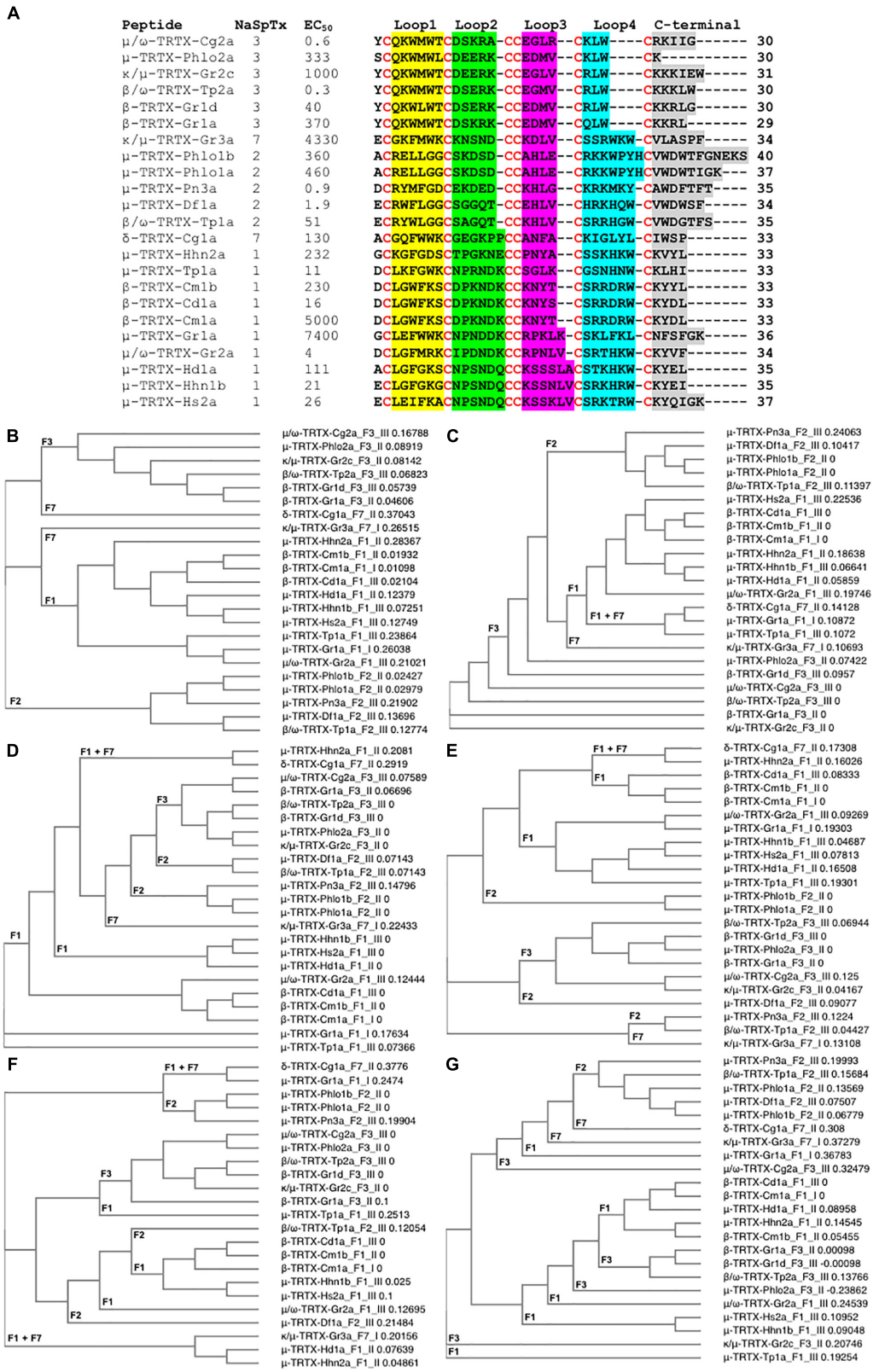

FIGURE 5 | Primary amino acids sequence alignment and phylogenetic analysis of NaSpTx peptides with described $Na_V1.7$ modulatory activity. **(A)** Primary sequences alignment of members of NaSpTx1, 2, 3, and 7, with EC_{50} values represented in nM, Loops, 1, 2, 3, 4, and C-terminal shaded in yellow, green, pink, (*Continued*)

FIGURE 5 | Continued
blue and gray, respectively, and cysteines colored in red. **(B)** Phylogenetic analysis of the full primary sequences of NaSpTx NaSpTx1, 2, 3, and 7, followed by Loop 1 **(C)**, Loop 2 **(D)**, Loop 3 **(E)**, Loop 4 **(F)**, and C-terminals **(G)**. For the phylogenetic trees, the peptides names are followed by their respective NaSpTx families represented by F1, F2, F3, and F7, and their $Na_V1.7$ potency represented by I (EC_{50} > 1 μM), II (EC_{50} between 1 and 0.1 μM), and III (EC_{50} < 0.1 μM). These analyses were performed using Clustal Omega (Sievers et al., 2011) and Simple Phylogeny (Saitou and Nei, 1987). The loops were flanked by cysteine for these analyses.

analog E17K had increased on-rate for $Na_V1.7$ compared to wild-type, but had no changes in the $Na_V1.7$ potency (Henriques et al., 2016) (**Table 1** and **Figure 2F**). Interestingly, all mutations at residues W to Y and K to R lead to a lower affinity for cell membranes. Changes in the structure of ICK peptides can also occur in the presence of lipids. This was observed in structural studies of ω-Aga-IVA (a Ca_V channel inhibitor ICK peptide) that undergoes changes in the presence of micelles (Ryu et al., 2017). More specifically, the C-terminal tail of ω-Aga-IVA assume a β-turn like conformation which is disordered in water.

The HwTx-IV mutant E1G/E4G/F6W/Y30W had increased affinity for the lipid membrane and higher potency for the inhibition of $hNa_V1.7$ compared to wild-type (Agwa et al., 2017) (**Table 1** and **Figure 2G**). Interestingly, the introduction of a PyroE in the N-terminal for HwTx-IV didn't alter the membrane interactions and potency for $Na_V1.7$. This confirmed previous observations for the naturally occurring PyroE-HwTx-IV that binds irreversibly to the Na_V channel voltage-sensor but at same potency of wild-type HwTx-IV (Rong et al., 2013). Although membrane interactions are key for the high affinity binding of ICK peptides over ion channels, such interactions have to-date had little influence on the selectivity for the Na_V channel family (Agwa et al., 2018).

BINDING SITES ON Na_V CHANNELS

The binding sites of spider ICK peptides at mammalian Na_V channels are starting to be characterized (Cardoso and Lewis, 2017). These gating-modifier toxins are known for their ability to change the voltage-dependence of activation and inactivation of Na_V channels to either inhibit or activate Na^+ currents. Overall, they have preference for binding to the site 4 in domain II of the Na_V channel to trap the voltage–sensor and inhibit Na^{2+} currents, and to site 3 in domain IV to slow channel inactivation and maintain Na^{2+} currents. These sites have been reported for a range of spider ICK peptides, including HwTx-IV, ProTx-I, ProTx-II, PaurTx3, CcoTx-1, Hd1a and Df1a that inhibit Na_V channels (Bosmans et al., 2008; Xiao et al., 2008a; Klint et al., 2015b; Shcherbatko et al., 2016; Cardoso et al., 2017) and to SGTx1 and Hm1a that slow Na_V channels inactivation (Bosmans et al., 2008; Osteen et al., 2016).

The crystal structure of the related double-ICK spider peptide Dc1a bound to the Na_VPaS was determined (Shen et al., 2018). Dc1a binds to a cleft between the VSD II and the pore loop of domain III of the Na_VPaS and induce minimal changes in the channel structure. On the other hand, the Dc1a peptide undergoes considerable rearrangement to achieve its fit into the cleft. This information brings new insights into the docking and binding of other ICK peptides into the mammalian channel, which although widely reported to bind to domain II and domain IV S3-S4 loops of mammalian Na_V channels, could also be interacting with other proximal regions of the channel to reaches its final fit and maximal activities.

More recently, the cryo-EM structure of the human $Na_V1.7$ channel was described in association of the auxiliary β1 and β2 subunits (**Figures 1A,B**) and the spider peptides HwTx-IV and ProTx-II (Shen et al., 2019). This study confirmed previous observations that HwTx-IV binds to the voltage-sensor of DII site 4 (Xiao et al., 2008a, 2010) and that ProTx-II binds to the voltage-sensors of DII and DIII sites 4 and 3 (Bosmans et al., 2008; Xiao et al., 2010). The cryo-EM structure of a chimeric $hNa_V1.7$-Na_VAb channel bound to ProTx-II was also described recently (**Figure 1C**) (Xu et al., 2019), which confirmed ProTx-II binds to the voltage-sensor of DII site 4 of the $Na_V1.7$ channel (Xiao et al., 2010). Although the determination of the three-dimensional structure of spider ICK peptides using X-ray or NMR are essential for the understanding of the SAR of these peptides, additional conformational changes are likely to happen for most of these ICK peptides when they achieved their final bound conformation with the Na_V channel and associated membrane lipids.

SAR INTEGRATION OF SPIDER ICK PEPTIDES

Prevalent features in the SAR of spider ICK peptides and Na_V channels have been disclosed (**Figure 4A** and **Table 1**). Amongst the remarkable positions associated to Na_V activity in the NaSpTx 1 toxins are the residues 5 and 6, which are typically occupied by the hydrophobic residue phenylalanine. Similarly, NaSpTx 3 toxins typically have positions 5 and 6 occupied by hydrophobic residues W and M, which are also critical for Na_V inhibitory activity. Another interesting aspect of these SAR studies is apparent in optimized analogs with increased Na_V potency and selectivity that often display a decrease in negative charge at the N-terminal compared to wild-type toxins. This is supported by the introduction of Pyro, Pra, CyA and the residues G and P at the N-terminal in optimized peptides belonging to NaSpTx families 1 and 3 (Rong et al., 2013; Shcherbatko et al., 2016; Flinspach et al., 2017; Moyer et al., 2018), and for the substitutions E1A, E1G and D1I in optimized peptides from NaSpTx 1 (Minassian et al., 2013; Revell et al., 2013; Shcherbatko et al., 2016; Rahnama et al., 2017; Zhang et al., 2018b). A decrease in negative charge at the N-terminal also enhances the lipid affinity of NaSpTx 1 toxins such as HwTx-IV (Henriques et al., 2016), suggesting these optimized peptides may have enhanced lipid binding in addition to any enhanced interactions directly with Na_V channels. This is

relevant when alterations to Na_V channel selectivity are sought, since enhanced lipid binding is unlikely to have less ability to influence Na_V channel subtype selectivity (Agwa et al., 2018).

Modifications in the C-terminal region that enhance inhibition of Na_V channels often involve the introduction of positive charges (**Figure 4A** and **Table 1**). This is observed for ICK peptides belonging to NaSpTx 1 and 3, as for the C-terminal amidation of HwTx-IV and CcoTx-1, the introduction of a $NHCH_3$ group in ProTx-II and the substitution D32K in CcoTx-1 (Minassian et al., 2013; Revell et al., 2013; Park et al., 2014; Shcherbatko et al., 2016). An increase in hydrophobicity in the C-terminal region also enhanced the Na_V inhibition properties of peptides in NaSpTx 1, especially Y33W in HwTx-IV and Y31W in CcoTx-1 (Revell et al., 2013; Shcherbatko et al., 2016; Rahnama et al., 2017). Interestingly, the reduction in hydrophobicity and introduction of negative charges in the C-terminal of the NaSpTx 3 peptide JZTX-V led to a decrease in Na_V affinity (analog I28E), but only at $Na_V1.4$ (Moyer et al., 2018). A similar reduction in hydrophobicity in the N-terminal region of the NaSpTx 1 analog F5A-GpTx-1 also decreased $Na_V1.4$ inhibition (Murray et al., 2015). As our SAR knowledge of NaSpTx 1 and 3 deepens, we anticipate further opportunities to develop more selective and/or potent inhibitors are expected to emerge.

Structural changes in optimized molecules suggest gain of affinity can be associated with regions of the ICK peptide beyond those associated with the local effects of the substitution. For example, structural rearrangements are observed in the HwTx-IV, JZTX-V and HNTX-I optimized analogs (**Figures 4B–D**) that alter the surface structure of wild-type vs. optimized peptide, with pronounced changes in the N-termini of JZVTX-V with the introduction of Pra (**Figure 4C**) and following the introduction of W7 in HNTX-I (**Figure 4D**). However, the three-dimensional structure of a NaSpTx inhibitor bound to a Na_V channel embedded in the cell membrane is still to be elucidated.

THE PHYLOGENY OF NaSpTx TARGETING $Na_V1.7$

In addition to the SAR studies of the nine NaSpTx discussed above, a number of other NaSpTx display interesting $Na_V1.7$ modulatory properties (**Figure 5**). To date, twenty-three other peptides belonging to NaSpTx 1, 2, 3, and 7 are described with potencies ranging from 0.3 nM to 7.4 μM for half-maximal activity for $Na_V1.7$ (**Figure 5A**). These include μ-TRTX-Pho1a, μ-TRTX-Pho1b and μ-TRTX-Pho2a (Chow et al., 2015), κ/μ-TRTX-Gr2c, κ/μ-TRTX-Gr3a, μ-TRTX-Gr1a, β-TRTX-Gr1d and β-TRTX-Gr1a (Redaelli et al., 2010), μ-TRTX-Pn3a (Deuis et al., 2017), μ-TRTX-Df1a (Cardoso et al., 2017), β/ω-TRTX-Tp2a (Priest et al., 2007), δ-TRTX-Cg1a (Xiao et al., 2005), μ-TRTX-Tp1a (Cardoso et al., 2015), β-TRTX-Cm1b and β-TRTX-Cd1a (Bosmans et al., 2006; Sousa et al., 2017) and μ-TRTX-Hd1a (Klint et al., 2015b). Amongst these, only

TABLE 2 | Therapeutical potential of NaSpTx peptides evaluated in pre-clinical rodent pain models.

Peptide	NaSpTx family	Spider species	Preferred Na_V subtypes	Therapeutic potential	References
Gr1b (GsAFI) Gr2c (GsAFII)	3	*Grammostola rosea*	$Na_V1.7 > 1.4 > 1.1 > 1.2$ $Na_V1.7 > 1.4 > 1.1$	Acute and inflammatory pain	Lampe, 1998
HwTx-IV	1	*Ornithoctonus huwena*	$Na_V1.7 > 1.2 > 1.3 > 1.4$	Inflammatory and SNI-induced neuropathic pain	Liu et al., 2014b
HnTx-IV	1	*Haplopelma hainanum*	$Na_V1.2 > 1.3 > 1.7$	SNI-induced neuropathic and formalin-induced inflammatory pain.	Liu et al., 2014a
ProTx-II	3	*Thrixopelma Pruriens*	$Na_V1.7 > 1.6 > 1.2 > 1.5 > 1.3 > 1.8$	Painful diabetic neuropathy Inflammatory pain	Tanaka et al., 2015; Flinspach et al., 2017
Hl1a	7	*Haplopelma lividum*	$Na_V1.8$	Inflammatory and neuropathic pain	Meng et al., 2016
Pn3a	2	*Pamphobeteus nigricolor*	$Na_V1.7 > 1.1$	Inflammatory (with opioid co-administration) and post-surgical pain	Deuis et al., 2017; Mueller et al., 2019
Ca1a	Unknown	*Cyriopagopus albostriatus*	$Na_V1.7 > 1.2 > 1.6 > 1.4 > 1.3$	Inflammatory and thermal pain	Zhang et al., 2018c
Ca2a	1	*Cyriopagopus albostriatus*	$Na_V1.7 > 1.2 > 1.6 > 1.3$	Inflammatory and thermal pain	Zhang et al., 2018a
Cyriotoxin-1a	1	*Cyriopagopus schioedtei*	$Na_V1.1 > 1.2 > 1.6 > 1.7 > 1.3$	Thermal pain	Goncalves et al., 2019

The NaSpTx peptide with respective family, spider species, preferred voltage-gated sodium channels (Na_V) subtypes and the pre-clinical pain model showing therapeutic efficacy are described. The preferred Na_V subtypes for some of these NaSpTx peptides were described in: Gr1b and Gr2c (Redaelli et al., 2010), HwTx-IV (Minassian et al., 2013), HnTx-IV (Cai et al., 2015), and ProTx-II (Middleton et al., 2002).

δ-TRTX-Cg1a activates $Na_V1.7$, while the other β- and μ-toxins are $Na_V1.7$ inhibitors. Although detailed SAR studies on these toxins have not been described, their sequences similarities make a detailed analysis of their primary structure using phylogenetic approaches useful.

Not surprisingly, NaSpTxs targeting $Na_V1.7$ show independent phylogenetic origins and generate well defined clades for NaSpTx 1, 2, and 3, while NaSpTx 7, with only two representatives, clustered as outliers (**Figure 5B**). These results support previous findings underpinning the classification of the NaSpTx into 12 families (Klint et al., 2012). However, examining relatedness within loops revealed some interesting differences. For example, loop 1 showed similar clustering as the complete primary sequences except NaSpTx 7 clustered with NaSpTx 1 (**Figure 5C**), while loop 2 had more complex phylogenetic origins, with a primitive ancestor possibly arising from NaSpTx 1 (**Figure 5D**). Loop 3 also showed complex phylogenetic origins. It was divided into a major clade including the NaspTx1, two members of NaSpTx 2 and one member of NaSpTx 7, a second clade containing NaSpTx 3 and one member of the NaSpTx 2 as outlier, and a small clade including NaSpTx 2 and 7 (**Figure 5E**). These observations suggest a less purifying selection in loop 3, with NaSpTx 3 remaining the most conservative loop 3 group. The complexity of the phylogenetic origins of the loop 4 and C-terminal regions are considerably higher compared to loops 1, 2, and 3 (**Figures 5F,G**). Loop 4 diverged into four clades containing a mix of NaSpTx members, and again the NaSpTx 3 clustered further in a single clade, but now with one member of the NaSpTx 1 as an outlier. Finally, the C-terminal was diverged into three major clades that also contained a mix of NaSpTx members. Interestingly, the C-terminals of NaSpTx 2 clustered further into a single clade, indicating that a more conservative evolutionary pressure is occurring in this region of the NaSpTx 2 members.

Overall, we observed that the NaSpTx 1, 2 and 3 families have independent phylogenetic origins. For the NaSpTx 7, more representatives of this family are essential for an appropriated phylogenetic analysis. Remarkably, the loops 2, 3, and 4 forming the peptides in NaSpTx 3 are under a more conservative pressure compared to NaSpTx 1 and 2. This agrees with the SAR studies for ProTx-II (β/ω-TRTX-Tp2a), where optimization was possible only with modifications located in less conserved regions, the C-terminal and in the loop 1, while modifications in loops 2, 3, and 4 were often deleterious for Na_V inhibition (Priest et al., 2007; Smith et al., 2007; Schmalhofer et al., 2008; Park et al., 2014; Flinspach et al., 2017). For NaSpTx 1, loop 2 was more conserved and appears to be in agreement with the SAR of CcoTx1 (β-TRTX-Cm1a) where modifications to loop 2 were not well tolerated, while loops 3, 4 and C-terminal tolerated multiple modification (Shcherbatko et al., 2016). Similarly, the C-terminal of NaSpTx 2 was also more conserved compared to the other NaSpTx families, but studies of SAR aiming to unravel the role this C-terminal region in Na_V inhibition are yet to be pursued. These patterns of evolutionary pressure provide clues to further explore the SAR of loops and C-terminal residues to that can help further expand the SAR of these Na_V channel toxins. However, a simple correlation between phylogenetic origins and potency at Na_V channels remains to be established.

PERSPECTIVES IN THERAPEUTIC DEVELOPMENT

Advances in understanding disease mechanisms and associated novel therapeutic targets position spider ICK peptides as novel drug leads of sufficient size and pharmacophore complexity to restrict their *in vivo* distribution and limit off-target effects. To fully exploit this potential, a deeper understanding of ICK peptide SAR and bio-engineering is required to address specific therapeutic needs. This undoubtedly involves bio-activity and three-dimensional structural determinations for a detailed view of the SAR features. Pre-clinical studies in rodent pain models showing reversal of different types of pain have been reported for spider toxins, including several lacking published SAR data (**Table 2**).

The NaSpTx3 peptides Gr1b and Gr2c reversed acute and inflammatory pain intrathecally (Lampe, 1998), while ProTx-II and its optimized analog JNJ63955918 reversed neuropathic and inflammatory pain when administered intrathecally or locally (Tanaka et al., 2015; Flinspach et al., 2017). The NaSpTx1 peptides HwTx-IV and HNTX-IV also reversed neuropathic and inflammatory pains intraperitonially (Liu et al., 2014a,b), while ides Ca2a and cyriotoxin-1a reversed inflammatory and thermal pain following intraperitoneal or intraplantar administration, respectively (Zhang et al., 2018a; Goncalves et al., 2019).

In contrast, the NaSpTx2 peptide Pn3a reversed inflammatory pain but only when co-administered with an intraperitoneal opioid (Deuis et al., 2017), despite reversing post-surgical pain following intraperitoneal or local administration (Mueller et al., 2019). Finally, the unclassified spider peptide Ca1a reversed inflammatory and thermal pain following intraperitoneal or intraplantar administrations, respectively (Zhang et al., 2018c). This review of the continuing advancements in the SAR of spider venom ICK peptides will hopefully facilitate efforts to optimize Na_V channel modulators for the treatment of complex channelopathies, including different forms of chronic pain.

AUTHOR CONTRIBUTIONS

FC performed the phylogenetic analysis, bibliography research, wrote the manuscript, and prepared the figures. RL provided scope, guidance and critically reviewed the manuscript.

FUNDING

The National Health and Medical Research Council of Australia APP1072113 provided research funding to RL that produced background to the review and APP1119056 provided a Fellowship to RL.

REFERENCES

Abraham, N., and Lewis, R. J. (2018). Neuronal nicotinic acetylcholine receptor modulators from cone snails. *Mar. Drugs* 16:E208. doi: 10.3390/md16060208

Agwa, A. J., Lawrence, N., Deplazes, E., Cheneval, O., Chen, R., Craik, D. J., et al. (2017). Spider peptide toxin HwTx-IV engineered to bind to lipid membranes has an increased inhibitory potency at human voltage-gated sodium channel hNaV1.7. *Biochim. Biophys. Acta* 1859, 835–844. doi: 10.1016/j.bbamem.2017.01.020

Agwa, A. J., Peigneur, S., Chow, C. Y., Lawrence, N., Craik, D. J., Tytgat, J., et al. (2018). Gating modifier toxins isolated from spider venom: modulation of voltage-gated sodium channels and the role of lipid membranes. *J. Biol. Chem.* 293, 9041–9052. doi: 10.1074/jbc.RA118.002553

Arnold, K., Bordoli, L., Kopp, J., and Schwede, T. (2006). The SWISS-MODEL workspace: a web-based environment for protein structure homology modelling. *Bioinformatics* 22, 195–201. doi: 10.1093/bioinformatics/bti770

Bosmans, F., Martin-Eauclaire, M. F., and Swartz, K. J. (2008). Deconstructing voltage sensor function and pharmacology in sodium channels. *Nature* 456, 202–208. doi: 10.1038/nature07473

Bosmans, F., Rash, L., Zhu, S., Diochot, S., Lazdunski, M., Escoubas, P., et al. (2006). Four novel tarantula toxins as selective modulators of voltage-gated sodium channel subtypes. *Mol. Pharmacol.* 69, 419–429. doi: 10.1124/mol.105.015941

Cai, T., Luo, J., Meng, E., Ding, J., Liang, S., Wang, S., et al. (2015). Mapping the interaction site for the tarantula toxin hainantoxin-IV (β-TRTX-Hn2a) in the voltage sensor module of domain II of voltage-gated sodium channels. *Peptides* 68, 148–156. doi: 10.1016/j.peptides.2014.09.005

Cardoso, F. C., Dekan, Z., Rosengren, K. J., Erickson, A., Vetter, I., Deuis, J. R., et al. (2015). Identification and characterization of ProTx-III [μ-TRTX-Tp1a], a new voltage-gated sodium channel inhibitor from the venom of the tarantula *Thrixopelma pruriens*. *Mol. Pharmacol.* 88, 291–303. doi: 10.1124/mol.115.098178

Cardoso, F. C., Dekan, Z., Smith, J. J., Deuis, J. R., Vetter, I., Herzig, V., et al. (2017). Modulatory features of the novel spider toxin μ-TRTX-Df1a isolated from the venom of the spider *Davus fasciatus*. *Br. J. Pharmacol.* 174, 2528–2544. doi: 10.1111/bph.13865

Cardoso, F. C., Hasan, M., Zhao, T., and Lewis, R. J. (2018). Toxins in pain. *Curr. Opin. Support. Palliat. Care* 12, 132–141. doi: 10.1097/SPC.0000000000000335

Cardoso, F. C., and Lewis, R. J. (2017). Sodium channels and pain: from toxins to therapies. *Br. J. Pharmacol.* 175, 2138–2157. doi: 10.1111/bph.13962

Chow, C. Y., Cristofori-Armstrong, B., Undheim, E. A., King, G. F., and Rash, L. D. (2015). Three peptide modulators of the human voltage-gated sodium channel 1.7, an important analgesic target, from the venom of an *Australian tarantula*. *Toxins* 7, 2494–2513. doi: 10.3390/toxins7072494

Cox, J. J., Reimann, F., Nicholas, A. K., Thornton, G., Roberts, E., Springell, K., et al. (2006). An SCN9A channelopathy causes congenital inability to experience pain. *Nature* 444, 894–898. doi: 10.1038/nature05413

DeLano, W. L. (2002). *The PyMOL Molecular Graphics System, Version 1.5.0.4 Schrödinger*. Scotts Valley, CA: LLC.

Deng, M., Luo, X., Jiang, L., Chen, H., Wang, J., He, H., et al. (2013). Synthesis and biological characterization of synthetic analogs of Huwentoxin-IV (μ-theraphotoxin-Hh2a), a neuronal tetrodotoxin-sensitive sodium channel inhibitor. *Toxicon* 71, 57–65. doi: 10.1016/j.toxicon.2013.05.015

Deuis, J. R., Dekan, Z., Wingerd, J. S., Smith, J. J., Munasinghe, N. R., Bhola, R. F., et al. (2017). Pharmacological characterisation of the highly NaV1.7 selective spider venom peptide pN3a. *Sci. Rep.* 7:40883. doi: 10.1038/srep40883

Diochot, S., Drici, M. D., Moinier, D., Fink, M., and Lazdunski, M. (1999). Effects of phrixotoxins on the KV4 family of potassium channels and implications for the role of Ito1 in cardiac electrogenesis. *Br. J. Pharmacol.* 126, 251–263. doi: 10.1038/sj.bjp.0702283

Dongol, Y., Dhananjaya, B. L., Shrestha, R. K., and Aryal, G. (2016). Wasp venom toxins as a potential therapeutic agent. *Protein Pept. Lett.* 23, 688–698. doi: 10.2174/0929866523666160511151039

Drenth, J. P., and Waxman, S. G. (2007). Mutations in sodium-channel gene SCN9A cause a spectrum of human genetic pain disorders. *J. Clin. Invest.* 117, 3603–3609. doi: 10.1172/JCI33297

Faber, C. G., Lauria, G., Merkies, I. S., Cheng, X., Han, C., Ahn, H. S., et al. (2012). Gain-of-function NaV1.8 mutations in painful neuropathy. *Proc. Natl. Acad. Sci. U.S.A.* 109, 19444–19449. doi: 10.1073/pnas.1216080109

Flinspach, M., Xu, Q., Piekarz, A. D., Fellows, R., Hagan, R., Gibbs, A., et al. (2017). Insensitivity to pain induced by a potent selective closed-state NaV1.7 inhibitor. *Sci. Rep.* 7:39662. doi: 10.1038/srep39662

Goncalves, T. C., Benoit, E., Kurz, M., Lucarain, L., Fouconnier, S., Combemale, S., et al. (2019). From identification to functional characterization of cyriotoxin-1a, an antinociceptive toxin from *Cyriopagopus schioedtei* spider. *Br. J. Pharmacol.* doi: 10.1111/bph.14628 [Epub ahead of print].

Grasso, G., Landi, A., and Alafaci, C. (2016). A novel pathophysiological mechanism contributing to trigeminal neuralgia. *Mol. Med.* 22, 452–454. doi: 10.2119/molmed.2016.00172

Henriques, S. T., Deplazes, E., Lawrence, N., Cheneval, O., Chaousis, S., Inserra, M., et al. (2016). Interaction of tarantula venom peptide ProTx-II with lipid membranes is a prerequisite for its inhibition of human voltage-gated sodium channel NaV1.7. *J. Biol. Chem.* 291, 17049–17065. doi: 10.1074/jbc.M116.729095

Huang, J., Han, C., Estacion, M., Vasylyev, D., Hoeijmakers, J. G., Gerrits, M. M., et al. (2014). Gain-of-function mutations in sodium channel NaV1.9 in painful neuropathy. *Brain* 137, 1627–1642. doi: 10.1093/brain/awu079

Kessler, P., Marchot, P., Silva, M., and Servent, D. (2017). The three-finger toxin fold: a multifunctional structural scaffold able to modulate cholinergic functions. *J. Neurochem.* 142(Suppl. 2), 7–18. doi: 10.1111/jnc.13975

Klein-Weigel, P. F., Volz, T. S., and Richter, J. G. (2018). Erythromelalgia. *Vasa* 47, 91–97. doi: 10.1024/0301-1526/a000675

Klint, J. K., Chin, Y. K., and Mobli, M. (2015a). Rational engineering defines a molecular switch that is essential for activity of spider-venom peptides against the analgesics target NaV1.7. *Mol. Pharmacol.* 88, 1002–1010. doi: 10.1124/mol.115.100784

Klint, J. K., Smith, J. J., Vetter, I., Rupasinghe, D. B., Er, S. Y., Senff, S., et al. (2015b). Seven novel modulators of the analgesic target NaV1.7 uncovered using a high-throughput venom-based discovery approach. *Br. J. Pharmacol.* 172, 2445–2458. doi: 10.1111/bph.13081

Klint, J. K., Senff, S., Rupasinghe, D. B., Er, S. Y., Herzig, V., Nicholson, G. M., et al. (2012). Spider-venom peptides that target voltage-gated sodium channels: pharmacological tools and potential therapeutic leads. *Toxicon* 60, 478–491. doi: 10.1016/j.toxicon.2012.04.337

Lampe, R. A. (1998). Analgesic peptides from venom of *Grammostola spatulata* and use thereof. U.S. Patent No 58,078,21A.

Lee, S. Y., and MacKinnon, R. (2004). A membrane-access mechanism of ion channel inhibition by voltage sensor toxins from spider venom. *Nature* 430, 232–235. doi: 10.1038/nature02632

Li, D., Xiao, Y., Xu, X., Xiong, X., Lu, S., Liu, Z., et al. (2004). Structure-activity relationships of hainantoxin-IV and structure determination of active and inactive sodium channel blockers. *J. Biol. Chem.* 279, 37734–37740. doi: 10.1074/jbc.M405765200

Liao, Z., Yuan, C., Deng, M., Li, J., Chen, J., Yang, Y., et al. (2006). Solution structure and functional characterization of jingzhaotoxin-XI: a novel gating modifier of both potassium and sodium channels. *Biochemistry* 45, 15591–15600. doi: 10.1021/bi061457+

Liu, Y., Tang, J., Zhang, Y., Xun, X., Tang, D., Peng, D., et al. (2014a). Synthesis and analgesic effects of μ-TRTX-Hhn1b on models of inflammatory and neuropathic pain. *Toxins* 6, 2363–2378. doi: 10.3390/toxins6082363

Liu, Y., Wu, Z., Tang, D., Xun, X., Liu, L., Li, X., et al. (2014b). Analgesic effects of Huwentoxin-IV on animal models of inflammatory and neuropathic pain. *Protein Pept. Lett.* 21, 153–158.

Liu, Z., Cai, T., Zhu, Q., Deng, M., Li, J., Zhou, X., et al. (2013). Structure and function of hainantoxin-III, a selective antagonist of neuronal tetrodotoxin-sensitive voltage-gated sodium channels isolated from the Chinese bird spider *Ornithoctonus hainana*. *J. Biol. Chem.* 288, 20392–20403. doi: 10.1074/jbc.M112.426627

Luiz, A. P., and Wood, J. N. (2016). Sodium channels in pain and cancer: new therapeutic opportunities. *Adv. Pharmacol.* 75, 153–178. doi: 10.1016/bs.apha.2015.12.006

Meisler, M. H., and Kearney, J. A. (2005). Sodium channel mutations in epilepsy and other neurological disorders. *J. Clin. Invest.* 115, 2010–2017. doi: 10.1172/JCI25466

Meng, P., Huang, H., Wang, G., Yang, S., Lu, Q., Liu, J., et al. (2016). A novel toxin from *Haplopelma lividum* selectively inhibits the NaV1.8 channel and possesses potent analgesic efficacy. *Toxins* 9:7. doi: 10.3390/toxins9010007

Middleton, R. E., Warren, V. A., Kraus, R. L., Hwang, J. C., Liu, C. J., Dai, G., et al. (2002). Two tarantula peptides inhibit activation of multiple sodium channels. *Biochemistry* 41, 14734–14747. doi: 10.1021/bi026546a

Mihailescu, M., Krepkiy, D., Milescu, M., Gawrisch, K., Swartz, K. J., and White, S. (2014). Structural interactions of a voltage sensor toxin with lipid membranes. *Proc. Natl. Acad. Sci. U.S.A.* 111, E5463–E5470. doi: 10.1073/pnas.1415324111

Milescu, M., Bosmans, F., Lee, S., Alabi, A. A., Kim, J. I., and Swartz, K. J. (2009). Interactions between lipids and voltage sensor paddles detected with tarantula toxins. *Nat. Struct. Mol. Biol.* 16, 1080–1085. doi: 10.1038/nsmb.1679

Minassian, N. A., Gibbs, A., Shih, A. Y., Liu, Y., Neff, R. A., Sutton, S. W., et al. (2013). Analysis of the structural and molecular basis of voltage-sensitive sodium channel inhibition by the spider toxin huwentoxin-IV (μ-TRTX-Hh2a). *J. Biol. Chem.* 288, 22707–22720. doi: 10.1074/jbc.M113.461392

Moyer, B. D., Murray, J. K., Ligutti, J., Andrews, K., Favreau, P., Jordan, J. B., et al. (2018). Pharmacological characterization of potent and selective NaV1.7 inhibitors engineered from *Chilobrachys jingzhao* tarantula venom peptide JzTx-V. *PLoS One* 13:e0196791. doi: 10.1371/journal.pone.0196791

Mueller, A., Starobova, H., Morgan, M., Dekan, Z., Cheneval, O., Schroeder, C. I., et al. (2019). Anti-allodynic effects of the selective NaV1.7 inhibitor Pn3a in a mouse model of acute post-surgical pain: evidence for analgesic synergy with opioids and baclofen. *Pain* [Epub ahead of print]. doi: 10.1097/j.pain.0000000000001567

Murray, J. K., Ligutti, J., Liu, D., Zou, A., Poppe, L., Li, H., et al. (2015). Engineering potent and selective analogues of GpTx-1, a tarantula venom peptide antagonist of the NaV1.7 sodium channel. *J. Med. Chem.* 58, 2299–2314. doi: 10.1021/jm501765v

Murray, J. K., Long, J., Zou, A., Ligutti, J., Andrews, K. L., Poppe, L., et al. (2016). Single residue substitutions that confer voltage-gated sodium ion channel subtype selectivity in the NaV1.7 inhibitory peptide GpTx-1. *J. Med. Chem.* 59, 2704–2717. doi: 10.1021/acs.jmedchem.5b01947

Ono, S., Kimura, T., and Kubo, T. (2011). Characterization of voltage-dependent calcium channel blocking peptides from the venom of the tarantula *Grammostola rosea*. *Toxicon* 58, 265–276. doi: 10.1016/j.toxicon.2011.06.006

Osteen, J. D., Herzig, V., Gilchrist, J., Emrick, J. J., Zhang, C., Wang, X., et al. (2016). Selective spider toxins reveal a role for the NaV1.1 channel in mechanical pain. *Nature* 534, 494–499. doi: 10.1038/nature17976

Park, J. H., Carlin, K. P., Wu, G., Ilyin, V. I., Musza, L. L., Blake, P. R., et al. (2014). Studies examining the relationship between the chemical structure of protoxin II and its activity on voltage gated sodium channels. *J. Med. Chem.* 57, 6623–6631. doi: 10.1021/jm500687u

Peng, K., Shu, Q., Liu, Z., and Liang, S. (2002). Function and solution structure of huwentoxin-IV, a potent neuronal tetrodotoxin (TTX)-sensitive sodium channel antagonist from Chinese bird spider *Selenocosmia huwena*. *J. Biol. Chem.* 277, 47564–47571. doi: 10.1074/jbc.M204063200

Phatarakijnirund, V., Mumm, S., Mcalister, W. H., Novack, D. V., Wenkert, D., Clements, K. L., et al. (2016). Congenital insensitivity to pain: fracturing without apparent skeletal pathobiology caused by an autosomal dominant, second mutation in SCN11A encoding voltage-gated sodium channel 1.9. *Bone* 84, 289–298. doi: 10.1016/j.bone.2015.11.022

Platnick, N. I. (2014). *The World Spider Catalog, version 15*. New York, NY: American Museum of Natural History.

Priest, B. T., Blumenthal, K. M., Smith, J. J., Warren, V. A., and Smith, M. M. (2007). ProTx-I and ProTx-II: gating modifiers of voltage-gated sodium channels. *Toxicon* 49, 194–201. doi: 10.1016/j.toxicon.2006.09.014

Rahnama, S., Deuis, J. R., Cardoso, F. C., Ramanujam, V., Lewis, R. J., Rash, L. D., et al. (2017). The structure, dynamics and selectivity profile of a NaV1.7 potency-optimised huwentoxin-IV variant. *PLoS One* 12:e0173551. doi: 10.1371/journal.pone.0173551

Redaelli, E., Cassulini, R. R., Silva, D. F., Clement, H., Schiavon, E., Zamudio, F. Z., et al. (2010). Target promiscuity and heterogeneous effects of tarantula venom peptides affecting Na+ and K+ ion channels. *J. Biol. Chem.* 285, 4130–4142. doi: 10.1074/jbc.M109.054718

Revell, J. D., Lund, P. E., Linley, J. E., Metcalfe, J., Burmeister, N., Sridharan, S., et al. (2013). Potency optimization of Huwentoxin-IV on hNaV1.7: a neurotoxin TTX-S sodium-channel antagonist from the venom of the Chinese bird-eating spider *Selenocosmia huwena*. *Peptides* 44, 40–46. doi: 10.1016/j.peptides.2013.03.011

Rong, M., Chen, J., Tao, H., Wu, Y., Jiang, P., Lu, M., et al. (2011). Molecular basis of the tarantula toxin jingzhaotoxin-III (β-TRTX-Cj1α) interacting with voltage sensors in sodium channel subtype Nav1.5. *FASEB J.* 25, 3177–3185. doi: 10.1096/fj.10-178848

Rong, M., Duan, Z., Chen, J., Li, J., Xiao, Y., and Liang, S. (2013). Native pyroglutamation of huwentoxin-IV: a post-translational modification that increases the trapping ability to the sodium channel. *PLoS One* 8:e65984. doi: 10.1371/journal.pone.0065984

Ryu, J. H., Jung, H. J., Konishi, S., Kim, H. H., Park, Z. Y., and Kim, J. I. (2017). Structure-activity relationships of ω-Agatoxin IVA in lipid membranes. *Biochem. Biophys. Res. Commun.* 482, 170–175. doi: 10.1016/j.bbrc.2016.11.025

Saitou, N., and Nei, M. (1987). The neighbor-joining method: a new method for reconstructing phylogenetic trees. *Mol. Biol. Evol.* 4, 406–425.

Salvatierra, J., Castro, J., Erickson, A., Li, Q., Braz, J., Gilchrist, J., et al. (2018). NaV1.1 inhibition can reduce visceral hypersensitivity. *JCI Insight* 3:121000. doi: 10.1172/jci.insight.121000

Schmalhofer, W. A., Calhoun, J., Burrows, R., Bailey, T., Kohler, M. G., Weinglass, A. B., et al. (2008). ProTx-II, a selective inhibitor of NaV1.7 sodium channels, blocks action potential propagation in nociceptors. *Mol. Pharmacol.* 74, 1476–1484. doi: 10.1124/mol.108.047670

Shcherbatko, A., Rossi, A., Foletti, D., Zhu, G., Bogin, O., Galindo Casas, M., et al. (2016). Engineering highly potent and selective microproteins against NaV1.7 sodium channel for treatment of pain. *J. Biol. Chem.* 291, 13974–13986. doi: 10.1074/jbc.M116.725978

Shen, H., Li, Z., Jiang, Y., Pan, X., Wu, J., Cristofori-Armstrong, B., et al. (2018). Structural basis for the modulation of voltage-gated sodium channels by animal toxins. *Science* 362:eaau2596. doi: 10.1126/science.aau2596

Shen, H., Liu, D., Wu, K., Lei, J., and Yan, N. (2019). Structures of human NaV1.7 channel in complex with auxiliary subunits and animal toxins. *Science* 363, 1303–1308. doi: 10.1126/science.aaw2493

Sievers, F., Wilm, A., Dineen, D., Gibson, T. J., Karplus, K., Li, W., et al. (2011). Fast, scalable generation of high-quality protein multiple sequence alignments using Clustal Omega. *Mol. Syst. Biol.* 7:539. doi: 10.1038/msb.2011.75

Sloan, G., Shillo, P., Selvarajah, D., Wu, J., Wilkinson, I. D., Tracey, I., et al. (2018). A new look at painful diabetic neuropathy. *Diabetes Res. Clin. Pract.* 144, 177–191. doi: 10.1016/j.diabres.2018.08.020

Smith, J. J., Alphy, S., Seibert, A. L., and Blumenthal, K. M. (2005). Differential phospholipid binding by site 3 and site 4 toxins. Implications for structural variability between voltage-sensitive sodium channel domains. *J. Biol. Chem.* 280, 11127–11133. doi: 10.1074/jbc.M412552200

Smith, J. J., Cummins, T. R., Alphy, S., and Blumenthal, K. M. (2007). Molecular interactions of the gating modifier toxin ProTx-II with NaV1.5: implied existence of a novel toxin binding site coupled to activation. *J. Biol. Chem.* 282, 12687–12697. doi: 10.1074/jbc.M610462200

Sousa, S. R., Wingerd, J. S., Brust, A., Bladen, C., Ragnarsson, L., Herzig, V., et al. (2017). Discovery and mode of action of a novel analgesic β-toxin from the African spider *Ceratogyrus darlingi*. *PLoS One* 12:e0182848. doi: 10.1371/journal.pone.0182848

Szepetowski, P. (2018). Genetics of human epilepsies: continuing progress. *Presse Med.* 47, 218–226. doi: 10.1016/j.lpm.2017.10.020

Tanaka, K., Sekino, S., Ikegami, M., Ikeda, H., and Kamei, J. (2015). Antihyperalgesic effects of ProTx-II, a NaV1.7 antagonist, and A803467, a NaV1.8 antagonist, in diabetic mice. *J. Exp. Pharmacol.* 7, 11–16. doi: 10.2147/JEP.S79973

Thompson, C. H., Kahlig, K. M., and George, A. L. Jr. (2011). SCN1A splice variants exhibit divergent sensitivity to commonly used antiepileptic drugs. *Epilepsia* 52, 1000–1009. doi: 10.1111/j.1528-1167.2011.03040.x

Wright, Z. V. F., Mccarthy, S., Dickman, R., Reyes, F. E., Sanchez-Martinez, S., Cryar, A., et al. (2017). The role of disulfide bond replacements in analogues of the tarantula toxin ProTx-II and their effects on inhibition of the voltage-gated sodium ion channel NaV1.7. *J. Am. Chem. Soc.* 139, 13063–13075. doi: 10.1021/jacs.7b06506

Xiao, Y., Bingham, J. P., Zhu, W., Moczydlowski, E., Liang, S., and Cummins, T. R. (2008a). Tarantula huwentoxin-IV inhibits neuronal sodium channels by binding to receptor site 4 and trapping the domain II voltage sensor in the closed configuration. *J. Biol. Chem.* 283, 27300–27313. doi: 10.1074/jbc.M708447200

Xiao, Y., Luo, X., Kuang, F., Deng, M., Wang, M., Zeng, X., et al. (2008b). Synthesis and characterization of huwentoxin-IV, a neurotoxin inhibiting central neuronal sodium channels. *Toxicon* 51, 230–239.

Xiao, Y., Blumenthal, K., Jackson, J. O. II, Liang, S., and Cummins, T. R. (2010). The tarantula toxins ProTx-II and huwentoxin-IV differentially interact with human NaV1.7 voltage sensors to inhibit channel activation and inactivation. *Mol. Pharmacol.* 78, 1124–1134. doi: 10.1124/mol.110.066332

Xiao, Y., Tang, J., Hu, W., Xie, J., Maertens, C., Tytgat, J., et al. (2005). Jingzhaotoxin-I, a novel spider neurotoxin preferentially inhibiting cardiac sodium channel inactivation. *J. Biol. Chem.* 280, 12069–12076. doi: 10.1074/jbc.M411651200

Xiao, Y., Tang, J., Yang, Y., Wang, M., Hu, W., Xie, J., et al. (2004). Jingzhaotoxin-III, a novel spider toxin inhibiting activation of voltage-gated sodium channel in rat cardiac myocytes. *J. Biol. Chem.* 279, 26220–26226. doi: 10.1074/jbc.M401387200

Xu, H., Li, T., Rohou, A., Arthur, C. P., Tzakoniati, F., Wong, E., et al. (2019). Structural basis of NaV1.7 inhibition by a gating-modifier spider toxin. *Cell* 176, 1238–1239. doi: 10.1016/j.cell.2019.01.047

Yuan, C., Yang, S., Liao, Z., and Liang, S. (2007). Effects and mechanism of Chinese tarantula toxins on the KV2.1 potassium channels. *Biochem. Biophys. Res. Commun.* 352, 799–804. doi: 10.1016/j.bbrc.2006.11.086

Zhang, F., Liu, Y., Zhang, C., Li, J., Yang, Z., Gong, X., et al. (2015). Natural mutations change the affinity of μ-theraphotoxin-Hhn2a to voltage-gated sodium channels. *Toxicon* 93, 24–30. doi: 10.1016/j.toxicon.2014.11.220

Zhang, Y., Peng, D., Huang, B., Yang, Q., Zhang, Q., Chen, M., et al. (2018a). Discovery of a novel NaV1.7 inhibitor from *Cyriopagopus albostriatus* venom with potent analgesic efficacy. *Front. Pharmacol.* 9:1158. doi: 10.3389/fphar.2018.01158

Zhang, Y., Yang, Q., Zhang, Q., Peng, D., Chen, M., Liang, S., et al. (2018b). Engineering gain-of-function analogues of the spider venom peptide HNTX-I, a potent blocker of the hNaV1.7 sodium channel. *Toxins* 10:E358. doi: 10.3390/toxins10090358

Zhang, Y. X., Peng, D. Z., Zhang, Q. F., Huang, B., Yang, Q. C., Tang, D. F., et al. (2018c). μ-TRTX-Ca1a: a novel neurotoxin from *Cyriopagopus albostriatus* with analgesic effects. *Acta Pharmacol. Sin.* doi: 10.1038/s41401-018-0181-9 [Epub ahead of print].

Ziegman, R., and Alewood, P. (2015). Bioactive components in fish venoms. *Toxins* 7, 1497–1531. doi: 10.3390/toxins7051497

Conflict of Interest Statement: The authors declare that the research was conducted in the absence of any commercial or financial relationships that could be construed as a potential conflict of interest.

frontiers in Pharmacology

ORIGINAL RESEARCH
published: 16 April 2019
doi: 10.3389/fphar.2019.00357

JZTX-V Targets the Voltage Sensor in Kv4.2 to Inhibit I_{to} Potassium Channels in Cardiomyocytes

Yiya Zhang[1,2,3], Ji Luo[3], Juan He[3], Mingqiang Rong[3] and Xiongzhi Zeng[3]**

[1] Department of Dermatology, Xiangya Hospital, Central South University, Changsha, China, [2] Key Laboratory of Organ Injury, Aging and Regenerative Medicine of Hunan Province, Central South University, Changsha, China, [3] The National and Local Joint Engineering Laboratory of Animal Peptide Drug Development, College of Life Sciences, Hunan Normal University, Changsha, China

Kv4 potassium channels are responsible for transient outward K^+ currents in the cardiac action potential (AP). Previous experiments by our group demonstrated that Jingzhaotoxin-V (JZTX-V) selectively inhibits A-type potassium channels. However, the specific effects of JZTX-V on the transient outward (I_{to}) current of cardiomyocytes and underlying mechanism of action remain unclear. In the current study, 100 nM JZTX-V effectively inhibited the I_{to} current and extended the action potential duration (APD) of neonatal rat ventricular myocytes (NRVM). We further analyzed the effects of JZTX-V on Kv4.2, a cloned channel believed to underlie the I_{to} current in rat cardiomyocytes. JZTX-V inhibited the Kv4.2 current with a half-maximal inhibitory concentration (IC_{50}) of 13 ± 1.7 nM. To establish the molecular mechanism underlying the inhibitory action of JZTX-V on Kv4.2, we performed alanine scanning mutagenesis of Kv4.2 and JZTX-V and assessed the effects of the mutations on binding activities of the proteins. Interestingly, the Kv4.2 mutations V285A, F289A, and V290A reduced the affinity for JZTX-V while I275A and L277A increased the affinity for JZTX-V. Moreover, mutation of positively charged residues (R20 and K22) of JZTX-V and the hydrophobic patch (formed by W5, M6, and W7) led to a significant reduction in toxin sensitivity, indicating that the hydrophobic patch and electrostatic interactions played key roles in the binding of JZTX-V with Kv4.2. Data from our study have shed light on the specific roles and molecular mechanisms of JZTX-V in the regulation of I_{to} potassium channels and supported its utility as a potential novel antiarrhythmic drug.

Keywords: JXTX-V, cardiomyocytes, action potential, Kv4.2 channel, hydrophobic patch

OPEN ACCESS

Edited by:
Jean-Francois Rolland, Axxam, Italy

Reviewed by:
Michel Vivaudou, UMR5075 Institut de Biologie Structurale (IBS), France
Elisabetta Cerbai, University of Florence, Italy

****Correspondence:***
Yiya Zhang
yiya0108@csu.edu.cn
Xiongzhi Zeng
zengxz@hunnu.edu.cn

Specialty section:
This article was submitted to Pharmacology of Ion Channels and Channelopathies, a section of the journal Frontiers in Pharmacology

Received: *09 September 2018*
Accepted: *21 March 2019*
Published: *16 April 2019*

Citation:
Zhang Y, Luo J, He J, Rong M and Zeng X (2019) JZTX-V Targets the Voltage Sensor in Kv4.2 to Inhibit I_{to} Potassium Channels in Cardiomyocytes. Front. Pharmacol. 10:357. doi: 10.3389/fphar.2019.00357

INTRODUCTION

Potassium channels play important roles in cellular signaling processes in both excitable and non-excitable cells. Voltage-gated K^+ channels containing the central pore domain and voltage sensor domains (S1–S4 segments) regulate several fundamental physiological processes, including action potential (AP) repolarization, hormone secretion, and neurotransmitter release (Shieh et al., 2000).

Abbreviations: HaTx, hanatoxin; ICK motif, inhibitor cystine knot motif; JZTX-V, tarantula toxin jingzhaotoxin-V; KChIP, Kv4 channel-interacting protein; WT, wild type.

The voltage-gated Kv4 channel expressed in most mammalian cardiomyocytes plays a pivotal role in initial rapid repolarization (phase 1) and determines the amplitudes, and duration of cardiac AP by carrying the transient outward K^+ current I_{to} (Stones et al., 2009). Moreover, I_{to} indirectly affects membrane repolarization by interfering with the subsequent ion currents, I_{Ca}, I_{Kr}, and I_{Ks}, at phases 2 and 3 (Yue et al., 1997). Considering the critical involvement of I_{to} in action potential duration (APD), inhibitors of Kv4 channels have been reported to act as anti-arrhythmic agents via an ionic mechanism (Feng et al., 1997; Ma et al., 2015).

Animal toxins are important resources for the development of new therapeutic drugs due to their high selectivity and specificity for molecular targets (Zambelli et al., 2016). ω-conotoxin MVIIA (named Ziconotide) obtained from snail *Conus magus* was the first marine-derived drug produced in 2004 (Molinski et al., 2009). Eptifibatide extracted from venom of *Sistrurus miliarius barbourin* is effectively used for treatment of acute coronary syndromes (Tcheng and O'Shea, 1999; Zambelli et al., 2016). Exenatide, a peptide from *lizard Heloderma suspectum*, is currently used for treatment of type 2 diabetes (Goud et al., 2015). Spider venom contains peptide toxins targeting ion channels, making it a valuable resource for several potential therapeutic applications (Peng et al., 2017). For example, Lycosin-II and Lycosin-I, the peptide toxins from *Lycosa singoriensis* display high antibacterial activity against multidrug-resistant *Acinetobacter baumannii* (Wang et al., 2014, 2016). mu-TRTX-Hhn1b (HNTX-IV) from *Ornithoctonus hainana* and Huwentoxin-XVI from *O. huwena* exert analgesic effects against inflammatory and neuropathic pain by specifically inhibiting the voltage-gated Nav1.7 channel (Liu et al., 2014), and N-type calcium channel (Deng et al., 2014), respectively. Recent experiments have further demonstrated that Lycosin-I has vasodilator and hypotensive effects (Ma et al., 2018).

Jingzhaotoxin-V (JZTX-V), a 29-residue peptide isolated from venom of the Chinese tarantula *Chilobrachys jingzhao*, effectively inhibits the transient outward potassium channels in dorsal root ganglion neurons of adult rats while barely affecting the currents of outward delay rectifier potassium channels (Yuan et al., 2007; Zeng et al., 2007). However, the specific effects of this peptide on cardiomyocyte function remain to be established. In the current study, we have focused on the effects of JZTX-V on the I_{to} current and APD in neonatal rat ventricular myocytes (NRVM) and the mechanism of JZTX-V binding to the Kv4.2 channel. Our results collectively support the utility of JZTX-V as a potential novel antiarrhythmic drug.

MATERIALS AND METHODS

JZTX-V Synthesis

Jingzhaotoxin-V and its mutants were synthesized using a solid-phase chemical approach with Fmoc-protected amino acids. The synthetic peptides were purified by reverse-phase HPLC and then subjected to oxidative refolding under the optimal conditions as previously described (Huang et al., 2014). The peptide toxins were used in laboratory only and the hazardous wastes were collected and sent for centralized treatment by Hunan Normal University.

Ventricular Myocyte Isolation

Neonatal rat ventricular myocytes cells were obtained from ventricles of neonatal Sprague–Dawley rats as previously reported (Sung et al., 2012; Yan et al., 2018). SD rats (Hunan SJA Laboratory Animal Co., Ltd., Changsha, China) were used according to the guidelines of the National Institutes of Health for Care and Use of Laboratory Animals. The experiments were approved by the Animal Care and Use Committee of Hunan Normal University.

Collection of the Venom

The venom from adult female *Jingzhao* spiders was collected by using an electro-pulse stimulator as previous described (Rong et al., 2011). The venom was used in laboratory only and the hazardous wastes were collected and sent for centralized treatment by Hunan Normal University.

Circular Dichroism (CD)

30 μM synthetic JZTX-V and its mutants were used for the CD spectra from 260 to 190 nm using a Jasco J-725 spectropolarimeter (Jasco, Osaka, Japan) as previous describe (Rong et al., 2011).

Expression of Kv4 Channels

Human embryonic kidney cell line (HEK293T) was obtained from Shanghai Institute of Cell Biology, Chinese Academy of Sciences (Shanghai, China) and maintained with 5% CO_2 at 37°C in DMEM supplemented with 10% heat-inactivated fetal calf and serum (FBS), penicillin (100 U/ml), and streptomycin (100 μg/ml). The WT/mutant Kv4.2 plasmids were transiently transfected into HEK293T by Lipofectamine^{TM} 2000 Reagent (Invitrogen), and the KChIP2 subunits were co-transfected with Kv4.2. The Kv4.2 mutations were constructed using the GeneTailor^{TM} Site-Directed Mutagenesis System (Invitrogen, Carlsbad, CA, United States) as previously described (Rong et al., 2011).

Homology Modeling

The DeepView program and Swiss-Model server were used for homology modeling. Three-dimensional models of ScTx1, JZTX-V, and Ctri8557 were obtained basing on ZTX-XI (PDB code 2a2v), PaTx1 (PDB code 1V7F), and Ia2 (PDB code 1lir), respectively.

Patch Clamp Recording and Data Analysis

Whole-cell patch-clamp recordings were performed by an Axon 700B patch-clamp amplifier (Axon Instruments, Irvine, CA, United States) as previous described (Rong et al., 2011). The extracellular buffer and pipette solution for AP, I_{to}, and Kv4.2 were used as follows.

The APs, Pipette solution contained (mM) 120 KCl, 1 $MgCl_2$, 10 EGTA, 10 Hepes, and 3 MgATP (pH = 7.4). The extracellular

buffer contained (mM) 140 NaCl, 5.4 KCl, 1.3 $CaCl_2$, 0.5 $MgCl_2$, 5 Hepes, and 5.5 glucose (pH = 7.4).

I_{to} currents, The Ca^{2+}-currents blocker $CdCl_2$ (200-μmol/L) were used in external solutions. To generate I_{to1} current, cells were held at −40 mV to inactivate the fast Na^+ current and then stepped to potentials of −40 mV to +60 mV in 10-mV increments. For the inhibition of JZTX-V on I_{to1}, I_{to1} current were elicited by +30 mV depolarizing voltage from a holding potential of −40 mV.

Kv4.2 current, The pipette solution contained (mM) 140 KF, 5 ATP-2Na, 1 EGTA, and 10 HEPEs (pH = 7.4). The external solution contained (mM) 137 NaCl, 5.9 KCl, 2.2 $CaCl_2$, 1.2 $MgCl_2$, 14 glucose, and 10 HEPEs (pH = 7.4). The Kv4.2 currents were elicited by a 300-ms depolarizing voltage of 10 mV from a holding potential of −80 mV. The steady-state activation of Kv4.2 was measured with the holding potential −80 mV and applied from −80 mV to 70 mV (10-mV increments). Steady-state inactivation of Kv4.2 channel measured with a series of a 300-ms depolarizing test potential of 10 mV followed a 1000-ms prepulse at potentials ranging from −120 to +70 mV with a 5-mV increment.

Data were analyzed using the clampfit (Axon) and Origin 9 software programs. All data points are shown as mean SEM. The significance was estimated using unpaired two-tailed *t*-tests, and a $P < 0.05$ was considered statistically significant. n stands for the number of the separate experimental cells. The IC_{50} value was calculated with Hill logistic equation: $y = 1 - \{(1 - f_{max})/[1 + [(Tx)/IC_{50}]_n\}$. The steady-state activation relationship was measured using Boltzmann function ($f(V) = 1/\{1 + \exp[-(V-V_{1/2})/k]\}^4$). Steady-state inactivation was measured using the Boltzmann function $f(V) = 1/\{1 + \exp[-(V - V_{1/2})/k]\}$.

RESULTS

JZTX-V Inhibits I_{to} and Extends APD in Cardiomyocytes

Jingzhaotoxin-V, an inhibitor cystine knot (ICK)-gating modifier, blocks A-type potassium channels in DRG cells with an IC_{50} value of 52.3 nM (Zeng et al., 2008). Based on this finding, we speculate that JZTX-V could affect cardiac AP by inhibiting the I_{to} current. The cell capacitance for the NRVM was 18 ± 3.1 pF. Average I–V relation curves of I_{to} in NRVMs normalized to cell capacitance treated with 100 nM JZTX-V. As shown in **Figure 1A**, JZTX-V at a concentration of 100 nM inhibited the I_{to1} current of NRVMs by 78 ± 4.32% at 30 mV (N = 4). For the AP of NRVMs (at 1 Hz), resting membrane potential was −70 ± 2.3 mV and the amplitude was 105 ± 12 mV in control group and the resting membrane potential in control group was −70 ± 2.3 mV, and the amplitude was 109 ± 12.3 mV. Although JZTX-V treatment modifies the amplitude of the AP, the difference was no statistically significant. JZTX-V (100 nM) prolonged the APD_{10} (123.53 ± 4.23%; APD_{50}, 124.34 ± 3.17%; and APD_{90}, 126.26 ± 3.23%), compared with that in the vehicle-treated group, but did not affect APD_{10-50}, and APD_{50-90} to a significant extent (N = 5; **Figure 1B**).

Effect of JZTX-V on the Kv4.2 Current

Kv4.2 is a cloned channel believed to underlie the I_{to} current in NRVMs. Here, the I_{to} current was recorded in HEK293t cells transfected with vectors co-expressing the Kv4.2 and KChIP2 subunits. As shown in **Figure 2A**, 10 nM JZTX-V induced a significant reduction in peak amplitude of the control potassium current by a maximum of 42.8 ± 8.2% (N = 7) and 100 nM JZTX-V inhibited the potassium current over 90% (N = 7). These inhibitory effects were concentration-dependent, with a half-maximal inhibitory concentration (IC_{50}) value of 13 ± 1.7 nM (**Figure 2B**; N = 7). Moreover, addition of JZTX-V (10 nM) led to alterations in the G–V curve of the Kv4.2 potassium channel. $V_{1/2}$ values were +20 mV and +30 mV in the absence and presence of JZTX-V, respectively (**Figure 2C**). During the steady-state inactivation process, 10 nM JZTX-V induced a slight shift in the Kv4.2 current with a half-maximal inactivation potential ($V_{in1/2}$) shift in the hyperpolarizing direction by 4.5 mV (from −44.5 to −50.0 mV) (**Figure 2D**).

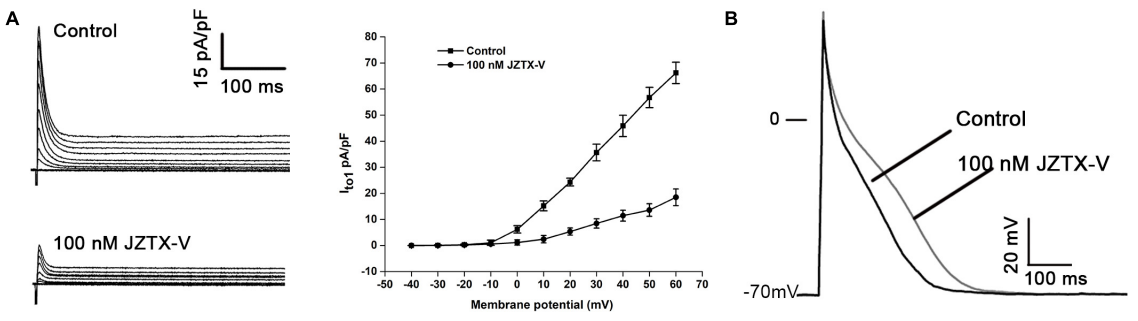

FIGURE 1 | Jingzhaotoxin-V inhibits I_{to} and extended APD in NRVMs isolated from SD rats. **(A)** Representative traces of I_{to} in NRVMs treated with 100 nM JZTX-V. The cell capacitance for the NRVM was 18 ± 3.1 pF. Average I–V relation curves of I_{to} in NRVMs normalized to cell capacitance treated with 100 nM JZTX-V. **(B)** Representative traces of action potential recorded in NRVMs treated with 100 nM JZTX-V. For the AP of NRVMs Treatment with the JZTX-V prolonged APD_{10} from 12 ± 1 ms to 15 ± 1.7 ms, APD_{50} from 88 ± 6 ms to 109 ± 8 ms, APD_{90} from 245 ± 7 ms to 309 ± 10 ms.

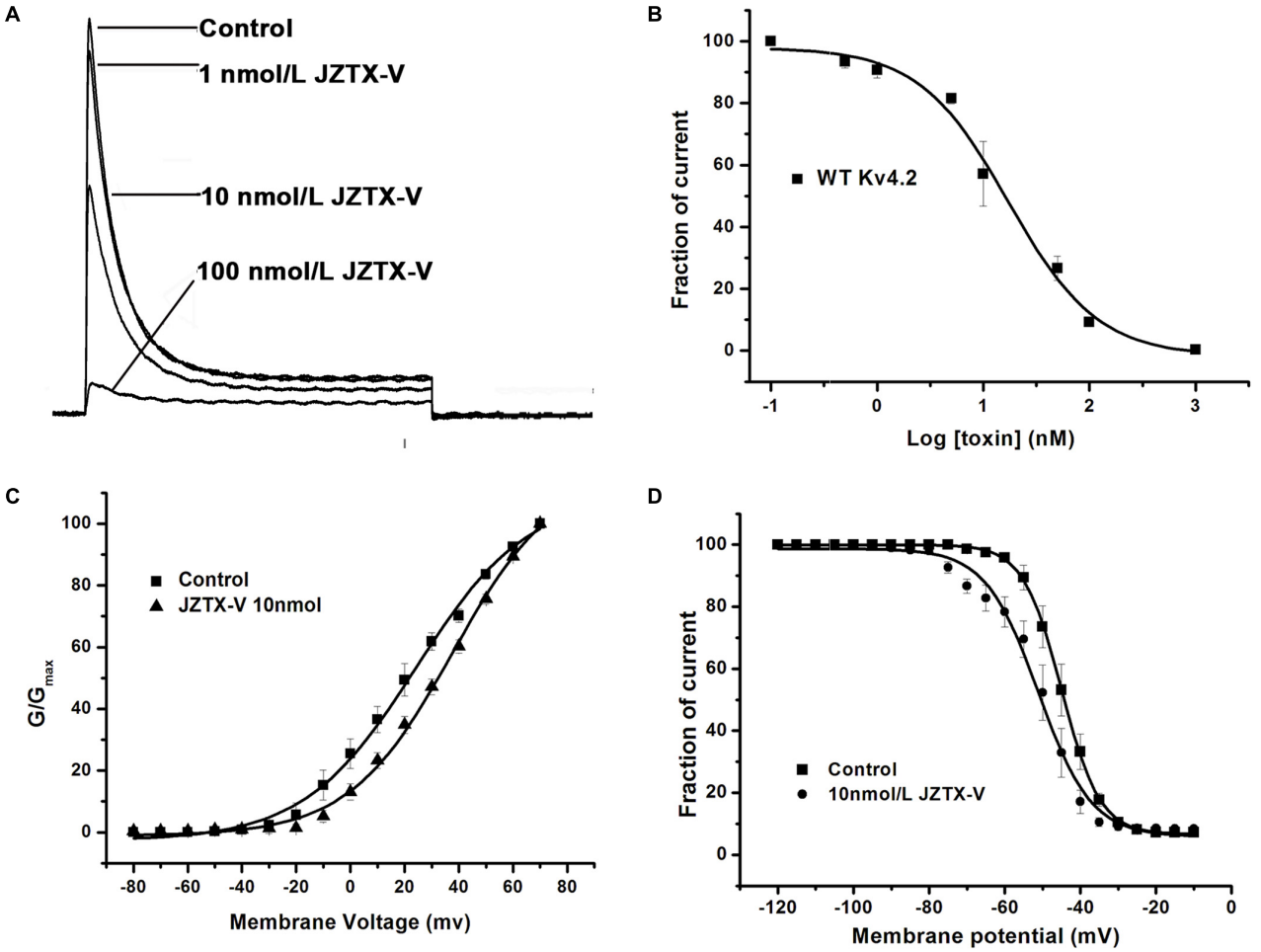

FIGURE 2 | Effects of JZTX-V on WT Kv4.2-kchip2 expressed in HEK293T cells. **(A)** Kv4.2 current traces. Data are normalized to the maximum peak current amplitude. **(B)** The concentration-dependent inhibition of WT Kv4.2 channel by JZTX-V. Data points (mean±SE) were fit with the Hill equation as described under the Section "Materials and Methods." **(C,D)** Effects of the JZTX-V on normalized steady-state activation and inactivation of WT Kv4.2.

Inhibitory Activity of JZTX-V on Kv4.2 Mutants

The majority of peptide toxins are reported to interact with linkers of transmembrane helices S3 and S4 in the Kv4 channel as gating modifiers (Ebbinghaus et al., 2004; DeSimone et al., 2009; Yuan et al., 2012; Xie et al., 2014). JZTX-V showed strong affinity for the Kv4 channel but low gating modification function. To elucidate the mechanism underlying JZTX-V binding to Kv4.2, the amino acid residues in the S1–S2 linker (**Figure 3A**) and S3b–S4 linker (**Figure 4A**) of Kv4.2 were mutated to Ala using the alanine scanning technique. Sequence comparisons revealed more positively charged residues (Arg) on the S1–S2 linker of Kv4.1 relative to Kv4.2, and Kv4.3 (**Figure 3A**). As shown in **Figures 3B,C**, all mutants displayed only a slight decrease in JZTX-V binding affinity, suggesting that the S1–S2 linker of Kv4.2 does not play a key role in JZTX-V-mediated inhibition. Alanine scanning on the S3b–S4 led to the identification of five component residues (Ile275, Leu277, Val285, Phe289, and Val290) critical for JZTX-V binding (**Figures 4B,C**). Mutation of Val285, Phe289, and Val290 reduced sensitivity to the toxin by ∼7-, 11-, and 12-fold with IC_{50} values of 88.6 ± 3.2, 141.2 ± 7.1, and 158.2 ± 5.9 nM, respectively ($N = 6$). Interestingly, two Kv4.2 mutants, Ile275A and Leu277A, displayed markedly increased affinity for JZTX-V (∼10- and 20-fold, respectively). Because Val has similar hydrophobic properties but a shorter β-carbon chain than Leu, we additionally mutated Leu277 to Val. Kv4.2 inhibited L277V mutation with an IC_{50} value of 6.3 nM. Based on the collective findings, we proposed that JZTX-V docked at the S3b–S4 linker of Kv4.2 and the hydrophobic amino acids within the S3b–S4 segment were potentially critical for toxin-mediated inhibition. In contrast to HaTx (Swartz and MacKinnon, 1997) and other well characterized ICK toxins, JZTX-V binding did not appear to require a charged amino acid.

Effects of JZTX-V Mutants on Kv4.2 Binding

Jingzhaotoxin-V contains a large hydrophobic patch comprising three aromatic and two aliphatic residues, which may be

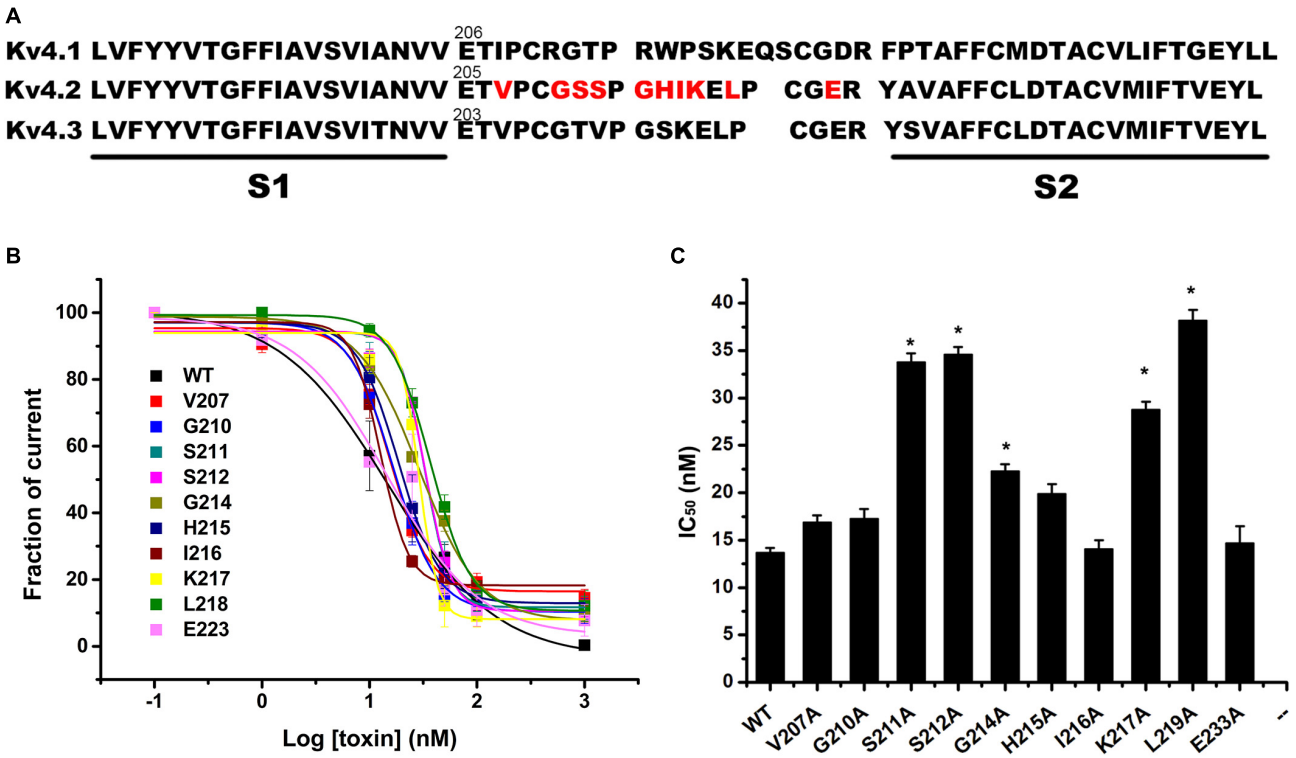

FIGURE 3 | Inhibition effects of site mutants in the S1–S2 linker of Kv4.2 by JZTX-V. **(A)** Sequence alignment of S1–S2 regions of Kv4 subfamily a-subunits (Red were used in alanine-scanning mutagenesis). **(B,C)** IC_{50} values on Kv4.2 channel of JZTX-V and analogs. Data shown are the means ±SEM ($N = 5$). *$P < 0.05$ compared with WT group.

responsible for binding to the Kv4.2 S3–S4 linker. Fifteen JZTX-V mutants located on the surface of the three-dimensional structure were efficiently synthesized via alanine screening mutagenesis. The structural integrity of JZTX-V and its mutations was determined by measuring the CD spectrum from 260 to 190 nm in 0.01 M sodium phosphate solution (pH 7.0) at room temperature. CD spectra of the JZTX-V mutants almost overlapped completely with that of wild-type toxin, indicating that the mutations do not induce significant alterations in the secondary structure (**Figure 5**).

Next, we measured the binding affinities of toxin mutants for the WT Kv4.2 channel expressed in HEK293 cells (**Figure 6A**). The concentration-dependent curves and estimated IC_{50} values are shown in **Figures 6B,C**. Alanine replacement of three hydrophobic residues (Trp5, Met6, and Trp7) reduced binding affinity of the toxin by 14-, 24-, and 13-fold, respectively. Surprisingly, mutation of two positively charged residues (R20A and K22A) reduced the toxin binding affinity for Kv4.2 by 15- and 9-fold, respectively. However, the IC_{50} values of other mutants were similar to that of wild-type JZTX-V, suggesting no major involvement of these residues in JZTX-V interactions with Kv4.2 ($N = 6$). These results collectively indicated that positively charged residues (R20 and K22) and an exposed hydrophobic patch formed by W5, M6, and W7 of JZTX-V comprised a functional surface for binding the Kv4.2 channel (**Figure 6D**).

DISCUSSION

The Kv4 channels are predominantly located in the heart and central nervous system. In ventricular myocytes of the majority of mammals, Kv4 channels are responsible for the fast recovering transient outward K^+ current (I_{to}) (Tamargo et al., 2004), which plays pivotal roles in the amplitudes and duration of cardiac AP. Inhibitors of Kv4 channels act as anti-arrhythmic drugs via an ionic mechanism (Feng et al., 1997; Ma et al., 2015). In this study, we examined the effects of JZTX-V on the I_{to} current and AP of cardiomyocytes and the potential underlying mechanisms.

Animal toxins target ion channels, and are thus valuable resources with potential therapeutic applications. The Kv4 subfamily from scorpion (Maffie et al., 2013; Xie et al., 2014) and spider venom (Escoubas et al., 2002; Ebbinghaus et al., 2004; Yuan et al., 2007, 2012; DeSimone et al., 2009) has a rich toxin pharmacology. HaTx, originally isolated from venom of the Chilean rose tarantula (*Grammostola spatulata*), inhibits Kv4.2 channels effectively, with similar affinity for Kv2.1 (Swartz and MacKinnon, 1995; Swartz, 2007). Other Kv4 channel inhibitors, Stromatoxin (ScTx1) from *Stromatopelma calceata* and heteroscodratoxins (HmTx1,2) from *Heteroscodra maculata,* are also reported to target Kv2 channels (Escoubas et al., 2002). The Kv4 channel gating-modifying toxin, Ctri9577, is also able to inhibit Kv1.3 potassium channels (Xie et al., 2014). Moreover, heteropodatoxins (HpTx1-3) from

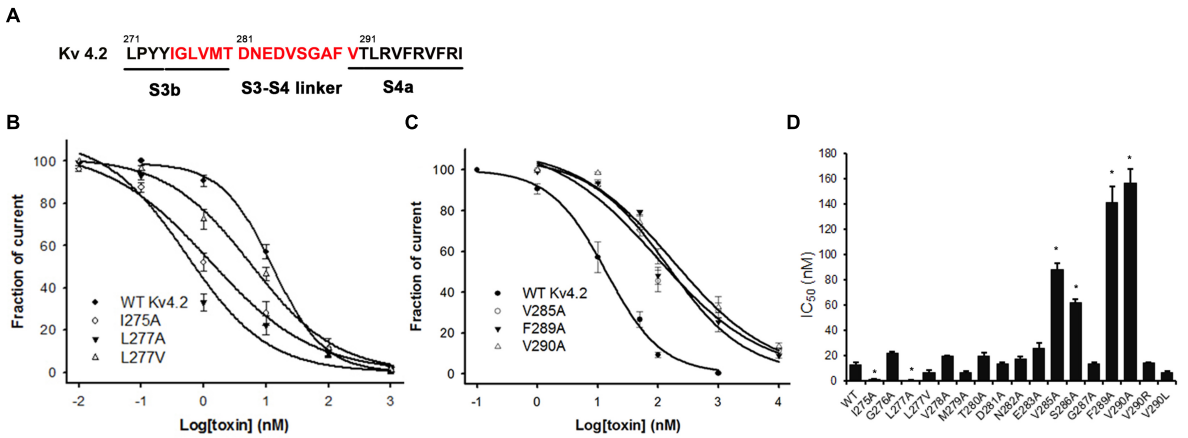

FIGURE 4 | Inhibition effects of site mutants in the S3b and S3–S4 linker of Kv4.2 by JZTX-V. **(A)** S3b–S4 regions of Kv4.2. Red amino acids are those used in alanine-scanning mutagenesis site mutants on the S3b and S3–S4 linker. **(B)** Concentration-response curves for JZTX-V acted on WT-Kv4.2 and the mutants I275A, L277A, and L277V significantly increase affinity to JZTX-V. **(C)** Hydrophobic residues mutants V285A, F289A, and V290A lose affinity to JZTX-V. **(D)** IC_{50} values on S3–S4 linker of Kv4.2 channel mutants of JZTX-V. $^*P < 0.05$ compared with WT group.

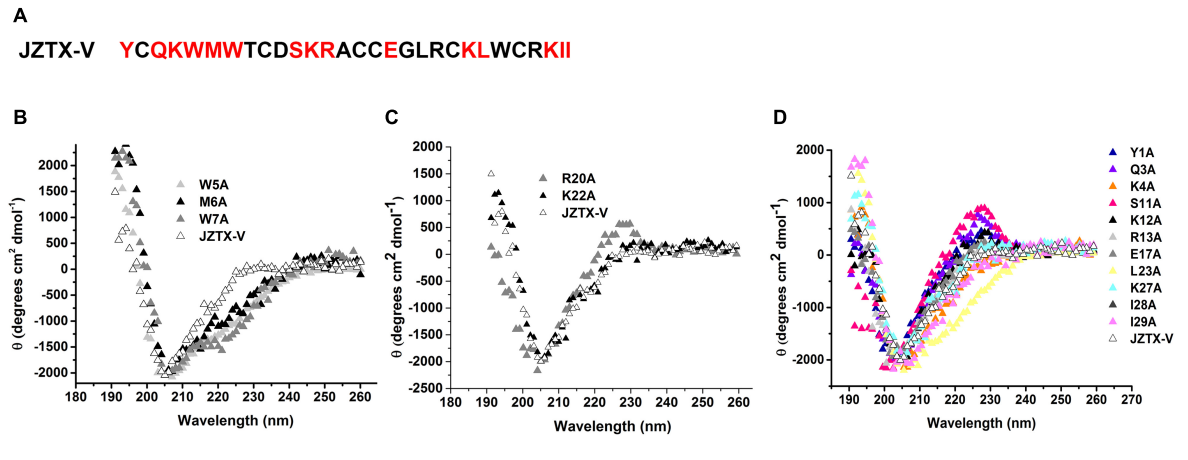

FIGURE 5 | Sequence and CD spectra of JZTX-V. **(A)** Amino acid sequence of JZTX-V and its mutant residues are shaded. **(B–D)** Comparison of the CD spectrum of JZTX-V and mutants with the critical hydrophobic residues **(B)**, and charged residues **(C)**, and other mutants **(D)**.

Heteropoda venatoria (Sanguinetti et al., 1997; Zarayskiy et al., 2005; Desimone et al., 2011), phrixotoxins (PaTx1,2) from *Phrixotrichus auratus* (Diochot et al., 1999), and TLTx1-3 from *Theraphosa blondi* venom (Ebbinghaus et al., 2004) primarily target Kv4 channels, but with IC_{50} values of >100 nM. Therefore, toxins that can effectively and specifically inhibit Kv4.2 are yet to be identified. Previous studies by our group demonstrated that JZTX-V selectively inhibits the Kv4.2 current and displays markedly lower affinity for other potassium channels (Zeng et al., 2007, 2008). In the present investigation, JZTX-V was determined as an efficient inhibitor of Kv4.2 channels (IC_{50} and 13 nM). Under the same set of calculation parameters, ScTx1 is the most potent inhibitor known for Kv4.2 channels with an IC_{50} value of 1.2 nM. However, the selectivity of ScTx1 is far from absolute as it also inhibits Kv2.1 channel with strong affinity (IC_{50} and 12.7 nM; **Supplementary Table S1**). Furthermore, we have shown for the first time that JZTX-V effectively inhibited the I_{to} current and extended the APD of NRVM. Our results indicated that JZTX-V acted as an efficient and highly selective inhibitor of the Kv4.2 channel, supporting its utility in the treatment of cardiac disorders.

Voltage sensor trapping is the mechanism underlying the modification effects of animal toxins on voltage-dependent gating potassium channels (Wang et al., 2004; Catterall et al., 2007; Swartz, 2007). Several channel mutagenesis studies have shown that toxin binding sites are often complex and involve either a combination of charged and hydrophobic amino acids or charged interactions alone (Swartz, 2007; Zhang et al., 2007; Bosmans et al., 2008). However, only hydrophobic contacts detected in the S3b–S4 linker of Kv4 have been shown to be crucial for channel interactions (DeSimone et al., 2009; Xie et al., 2014). JZTX-V is part of a growing list of peptide-gating modifier toxins that interact with the outer portion of S3b or the S3–S4 linker of voltage-gated ion channels. As shown in

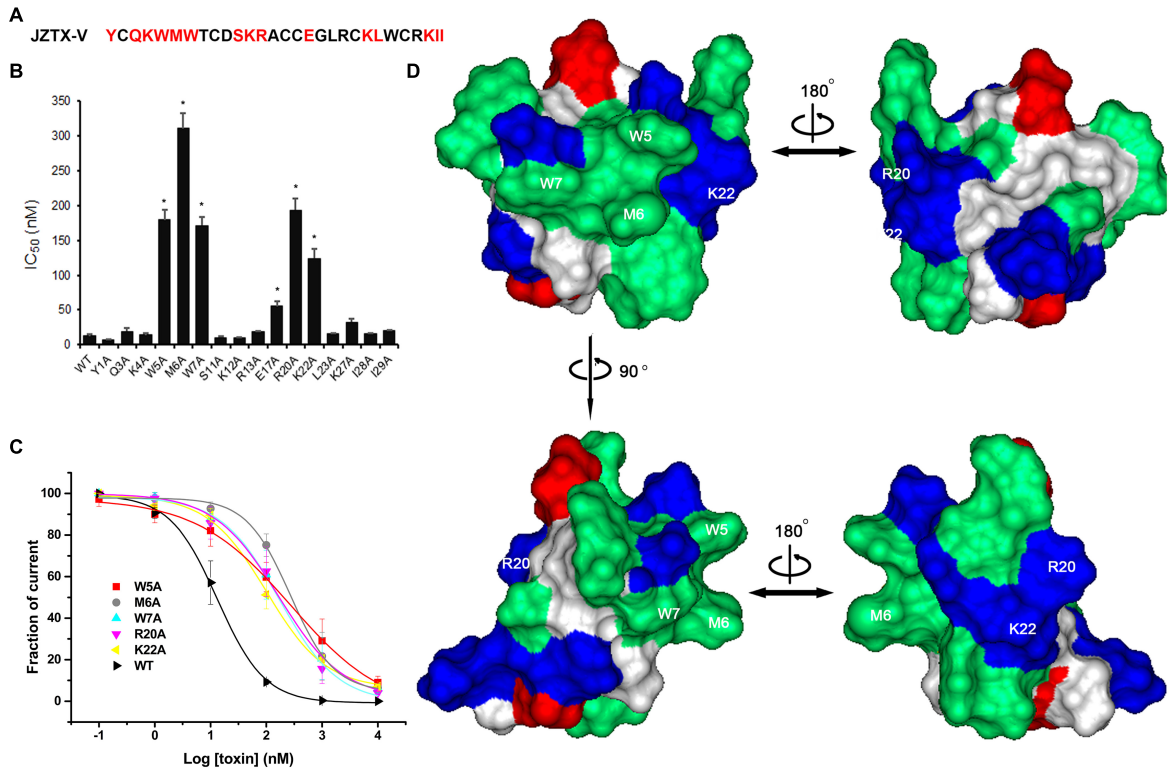

FIGURE 6 | Effects of JZTX-V and analogs on Kv4.2 current. Inhibitory activity of JZTX-V and mutants on Kv4.2 channel. **(A)** the residues mutated to Ala are shaded in red. **(B)** IC_{50} values on Kv4.2 channel of JZTX-V and analogs. **(C)** concentration dependence for the inhibition of five JZTX-V mutants (W5A, M6A, W7A, R20A, and K22A) on Kv4.2. **(D)** bioactive surface profile of JZTX-V binding to Kv4.2. The left and right structures were rotated 180° relative to one another about a vertical axis. $*P < 0.05$ compared with WT group.

Figure 4, the hydrophobic patch formed by V285, F289, and V290 within the S3–S4 linker is critical for interactions with JZTX-V. However, although the toxin binding motifs are structurally conserved, divergence with regard to the composition and arrangement of crucial residues in the voltage sensor were observed (**Supplementary Figure S2A**). For example, L274 and V275 in the S3b region of Kv4.3 are crucial determinants for binding to toxins PaTx2 and Ctr9577 (Wang et al., 2007; DeSimone et al., 2009). V288 on Kv4.3 promotes binding to Ctri9577 but not PaTx1. Unexpectedly, hydrophobic I275 and L277 within S3b of the Kv4 channel, seem to be a common binding site for PaTx2 and Ctr9577, observed the opposite role for interactions with JZTX-V. Interestingly, alanine mutants (I275A and L277A) of Kv4.2 increased the affinity for JZTX-V by 10- and 20-fold, respectively. N280 and E281 play similar roles in interactions between toxin and the Kv4.3 channel, and mutation of these residues to Ala promoted binding of HpTx2 and Ctri9577 toxins to Kv4.3. However, the reason for the observed increase in binding affinity is unclear. One possibility is limitations for the introduction of secondary conformational and physiochemical changes (DeSimone et al., 2009). Interestingly, Ctri9577 exerts similar potency as PaTx1, although alanine mutants (N280A) of the Kv4.3 channel display decreased Ctri9577 affinity and the E281A mutant shows higher Ctri9577 sensitivity. The results indicated that diverse toxins use partially overlapping bioactive surfaces to target the S3b–S4 linker of the Kv4 channel. On the one hand, hydrophobic interactions are common and improve toxin binding to Kv4, and on the other hand, the steric effects of several residues on S3–S4 linker disrupt the binding of toxins owing to diverse three-dimensional structures.

Toxins bound to Kv4 channels show a highly conserved three-dimensional structure. One of the striking structural features of voltage sensor toxins is their amphipathic nature (**Supplementary Figure S2B**), with one face containing a cluster of hydrophobic residues (green) that exhibit an unusually high degree of solvent exposure surrounded by basic (blue), acidic (red), and other highly polar residues. Although the overall fold and amphipathic nature of the voltage sensor toxins are similar, a number of differences exist, in particular for residues comprising the hydrophobic surface. As shown in **Supplementary Figure S2B**, four blockers of Kv4 channels, HpTx (1,2), ScTx1, and TLTx1, show low sequence similarity with JZTX-V but contain a common hydrophobic surface. In HaTx1, the hydrophobic surface comprises Y4, L5, F6, Y27, and W30, with Y4, F6, and W30 forming an aromatic sandwich around L5 (**Supplementary Figure S2B**). Four hydrophobic residues, W30, M5, F6, and Y7, forming the hydrophobic surface of ScTx1 are located in a straight line. The structure of HpTx1 is similar to that of HaTx1, with L6, F7, W25, and L28 occupying positions equivalent to L5, F6, Y27, and W30, respectively. HpTx2 lacks

the equivalent of Y4 in HaTx1 but contains three additional hydrophobic residues (W30, Y20, and V21) that contribute to the solvent-exposed hydrophobic surface. As shown in **Supplementary Figure S1**, PaTx1 and PaTx2 show high sequence similarity to JZTX-V and share the same hydrophobic surface encompassing W5, M6, W7, and W24 (**Supplementary Figure S2B**). Alanine scanning mutagenesis of JZTX-V has provided an essentially complete map of the functionally important surfaces of the toxin. The active face of the toxin contains the solvent-exposed hydrophobic surface, which is involved in interactions with the Kv4.2 channel. These findings validated the theory that hydrophobic force plays an important role in toxin binding to Kv4 channels. The active hydrophobic surface of SGTx provides residues that interact with the Kv channel (Wang et al., 2004). Ctri9577, a novel toxin from scorpion *Chaerilus tricostatus* containing few hydrophobic residues, shows lower affinity for Kv4.2 than other toxins, with an IC_{50} value of 1.34 μM (**Supplementary Table S1**). Although studies on channel toxins have highlighted the importance of protein-protein interactions in toxin binding to voltage-activated channels, it is also possible that lipids constitute an important part of the toxin receptor (Lee et al., 2003; Schmidt and MacKinnon, 2008; Swartz, 2008). JZTX-V contains four basic residues (K4, R20, K22, and R26) positioned on the side of hydrophobic patch and two basic residues (R13 and K26) on the opposite surface. Phospholipid membrane binding experiments reveal that basic residues in the functionally important surface of JZTX-V interact with negatively charged phospholipids (Zeng et al., 2007). Alanine mutants of basic residues (R20 and K22) decreased the toxin binding affinity by 15- and 9-fold, respectively. We speculate that electrostatic interactions mediated by R20 and K22 of JZTX-V are involved in binding to phospholipid membranes. In contrast to the results obtained for other spider toxins, mutation of acid residues failed to alter the affinity of toxin for Kv4.2 (Cohen et al., 2005; Rong et al., 2011).

CONCLUSION

In conclusion, JZTX-V effectively inhibited the I_{to} current and extended theAPD. The molecular mechanism underlying the inhibitory action of JZTX-V on I_{to} may involve recognition of a conserved binding motif on the S3–S4 linker. Hydrophobic force plays an important role in interactions between the toxin and channel, and the extracellular conformational space of Kv4 modulates toxin affinity. Moreover, the phospholipid membrane may be involved in binding to toxin. These findings broadened our understanding of the effects of JZTX-V on cardiac electrophysiology and further clarified the molecular mechanisms underlying the inhibitory action of JZTX-V on I_{to} potassium channels, supporting its development as a potential novel antiarrhythmic drug.

ETHICS STATEMENT

SD rats (Hunan SJA Laboratory Animal Co., Ltd., Changsha, China) were used according to the guidelines of the National Institutes of Health for Care and Use of Laboratory Animals. The experiments were approved by the Animal Care and Use Committee of Hunan Normal University.

AUTHOR CONTRIBUTIONS

YZ and JL designed the research. YZ and JH performed the research and contributed new reagents or analytic tools. YZ and MR analyzed the data. YZ and XZ wrote the manuscript.

FUNDING

This work was supported by the National Natural Science Foundation of China (81703149).

ACKNOWLEDGMENTS

We are thankful to Dr. Ying Wang, Meichi Wang, and Zhonghua Liu for knowledge support.

SUPPLEMENTARY MATERIAL

The Supplementary Material for this article can be found online at: https://www.frontiersin.org/articles/10.3389/fphar.2019.00357/full#supplementary-material

REFERENCES

Bosmans, F., Martin-Eauclaire, M. F., and Swartz, K. J. (2008). Deconstructing voltage sensor function and pharmacology in sodium channels. *Nature* 456, 202–208. doi: 10.1038/nature07473

Catterall, W. A., Cestele, S., Yarov-Yarovoy, V., Yu, F. H., Konoki, K., and Scheuer, T. (2007). Voltage-gated ion channels and gating modifier toxins. *Toxicon* 49, 124–141. doi: 10.1016/j.toxicon.2006.09.022

Cohen, L., Karbat, I., Gilles, N., Ilan, N., Benveniste, M., Gordon, D., et al. (2005). Common features in the functional surface of scorpion beta-toxins and elements that confer specificity for insect and mammalian voltage-gated sodium channels. *J. Biol. Chem.* 280, 5045–5053. doi: 10.1074/jbc.m408427200

Deng, M., Luo, X., Xiao, Y., Sun, Z., Jiang, L., Liu, Z., et al. (2014). Huwentoxin-XVI, an analgesic, highly reversible mammalian N-type calcium channel antagonist from Chinese tarantula *Ornithoctonus huwena*. *Neuropharmacology* 79, 657–667. doi: 10.1016/j.neuropharm.2014.01.017

DeSimone, C. V., Lu, Y., Bondarenko, V. E., and Morales, M. J. (2009). S3b amino acid substitutions and ancillary subunits alter the affinity of *Heteropoda venatoria* toxin 2 for Kv4.3. *Mol. Pharmacol.* 76, 125–133. doi: 10.1124/mol.109.055657

Desimone, C. V., Zarayskiy, V. V., Bondarenko, V. E., and Morales, M. J. (2011). Heteropoda toxin 2 interaction with kv4.3 and kv4.1 reveals differences in gating modification. *Mol. Pharmacol.* 80, 345–355. doi: 10.1124/mol.111.072405

Diochot, S., Drici, M. D., Moinier, D., Fink, M., and Lazdunski, M. (1999). Effects of phrixotoxins on the Kv4 family of potassium channels and implications for the role of Ito1 in cardiac electrogenesis. *Br. J. Pharmacol.* 126, 251–263. doi: 10.1038/sj.bjp.0702283

Ebbinghaus, J., Legros, C., Nolting, A., Guette, C., Celerier, M. L., Pongs, O., et al. (2004). Modulation of Kv4.2 channels by a peptide isolated from the venom of the giant bird-eating tarantula *Theraphosa leblondi*. *Toxicon* 43, 923–932. doi: 10.1016/j.toxicon.2003.12.012

Escoubas, P., Diochot, S., Celerier, M. L., Nakajima, T., and Lazdunski, M. (2002). Novel tarantula toxins for subtypes of voltage-dependent potassium channels in the Kv2 and Kv4 subfamilies. *Mol. Pharmacol.* 62, 48–57. doi: 10.1124/mol.62.1.48

Feng, J., Wang, Z., Li, G. R., and Nattel, S. (1997). Effects of class III antiarrhythmic drugs on transient outward and ultra-rapid delayed rectifier currents in human atrial myocytes. *J. Pharmacol. Exp. Ther.* 281, 384–392.

Goud, A., Zhong, J., and Rajagopalan, S. (2015). Emerging utility of once-weekly exenatide in patients with type 2 diabetes. *Diabetes Metab. Syndr. Obes.* 8, 505–512. doi: 10.2147/DMSO.S69354

Huang, P., Zhang, Y., Chen, X., Zhu, L., Yin, D., Zeng, X., et al. (2014). The activation effect of hainantoxin-I, a peptide toxin from the Chinese spider, *Ornithoctonus hainana*, on intermediate-conductance Ca2+-activated K+ channels. *Toxins* 6, 2568–2579. doi: 10.3390/toxins6082568

Lee, H. C., Wang, J. M., and Swartz, K. J. (2003). Interaction between extracellular Hanatoxin and the resting conformation of the voltage-sensor paddle in Kv channels. *Neuron* 40, 527–536. doi: 10.1016/s0896-6273(03)00636-6

Liu, Y., Tang, J., Zhang, Y., Xun, X., Tang, D., Peng, D., et al. (2014). Synthesis and analgesic effects of mu-TRTX-Hhn1b on models of inflammatory and neuropathic pain. *Toxins* 6, 2363–2378. doi: 10.3390/toxins6082363

Ma, B., Xi, Z., Li, J., Gao, T., Liao, R., Wang, S., et al. (2018). Vasodilator and hypotensive effects of the spider peptide Lycosin-I in vitro and in vivo. *Peptides* 99, 108–114. doi: 10.1016/j.peptides.2017.12.011

Ma, S. F., Luo, Y., Ding, Y. J., Chen, Y., Pu, S. X., Wu, H. J., et al. (2015). Hydrogen sulfide targets the Cys320/Cys529 motif in Kv4.2 to inhibit the ito potassium channels in cardiomyocytes and regularizes fatal arrhythmia in myocardial infarction. *Antioxid. Redox Signal.* 23, 129–147. doi: 10.1089/ars.2014.6094

Maffie, J. K., Dvoretskova, E., Bougis, P. E., Martin-Eauclaire, M. F., and Rudy, B. (2013). Dipeptidyl-peptidase-like-proteins confer high sensitivity to the scorpion toxin AmmTX3 to Kv4-mediated A-type K+ channels. *J. Physiol.* 591(Pt 10), 2419–2427. doi: 10.1113/jphysiol.2012.248831

Molinski, T. F., Dalisay, D. S., Lievens, S. L., and Saludes, J. P. (2009). Drug development from marine natural products. *Nat. Rev. Drug Discov.* 8, 69–85. doi: 10.1038/nrd2487

Peng, X., Dai, Z., Lei, Q., Liang, L., Yan, S., and Wang, X. (2017). Cytotoxic and apoptotic activities of black widow spiderling extract against HeLa cells. *Exp. Ther. Med.* 13, 3267–3274. doi: 10.3892/etm.2017.4391

Rong, M., Chen, J., Tao, H., Wu, Y., Jiang, P., Lu, M., et al. (2011). Molecular basis of the tarantula toxin jingzhaotoxin-III ({beta}-TRTX-Cj1{alpha}) interacting with voltage sensors in sodium channel subtype Nav1.5. *FASEB J.* 25, 3177–3185. doi: 10.1096/fj.10-178848

Sanguinetti, M. C., Johnson, J. H., Hammerland, L. G., Kelbaugh, P. R., Volkmann, R. A., Saccomano, N. A., et al. (1997). Heteropodatoxins: peptides isolated from spider venom that block Kv4.2 potassium channels. *Mol. Pharmacol.* 51, 491–498.

Schmidt, D., and MacKinnon, R. (2008). Voltage-dependent K+ channel gating and voltage sensor toxin sensitivity depend on the mechanical state of the lipid membrane. *Proc. Natl. Acad. Sci. U.S.A.* 105, 19276–19281. doi: 10.1073/pnas.0810187105

Shieh, C. C., Coghlan, M., Sullivan, J. P., and Gopalakrishnan, M. (2000). Potassium channels: molecular defects, diseases, and therapeutic opportunities. *Pharmacol. Rev.* 52, 557–594.

Stones, R., Billeter, R., Zhang, H., Harrison, S., and White, E. (2009). The role of transient outward K+ current in electrical remodelling induced by voluntary exercise in female rat hearts. *Basic Res. Cardiol.* 104, 643–652. doi: 10.1007/s00395-009-0030-6

Sung, D. J., Kim, J. G., Won, K. J., Kim, B., Shin, H. C., Park, J. Y., et al. (2012). Blockade of K+ and Ca2+ channels by azole antifungal agents in neonatal rat ventricular myocytes. *Biol. Pharm. Bull.* 35, 1469–1475. doi: 10.1248/bpb.b12-00002

Swartz, K. J. (2007). Tarantula toxins interacting with voltage sensors in potassium channels. *Toxicon* 49, 213–230. doi: 10.1016/j.toxicon.2006.09.024

Swartz, K. J. (2008). Sensing voltage across lipid membranes. *Nature* 456, 891–897. doi: 10.1038/nature07620

Swartz, K. J., and MacKinnon, R. (1995). An inhibitor of the Kv2.1 potassium channel isolated from the venom of a *Chilean tarantula*. *Neuron* 15, 941–949. doi: 10.1016/0896-6273(95)90184-1

Swartz, K. J., and MacKinnon, R. (1997). Mapping the receptor site for hanatoxin, a gating modifier of voltage-dependent K+ channels. *Neuron* 18, 675–682. doi: 10.1016/s0896-6273(00)80307-4

Tamargo, J., Caballero, R., Gomez, R., Valenzuela, C., and Delpon, E. (2004). Pharmacology of cardiac potassium channels. *Cardiovasc. Res.* 62, 9–33. doi: 10.1016/j.cardiores.2003.12.026

Tcheng, J. E., and O'Shea, J. C. (1999). Eptifibatide: a potent inhibitor of the platelet receptor integrin, glycoprotein IIb/IIIa. *Expert. Opin. Investig. Drugs* 8, 1893–1905. doi: 10.1517/13543784.8.11.1893

Wang, J. M., Roh, S. H., Kim, S., Lee, C. W., Kim, J. I., and Swartz, K. J. (2004). Molecular surface of tarantula toxins interacting with voltage sensors in K(v) channels. *J. Gen. Physiol.* 123, 455–467. doi: 10.1085/jgp.200309005

Wang, L., Wang, Y. J., Liu, Y. Y., Li, H., Guo, L. X., Liu, Z. H., et al. (2014). In vitro potential of Lycosin-I as an alternative antimicrobial drug for treatment of multidrug-resistant *Acinetobacter baumannii* infections. *Antimicrob. Agents Chemother.* 58, 6999–7002. doi: 10.1128/aac.03279-14

Wang, X. C., Duan, Z. G., Yang, J., Yan, X. J., Zhou, H., He, X. Z., et al. (2007). Physiological and biochemical analysis of L. tredecimguttatus venom collected by electrical stimulation. *J. Physiol. Biochem.* 63, 221–230. doi: 10.1007/bf03165785

Wang, Y., Wang, L., Yang, H., Xiao, H., Farooq, A., Liu, Z., et al. (2016). The spider venom peptide lycosin-II has potent antimicrobial activity against clinically isolated bacteria. *Toxins* 8:E119. doi: 10.3390/toxins8050119

Xie, C., Li, T., Xu, L., Yu, C., Cao, Z., Li, W., et al. (2014). Kv1.3 potassium channel-blocking toxin Ctri9577, novel gating modifier of Kv4.3 potassium channel from the scorpion toxin family. *Biochem. Biophys. Res. Commun.* 444, 406–410. doi: 10.1016/j.bbrc.2014.01.094

Yan, S., Huang, P., Wang, Y., Zeng, X., and Zhang, Y. (2018). The Venom of *Ornithoctonus huwena* affect the electrophysiological stability of neonatal rat ventricular myocytes by inhibiting sodium, potassium and calcium current. *Channels* 12, 109–118. doi: 10.1080/19336950.2018.1449497

Yuan, C., Liu, Z., Hu, W., Gao, T., and Liang, S. (2012). JZTX-XIII, a Kv channel gating modifier toxin from Chinese tarantula *Chilobrachys jingzhao*. *Toxicon* 59, 265–271. doi: 10.1016/j.toxicon.2011.11.021

Yuan, C., Yang, S., Liao, Z., and Liang, S. (2007). Effects and mechanism of Chinese tarantula toxins on the Kv2.1 potassium channels. *Biochem. Biophys. Res. Commun.* 352, 799–804. doi: 10.1016/j.bbrc.2006.11.086

Yue, L., Feng, J., Gaspo, R., Li, G. R., Wang, Z., and Nattel, S. (1997). Ionic remodeling underlying action potential changes in a canine model of atrial fibrillation. *Circ. Res.* 81, 512–525. doi: 10.1161/01.res.81.4.512

Zambelli, V. O., Pasqualoto, K. F., Picolo, G., Chudzinski-Tavassi, A. M., and Cury, Y. (2016). Harnessing the knowledge of animal toxins to generate drugs. *Pharmacol. Res.* 112, 30–36. doi: 10.1016/j.phrs.2016.01.009

Zarayskiy, V. V., Balasubramanian, G., Bondarenko, V. E., and Morales, M. J. (2005). Heteropoda toxin 2 is a gating modifier toxin specific for voltage-gated K+ channels of the Kv4 family. *Toxicon* 45, 431–442. doi: 10.1016/j.toxicon.2004.11.015

Zeng, X., Deng, M., Lin, Y., Yuan, C., Pi, J., and Liang, S. (2007). Isolation and characterization of Jingzhaotoxin-V, a novel neurotoxin from the venom of the

spider *Chilobrachys jingzhao*. *Toxicon* 49, 388–399. doi: 10.1016/j.toxicon.2006.10.012

Zeng, X.-Z., Deng, M.-C., Sun, Z.-H., Wang, X.-C., and Liang, S.-P. (2008). Synthesis, refolding and characterization of JZTX-V and its effect on potassium channels. *Chin. J. Biochem. Mol. Biol.* 24, 463–468.

Zhang, M., Liu, X. S., Diochot, S., Lazdunski, M., and Tseng, G. N. (2007). APETx1 from sea anemone *Anthopleura elegantissima* is a gating modifier peptide toxin of the human ether-a-go-go- related potassium channel. *Mol. Pharmacol.* 72, 259–268. doi: 10.1124/mol.107.035840

Conflict of Interest Statement: The authors declare that the research was conducted in the absence of any commercial or financial relationships that could be construed as a potential conflict of interest.

frontiers in Pharmacology

REVIEW
published: 30 April 2019
doi: 10.3389/fphar.2019.00343

Lynx Prototoxins: Roles of Endogenous Mammalian Neurotoxin-Like Proteins in Modulating Nicotinic Acetylcholine Receptor Function to Influence Complex Biological Processes

Julie M. Miwa, Kristin R. Anderson and Katie M. Hoffman*

Department of Biological Sciences, Lehigh University, Bethlehem, PA, United States

OPEN ACCESS

Edited by:
Annette Nicke,
Ludwig Maximilian University of Munich, Germany

Reviewed by:
Victor I. Tsetlin,
Institute of Bioorganic Chemistry (RAS), Russia
Antonio R. Artalejo,
Universidad Complutense de Madrid, Spain
Ekaterina Lyukmanova,
Institute of Bioorganic Chemistry (RAS), Russia

****Correspondence:***
Julie M. Miwa
jmm312@lehigh.edu

Specialty section:
This article was submitted to Pharmacology of Ion Channels and Channelopathies, a section of the journal Frontiers in Pharmacology

Received: *25 October 2018*
Accepted: *19 March 2019*
Published: *30 April 2019*

Citation:
Miwa JM, Anderson KR and Hoffman KM (2019) Lynx Prototoxins: Roles of Endogenous Mammalian Neurotoxin-Like Proteins in Modulating Nicotinic Acetylcholine Receptor Function to Influence Complex Biological Processes. Front. Pharmacol. 10:343. doi: 10.3389/fphar.2019.00343

The cholinergic system modulates many biological functions, due to the widespread distribution of cholinergic neuronal terminals, and the diffuse release of its neurotransmitter, acetylcholine. Several layers of regulation help to refine and control the scope of this excitatory neurotransmitter system. One such regulatory mechanism is imparted through endogenous toxin-like proteins, prototoxins, which largely control the function of nicotinic receptors of the cholinergic system. Prototoxins and neurotoxins share the distinct three finger toxin fold, highly effective as a receptor binding protein, and the former are expressed in the mammalian brain, immune system, epithelium, etc. Prototoxins and elapid snake neurotoxins appear to be related through gene duplication and divergence from a common ancestral gene. Protein modulators can provide a graded response of the cholinergic system, and within the brain, stabilize neural circuitry through direct interaction with nicotinic receptors. Understanding the roles of each prototoxin (e.g., lynx1, lynx2/lypd1, PSCA, SLURP1, SLURP2, Lypd6, lypd6b, lypdg6e, PATE-M, PATE-B, etc.), their binding specificity and unique expression profile, has the potential to uncover many fascinating cholinergic-dependent mechanisms in the brain. Each family member can provide a spatially restricted level of control over nAChR function based on its expression in the brain. Due to the difficulty in the pharmacological targeting of nicotinic receptors in the brain as a result of widespread expression patterns and similarities in receptor sequences, unique interfaces between prototoxin and nicotinic receptor could provide more specific targeting than nicotinic receptors alone. As such, this family is intriguing from a long-term therapeutic perspective.

Keywords: nicotine, toxins, cholinergic modulation, learning, plasticity

Abbreviations: α-btx, alpha-bungarotoxin; 5-HT_{3A}R, 5-hydroxytryptamine receptors; Aβ, beta-amyloid; AChBP, acetylcholine binding protein; DHβE, dihydro-β-erythroidine; EC_{50}, Effective concentration, 50%; E_{max}, efficacy, maximal response; ERK, Extracellular Signal-regulated Kinase-1; GPI, glycosylphosphatidylinositol; HEK, human embryonic kidney; HS, high sensitivity; KO, knockout; LS, low sensitivity; ly6, lymphocyte antigen 6; Lynx, Ly6/neurotoxin; MEGA, Molecular Evolutionary Genetics Analysis; nAChR, nicotinic acetylcholine receptor; NMR, nuclear magnetic resonance; PATE, prostate and testes expression; PI-PLC, phosphoinositide phospholipase C; PSCA, prostate stem cell antigen; rSLURP, recombinant SLURP; SLURP1, secreted ly6/uPAR-related protein 1; SLURP2, secreted ly6/uPAR-related protein 2; sSLURP, synthetic SLURP; uPAR, urokinase-type plasminogen activator receptors; V1, visual cortex area 1; WTX, weak neurotoxin.

INTRODUCTION

The highly successful toxin fold structure found in many venomous snake toxins also has a counterpart in mammals: prototoxins. Prototoxins are non-venomous proteins with significant similarities to elapid α-neurotoxins, most notably with regard to their cysteine-rich, three-fingered β-fold structure. The mammalian counterparts have 10–12 cysteine residues and the signature motif of 10 cysteines participating in five disulfide bonds stabilizing a β-fold structure. Prototoxins have been found in the brain, epithelium, and immune system, etc. (reviewed in Miwa et al., 2011; Tsetlin, 2015; Vasilyeva et al., 2017). Within the prototoxin family, there are membrane-bound GPI anchored (i.e., lynx1, lynx2, PSCA, etc.) and secreted forms of the protein (i.e., secreted ly6/uPAR related proteins SLURPs) (Yan et al., 1998; Adermann et al., 1999).

Snake toxins employ functional mimicry of pathways operating in the prey. The cloning of a cDNA from the mammalian brain (Kuhar et al., 1993) with the cysteine-rich signature of α-neurotoxins, was suggestive that it acted on a similar molecular target as α-neurotoxins (Miwa et al., 1999). Although orphan members of the mammalian superfamily had been previously identified (Ploug and Ellis, 1994), the understanding that toxins employ functional mimicry of pathways operating in the prey led to a candidate approach for investigating their function, ultimately resulting in the discovery of the initial functionally characterized prototoxin with nicotinic receptor modulatory capability, lynx1 (Miwa et al., 1999; Ibanez-Tallon et al., 2002).

Current evidence suggests snake toxins arose through gene duplication and divergence from a prototoxin-like ancestral gene (Adermann et al., 1999). The presence of these two forms of prototoxins, GPI and secreted, could provide clues to understanding the evolutionary relationship of venoms and prototoxins.

In the secreted SLURP genes, a stop codon occurs prior to genomic sequence which could code for the amino acid consensus sequence for GPI-attachment, suggests that the membrane-bound forms evolved prior to the secreted forms [i.e., secreted ly6/uPAR-related proteins (SLURPs)] (Yan et al., 1998; Adermann et al., 1999). Loss of the GPI anchor via introduction of a stop-gain mutation to generate a secreted version of the protein may be an important intermediate step in the progression from an ancestral prototoxin to the first α-neurotoxin. On the other hand, evidence of accelerated evolution in the membrane-bound form may support that notion that the GPI-anchored version evolved more recently (Dorus et al., 2004). Regardless, the three-fingered fold toxin-like proteins seems to have occurred once, prior to the split between the venomous elapid snakes and the non-venomous colubrid snake family. This is supported by previous research which isolated and characterized three-fingered toxins from non-venomous colubrid snakes, demonstrating that this toxin type exhibits basal α-neurotoxic activity (Fry et al., 2003a). This evidence suggests that gene recruitment occurred via a non-toxic gene in the body (Fry and Wüster, 2004). Venom development requires a transition of genes to expression in the secretory venom gland of the snake (Kessler et al., 2017), either via recruitment from a gene in the body (Fry, 2005) or restricted expression of a gene with wider expression, such as those in the salivary glands (Reyes-Velasco et al., 2015).

A few three-fingered fold protein family members have been reported to exhibit expression in the salivary gland of non-venomous species, providing possibilities for more neutral selection (Hijazi et al., 2009). More in-depth genomic and transcriptomic analyses of the non-venomous family will be required as more data on the snake genome become available. Although other genes, such as digestive track enzymes or ribonucleases (Strydom, 1973), have been proposed as the ancestral gene giving rise to α-neurotoxins, separate recruitment events seem to be involved (Fry, 2005). Gene duplication aids in the development of venoms, as it allows for divergence in either amino acid sequence to more virulent forms or in regulatory elements to allow such changes in gene expression patterns. There is substantial evidence for gene duplication within mammalian prototoxins/non-venomous species allowing for such sub-functionalization, although the presence of clustered ly6 genes in mice, but not in humans, suggests that at least some of this duplication occurred relatively recently after the divergence of mice and humans (Loughner et al., 2016). Furthermore, snake toxins have the ability to undergo accelerated evolution and selective expression in the snake venom gland (Fry et al., 2003b; Kessler et al., 2017). The evolutionary relationships between members of the prototoxin gene family, WTX, venomous snakes, and colubrid family members are depicted in **Figure 1**.

INTRODUCING THE PROTOTOXIN GENE FAMILY

The prototoxin genes are members of the ly6/uPAR superfamily, whose members adopt the receptor binding structural motif observed within elapid snake venom α-neurotoxins, due to highly conserved cysteine residues that participate in disulfide bonding (Lyukmanova et al., 2011; Tsetlin, 2015; Vasilyeva et al., 2017). Among these family members are the well-studied single-domain snake venom α-neurotoxins and cardiotoxins (Fleming et al., 1993; Ploug and Ellis, 1994). Three-fingered proteins are larger and generally more variable than α-neurotoxins (Kessler et al., 2017). Although α-bungarotoxin (α-btx) is one of the most widely used snake toxins in neuroscience, exhibiting nearly irreversible affinity, ly6/uPAR family members have shown variability in their ability to compete with other nAChR ligands, suggesting more modest receptor affinities and potentially allosteric effects on receptor function. The expression of three-fingered proteins in the brain and body allows for biological regulation over complex nicotinic receptor-based processes across multiple systems. Members of the uPAR superfamily include CD59, lymphocyte antigen genes, ly6A-H, transforming growth factor β receptor ectodomains, and uPAR. In total, at least 2,583 sequences within seven subfamilies have been identified (PFAM database) (Kessler et al., 2017). Further, the human genome encodes for at least 45 genes containing the three-fingered domain (Galat, 2008). Three-fingered proteins exert an influence over a wide-array of physiological processes, including proliferation, cellular

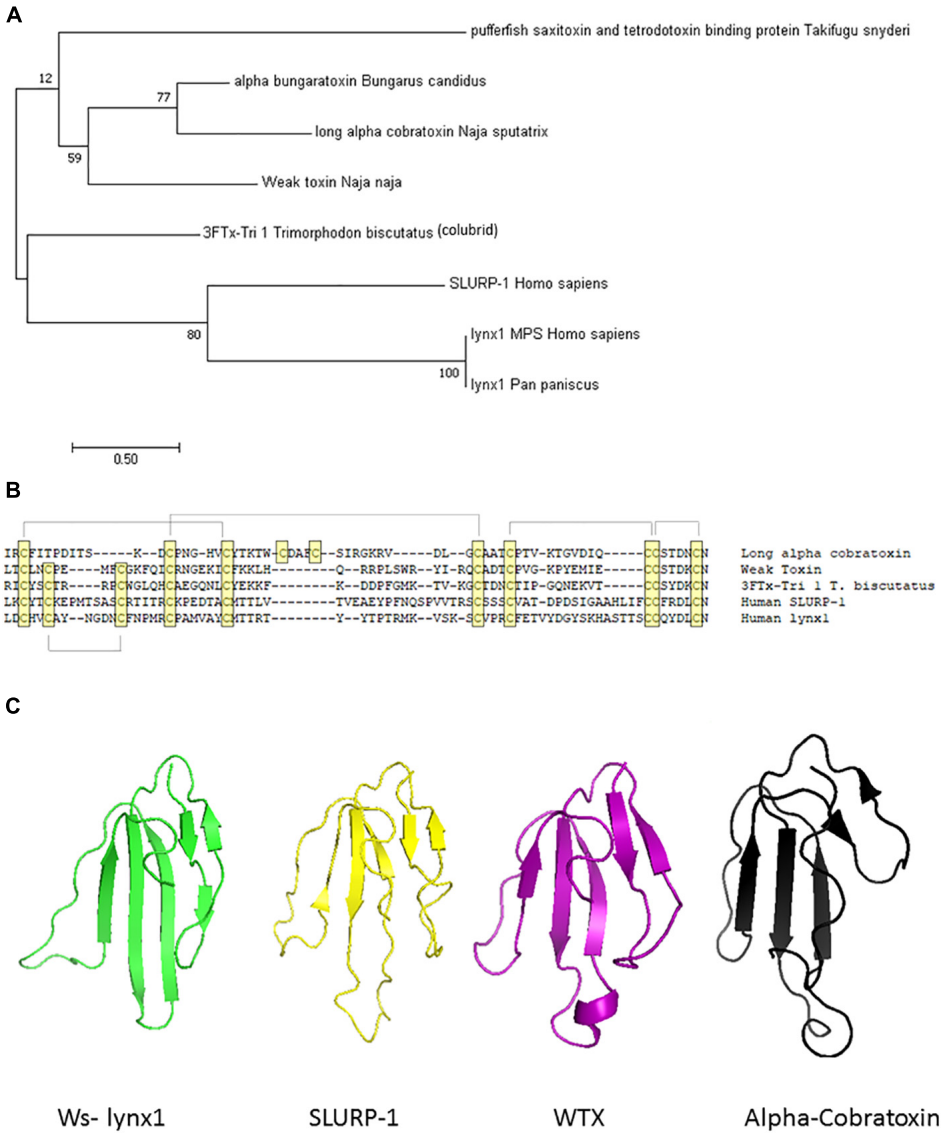

FIGURE 1 | Molecular, phylogenetic, and structural analysis of the prototoxin gene family. **(A)** Bootstrap consensus tree of molecular evolutionary relationship. The percentage of replicate trees in which the associated taxa clustered together in the bootstrap test (500 replicates) are shown next to the branches. **(B)** Amino acid comparison of selected family members. Cysteines are highlighted in yellow and disulfide bridges are outlined. **(C)** Structural comparison of selected family members from the pdb database: Ws-lynx1 (2L03, green), SLURP-1 (2MUO, yellow), Weak toxin (2MJO, purple), Cobratoxin (2CTX, black).

differentiation, and inflammation, among others. The present review focuses on members of this family with demonstrated nAChR modulatory/binding function, with special emphasis on those expressed in the mammalian brain. Within this large superfamily, members with significant expression in the brain include lynx1 (Miwa et al., 1999), lynx2/lypd1 (Dessaud et al., 2006; Wu et al., 2015), lypd6 (Darvas et al., 2009; Zhang et al., 2010), lypd6B (Demars and Morishita, 2014), PSCA (Jensen et al., 2015), and ly6h (Horie et al., 1998). SLURPs, which are expressed mostly outside the brain, have been documented in several disease states and will be also be reviewed (Grando, 2008; Vasilyeva et al., 2017).

STRUCTURAL FEATURES OF THE PROTOTOXIN AND ly6/uPAR SUPERFAMILY

Prototoxins share structural and functional similarities to one another. Among their most notable structural features are cysteine bonds that stabilize a three-loop/three-fingered β-rich fold structure. The ly6/uPAR superfamily contains 10–12 cysteines, with one of the extra disulfide bonds in the first loop, placing this mammalian family closer to the weak toxins depicted in **Figure 1**. NMR solution structures have greatly enhanced our understanding of this class of proteins

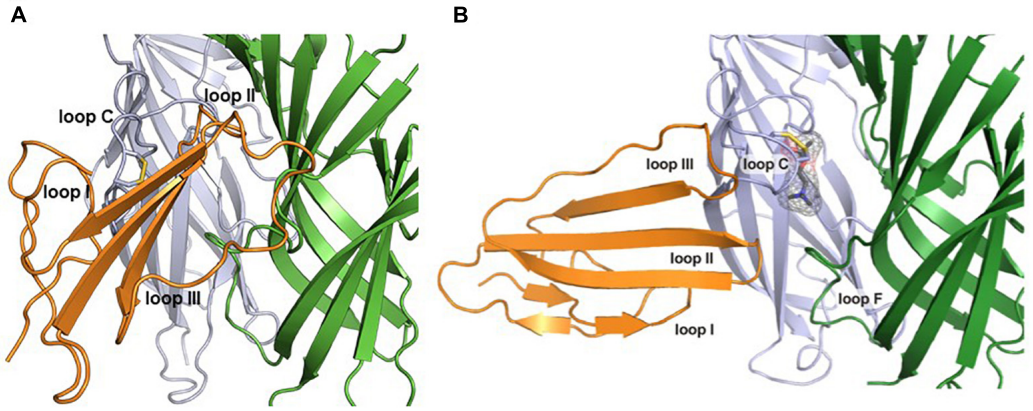

FIGURE 2 | Computational models of lynx1 interaction with nicotinic receptor subunits. **(A)** Co-model of ws-lynx1 and α4: α4 nAChR interface (Nissen et al., 2018). **(B)** Co-model of ws-lynx1 and α7 nAChRs (Lyukmanova et al., 2011).

(Lyukmanova et al., 2011, 2014, 2016b; Paramonov et al., 2017). A recombinant version of lynx1 was engineered such that the sequence for GPI anchor attachment sequence was removed, water soluble lynx1 (ws-lynx1) (Lyukmanova et al., 2011). The NMR solution structure of ws-lynx1 demonstrated that the overall topology is similar to that of α-neurotoxins, although the protein is characterized by a large and mostly disordered loop III (Lyukmanova et al., 2011). The addition of a disulfide bond in loop I is common among other prototoxins and weak/unconventional snake toxins. NMR evaluation was performed for SLURP-1, synthetically derived using peptide ligation (sSLURP-1), and exhibits excellent agreement to that of rSLURP-1 in two- and three-dimensional spectral analyses (Durek et al., 2017). Unfortunately, to date, few crystal structures of prototoxins have been solved, although computational models have been developed for prototoxins and their cognate receptors (**Figure 2**). Solution and crystal structures have been identified for members of the larger superfamily, including CD59 (Fletcher et al., 1994; Huang et al., 2007). CD59 as well as lypd6 and lypd6b (Paramonov et al., 2017) contains an α-helical domain in loop III, which is not found in the NMR structures of lynx1 (Lyukmanova et al., 2011), underscoring the notion that there is more structural variability among the three-fingered proteins of the superfamily than within three-fingered α-neurotoxins (Kessler et al., 2017).

THE CHOLINERGIC SYSTEM

The cholinergic system is a widespread modulatory excitatory neurotransmitter system that enables controlled regulation over multiple neural circuits. Cholinergic neurons release the endogenous neurotransmitter acetylcholine in a diffuse manner. Cholinergic projection neurons are located in the basal forebrain and brain stem, and their terminals radiate broadly throughout the central nervous system (Guo et al., 2015) onto a wide range of targets. This widespread architecture and the fact that neurotransmitter release is not confined to the synaptic cleft contribute to the modulatory capabilities of the cholinergic system. Interestingly, the activity-response relationship of the cholinergic system falls along an inverted U-shaped curve, whereby both impaired and excessive activation can exert deleterious or suboptimal effects (Picciotto, 2003). The cholinergic system operates along a gradient, with detrimental effects observed at the extremes of the range, and is therefore dependent on several regulatory mechanisms (Miwa et al., 2012).

Such fine-tuning of the cholinergic system can be exerted by several factors, including the number and activity of cholinergic neurons, the level of acetylcholine release, the presence of acetylcholinesterase, and the profile of the target receptors. Cholinergic receptors can be divided into muscarinic and nicotinic receptors, which are located mainly in the peripheral and central nervous systems (PNS and CNS), respectively. In addition to acetylcholine, nicotinic receptors bind the exogenous drug of abuse, nicotine. Nicotinic AChRs exist as pentamers composed of many variations of 15 possible subunits. For instance, nicotinic receptors typically exist as heteromeric combinations of α (2–10) and β (2–4) subunits (most commonly α4β2) or as α homopentamers (α7, α9, etc.) (Picciotto, 2003; Albuquerque et al., 2009). Receptor composition gives rise to specificity, as each combination displays distinct biophysical and pharmacological properties. In addition, differences in stoichiometry among subunits allow for differential response profiles and sensitivity to agonist.

Prototoxin proteins can form stable associations with nicotinic receptors, and the binding preference of prototoxin proteins for specific subtypes of nAChRs can further fine tune cholinergic activity by altering a selective subtype or group of receptor subtypes. Further spatial control can be imparted because prototoxins exhibit mostly non-overlapping expression patterns in the CNS (Miwa et al., 2012). Indeed, multifactorial mechanisms such as receptor assembly, expression, and binding specificity contribute to the wide variety of reported effects for each family member (Miwa et al., 2011).

Lynx1

Lynx1 Binding and Insights Using Recombinant ws-lynx1

Previous studies have revealed that a recombinant, water-soluble variant of lynx1, ws-lynx1, can inhibit α7, α4β2, and α3β2, although the functional effects are most pronounced for α4β2. The inhibitory effect is concentration-specific and non-competitive (Lyukmanova et al., 2011). Residues on loops II and III are important for the interaction (Lyukmanova et al., 2013). Although recombinant ws-lynx1 studies have been highly informative, the effects may differ from those of endogenous lynx1, since lynx1 is usually attached to the cell surface via a GPI anchor. Researchers have observed differential biological effects between cerebellum-directed transgenic mice expressing a soluble version of lynx1 (minus the amino acid sequence directing the GPI attachment) which leads to augmentations in motor learning, and those expressing normal GPI-bound lynx1 which demonstrates no effect (Miwa et al., 2012). This is in accordance with the differential effects *in vitro* of ws-lynx1 which enhances ACh-evoked current amplitude vs. GPI-linked endogenous lynx1 which causes acceleration of desensitization and lowering of agonist affinity (Miwa et al., 1999; Ibanez-Tallon et al., 2002). The GPI-anchor exhibits an affinity for cholesterol-rich domains (Lester et al., 2012), and the effective concentration (EC_{50}) may be higher for the membrane-bound form of lynx1.

Mechanisms Underlying the Effects of Lynx1 on Receptor Function

Lynx1 exerts its modulatory effect on the cholinergic system via direct interactions with nAChR (Ibanez-Tallon et al., 2002; Nichols et al., 2014). The effects of this interaction on receptor function are multi-factorial, influencing agonist affinity, desensitization, and recovery from desensitization. In *in vitro* studies involving *Xenopus* oocytes, cells co-expressing α4β2 nicotinic receptors and lynx1 (Ibanez-Tallon et al., 2002) demonstrate reduced agonist sensitivity via co-expression of lynx1, as indicated by a rightward shift in the EC_{50} to acetylcholine (Ibanez-Tallon et al., 2002). Furthermore, nAChRs exhibit a faster rate of desensitization to agonists when co-expressed with lynx1, and prolonged recovery from desensitization as assessed by dual application of agonists (Ibanez-Tallon et al., 2002). This finding is in contrast to those of some previous reports (Miwa et al., 1999), which indicated that exogenous application of lynx1 protein to oocytes expressing α4β2 nAChRs increases the amplitude of ACh currents recorded in two-electrode voltage clamp mode.

Effects of lynx1 on Nicotinic Receptor Assembly

Single-channel activity in α4β2 exhibits a shift toward the expression of high-conductance events and short channel open times (Ibanez-Tallon et al., 2002). This phenotype is associated with the low-sensitivity (LS) $(\alpha4)_3(\beta2)_2$ stoichiometry. Preferential interaction of lynx with α4: α4 dimers over β2:β2 dimers in the endoplasmic reticulum can help to explain the expression of mature pentamers at the plasma membrane of the LS stoichiometry $(\alpha4)_3(\beta2)_2$ over the high sensitivity, HS $(\alpha4)_2(\beta2)_3$ stoichiometry (Nichols et al., 2014). Co-expression studies can be influenced by stoichiometry and assembly, as well as gating activity of nAChRs at the neuronal cell surface of the plasma membrane. It can be difficult to discern the relative contributions of these two effects without cleaving off the GPI anchor via PI-PLC.

George et al. (2017) constrained the number of variables using concatemeric nAChRs, in which five subunit cDNAs are fused into a single polypeptide, fixing the receptor stoichiometry. Co-expression of lynx1 with α3β4* nAChRs (*-containing) suggests a role of lynx1 in altering channel opening, while previous studies have indicated that receptor number is altered only in some isoforms, depending on the subunit identity in the fifth position (George et al., 2017). Lynx1 reduces $(\alpha3)_2(\beta4)_3$ cell-surface expression, whereas single-channel effects were primarily responsible for reducing $(\alpha3)_3(\beta4)_2$ function by enhancing closed dwell times, and by reducing conductance and the number of long bursts. Reduced cell-surface expression and increased closed dwell times accounted for the reduction in $(\alpha3)_2(\beta4)_2\alpha5$ function mediated by lynx1. These data suggest a model of lynx binding in which the ratio of lynx1 to receptor depends on the receptor isoform (**Figure 3**). Along with expression studies of lynx1 in regions related to nicotine intake/aversion, these studies highlight the potential significance of lynx1 in nicotine addiction.

Expression of Lynx1 in the CNS

Lynx1 is widely expressed throughout the CNS, although levels are relatively higher in the hippocampus, cortex, and cerebellum (Miwa et al., 1999; Thomsen et al., 2014). In addition to its extensive expression in the brain, lynx1 can be found in the retina (Maneu et al., 2010), lung (Fu et al., 2012), and spinal cord (Meyer, 2014). Previous studies have noted the interesting temporal expression profile of lynx1, which can be observed beginning around postnatal week 2 or 3 in mouse models (Miwa et al., 1999; Thomsen et al., 2014), exhibiting a close correlation with the critical period in the visual system. Changes in gene expression levels have been reported for lynx1 due to pharmacological and genetic treatment (Miwa et al., 2012).

Lynx1 and Cortical Plasticity

Lynx1 acts as a negative regulator of plasticity in regions such as the hippocampus and cerebellum, and the interaction of lynx1 with nicotinic receptors has been shown to alter plasticity in the adult visual and auditory cortices (Morishita et al., 2010; Takesian et al., 2018). Due to the experience and nAChR-dependent plasticity that occurs in the visual cortex (V1), it is a well-defined model for understanding the age-dependent molecular effects of lynx1 interactions with nAChRs. Lynx1 mRNA and protein levels increase in V1 at the end of the critical period, thereby decreasing ocular dominance plasticity (Morishita et al., 2010; Sadahiro et al., 2016). For example, the effects of lynx1 on ocular plasticity are demonstrated by an increase in responsiveness in the visual cortex in adult lynx1-null mutant KO mice during arousal, and by the discovery of a juvenile form of plasticity mediated by an interaction between

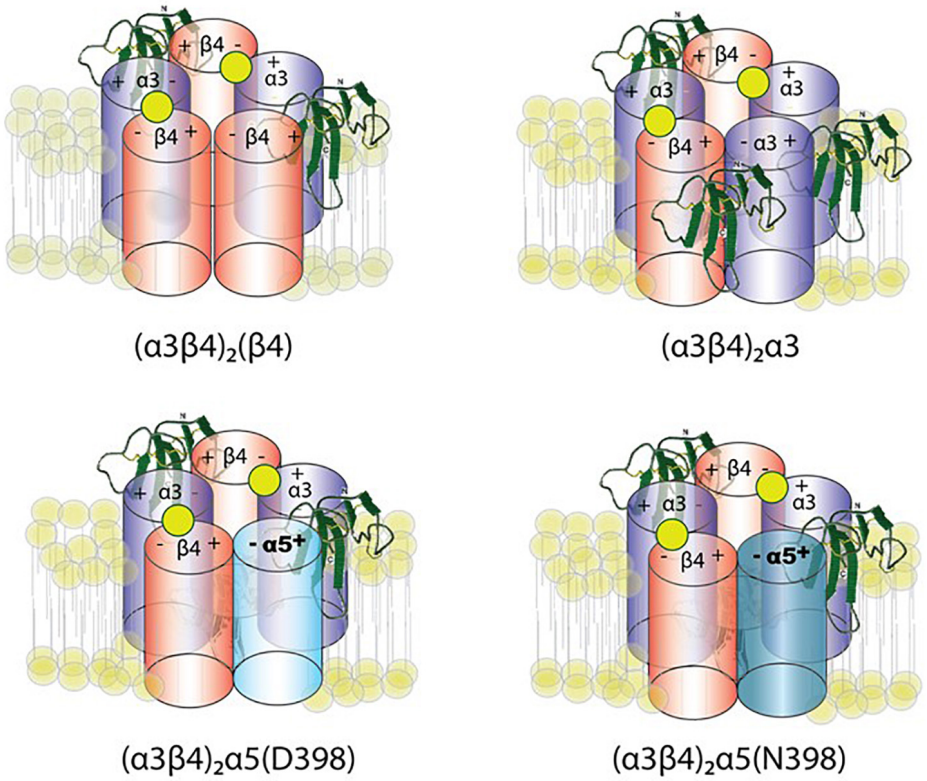

FIGURE 3 | Working model of lynx1 modulation of α3β4- and α3β4α5-nAChR function. Lynx1, depicted in green, interacts with nAChRs that contain an α3(–) subunit interface (George et al., 2017). D398N mutation is associated with higher nicotine intake and relapse from quit attempts in humans. The N at position 398 is the risk allele.

lynx1 and tissue plasminogen activator (Morishita et al., 2010; Bukhari et al., 2015). Furthermore, apical spine turnover in pyramidal neurons of layers 5 and 2/3 is doubled in the V1 of lynx1KO mice, and a selectively higher rate of loss is observed in the layer 5 of adults lacking lynx1 (Sajo et al., 2016). Taken together, these results suggest that lynx1 plays a role in the structural remodeling and spine dynamics required for plasticity in the visual cortex.

Recently, lynx1 has also been linked to a reduction in auditory plasticity via associations with the α4-containing nAChR in 5-HT_{3A}R-positive cells (Takesian et al., 2018). In these studies, a nearly two-fold developmental increase in lynx1 expression in primary auditory cells was observed between P11 and P20, along with a decrease in nAChR sensitivity in 5-HT_{3A}R cells. Furthermore, heightened nicotine sensitivity can be observed in lynx1KO mice, and such sensitivity can be attenuated using the α4 nAChR-specific antagonist DHβE (Takesian et al., 2018).

Lynx1 and Associative Learning

Lynx1KO mice exhibit improvements in cognitive ability, for example, improved associative learning and memory behaviors (Miwa et al., 2006). Contextual memory (assessed using the Morris Water Maze, passive avoidance conditioning, and contextual fear conditioning) does not significantly differ between wild-type and lynx1KO mice, suggesting a specific role of lynx1 in associative learning. To further investigate phenotypic specificity, lynx1KO mice were tested for pain sensitivity (Nissen et al., 2018). Since the fear conditioning paradigm involves shock/tone pairing, this would serve as an important control test for the specificity of the learning phenotype. In one test of nociceptive signaling, the hot-plate test, lynx1KO mice exhibited no significant differences in performance when compared to their wild-type counterparts (Nissen et al., 2018). Indeed, nicotine administration reduced nociceptive behavior in lynx1KO mice (Nissen et al., 2018), suggesting a possible link between lynx1 and analgesia. Because dopamine levels may also influence associative learning/Pavlovian conditioning (Ikegami et al., 2014), researchers have investigated dopamine levels in lynx1KO mice (Parker et al., 2017). Such studies have revealed that lynx1KO mice exhibit dose-dependent decreases in dopamine levels when compared with their wild-type counterparts. Lastly, although lynx1 does seem to influence the function (but not assembly) of α6 nAChRs, as well as subsequent motor activity, such influence does not seem to extend to nicotine conditioned-place preference (Parker et al., 2017). The effects of lynx1 on α6* nAChRs seem subtle and are therefore unlikely to be a factor in associative learning as studied using these behavioral paradigms. Taken together, the effects of lynx1 are moderately specific to plasticity and associative learning.

Role of Lynx1 in Alzheimer's Disease (AD) Pathology

Alzheimer's disease pathology is associated with an increase in soluble β-amyloid (Aβ), a peptide cleaved from the Alzheimer's precursor protein (Inestrosa et al., 2013; Thomsen et al., 2016). Recent evidence suggests that lynx1 and $A\beta_{1-42}$ compete for binding to nAChRs. In pull-down experiments from rat cortical extracts, ws-lynx1 pulled down all nAChR subunits tested (α3-7, β2, and β4), but the only subunits in which $A\beta_{1-42}$ led to reduced lynx1/nAChR interactions were the α3, α4, α5, and α7 nAChR subunits. In contrast, the α6, β2, and β4 nAChR subunits were not sensitive to $A\beta_{1-42}$ competition (Thomsen et al., 2016). Although the authors speculated that the interactions occurred at the neuronal cell surface because the incubation period was relatively short, the fact that interactions were insensitive to β subunits suggests a significant association of lynx1 with individual α subunits or non-pentameric receptors, since only α7 subunits from this list have been shown to form homopentamers. These interactions are likely to occur beneath the membrane surface, consistent with the reported interaction of lynx1 with nAChR dimers in the endoplasmic reticulum (Nichols et al., 2014). Conversely, when $A\beta_{1-42}$ was used as the bait in pull-down experiments, it also pulled down all nAChRs tested, and lynx1 could compete at α7 and β2 subunits. Such findings are in accordance with the results of previous studies, which reported that $A\beta_{1-42}$ can bind α7, α4β2, and α4α5β2 receptors (Dougherty et al., 2003; Wu et al., 2004; Lamb et al., 2005). These results indicate that lynx1 and $A\beta_{1-42}$ bind at similar sites on nAChRs. Although $A\beta_{1-42}$ is thought to bind at the orthosteric binding site, it is possible for two peptides to bind at different sites and still provide orthosteric hindrance to receptor binding. If the lynx1 and $A\beta_{1-42}$ interactions are significant *in vivo*, lynx1 may exert protective effects against the pathological progression of AD (Thomsen et al., 2016), highlighting the need for further studies on the entire receptor complex (Thomsen and Mikkelsen, 2012). In support of this, the toxic effect of $A\beta_{1-42}$ in primary neuronal culture was reduced in the presence of ws-lynx1 (Thomsen et al., 2016). This notion is further supported by previous studies that have demonstrated the protective effects of lynx1 in neuronal health (Miwa et al., 2006; Kobayashi et al., 2014). Importantly, in the AD mouse model (3xTg AD), a reduction of lynx1 protein of 10% in the cortex was observed (Thomsen et al., 2016), suggesting a link between lynx1 and AD pathology. Thus, further studies are required to elucidate the role of $A\beta_{1-42}$ in normal and disease states (Kroker et al., 2013).

Lynx2/Lypd1

The existence of multiple lynx family members is advantageous in that it allows for better spatial or temporal control over the cholinergic system since each exhibits varying expression patterns in different circuits. For instance, lynx1 and lynx2 exhibit complementary and non-overlapping expression patterns (e.g., hippocampal CA3 for lynx1 and CA1 for lynx2) (Miwa et al., 1999; Dessaud et al., 2006; Tekinay et al., 2009). The lynx2 gene expression also is enriched in well-described anxiety pathways, such as the amygdala and prefrontal cortex, which lends itself as a modulator of anxiety (Tekinay et al., 2009). Characteristic of the three-looped structure of the ly6/uPAR super family (Dessaud et al., 2006), the lynx2 protein binds to and suppresses the activity of nAChRs (Tekinay et al., 2009; Wu et al., 2015). *In vitro* immunoprecipitation experiments have demonstrated that lynx2 forms stable complexes with α7, α4β2, and α4β4 nAChRs (Tekinay et al., 2009; Wu et al., 2015). Co-expression of lynx2 and α4β2 leads to faster desensitization kinetics in response to acetylcholine (Tekinay et al., 2009) and a shift in the EC_{50} for acetylcholine (Tekinay et al., 2009), nicotine, and epibatidine (Wu et al., 2015) in the presence of lynx2. The presence of lynx2 also decreases the expression of α4β2 at the cell surface, suggesting a potential mechanism for the decreased response to agonists (Wu et al., 2015). There is also evidence that the lynx2 protein can blunt nicotine-induced upregulation of α4β2 (Wu et al., 2015). Lynx2-null mutant mice (lynx2KO) exhibit increased sensitivity to nicotine within the medial prefrontal cortex when compared to wild-type controls (Tekinay et al., 2009). These data suggest that ligand sensitivity is altered in the presence of lynx2, and that lynx2 also acts to inhibit the activity of nAChRs. The functional consequences of lynx2 removal include increased anxiety-like behaviors across several paradigms of anxiety, as well as reduced social interaction, suggesting that lynx2KO can be established as a robust mouse models of anxiety. Further studies into the removal of nAChR inhibition in lynx2KO mice are underway in order to determine the role of lynx2 in regulating specific nAChR subtypes *in vivo*. These studies underscore the importance of fine tuning the cholinergic system in a spatially controlled manner. The anxiety response includes a set of physiological changes that occur in response to a perceived threat. In the short term, this response is adaptive and helps defend against the threatening situation, but if the response is not regulated properly, it can lead to the development of anxiety disorders and significantly impact quality of life. Thus, lynx2 may play an important role in limiting or regulating the function of its cognate receptors to respond adaptively in circuits mediating anxiety-like behavior.

SLURPs

The Ly6/uPAR superfamily members discussed thus far are a part of the subfamily composed of membrane-bound GPI-anchored proteins. The other subfamily is composed of non-GPI anchored proteins (Adermann et al., 1999). The non-GPI anchored proteins are secreted and can exert a wide array of functions (Adermann et al., 1999; Fischer et al., 2001; Chimienti et al., 2003; Lyukmanova et al., 2014). SLURP-1 and SLURP-2 proteins represent two of these secreted, hormone-like cholinergic peptides of the ly6/uPAR superfamily (Adermann et al., 1999; Chimienti et al., 2003). SLURP proteins are found in the cytoplasm and function widely in non-neuronal cells, regulating growth and finely tuning the cell cycle (Moriwaki et al., 2009; Kessler et al., 2017). While SLURP proteins also largely target nAChRs, SLURP-2 can also interact with muscarinic receptors (Lyukmanova et al., 2016b). Most studies on SLURP function utilize recombinant or synthetic human SLURP

proteins, as there are several methodological issues in obtaining the protein, such as an inability to obtain adequate amounts from natural sources, problems with production systems, and issues with protein folding (Lyukmanova et al., 2016a).

SLURP-1 is expressed in keratinocytes, where its presence modifies ACh signaling and epidermal homeostasis during cutaneous inflammation (Fischer et al., 2001; Chimienti et al., 2003); in primary sensory neurons in the dorsal horn of the spinal cord (Moriwaki et al., 2009); in airway epithelial cells, where its presence stimulates ciliary beating and decreases airway inflammation (Narumoto et al., 2010, 2013); and in corneal and ocular tissue (Swamynathan et al., 2015). Such studies have demonstrated the role of SLURP-1 in Mal de Meleda keratoderma (Fischer et al., 2001), nociception (Moriwaki et al., 2009), asthma (Narumoto et al., 2010, 2013), and pro-inflammatory conditions of the ocular surface (Swamynathan et al., 2015). Consistent with these studies, the SLURP-1KO mouse displays a palmoplantar keratoderma phenotype (Adeyo et al., 2014).

Studies using recombinant human SLURP-1 (rSLURP-1) are detailed in **Table 1**. Data for similar experimental conditions differed among some studies, likely due to the use of different recombinant versions. Taken together, the evidence suggests that SLURP-1 functions as an allosteric modulator of α7 nAChRs (Chimienti et al., 2003; Narumoto et al., 2013; Lyukmanova et al., 2014, 2016a, 2018; Durek et al., 2017). SLURP-1 can be immunoprecipitated and co-localized with α7 nAChRs (Lyukmanova et al., 2016a, 2018). Further studies have indicated that SLURP-1 does not compete with α-btx in oocytes or cause any changes in function on its own (i.e., without the presence of Ach as a ligand), suggesting an allosteric mode of action (Chimienti et al., 2003; Lyukmanova et al., 2016a; Durek et al., 2017). There is conflicting data on the role of SLURP-1, which has been shown to both increase and decrease the E_{max}, and to alter and not alter the EC_{50} (Chimienti et al., 2003; Lyukmanova et al., 2016a; Durek et al., 2017).

Although such findings remain controversial, highlighting the need for characterization standards, further evidence suggests that SLURP-1 can also mediate inhibition of human α3β4, α4β4, and α3β2 nAChRs, as well as human and rat α9α10 nAChRs (Durek et al., 2017). The relevant data were derived from synthetically generated SLURP-1 (sSLURP-1), which exhibits similar structural yet different functional features when compared to rSLURP-1 (Durek et al., 2017). For instance, α-btx binding is not influenced by sSLURP-1 in torpedo membranes (muscle type nAChRs) or AChBP from either *A. Californica* or *L. Stagnalis*, whereas rSLURP-1 can compete with α-btx binding in torpedo membranes and AChBP from *L. Stagnalis*, although such findings were not observed at α7* nAChRs (Shulepko et al., 2013; Lyukmanova et al., 2016a). Functionally, sSLURP-1 exerts no effect on α7* nAChR responses in oocytes. When the α7 component was potentiated by a PAM in mammalian, chaperone co-transfected Neuro-2A cells, however, high doses of agonist were associated with alterations in the E_{max} of epibatidine. In such experiments, calcium-sensitive dyes were used to measure activity indirectly. In oocyte expression systems, sSLURP-1 exerts more robust inhibitory effects on α3β4 nAChRs, although effects can also be observed at α4β4 and α9α10 nAChRs. Based on the accumulated evidence, researchers have speculated that sSLURP-1 acts as a "silent" negative allosteric modulator, exerting its effects only when the nAChR is in the open state (Durek et al., 2017). Despite structural similarities (e.g., differences in the sequence of the N-terminal methionine only), rSLURP-1 and sSLURP-1 need to be tested side by side in the same assay in order to understand potential functional differences, highlighting the need for strict compound characterization standards if results are to be reproducible and transferable (Durek et al., 2017).

TABLE 1 | SLURP and nAChR studies.

SLURP	Functional Effect	Tag	Study
rSLURP-1 human	Increase in E_{max} Shift to left of EC_{50}	C-terminal myc tag N-terminal HA tag	Chimienti et al., 2003
rSLURP-1	N/A	N-terminal Flag, C-terminal GPI	Moriwaki et al., 2009
rSLURP-1	Suppresses cytokine production	N-terminal MBP tag	Narumoto et al., 2013
rSLURP-1	Competes with α-bgtx at AChBPs but not at α7 nAChRs, decrease in E_{max}, no change in EC_{50}	N-terminal Met	Lyukmanova et al., 2016a
sSLURP-1	No α-btx competition at α7 nAChRs or AChBP	Chemical peptide synthesis of human SLURP-1	Durek et al., 2017
rSLURP-2	Reduces cell number, competes with epi and nic binding, partially competes with α-btx binding	Mature SLURP cleaved from His-SUMO	Arredondo et al., 2006
rSLURP-2 and rSLURP-1	Reduces cancer cell number (colorectal)	N-terminal Met	Lyukmanova et al., 2014
rSLURP-2	SLURP-2 increases cytokine production in NHEK cells	N-terminal FLAG epitope-tagged	Moriwaki et al., 2015
rSLURP-2	Decreases α7 currents except at low [SLURP-2]. Increases keratinocyte growth, binds multiple nAChRs	N-terminal Met	Lyukmanova et al., 2016a
rSLURP-2 and rSLURP-1	May decrease growth in five of six α7-expressing cell lines	N-terminal Met	Lyukmanova et al., 2018

SLURP-2 is also an endogenous modulator of nAChRs with 10 cysteine residues and a 28–34% amino acid homology with Ly6 family members (Tsuji et al., 2003; Moriwaki et al., 2009; Peters et al., 2014). Historically, the LYNX1 gene was thought to give rise to both lynx1 and SLURP-2 due to alternative splicing, but recent evidence suggests that the genes are in close proximity but under the control of different transcription units (Moriwaki et al., 2015; Loughner et al., 2016). SLURP-2 differs from both SLURP-1 and lynx1 in that it has an overall negative charge (Lyukmanova et al., 2016b). Compared to SLURP-1, SLURP-2 (also studied via rSLURP2, see **Table 1**) immunoprecipitates with several nAChR subtypes (α3-α7, β2, and β4) (Lyukmanova et al., 2016b) and competes more efficiently with epibatidine than nicotine (Arredondo et al., 2006). SLURP-2 has been shown to interact with mAChRs in an heterologous CHO overexpression system (Lyukmanova et al., 2016b). Confirmation of pull down of native complexes in tissue or genetic confirmation to verify this finding will be informative. SLURP-2 is expressed in human epidermal and oral keratinocytes (Arredondo et al., 2006; Moriwaki et al., 2009, 2015), and in various tissues throughout the body, including epithelial tissue, the stomach, duodenum, esophagus, thymus, cervix, and uterus (Tsuji et al., 2003). Additional studies have indicated that SLURP-2 is upregulated in psoriatic lesional skin and in atopic dermatitis after a stress response, demonstrating its role in regulating stress-related cytokines in the skin (Tsuji et al., 2003; Peters et al., 2014; Moriwaki et al., 2015). The SLURP-2 KO mouse model also exhibits a palmoplantar skin disease phenotype (Allan et al., 2016). Both SLURP-1 and SLURP-2 can inhibit growth in cancer cell lines, suggesting an anticancer potential for these genes (Lyukmanova et al., 2014, 2018). However, overall, SLURP-2 acts in opposition to SLURP-1 to prevent apoptosis (Arredondo et al., 2006; Lyukmanova et al., 2016b).

PROSTATE STEM CELL ANTIGEN (PSCA)

Prostate stem cell antigen is a GPI-anchored cell surface protein localized on lipid rafts (Reiter et al., 1998; Saeki et al., 2010). Although PSCA was originally characterized as a gene upregulated in prostate cancer, it is also expressed in the mammalian (Jensen et al., 2015; Ono et al., 2018) and avian brain (Hruska et al., 2009), and is up-regulated 70% in the cortex of AD patients (Jensen et al., 2015). Affinity purification studies have demonstrated that PSCA forms a stable complex with the α4 nAChR subunit but not the α7 subunit in the human temporal cortex (Jensen et al., 2015). However, its expression in the choroid plexus is worth noting since it is predicted to play a role in cell differentiation and proliferation in epithelial tissues (Ono et al., 2018). In one previous study, PSCA exerted an inhibitory effect on cell death induction in the chick ciliary ganglion via α7-containing nAChRs (Hruska et al., 2009). Furthermore, Jensen et al. (2015) revealed that PSCA decreases nicotine-induced ERK phosphorylation in PC12 cells and is dysregulated in the frontal cortex of patients with Alzheimer's disease, highlighting the potential role of PSCA in pathologies that alter cognitive function.

Lypd6

Another family member, lypd6, is highly expressed in the brain and spinal cord of mice and humans (Darvas et al., 2009; Zhang et al., 2010). Lypd6 regulates nicotinic receptor activity by enhancing Ca^{+2} currents through α/β-heterodimers in mice (Darvas et al., 2009). Lypd6 forms complexes with α3, α4, α5, α6, α7, β2, and β4 nAChR subunits and competes with α-btx for binding α7 subunits (Arvaniti et al., 2016). However, previous studies have also reported that blockade of α7 with α-btx and methyllycaconitine does not affect the modulation of nicotine-induced currents by lypd6 (Darvas et al., 2009). In contrast to the expression of lynx1 in parvalbumin cells, lypd6 is selectively expressed in somatostatin interneurons in cortical layers 5 and 6 of visual cortex region V1 (Darvas et al., 2009).

The function of lypd6 has been demonstrated in several model systems. For example, in PC12 cells, a soluble version of lypd6 completely inhibits nicotine-induced phosphorylation of ERK, which is an important pathway activated during plasticity induction. In addition, decreases in nicotine-induced currents can be observed when water-soluble lypd6 is applied to hippocampal slices (Arvaniti et al., 2016). In lypd6 overexpression studies, mice have demonstrated an increase in sensitivity to nicotine and behavior consistent with an increase in cholinergic tone, such as locomotor arousal, hypoalgesia, and pre-pulse inhibition of the acoustic startle response (Darvas et al., 2009). Furthermore, lypd6 KO mice exhibit decreased baseline levels of anxiety-like behavior in two-independent behavioral assessments (i.e., elevated plus maze and marble burying tests) (Arvaniti et al., 2018). Taken together, these results suggest that lypd6 plays a role in the negative modulation of nAChRs. Lypd6, however, also contains a Nxl motif, which allows it to bind LRP5/6, a member of the Wnt signaling pathway (Zhao et al., 2018), and therefore some of the phenotypes may be mediated by the Wnt coreceptor, low density lipoprotein receptor-related protein 6 LRP5/6.

Lypd6b/Lypd7

Lypd6b, a member with large sequence similarity to lypd6, modulates nAChRs in a subtype-specific manner, and is expressed in glutamatergic neurons of the deep layer of the mammalian visual cortex (Demars and Morishita, 2014). Studies involving *Xenopus* oocytes have demonstrated that lypd6b displays isoform selectivity for inhibiting nAChR-mediated currents through α3β4 nAChRs; however, its presence does not alter α7 subtype-mediated currents (Ochoa et al., 2016). Furthermore, whole-cell recordings have revealed that lypd6b selectively reduces nAChR-mediated currents through α3β4, indicating that modulation of the receptor may occur at the α-α interface (Ochoa et al., 2016). The subtype selectivity and stoichiometry of lypd6b indicate that this prototoxin plays a highly specialized and complex role in nAChR modulation. Lypd7 was cloned from a human testis library, and is primarily expressed in the testes, prostate, stomach, and lung (Ni et al., 2009).

Ly6h

In a previous *in vitro* study involving HEK cells expressing α7 nAChRs, a calcium-based FRET assay was used to determine the relative effect of a number of co-transfected ly6 proteins. To minimize receptor desensitization, the cells were treated with a positive allosteric modulator, PNU-120596, to allow for steady-state over kinetic measurements. The results indicated that there was a shift to the right of nicotine or epibatidine-evoked α7 responses when co-expressed with ly6h, similar to the shifts observed for lynx2 (Puddifoot et al., 2015). Ly6h also caused a reduction in the maximal response and surface expression of α7 nAChRs, suggesting a role for ly6h in receptor trafficking and gating. Prior to this study, the ly6 antigens, which are primarily expressed outside the brain, were not implicated in nAChR regulation. Ly6h has also been shown to influence α4β2 nAChRs in a similar FRET assay, although the effects of ly6h on nAChR trafficking were too pronounced to calculate a reliable EC_{50} in these studies (Wu et al., 2015). Interestingly, ly6h exerted no effects when co-expressed with α4β2 nAChRs in pull-down studies in HEKtsa or on desensitization rates of ACh-evoked responses in oocytes, in contrast to the significant effects observed for lynx2 (Tekinay et al., 2009). Differences in the heterologous systems or tagged proteins may have influenced these results.

In studies involving cells expressing α4β2 nAChRs, although there was a decrease in response to epibatidine by over 50% in the presence of lynx2 or ly6h, less pronounced effects were observed when to ly6e and ly6g6d were present. Such studies have revealed that ly6c1, ly6a, ly6c2, and lypd2 do not modulate α4β2 receptor activity. Furthermore, ly6a does not co-immunoprecipitate, change α4β2 expression at the surface, or interfere with nicotine-mediate up-regulation of α4β2 receptors (Wu et al., 2015).

Ly6g6e

A relatively uncharacterized ly6 family member, ly6g6e, exhibits differences in function and mechanism from other members. Ly6g6e forms a complex with α4β2 nAChRs, and its presence potentiates rather than suppresses these receptors (Wu et al., 2015). Evidence suggests potentiation occurs due to direct modulation by ly6g6e at the cell surface. Cleaving the GPI anchor results in a loss of ly6g6e potentiation (Wu et al., 2015). Additional studies have indicated that ly6g6e can slow the desensitization of nAChRs (Wu et al., 2015). The potential mechanisms displayed by other family members, such as alterations in receptor expression at the cell surface or changes in nAChR ion selectivity, are unlikely, as ly6g6e does not alter the number of receptors at the membrane, and its effects persist in the absence of extracellular calcium (Wu et al., 2015). Ly6g6e expression has been detected in the hippocampus, cortical neurons, and in the midbrain (Wu et al., 2015). Based on its expression patterns and interactions with α4β2 nAChRs, which represent the main nAChRs contributing to nicotine addiction (Flores et al., 1992), ly6g6e may be involved in nicotine reward. Further studies are required to verify this possibility. The differential effects of ly6g6e on nAChRs demonstrate the diverse mechanisms of action present within the superfamily (**Supplementary Table 1**).

PREFERENTIAL PROSTATE AND TESTES EXPRESSION (PATE)-M AND PATE-B

Preferential prostate and testes expression proteins conform to three-fingered protein/ly6/urokinase-type plasminogen activator receptor (uPAR) domains that shape three-fingered proteins in a manner similar to that of the prototoxins discussed above. Three human PATE genes (PATE-M, PATE-DJ, and PATE-B) have been identified and have demonstrated effects on nicotinic receptor function (Levitin et al., 2008). Two (hPATE-B and mPATE-C) enhance ACh-evoked net charge in oocytes expressing the homomeric α7 nAChR, while one (mPATE-P) reduces ACh-evoked net charge in oocytes expressing the α4β2 heteromeric nAChR (Levitin et al., 2008).

OTHER MEMBERS OF THE FAMILY

The ly6/uPAR superfamily continues to expand as more genes are characterized. Furthermore, interesting functions have been noted for members in invertebrate species, and 35 family members have been cloned from *Drosophila*, including *Coiled*, *Boudin* (Hijazi et al., 2009, 2011), and *Sleepless* (Koh et al., 2008). Interestingly, the protein bou is expressed in salivary glands and can incorporate into other cells, indicating a possible non-cell autonomous role.

PROTOTOXIN BINDING SITES ON nAChRs

Once the co-crystals of prototoxins and nAChRs have been identified, researchers should aim to determine the relevant binding sites, and whether these are associated with orthosteric or allosteric effects. The functional properties of prototoxins effects on nAChR function, such as desensitization and recovery from desensitization, although the effect of the GPI-anchored proteins on receptor trafficking, assembly, and stoichiometry may also account for these effects. Various reports have commented on the ability of prototoxins to compete on nAChRs with ligands that bind at the active site, such as nicotine, epibatidine, and α-btx (Lyukmanova et al., 2011; Durek et al., 2017; Arvaniti et al., 2018). Thus, differences in receptor types and the ligands used must be carefully considered (Xiu et al., 2009). An exogenously applied prototoxin that exerts modulatory effects on receptor function without competing with ligands provides support for allosterism.

While α-btx competition and nicotinic receptor upregulation studies have indicated that prototoxins may be involved in orthosteric interactions (Lyukmanova et al., 2013, 2016b; Wu et al., 2015), they are generally considered to be allosteric modulators (Ibanez-Tallon et al., 2002; Tsetlin, 2015; Lyukmanova et al., 2016a). Prototoxins that potentiate ligand-elicited currents can be regarded as positive allosteric modulators

if they require acetylcholine or an agonist to open the receptor. Studies regarding the effect of lynx2 on nicotine-mediated up-regulation have suggested that lynx2 and nicotine operate at the same point in the receptor maturation pathway, potentially competing for binding at the ligand binding site. However, there are mechanisms that may allow for effects on receptor maturation that do not involve direct interaction at the same site on the receptor. Mutant cycle analyses have confirmed that actions at one part of the receptor can be communicated even across long distances from the receptor to the active site (Gleitsman et al., 2009).

There is a low-potency, high-efficacy, tertiary binding site on the α4: α4 interface of $(\alpha4)_3(\beta2)_2$ nAChRs that can potentiate activation of the receptor by ACh (Indurthi et al., 2016). The presence of a third ligand at the two classical sites can lead to receptor transitions, detectable in both E_{max} and changes in the Hill slope. The authors contend that this is indicative of a pre-activational state similar to that of the benzodiazepine binding site on the GABA receptor (Indurthi et al., 2016). At present, it remains unknown how prototoxins interact with this third, low-potency site. Lyukmanova et al. (2016b) have suggested that SLURP-2 acts as a co-ligand for α7 nAChRs by priming it at low SLURP-2 concentrations. Although they postulate that SLURP-2 can work in concert with a single-bound ACh by binding at the orthosteric site, this only occurs at low SLURP-2 concentrations and is not accompanied by evident changes in Hill slope (Lyukmanova et al., 2016b). However, it would be interesting if a similar third binding site for agonists, with an ability to interact with prototoxins, were found to exist for α7 nAChRs. The differences in functional effects between rSLURP-1 and sSLURP-1 are most likely explained by the mode of synthesis vs. expression in *E. coli* vs. mammalian/insect cells and structural differences in nAChR types. With larger modulatory proteins, it is likely that both allosteric and orthosteric effects can be observed at nAChRs.

THE CASE FOR *IN VIVO* TESTS OF PROTOTOXIN BINDING IN THE BODY AND BRAIN

To our knowledge, there have been no unbiased investigations of prototoxin receptors to isolate every interacting partner of a prototoxin. This leaves open the possibility that prototoxins may bind to other classes of receptors outside of nAChRs *in vivo*. All tests of receptor interaction, whether positive (e.g., nAChRs (Ibanez-Tallon et al., 2002; Puddifoot et al., 2015), mAChRs (Lyukmanova et al., 2011, 2016b), LRP6 (Zhao et al., 2018), shaker potassium channels (Wu et al., 2016), or negative (e.g., glutamate, 5-HT3, etc.) have used either heterologously expressed receptor complexes, or have added the prototoxin to brain tissue. Only one study has isolated native complexes from the mammalian brain. In this study, β2* nAChR-containing receptors and lynx1 were identified using pull down studies from the mouse brain (Nissen et al., 2018), while ws-lynx1, SLURP-1 and SLURP-2 has been successfully mixed with human brain tissue to pull down multiple nAChR subtypes (Lyukmanova et al., 2016a,b; Thomsen et al., 2016). To support the *in vivo* interaction studies, a lynx1KO phenotype was ameliorated by crossing these mice into mutant mice null for α7 and β2 nAChR genes (Miwa et al., 2006). These *in vivo* studies provide an important biological context for the interactions observed within *in vitro* systems.

It should be noted that, even within brain tissues, many of these interactions may take place in the cytoplasm, and may therefore be independent of gating functions on the mature receptor pentamers at the cell surface. Receptor number can be reduced via the co-expression of prototoxin (Puddifoot et al., 2015; Wu et al., 2015; George et al., 2017), suggesting an effect on receptor retention or slowing of receptor maturation. Additional studies have indicated that the receptor complexes that escape to the cell surface may form complexes prototoxins (Nichols et al., 2014; Puddifoot et al., 2015; Wu et al., 2015), retaining their modulatory functions. Except in limited cases, however (Wu et al., 2015; George et al., 2017), prototoxins have been demonstrated to retain functional effects even when they have been cleaved from the GPI-anchor using PI-PLC, suggestive of stronger intracellular functions. Antibodies against these proteins that can discriminate cellular localization and surface vs. intracellular prototoxins are greatly needed to determine which of the multiple possible effects demonstrated thus far occur within the brain. Clearly, the interactions between prototoxins and their cognate receptors can be long-term, exerting varied (e.g., assembly and gating) and multiple (e.g., orthosteric and allosteric) effects throughout the life-time of a receptor (**Supplementary Table 1**).

PROMISE OF PROTOTOXIN STUDIES FOR THERAPEUTIC DEVELOPMENT

Numerous studies have indicated that α4β2 and α7 nAChRs may represent targets for the treatment of various neurological and neuropsychiatric disorders (Graham et al., 2002; Picciotto and Zoli, 2008; Brunzell and McIntosh, 2012; Quik et al., 2012; Callahan et al., 2013; Nie et al., 2013; Wallace and Bertrand, 2013; Fan et al., 2015). Among the limitations in successfully targeting nAChRs are the sequence similarities amongst the individual subunits, as well as their widespread expression patterns. The elucidation of prototoxin function has potentially important consequences from a therapeutic perspective. The receptor/prototoxin complexes in specific tissues provide unique interfaces with more restricted expression profiles, allowing for more specific therapeutic modulation than the receptor alone. Furthermore, most prototoxins exhibit multiple binding specificities, which may be advantageous for regulating a multiplicity of nAChR subtypes in concert which govern a pathway, circuit, or biological function. Rather than targeting multiple nAChR subunits with multiple therapeutics, naturally evolving regulators of physiologically relevant functions, via allosteric interventions on nAChRs, may provide safer and more specific effects. Such an approach would enable a much more specific level of cholinergic regulation

than can be achieved by targeting ACh levels or nicotinic receptor subtypes alone.

METHODS

Molecular Phylogenetic Analysis

Reference protein sequences were obtained from GenBank or BLAST. Evolutionary analyses were conducted in MEGA7 (Molecular Evolutionary Genetics Analysis) (Kumar et al., 2016). Protein sequences obtained from GenBank were aligned using the MUSCLE algorithm within MEGA7 program. The evolutionary history was inferred by using the Maximum Likelihood method based on the Dayhoff matrix based model (Swartz and Dayhoff, 1979). Several substitution models were considered prior to selecting the Dayhoff model using MEGA7 model selection algorithms. Initial trees for the heuristic search were obtained automatically by applying Neighbor-Join and BioNJ algorithms to a matrix of pairwise distances estimated using a JTT model, and then selecting the topology with superior log likelihood value. The final bootstrap consensus tree inferred from 500 replicates (Felsenstein, 1985) was taken to represent the evolutionary history of the taxa analyzed. Branches corresponding to partitions reproduced in less than 50% bootstrap replicates were collapsed.

AUTHOR CONTRIBUTIONS

JM, KA, and KH wrote the manuscript. All authors have read and approved the manuscript. KA built tree and models for **Figure 1**.

FUNDING

This work was supported by NIH NIDA (NIH DA043567) and NSF (NSF BCS-1745823) (JM and KA).

ACKNOWLEDGMENTS

We would like to acknowledge Hui Sun Lee and Wonpil Im for modeling assistance and the support of the entire Biological Sciences Department at Lehigh University.

SUPPLEMENTARY MATERIAL

The Supplementary Material for this article can be found online at: https://www.frontiersin.org/articles/10.3389/fphar.2019.00343/full#supplementary-material

REFERENCES

Adermann, K., Wattler, F., Wattler, S., Heine, G., Meyer, M., Forssmann, W. G., et al. (1999). Structural and phylogenetic characterization of human SLURP-1, the first secreted mammalian member of the Ly-6/uPAR protein superfamily. *Protein Sci.* 8, 810–819. doi: 10.1110/ps.8.4.810

Adeyo, O., Allan, B. B., Barnes, R. H. II, Goulbourne, C. N., Tatar, A., Tu, Y., et al. (2014). Palmoplantar keratoderma along with neuromuscular and metabolic phenotypes in Slurp1-deficient mice. *J. Invest. Dermatol.* 134, 1589–1598. doi: 10.1038/jid.2014.19

Albuquerque, E. X., Pereira, E. F., Alkondon, M., and Rogers, S. W. (2009). Mammalian nicotinic acetylcholine receptors: from structure to function. *Physiol. Rev.* 89, 73–120. doi: 10.1152/physrev.00015.2008

Allan, C. M., Procaccia, S., Tran, D., Tu, Y., Barnes, R. H. II, Larsson, M., et al. (2016). Palmoplantar keratoderma in *Slurp2*-deficient mice. *J. Invest. Dermatol.* 136, 436–443. doi: 10.1016/j.jid.2015.11.003

Arredondo, J., Chernyavsky, A. I., Jolkovsky, D. L., Webber, R. J., and Grando, S. A. (2006). SLURP-2: a novel cholinergic signaling peptide in human mucocutaneous epithelium. *J. Cell. Physiol.* 208, 238–245. doi: 10.1002/jcp.20661

Arvaniti, M., Jensen, M. M., Soni, N., Wang, H., Klein, A. B., Thiriet, N., et al. (2016). Functional interaction between Lypd6 and nicotinic acetylcholine receptors. *J. Neurochem.* 138, 806–820. doi: 10.1111/jnc.13718

Arvaniti, M., Polli, F. S., Kohlmeier, K. A., Thomsen, M. S., and Andreasen, J. T. (2018). Loss of Lypd6 leads to reduced anxiety-like behaviour and enhanced responses to nicotine. *Prog. Neuropsychopharmacol. Biol. Psychiatry* 82, 86–94. doi: 10.1016/j.pnpbp.2017.11.025

Brunzell, D. H., and McIntosh, J. M. (2012). Alpha7 nicotinic acetylcholine receptors modulate motivation to self-administer nicotine: implications for smoking and schizophrenia. *Neuropsychopharmacology* 37, 1134–1143. doi: 10.1038/npp.2011.299

Bukhari, N., Burman, P. N., Hussein, A., Demars, M. P., Sadahiro, M., Brady, D. M., et al. (2015). Unmasking proteolytic activity for adult visual cortex plasticity by the removal of Lynx1. *J. Neurosci.* 35, 12693–12702. doi: 10.1523/JNEUROSCI.4315-14.2015

Callahan, P. M., Hutchings, E. J., Kille, N. J., Chapman, J. M., and Terry, A. V. (2013). Positive allosteric modulator of alpha7 nicotinic-acetylcholine receptors, PNU-120596 augments the effects of donepezil on learning and memory in aged rodents and non-human primates. *Neuropharmacology* 67, 201–212. doi: 10.1016/j.neuropharm.2012.10.019

Chimienti, F., Hogg, R. C., Plantard, L., Lehmann, C., Brakch, N., Fischer, J., et al. (2003). Identification of SLURP-1 as an epidermal neuromodulator explains the clinical phenotype of Mal de Meleda. *Hum. Mol. Genet.* 12, 3017–3024. doi: 10.1093/hmg/ddg320

Darvas, M., Morsch, M., Racz, I., Ahmadi, S., Swandulla, D., and Zimmer, A. (2009). Modulation of the Ca2+ conductance of nicotinic acetylcholine receptors by Lypd6. *Eur. Neuropsychopharmacol.* 19, 670–681. doi: 10.1016/j.euroneuro.2009.03.007

Demars, M. P., and Morishita, H. (2014). Cortical parvalbumin and somatostatin GABA neurons express distinct endogenous modulators of nicotinic acetylcholine receptors. *Mol. Brain* 7, 75–86. doi: 10.1186/s13041-014-0075-9

Dessaud, E., Salaun, D., Gayet, O., Chabbert, M., and deLapeyriere, O. (2006). Identification of lynx2, a novel member of the ly-6/neurotoxin superfamily, expressed in neuronal subpopulations during mouse development. *Mol. Cell. Neurosci.* 31, 232–242. doi: 10.1016/j.mcn.2005.09.010

Dorus, S., Vallender, E. J., Evans, P. D., Anderson, J. R., Gilbert, S. L., Mahowald, M., et al. (2004). Accelerated evolution of nervous system genes in the origin of Homo sapiens. *Cell* 119, 1027–1040. doi: 10.1016/j.cell.2004.11.040

Dougherty, J. J., Wu, J., and Nichols, R. A. (2003). β-Amyloid regulation of presynaptic nicotinic receptors in rat hippocampus and neocortex. *J. Neurosci.* 23, 6740–6747. doi: 10.1523/JNEUROSCI.23-17-06740.2003

Durek, T., Shelukhina, I. V., Tae, H. S., Thongyoo, P., Spirova, E. N., Kudryavtsev, D. S., et al. (2017). Interaction of synthetic human SLURP-1 with the nicotinic acetylcholine receptors. *Sci. Rep.* 7:16606. doi: 10.1038/s41598-017-16809-0

Fan, H., Gu, R., and Wei, D. (2015). The alpha7 nAChR selective agonists as drug candidates for Alzheimer's disease. *Adv. Exp. Med. Biol.* 827, 353–365. doi: 10.1007/978-94-017-9245-5_21

Felsenstein, J. (1985). Confidence limits on phylogenies: an approach using the bootstrap. *Evolution* 39, 783–791. doi: 10.1111/j.1558-5646.1985.tb00420.x

Fischer, M., Corringer, P. J., Schott, K., Bacher, A., and Changeux, J. P. (2001). A method for soluble overexpression of the alpha7 nicotinic acetylcholine receptor extracellular domain. *Proc. Natl. Acad. Sci. U.S.A.* 98, 3567–3570. doi: 10.1073/pnas.041594798

Fleming, T. J., O'hUigin, C., and Malek, T. R. (1993). Characterization of two novel Ly-6 genes. Protein sequence and potential structural similarity to alpha-bungarotoxin and other neurotoxins. *J. Immunol.* 150, 5379–5390.

Fletcher, C. M., Harrison, R. A., Lachmann, P. J., and Neuhaus, D. (1994). Structure of a soluble, glycosylated form of the human complement regulatory protein CD59. *Structure* 2, 185–199. doi: 10.1016/S0969-2126(00)00020-4

Flores, C. M., Rogers, S. W., Pabreza, L. A., Wolfe, B. B., and Kellar, K. J. (1992). A subtype of nicotinic cholinergic receptor in rat brain is composed of alpha 4 and beta 2 subunits and is up-regulated by chronic nicotine treatment. *Mol. Pharmacol.* 41, 31–37.

Fry, B. G. (2005). From genome to "venome": molecular origin and evolution of the snake venom proteome inferred from phylogenetic analysis of toxin sequences and related body proteins. *Gen. Res.* 15, 403–420. doi: 10.1101/gr.3228405

Fry, B. G., Lumsden, N. G., Wüster, W., Wickramaratna, J. C., Hodgson, W. C., and Kini, R. M. (2003a). Isolation of a neurotoxin (alpha-colubritoxin) from a 'non-venomous' colubrid: evidence for early origin of venom in snakes. *J. Mol. Evol.* 57, 446–452.

Fry, B. G., Wüster, W., Kini, R. M., Brusic, V., Khan, A., Venkataraman, D., et al. (2003b). Molecular evolution and phylogeny of elapid snake venom three-finger toxins. *J. Mol. Evol.* 57, 110–112.

Fry, B. G., and Wüster, W. (2004). Assembling an arsenal: origin and evolution of the snake venom proteome inferred from phylogenetic analysis of toxin sequences. *Mol. Biol. Evol.* 21, 870–883. doi: 10.1093/molbev/msh091

Fu, X. W., Rekow, S. S., and Spindel, E. R. (2012). The ly-6 protein, lynx1, is an endogenous inhibitor of nicotinic signaling in airway epithelium. *Am. J. Physiol. Lung. Cell. Mol. Physiol.* 303, L661–L668. doi: 10.1152/ajplung.00075.2012

Galat, A. (2008). The three-fingered protein domain of the human genome. *Cell. Mol. Life Sci.* 65, 3481–3493. doi: 10.1007/s00018-008-8473-8

George, A. A., Bloy, A., Miwa, J. M., Lindstrom, J. M., Lukas, R. J., and Whiteaker, P. (2017). Isoform-specific Mechanisms of α3β4 nicotinic acetylcholine receptor modulation by the prototoxin lynx1. *FASEB J.* 31, 1398–1420. doi: 10.1096/fj.201600733R

Gleitsman, K. R., Shanata, J. A., Frazier, S. J., Lester, H. A., and Dougherty, D. A. (2009). Long-range coupling in an allosteric receptor revealed by mutant cycle analysis. *Biophys. J.* 96, 3168–3178. doi: 10.1016/j.bpj.2008.12.3949

Graham, A. J., Martin-Ruiz, C. M., Teaktong, T., Ray, M. A., and Court, J. A. (2002). Human brain nicotinic receptors, their distribution and participation in neuropsychiatric disorders. *Curr. Drug Targets CNS Neurol. Disord.* 1, 387–397. doi: 10.2174/1568007023339283

Grando, S. A. (2008). Basic and clinical aspects of non-neuronal acetylcholine: biological and clinical significance of non-canonical ligands of epithelial nicotinic acetylcholine receptors. *J. Pharmacol. Sci.* 106, 174–179. doi: 10.1254/jphs.FM0070087

Guo, Q., Wang, D., He, X., Feng, Q., Lin, R., Xu, F., et al. (2015). Whole-brain mapping of inputs to projection neurons and cholinergic interneurons in the dorsal striatum. *PLoS One* 10:e0123381. doi: 10.1371/journal.pone.0123381

Hijazi, A., Haenlin, M., Waltzer, L., and Roch, F. (2011). The Ly6 protein coiled is required for septate junction and blood brain barrier organisation in Drosophila. *PLoS One* 6:e17763. doi: 10.1371/journal.pone.0017763

Hijazi, A., Masson, W., Augé, B., Waltzer, L., Haenlin, M., and Roch, F. (2009). *Boudin* is required for septate junction organisation in *Drosophila* and codes for a diffusible protein of the Ly6 superfamily. *Development* 136, 2199–2209. doi: 10.1242/dev.033845

Horie, M., Okutomi, K., Taniguchi, Y., Ohbuchi, Y., Suzuki, M., and Takahashi, E. (1998). Isolation and characterization of a new member of the human Ly6 gene family (LY6H). *Genomics* 53, 365–368. doi: 10.1006/geno.1998.5462

Hruska, M., Keefe, J., Wert, D., Tekinay, A. B., Hulce, J. J., Ibañez-Tallon, I., et al. (2009). Prostate stem cell antigen is an endogenous lynx1-like prototoxin that antagonizes alpha7-containing nicotinic receptors and prevents programmed cell death of parasympathetic neurons. *J. Neurosci.* 29, 14847–14854. doi: 10.1523/JNEUROSCI.2271-09.2009

Huang, Y., Fedarovich, A., Tomlinson, S., and Davies, C. (2007). Crystal structure of CD59: implications for molecular recognition of the complement proteins C8 and C9 in the membrane-attack complex. *Acta Crystallogr. D Biol. Crystallogr.* 63, 714–721. doi: 10.1107/S0907444907015557

Ibanez-Tallon, I., Miwa, J. M., Wang, H. L., Adams, N. C., Crabtree, G. W., Sine, S. M., et al. (2002). Novel modulation of neuronal nicotinic acetylcholine receptors by association with the endogenous prototoxin lynx1. *Neuron* 33, 893–903. doi: 10.1016/S0896-6273(02)00632-3

Ikegami, M., Uemura, T., Kishioka, A., Sakimura, K., and Mishina, M. (2014). Striatal dopamine D1 receptor is essential for contextual fear conditioning. *Sci. Rep.* 4:3976. doi: 10.1038/srep03976

Indurthi, D. C., Lewis, T. M., Ahring, P. K., Balle, T., Chebib, M., and Absalom, N. L. (2016). Ligand binding at the 4-4 agonist-binding site of the 42 nAChR triggers receptor activation through a pre-activated conformational state. *PLoS One* 11:e0161154. doi: 10.1371/journal.pone.0161154

Inestrosa, N. C., Godoy, J. A., Vargas, J. Y., Arrazola, M. S., Rios, J. A., Carvajal, F. J., et al. (2013). Nicotine prevents synaptic impairment induced by amyloid-beta oligomers through alpha7-nicotinic acetylcholine receptor activation. *Neuromolecular Med.* 15, 549–569. doi: 10.1007/s12017-013-8242-1

Jensen, M. M., Arvaniti, M., Mikkelsen, J. D., Michalski, D., Pinborg, L. H., Härtig, W., et al. (2015). Prostate stem cell antigen interacts with nicotinic acetylcholine receptors and is affected in Alzheimer's disease. *Neurobiol. Aging* 36, 1629–1638. doi: 10.1016/j.neurobiolaging.2015.01.001

Kessler, P., Marchot, P., Silva, M., and Servent, D. (2017). The three-finger toxin fold: a multifunctional structural scaffold able to modulate cholinergic functions. *J. Neurochem.* 142(Suppl. 2), 7–18. doi: 10.1111/jnc.13975

Kobayashi, A., Parker, R. L., Wright, A. P., Brahem, H., Ku, P., Oliver, K. M., et al. (2014). Lynx1 supports neuronal health in the mouse dorsal striatum during aging: an ultrastructural investigation. *J. Mol. Neurosci.* 53, 525–536. doi: 10.1007/s12031-014-0352-1

Koh, K., Joiner, W. J., Wu, M. N., Yue, Z., Smith, C. J., and Sehgal, A. (2008). Identification of SLEEPLESS, a novel sleep-promoting factor. *Science* 321, 372–376. doi: 10.1126/science.1155942

Kroker, K. S., Moreth, J., Kussmaul, L., Rast, G., and Rosenbrock, H. (2013). Restoring long-term potentiation impaired by amyloid-beta oligomers: comparison of an acetylcholinesterase inhibitor and selective neuronal nicotinic receptor agonists. *Brain Res. Bull.* 96, 28–38. doi: 10.1016/j.brainresbull.2013.04.006

Kuhar, S. G., Feng, L., Vidan, S., Ross, M. E., Hatten, M. E., and Heintz, N. (1993). Changing patterns of gene expression define four stages of cerebellar granule neuron differentiation. *Development* 117, 97–104.

Kumar, S., Stecher, G., and Tamura, K. (2016). MEGA7: molecular evolutionary genetics analysis version 7.0 for bigger datasets. *Mol. Biol. Evol.* 33, 1870–1874. doi: 10.1093/molbev/msw054

Lamb, P. W., Melton, M. A., and Yakel, J. L. (2005). Inhibition of neuronal nicotinic acetylcholine receptor channels expressed in *Xenopus* oocytes by beta-amyloid1-42 peptide. *J. Mol. Neurosci.* 27, 13–21. doi: 10.1385/JMN:27:1:013

Lester, H. A., Miwa, J. M., and Srinivasan, R. (2012). Psychiatric drugs bind to classical targets within early exocytotic pathways: therapeutic effects. *Biol. Psychiatry* 72, 907–915. doi: 10.1016/j.biopsych.2012.05.020

Levitin, F., Weiss, M., Hahn, Y., Stern, O., Papke, R. L., Matusik, R., et al. (2008). PATE gene clusters code for multiple, secreted TFP/Ly-6/uPAR proteins that are expressed in reproductive and neuron-rich tissues and possess neuromodulatory activity. *J. Biol. Chem.* 283, 16928–16939. doi: 10.1074/jbc.M801454200

Loughner, C. L., Bruford, E. A., McAndrews, M. S., Delp, E. E., Swamynathan, S., and Swamynathan, S. K. (2016). Organization, evolution and functions of the human and mouse Ly6/uPAR family genes. *Hum. Genomics* 10:10. doi: 10.1186/s40246-016-0074-2

Lyukmanova, E. N., Bychkov, M. L., Sharonov, G. V., Efremenko, A. V., Shulepko, M. A., Kulbatskii, D. S., et al. (2018). Human secreted proteins SLURP-1 and SLURP-2 control the growth of epithelial cancer cells via interaction with nicotinic acetylcholine receptors: action of human SLURP proteins on cancer cells. *BJP* 175, 1973–1986. doi: 10.1111/bph.14194

Lyukmanova, E. N., Shenkarev, Z. O., Shulepko, M. A., Mineev, K. S., D'Hoedt, D., Kasheverov, I. E., et al. (2011). NMR structure and action on nicotinic acetylcholine receptors of water-soluble domain of human LYNX1. *J. Biol. Chem.* 286, 10618–10627. doi: 10.1074/jbc.M110.189100

Lyukmanova, E. N., Shulepko, M. A., Buldakova, S. L., Kasheverov, I. E., Shenkarev, Z. O., Reshetnikov, R. V., et al. (2013). Water-soluble LYNX1 residues important for interaction with muscle-type and/or neuronal nicotinic receptors. *J. Biol. Chem.* 288, 15888–15899. doi: 10.1074/jbc.M112.436576

Lyukmanova, E. N., Shulepko, M. A., Bychkov, M. L., Shenkarev, Z. O., Paramonov, A. S., Chugunov, A. O., et al. (2014). Human SLURP-1 and SLURP-2 Proteins acting on nicotinic acetylcholine receptors reduce proliferation of human colorectal adenocarcinoma HT-29 cells. *Acta Naturae* 6, 60–66.

Lyukmanova, E. N., Shulepko, M. A., Kudryavtsev, D., Bychkov, M. L., Kulbatskii, D. S., Kasheverov, I. E., et al. (2016a). Human secreted Ly-6/uPAR related protein-1 (SLURP-1) is a selective allosteric antagonist of α7 nicotinic acetylcholine receptor. *PLoS One* 11:e0149733. doi: 10.1371/journal.pone.0149733

Lyukmanova, E. N., Shulepko, M. A., Shenkarev, Z. O., Bychov, M. L., Paramonov, A. S., Chugunov, A. O., et al. (2016b). Secreted isoform of human Lynx1 (SLURP-2): spatial structure and pharmacology of interactions with different types of acetylcholine receptors. *Sci. Rep.* 6:30698. doi: 10.1038/srep30698

Maneu, V., Gerona, G., Fernandez, L., Cuenca, N., and Lax, P. (2010). Evidence of alpha 7 nicotinic acetylcholine receptor expression in retinal pigment epithelial cells. *Vis. Neurosci.* 27, 139–147. doi: 10.1017/S0952523810000246

Meyer, M. A. (2014). Identification of 17 highly expressed genes within mouse lumbar spinal cord anterior horn region from an in-situ hybridization atlas of 3430 genes: implications for motor neuron disease. *Neurol. Int.* 6:5367. doi: 10.4081/ni.2014.5367

Miwa, J. M., Freedman, R., and Lester, H. A. (2011). Neural systems governed by nicotinic acetylcholine receptors: emerging hypotheses. *Neuron* 70, 20–33. doi: 10.1016/j.neuron.2011.03.014

Miwa, J. M., Ibanez-Tallon, I., Crabtree, G. W., Sanchez, R., Sali, A., Role, L. W., et al. (1999). Lynx1, an endogenous toxin-like modulator of nicotinic acetylcholine receptors in the mammalian CNS. *Neuron* 23, 105–114. doi: 10.1016/S0896-6273(00)80757-6

Miwa, J. M., Lester, H. A., and Walz, A. (2012). Optimizing cholinergic tone through lynx modulators of nicotinic receptors: implications for plasticity and nicotine addiction. *Physiology* 27, 187–199. doi: 10.1152/physiol.00002.2012

Miwa, J. M., Stevens, T. R., King, S. L., Caldarone, B. J., Ibanez-Tallon, I., Xiao, C., et al. (2006). The prototoxin lynx1 acts on nicotinic acetylcholine receptors to balance neuronal activity and survival in vivo. *Neuron* 51, 587–600. doi: 10.1016/j.neuron.2006.07.025

Morishita, H., Miwa, J., Heintz, N., and Hensch, T. K. (2010). Lynx1, a cholinergic brake, limits plasticity in adult visual cortex. *Science* 330, 1238–1240. doi: 10.1126/science.1195320

Moriwaki, Y., Takada, K., Tsuji, S., Kawashima, K., and Misawa, H. (2015). Transcriptional regulation of SLURP2, a psoriasis-associated gene, is under control of IL-22 in the skin: a special reference to the nested gene LYNX1. *Int. Immunophamacol.* 29, 71–75. doi: 10.1016/j.intimp.2015.05.030

Moriwaki, Y., Watanabe, Y., Shinagawa, T., Kai, M., Miyazawa, M., Okuda, T., et al. (2009). Primary sensory neuronal expression of SLURP-1, an endogenous nicotinic acetylcholine receptor ligand. *Neurosci. Res.* 64, 403–412. doi: 10.1016/j.neures.2009.04.014

Narumoto, O., Horiguchi, K., Horiguchi, S., Moriwaki, Y., Takano-Ohmuro, H., Shoji, S., et al. (2010). Down-regulation of secreted lymphocyte antigen-6/urokinase-type plasminogen activator receptor-related peptide-1 (SLURP-1), an endogenous allosteric alpha7 nicotinic acetylcholine receptor modulator, in murine and human asthmatic conditions. *Biochem. Biophys. Res. Commun.* 398, 713–718. doi: 10.1016/j.bbrc.2010.07.006

Narumoto, O., Niikura, Y., Ishii, S., Morihara, H., Okashiro, S., Nakahari, T., et al. (2013). Effect of secreted lymphocyte antigen-6/urokinase-type plasminogen activator receptor-related peptide-1 (SLURP-1) on airway epithelial cells. *Biochem. Biophys. Res. Commun.* 438, 175–179. doi: 10.1016/j.bbrc.2013.07.048

Ni, J., Lang, Q., Bai, M., Zhong, C., Chen, X., Wan, B., et al. (2009). Cloning and characterization of a human LYPD7, a new member of the Ly-6 superfamily. *Mol. Biol. Rep.* 36, 689–703. doi: 10.1007/s11033-008-9231-6

Nichols, W. A., Henderson, B. J., Yu, C., Parker, R. L., Richards, C. I., Lester, H. A., et al. (2014). Lynx1 shifts alpha4beta2 nicotinic receptor subunit stoichiometry by affecting assembly in the endoplasmic reticulum. *J. Biol. Chem.* 289, 31423–31432. doi: 10.1074/jbc.M114.573667

Nie, H., Wang, Z., Zhao, W., Lu, J., Zhang, C., Lok, K., et al. (2013). New nicotinic analogue ZY-1 enhances cognitive functions in a transgenic mice model of Alzheimer's disease. *Neurosci. Lett.* 537, 29–34. doi: 10.1016/j.neulet.2013.01.001

Nissen, N. I., Anderson, K. R., Wang, H., Lee, H. S., Garrison, C., Eichelberger, S., et al. (2018). Augmenting the antinociceptive effects of nicotinic acetylcholine receptor activity through lynx1 modulation. *PLoS One* 13:e0199643. doi: 10.1371/journal.pone.0199643

Ochoa, V., George, A. A., Nishi, R., and Whiteaker, P. (2016). The prototoxin LYPD6B modulates heteromeric α3β4-containing nicotinic acetylcholine receptors, but not α7 homomers. *FASEB J.* 30, 1109–1119. doi: 10.1096/fj.15-274548

Ono, H., Sakamoto, H., Yoshida, T., and Saeki, N. (2018). Prostate stem cell antigen is expressed in normal and malignant human brain tissues. *Oncol. Lett.* 15, 3081–3084. doi: 10.3892/ol.2017.7632

Paramonov, D. S., Kulbatskii, E. V., Loktyushov, A. V., Tsarev, D. A., Dolgikh, D. A., Shenkarev, Z. O., et al. (2017). Recombinant production and structural studies of the human Lypd6 and Lypd6b proteins. *Russ. J. Bioorgan. Chem.* 43, 620–630. doi: 10.1134/S1068162017060127

Parker, R. L., O'Neill, H., Henley, B. M., Wageman, C. R., Drenan, R. M., Marks, M. J., et al. (2017). Deletion of lynx1 reduces the function of α6* nicotinic receptors. *PLoS One* 12:e0188715. doi: 10.1371/journal.pone.0188715

Peters, E. M., Michenko, A., Kupfer, J., Kummer, W., Wiegand, S., Niemeier, V., et al. (2014). Mental stress in atopic dermatitis–neuronal plasticity and the cholinergic system are affected in atopic dermatitis and in response to acute experimental mental stress in a randomized controlled pilot study. *PLoS One* 9:e113552. doi: 10.1371/journal.pone.0113552

Picciotto, M. R. (2003). Nicotine as a modulator of behavior: beyond the inverted U. *Trends Pharmacol. Sci.* 24, 493–499. doi: 10.1016/S0165-6147(03)00230-X

Picciotto, M. R., and Zoli, M. (2008). Neuroprotection via nAChRs: the role of nAChRs in neurodegenerative disorders such as Alzheimer's and Parkinson's disease. *Front. Biosci.* 13, 492–504. doi: 10.2741/2695

Ploug, M., and Ellis, V. (1994). Structure-function relationships in the receptor for urokinase-type plasminogen activator. Comparison to other members of the Ly-6 family and snake venom alpha-neurotoxins. *FEBS Lett.* 349, 163–168. doi: 10.1016/0014-5793(94)00674-1

Puddifoot, C. A., Wu, M., Sung, R. J., and Joiner, W. J. (2015). Ly6h regulates trafficking of alpha7 nicotinic acetylcholine receptors and nicotine-induced potentiation of glutamatergic signaling. *J. Neurosci.* 35, 3420–3430. doi: 10.1523/JNEUROSCI.3630-14.2015

Quik, M., Perez, X. A., and Bordia, T. (2012). Nicotine as a potential neuroprotective agent for Parkinson's disease. *Mov. Disord.* 27, 947–957. doi: 10.1002/mds.25028

Reiter, R. E., Gu, Z., Watabe, T., Thomas, G., Szigeti, K., Davis, E., et al. (1998). Prostate stem cell antigen: a cell surface marker overexpressed in prostate cancer. *Proc. Natl. Acad. Sci. U.S.A.* 95, 1735–1740. doi: 10.1073/pnas.95.4.1735

Reyes-Velasco, J., Card, D. C., Andrew, A. L., Shaney, K. J., Adams, R. H., Schield, D. R., et al. (2015). Expression of venom gene homologs in diverse python tissues suggests a new model for the evolution of snake venom. *Mol. Biol. Evol.* 32, 173–183. doi: 10.1093/molbev/msu294

Sadahiro, M., Sajo, M., and Morishita, H. (2016). Nicotinic regulation of experience-dependent plasticity in visual cortex. *J. Physiol. Paris* 110, 29–36. doi: 10.1016/j.jphysparis.2016.11.003

Saeki, N., Gu, J., Yoshida, T., and Wu, X. (2010). Prostate stem cell antigen: a Jekyll and Hyde molecule? *Clin. Cancer Res.* 16, 3533–3538. doi: 10.1158/1078-0432.CCR-09-3169

Sajo, M., Ellis-Davies, G., and Morishita, H. (2016). Lynx1 limits dendritic spine turnover in the adult visual cortex. *J. Neurosci.* 36, 9472–9478. doi: 10.1523/JNEUROSCI.0580-16.2016

Shulepko, M. A., Lyukmanova, E. N., Paramonov, A. S., Lobas, A. A., Shenkarev, Z. O., Kasheverov, I. E., et al. (2013). Human neuromodulator SLURP-1: bacterial expression, binding to muscle-type nicotinic acetylcholine receptor, secondary structure, and conformational heterogeneity in solution. *Biochemistry* 78, 204–211. doi: 10.1134/S0006297913020090

Strydom, D. J. (1973). Protease inhibitors as snake venom toxins. *Nat. New Biol.* 243, 88–89.

Swamynathan, S., Delp, E. E., Harvey, S. A., Loughner, C. L., Raju, L., and Swamynathan, S. K. (2015). Corneal expression of SLURP-1 by age, sex, genetic strain, and ocular surface health. *Invest. Ophthalmol. Vis. Sci.* 56, 7888–7896. doi: 10.1167/iovs.15-18206

Swartz, R., and Dayhoff, M. (1979). "Matrices for detecting distant relationships," in *Atlas of Protein Sequences*, ed. M. Dayhoff (Washington, DC: National Biomedical Research Foundation), 353–358.

Takesian, A. E., Bogart, L. J., Lichtman, J. W., and Hensch, T. K. (2018). Inhibitory circuit gating of auditory critical-period plasticity. *Nat. Neurosci.* 21, 218–227. doi: 10.1038/s41593-017-0064-2

Tekinay, A. B., Nong, Y., Miwa, J. M., Lieberam, I., Ibanez-Tallon, I., Greengard, P., et al. (2009). A role for LYNX2 in anxiety-related behavior. *Proc. Natl. Acad. Sci. U.S.A.* 106, 4477–4482. doi: 10.1073/pnas.0813109106

Thomsen, M. S., Arvaniti, M., Jensen, M. M., Shulepko, M. A., Dolgikh, D. A., Pinborg, L. H., et al. (2016). Lynx1 and Aβ1-42 bind competitively to multiple nicotinic acetylcholine receptor subtypes. *Neurobiol. Aging* 46, 13–21. doi: 10.1016/j.neurobiolaging.2016.06.009

Thomsen, M. S., Cinar, B., Jensen, M. M., Lyukmanova, E. N., Shulepko, M. A., Tsetlin, V., et al. (2014). Expression of the Ly-6 family proteins Lynx1 and Ly6H in the rat brain is compartmentalized, cell-type specific, and developmentally regulated. *Brain Struct. Funct.* 219, 1923–1934. doi: 10.1007/s00429-013-0611-x

Thomsen, M. S., and Mikkelsen, J. D. (2012). The α7 nicotinic acetylcholine receptor complex: one, two or multiple drug targets? *Curr. Drug Targets* 13, 707–720. doi: 10.2174/138945012800399035

Tsetlin, V. I. (2015). Three-finger snake neurotoxins and Ly6 proteins targeting nicotinic acetylcholine receptors: pharmacological tools and endogenous modulators. *Trends Pharmacol. Sci.* 36, 109–123. doi: 10.1016/j.tips.2014.11.003

Tsuji, H., Okamoto, K., Matsuzaka, Y., Iizuka, H., Tamiya, G., and Inoko, H. (2003). SLURP-2, a novel member of the human Ly-6 superfamily that is up-regulated in psoriasis vulgaris. *Genomics* 81, 26–33. doi: 10.1016/S0888-7543(02)00025-3

Vasilyeva, N. A., Loktyushov, E. V., Bychkov, M. L., Shenkarev, Z. O., and Lyukmanova, E. N. (2017). Three-finger proteins from the Ly6/uPAR family: functional diversity within one structural motif. *Biochemistry* 82, 1702–1715. doi: 10.1134/S0006297917130090

Wallace, T. L., and Bertrand, D. (2013). Alpha7 neuronal nicotinic receptors as a drug target in schizophrenia. *Expert Opin. Ther. Targets* 17, 139–155. doi: 10.1517/14728222.2013.736498

Wu, J., George, A. A., Schroeder, K. M., Xu, L., Marxer-Miller, S., Lucero, L., et al. (2004). Electrophysiological, pharmacological, and molecular evidence for alpha7-nicotinic acetylcholine receptors in rat midbrain dopamine neurons. *J. Pharmacol. Exp. Ther.* 311, 80–91. doi: 10.1124/jpet.104.070417

Wu, M., Liu, C. Z., and Joiner, W. J. (2016). Structural analysis and deletion mutagenesis define regions of QUIVER/SLEEPLESS that are responsible for interactions with shaker-type potassium channels and nicotinic acetylcholine receptors. *PLoS One* 11:e0148215. doi: 10.1371/journal.pone.0148215

Wu, M., Puddifoot, C. A., Taylor, P., and Joiner, W. J. (2015). Mechanisms of inhibition and potentiation of α4β2 nicotinic acetylcholine receptors by members of the Ly6 protein family. *J. Biol. Chem.* 290, 24509–24518. doi: 10.1074/jbc.M115.647248

Xiu, X., Puskar, N. L., Shanata, J. A., Lester, H. A., and Dougherty, D. A. (2009). Nicotine binding to brain receptors requires a strong cation-pi interaction. *Nature* 458, 534–537. doi: 10.1038/nature07768

Yan, W., Shen, F., Dillon, B., and Ratnam, M. (1998). The hydrophobic domains in the carboxyl-terminal signal for GPI modification and in the amino-terminal leader peptide have similar structural requirements. *J. Mol. Biol.* 275, 25–33. doi: 10.1006/jmbi.1997.1447

Zhang, Y., Lang, Q., Li, J., Xie, F., Wan, B., and Yu, L. (2010). Identification and characterization of human LYPD6, a new member of the Ly-6 superfamily. *Mol. Biol. Rep.* 37, 2055–2062. doi: 10.1007/s11033-009-9663-7

Zhao, Y., Ren, J., Lu, W., Harlos, K., and Jones, E. Y. (2018). Structure of the Wnt signaling enhancer LYPD6 and its interactions with the Wnt coreceptor LRP6. *FEBS Lett.* 592, 3152–3162. doi: 10.1002/1873-3468.13212

Conflict of Interest Statement: JM is founder of Ophidion, Inc.

The remaining authors declare that the research was conducted in the absence of any commercial or financial relationships that could be construed as a potential conflict of interest.

The handling Editor and reviewer VT declared their involvement as co-editors in the Research Topic, and confirm the absence of any other collaboration.

frontiers in Pharmacology

ORIGINAL RESEARCH
published: 01 May 2019
doi: 10.3389/fphar.2019.00474

Crystal Structure of the Monomeric Extracellular Domain of α9 Nicotinic Receptor Subunit in Complex With α-Conotoxin RgIA: Molecular Dynamics Insights Into RgIA Binding to α9α10 Nicotinic Receptors

Marios Zouridakis[1], Athanasios Papakyriakou[2], Igor A. Ivanov[3], Igor E. Kasheverov[3,4], Victor Tsetlin[3,5], Socrates Tzartos[1,6] and Petros Giastas[1]**

[1] Department of Neurobiology, Hellenic Pasteur Institute, Athens, Greece, [2] Institute of Biosciences and Applications, NCSR "Demokritos", Athens, Greece, [3] Shemyakin-Ovchinnikov Institute of Bioorganic Chemistry, Russian Academy of Sciences, Moscow, Russia, [4] Institute of Molecular Medicine, Sechenov First Moscow State Medical University, Moscow, Russia, [5] PhysBio of MEPhI, Moscow, Russia, [6] Department of Pharmacy, University of Patras, Patras, Greece

The α9 subunit of nicotinic acetylcholine receptors (nAChRs) exists mainly in heteropentameric assemblies with α10. Accumulating data indicate the presence of three different binding sites in α9α10 nAChRs: the α9(+)/α9(−), the α9(+)/α10(−), and the α10(+)/α9(−). The major role of the principal (+) side of the extracellular domain (ECD) of α9 subunit in binding of the antagonists methyllylcaconitine and α-bungarotoxin was shown previously by the crystal structures of the monomeric α9-ECD with these molecules. Here we present the 2.26-Å resolution crystal structure of α9-ECD in complex with α-conotoxin (α-Ctx) RgIA, a potential drug for chronic pain, the first structure reported for a complex between an nAChR domain and an α-Ctx. Superposition of this structure with those of other α-Ctxs bound to the homologous pentameric acetylcholine binding proteins revealed significant similarities in the orientation of bound conotoxins, despite the monomeric state of the α9-ECD. In addition, ligand-binding studies calculated a binding affinity of RgIA to the α9-ECD at the low micromolar range. Given the high identity between α9 and α10 ECDs, particularly at their (+) sides, the presented structure was used as template for molecular dynamics simulations of the ECDs of the human α9α10 nAChR in pentameric assemblies. Our results support a favorable binding of RgIA at α9(+)/α9(−) or α10(+)/α9(−) rather than the α9(+)/α10(−) interface, in accordance with previous mutational and functional data.

Keywords: nicotinic acetylcholine receptors, α-conotoxins, RgIA, structure, molecular modeling, molecular dynamics

Abbreviations: ACh, acetylcholine; AChBP, acetylcholine-binding protein; ECD, extracellular domain; MD, molecular dynamics; MLA, methyllylcaconitine; nAChRs, nicotinic acetylcholine receptors; RMSD, root mean square deviation; α-Bgtx, α-bungarotoxin; α-Ctx, α-conotoxin; (+) side, principal side; (−) side, complementary side.

OPEN ACCESS

Edited by:
Mounir Tarek,
Centre National de la Recherche Scientifique (CNRS), France

Reviewed by:
Vishwanath Jogini,
D. E. Shaw Research, United States
Chris Ulens,
KU Leuven, Belgium
Marco Cecchini,
Université de Strasbourg, France

****Correspondence:***
Petros Giastas
petrosgiastas@gmail.com
Marios Zouridakis
marzouri@gmail.com

Specialty section:
This article was submitted to Pharmacology of Ion Channels and Channelopathies, a section of the journal Frontiers in Pharmacology

Received: *15 November 2018*
Accepted: *15 April 2019*
Published: *01 May 2019*

Citation:
Zouridakis M, Papakyriakou A, Ivanov IA, Kasheverov IE, Tsetlin V, Tzartos S and Giastas P (2019) Crystal Structure of the Monomeric Extracellular Domain of α9 Nicotinic Receptor Subunit in Complex With α-Conotoxin RgIA: Molecular Dynamics Insights Into RgIA Binding to α9α10 Nicotinic Receptors. Front. Pharmacol. 10:474. doi: 10.3389/fphar.2019.00474

INTRODUCTION

Nicotinic acetylcholine receptors are the prototypic members of the Cys-loop family of pentameric ligand-gated ion channels, including also the 5-HT_3, $GABA_A$, and glycine receptors (Lester et al., 2004; Sine and Engel, 2006; Albuquerque et al., 2009; Nemecz et al., 2016). Muscle and neuronal nAChRs are found at the neuromuscular junction and in central and peripheral neurons, respectively. Neuronal nAChRs regulate neuronal excitability and neurotransmitter release and, in humans, are composed of a combination of eight α (α2–7, α9–10) and three β (β2–4) subunits, forming either homopentamers or heteropentamers (e.g., α7, α4β2, α7β2, and α9α10 nAChRs) (Albuquerque et al., 2009; Millar and Gotti, 2009; Engel et al., 2015). These receptors are also found in the immune system and in various peripheral tissues (Wessler and Kirkpatrick, 2008; Beckmann and Lips, 2013). Each neuronal nAChR subtype has distinct pharmacological and electrophysiological properties and distinct localization within the central and peripheral nervous system (Gotti et al., 2006, 2007; Millar and Gotti, 2009; Taly et al., 2009).

Due to their implications in smoking addiction and in various neurological and non-neurological diseases and disorders (e.g., Alzheimer's and Parkinson's diseases, schizophrenia, neuropathic pain, and inflammation), neuronal nAChRs are important drug targets (Taly et al., 2009; Quik et al., 2011; Dineley et al., 2015; Hone and McIntosh, 2018). However, due to the high similarity in the orthosteric ligand-binding site of neuronal nAChRs, the development of drugs targeting specifically a distinct nAChR subtype is a very challenging task, requiring detailed structural information. This site consists of loops A, B, and C of the principal (+) side of the ECD of an α subunit and of loops D, E, and F of the complementary (−) side of the ECD of the adjacent α or β subunit (Brejc et al., 2001; Unwin, 2005). Whereas the highly conserved (+) side of the ligand-binding site seems to play an important role in the orientation of the bound ligand (Dellisanti et al., 2007; Zouridakis et al., 2014), it is the less conserved (−) side that determines the selectivity on a specific nAChR subtype (Rucktooa et al., 2009; Bourne et al., 2015; Giastas et al., 2018).

Apart from the early breakthrough cryo-electron microscopy studies of the *Torpedo* muscle-type nAChR (Unwin, 1995, 2005), our understanding of the structure of neuronal nAChR ligand-binding sites was greatly advanced by the X-ray crystal structures of the molluscan AChBPs (Brejc et al., 2001; Celie et al., 2004). AChBPs share up to 24% sequence identity with the ECDs of nAChRs and, most importantly, almost all residues that are conserved in the ligand-binding sites of nAChRs are also found in them. In addition, the X-ray structures of mutated or chimeric AChBPs, carrying single-point mutations or region replacements, respectively, to mimic some nAChR-ECDs, have shed light on the structure of the ligand-binding sites formed between α7 or α4 or between α3 and β4 nAChR subunits (Li et al., 2011; Nemecz and Taylor, 2011; Shahsavar et al., 2015; Abraham et al., 2017). Recent breakthrough X-ray and electron microscopy studies of the almost intact α4β2 nAChR (Morales-Perez et al., 2016; Walsh et al., 2018) with nicotine bound, elucidated the 3D structure of α4(+)/α4(−) and α4(+)/β2(−) binding sites in high detail. Also, the crystal structure of the α2(+)/α2(−) binding site, present in α2β2 nAChRs, was solved previously with the agonist epibatidine bound (Kouvatsos et al., 2016), succeeding the crystal structure of the monomeric α9-ECD in its free and antagonist [methyllylcaconitine (MLA) or α-bungarotoxin (α-Bgtx)]-bound forms (Zouridakis et al., 2014).

Subtype-specific inhibitors of nAChRs, apart from valuable tools for dissecting the roles of the various nAChRs, may also be important therapeutic agents. A good example of subtype-specific nAChR antagonists are α-conotoxins (α-Ctxs), peptides isolated from the venom of snails belonging to the *Conus* genus (see reviews Nicke et al., 2004; Janes, 2005; Azam and McIntosh, 2009; Rucktooa et al., 2009; Tsetlin et al., 2009). α-Ctxs range in size from 12 to 19 amino acid residues and contain two disulfide bonds with a Cys1-Cys3 and Cys2-Cys4 connectivity, forming two backbone loops (loop 1 and loop 2, respectively). RgIA, on which the present study is focused, is a 4/3 subclass α-Ctx (containing four and three residues in loops 1 and 2, respectively), and is highly selective for the α9α10 nAChR (Ellison et al., 2006, 2008; Clark et al., 2008). This neuronal nAChR subtype has two stoichiometries, the $(\alpha9)_2(\alpha10)_3$ and $(\alpha9)_3(\alpha10)_2$ (Plazas et al., 2005; Indurthi et al., 2014), and is mainly expressed in the hair cells of the cochlea (Elgoyhen et al., 1994, 2001) and in a variety of immune cells (Lustig et al., 2001; Peng et al., 2004; Hecker et al., 2015). Mutational and functional data suggest that there are three ligand-binding sites in α9α10 nAChRs, namely the α9(+)/α9(−), α9(+)/α10(−) and the α10(+)/α9(−) (Ellison et al., 2008; Indurthi et al., 2014; Azam et al., 2015; Boffi et al., 2017).

There are many X-ray structures of different AChBPs in complexes with various α-Ctxs, but here we present the first X-ray crystal structure of an α-Ctx (RgIA) bound to the nAChR α9-ECD, solved at 2.26-Å resolution. As the protein is in a monomeric state, the interactions of RgIA with the (+) side of the α9-ECD were revealed and were found to be similar to those between the (+) side of AChBP protomer and, the similar to RgIA, α4/3-Ctx ImI (Hansen et al., 2005; Ulens et al., 2006). Moreover, RgIA in its complex with α9-ECD superimposed very well with other α-Ctxs bound to pentameric AChBPs, denoting that the α9(+) side in α9α10 nAChRs is instrumental for the orientation of the bound RgIA, similarly to what was previously shown for MLA and α-Bgtx binding to α9-ECD (Zouridakis et al., 2014). In addition, based on the crystal structure of α9-ECD/RgIA, MD simulations of the complexes of RgIA at α9(+)/α9(−), α9(+)/α10(−), and α10(+)/α9(−) binding sites in human nAChR α9α10-ECDs were performed. These studies indicated that the favorable binding sites for RgIA are the α9(+)/α9(−) and/or α10(+)/α9(−), rather than the α9(+)/α10(−), in accordance with previous mutational and functional data. Since the α9α10 nAChR is a possible pharmacotherapeutic target for the auditory disease tinnitus and for the chronic neuropathic pain (Elgoyhen et al., 2009; Elgoyhen and Langguth, 2010; Hone and McIntosh, 2018), this study may provide useful information for the design of highly selective improved RgIA analogs for use against such diseases.

MATERIALS AND METHODS

Materials

The materials and reagents used for purification and deglycosylation of nAChR α9-ECD were Ni^{2+}-NTA resin (Qiagen, United States) and $EndoH_f$ (NEB, United States). All other chemicals used were of analytical grade (SIGMA-ALDRICH, United States). For the solid-phase peptide synthesis of α-Ctx RgIA, we used: Fmoc-protected amino acids and diisopropylcarbodiimide (Iris Biotech GmbH, Germany), a block-copolymer resin Tentagel HL-NH2 modified with Knorr linker (Tentagel-RAM, Rapp Polymere, Germany), 4-methylpiperidine (Acros Organics, Belgium), hydroxybenzotriazole (Riyn Group, China), trifluoroacetic acid (Solvay Chemicals, Belgium). Other reagents were acquired from local supplier. All reagents and solvents were used without additional purification.

Protein Expression and Purification

The human nAChR α9-ECD was expressed as a C-terminal six-histidine tagged protein in the yeast *Pichia pastoris* system and purified by metal affinity and size exclusion chromatography (SEC); enzymatic deglycosylation was carried out with endoglycosidase $EndoH_f$, as also described in Zouridakis et al. (2014).

Ligand-Binding and Competition Experiments

Ligand-binding experiments to test [^{125}I]α-Bgtx binding to the glyco- and deglycosylated α9-ECD were described and performed previously (Zouridakis et al., 2014). The K_d values of [^{125}I]α-Bgtx for the glyco- and deglycosylated protein were 30 and 19 nM, respectively (Zouridakis et al., 2014). Competition experiments of [^{125}I]α-Bgtx binding to the α9-ECD by α-Ctx RgIA were performed with SEC-purified monomeric glycosylated or deglycosylated histidine-tagged α9-ECD bound to Ni^{2+}-NTA beads. The beads were washed twice with 10 volumes of phosphate buffer saline (PBS) and then diluted 10 times with PB-BSA buffer [10 mM potassium phosphate buffer, 0.2% bovine serum albumin (BSA), 0.05% NaN_3, pH 7.4]; 10 μl of this dilution were used in each reaction. The protein concentration was 100 nM and the specific activity of [^{125}I]α-Bgtx was 30 cpm $fmol^{-1}$. Reaction volume was fixed to 50 μl by addition of PB-BSA buffer. Competition experiments were performed with fixed [^{125}I]α-Bgtx concentration at 50 nM and variable unlabeled RgIA concentrations (1 nM–200 μM). Serial dilutions of the stock buffer of RgIA (initial concentration of 4.8 mM) were done in PB-BSA buffer. Incubation of reaction mixtures was performed overnight at 4°C. The beads were then washed three times in 1 ml of 20 mM Tris and 0.05% Triton X-100, pH 7.5, followed by a final centrifugation at 1000 *g*, 5 min at 4°C. Finally, the bound radioactivity was measured on a gamma counter. Non-specific binding was measured in samples with the same ingredients but without the α9-ECD. All assays were performed in triplicate, and binding data were evaluated with an algorithm of GraphPad Prism 5.0 (GraphPad Software), accounting for ligand depletion. All numerical data are presented as mean ± SEM for at least three independent experiments.

Synthesis of α-Ctx RgIA Globular Isomer

The globular isomer of α-Ctx RgIA was synthesized similarly to Ellison et al. (2008) by the solid-phase method, using Fmoc-protected amino acids with the Trt- and Acm- protection of cysteines for the first (1–3) and second (2–4) disulfide bonds, respectively, and DIC/HOBt as a coupling reagent. Linear peptide was totally deprotected and cleaved from the polymer with TFA/DTT/H2O 93:4:3 cocktail. A crude peptide was isolated by ether precipitation and subsequent purification was performed on YMC Triart C18 10 u 150 mm × 30 mm column, using Gilson 333/334 binary gradient HPLC system with spectrophotometric detection at 210-nm wavelength. The purified linear RgIA was subjected to a closure of the first disulfide bond by atmospheric oxygen at high pH. Briefly, linear peptide was dissolved in aqueous 50 mM ammonium bicarbonate to a final concentration of 0.5 g/L, stirred on air for 72 h and lyophilized. Purification of monocyclic intermediate was performed under the same conditions as linear ones. Deprotection of Acm-protected cysteines and oxidation were performed by treatment with iodine solution in glacial acetic acid. Excess of iodine was quenched by aqueous citric acid. The reaction mixture was freeze-dried, and the final product was purified on a C8 reverse-phase column. Its purity was confirmed by UPLC/MS analysis.

Crystallization and Data Collection

Crystals of the deglycosylated α9-ECD in complex with α-Ctx RgIA were grown by the sitting-drop vapor-diffusion method in 100 mM HEPES, pH 7.5, 20% PEG 10000 at a protein concentration of 3.5 mg ml^{-1} and a molar ratio of protein to RgIA equal to 1:3. Cryoprotection of the crystals was achieved by immersion in a solution containing the precipitant and 20% ethylene glycol for ∼10 s. Subsequently, the crystals were vitrified in liquid N_2. Data were collected at 100 K at a wavelength of 1.0 Å on beamline I04 of the Diamond Light Source, Didcot, United Kingdom. The reflections were integrated with XDS (Kabsch, 2010), the space group was determined with POINTLESS (Evans, 2011), and the data merging was carried out with SCALA (Evans, 2006) of the CCP4 (Winn et al., 2011) suite.

Structure Determination and Refinement

The structure of the α9-ECD/RgIA complex was solved by molecular replacement with PHASER (McCoy et al., 2007), using as a search model the apo structure of α9-ECD (PDB ID: 4D01) (Zouridakis et al., 2014). The electron density maps clearly showed the presence of a large and continuous electron density in the binding site region, attributed to α-Ctx RgIA. The structure was refined with PHENIX (Afonine et al., 2012) with restrained refinement and TLS refinement implemented in the final stages. Model building and real-space refinement were performed in COOT (Emsley et al., 2010). The high-resolution limit was determined with the CC1/2 and mean (I/σI) criteria (Karplus and Diederichs, 2012), using as cutoff the values of 60% and 1.5, respectively. Almost 99% of the residues of α9 ECD were in Ramachandran favored or allowed regions, and 1% were outliers,

whereas the overall geometry inspection showed no outliers in rotameric and omega angle analyses. The electron density for the region 102–104 of α9-ECD could not be determined and therefore the corresponding residues were not built in the model. The atomic coordinates and structure factors of the α9-ECD/RgIA complex were deposited in the Protein Data Bank, under the accession code 6HY7. The PyMOL program[1] was used for structure visualization and for generation of the figures.

Computational Methods

The homology model of human nAChR α10-ECD was based on the X-ray crystal structure of human α9-ECD complex with the α-Ctx RgIA presented here (PDB ID: 6HY7). All non-protein atoms were removed from the template structure. Sequence alignment between human α9 and α10 ECDs (**Figure 2D**) was performed using Clustal Omega and the UNIPROT accession codes Q9UGM1 and Q9GZZ6 for α9 and α10, respectively (67% sequence identity for 212 residues). From a total of 30 homology models of human α10-ECD that were generated using Modeller v9.10 (Fiser and Sali, 2003), we selected the lowest DOPE score model, which was used without any further optimization. The models of pentameric $(\alpha9)_2(\alpha10)_3$ and $(\alpha9)_3(\alpha10)_2$ ECDs were prepared by superimposing the two human monomers (either free or RgIA-bound) on the crystallographic structure of the *Aplysia californica* AChBP in complex with α-Ctx ImI (PDB ID: 2C9T) (Ulens et al., 2006), using the MULTISEQ plugin of VMD v1.9.4 (Humphrey et al., 1996). RgIA was placed at only one binding site in the modeled pentamers, formed between either α9(+)/α9(−), or α9(+)/α10(−), or between α10(+)/α9(−) interfaces.

Molecular Dynamics (MD) Simulations

Molecular dynamics simulations were performed using the GPU-accelerated version of PMEMD in AMBER v16 (Case et al., 2005; Salomon-Ferrer et al., 2013) and the ff14SB force field parameters (Maier et al., 2015). The systems were solvated in truncated octahedron boxes of TIP3P waters with a minimum extension of 12 Å from the solute and the total charge was neutralized with the addition of sodium ions. All simulations were performed with a 4-fs time step by applying the hydrogen mass repartitioning method (Hopkins et al., 2015). The Particle Mesh Ewald method was used for long-range electrostatic interactions with a real space cutoff of 9 Å. Temperature was regulated using a Langevin thermostat with a collision frequency of 1.0 ps^{-1} and the pressure was regulated at 1.0 bar using the Berendsen weak-coupling algorithm with a relaxation time of 1.0 ps. First, each system was energy minimized without restraints for 2000 steps to remove steric clashes. Then, the temperature was increased to 200 K within 100 ps under constant volume (NVT ensemble), using harmonic positional restraints of 100 kcal/mol $Å^2$ on all protein atoms. Within the next 200 ps, temperature was increased to 300 K under constant pressure (NPT ensemble), while reducing the restraints to 50 kcal/mol $Å^2$. Pressure equilibration was performed for a total of 2 ns at 300 K in the NPT with restraints applied only on the (+) side and RgIA Cα atoms. These restraints were gradually decreased from 25 to 1.0 kcal/mol $Å^2$ within the first 1 ns of equilibration and were retained during the remaining equilibration. In subsequent unrestraint production simulations of 0.5 μs at 300 K in the canonical ensemble (NVT) we observed that RgIA sampled a large conformational space rendering analysis of residue-specific interactions at either (+) or (−) sides very difficult. Therefore, we retained weak restraints of 1.0 kcal/mol $Å^2$ only on the 211 Cα atoms of the α9 or α10 ECD comprising each time the (+) side of the binding site and on the 13 Cα atoms of RgIA for 0.2 μs of the production runs. These restraints were then reduced to 0.1 kcal/mol $Å^2$ for additional 0.2 μs, while the side chains of all residues were kept unrestrained during the whole simulation time. In contrast, the ECD participating at the (−) side of the binding site and the other three ECDs in each pentameric system were unrestrained, allowing for the sampling of potential interactions of RgIA with the (−) side of the α9 or α10 ECD. Trajectory snapshots were collected every 10 ps and were processed using the CPPTRAJ module of AMBER. The non-bonded interaction energy terms (electrostatic and van der Waals) between RgIA and the nAChR ECDs were calculated within the LIE methodology implemented in CPPTRAJ with the default 12-Å cutoff. Clustering of the trajectory snapshots was performed using a hierarchical agglomerative approach with a minimum distance between clusters of 2.0 Å, after mass-weighted, root-mean-square deviation fitting of the Ca atoms at the two binding subunits of RgIA. Calculations were performed on Linux workstations equipped with NVIDIA GTX 1080 GPUs.

RESULTS

Overall Structure of the α9-ECD/RgIA Complex

The crystal structure of the complex of the deglycosylated human nAChR α9-ECD in complex with the C-terminally amidated α-Ctx RgIA was solved at 2.26-Å resolution (**Figures 1A,B**, **Supplementary Figure S1** and **Supplementary Table S1**). Whereas the structure of the α9-ECD in this complex was very similar to the previously determined structure of the apo α9-ECD (Zouridakis et al., 2014), presenting a RMSD value of 0.497 Å for their paired Cα atoms, the crystal structure of RgIA bound to α9-ECD presented an RMSD value for Cα atoms of 1.905 Å compared to its NMR structure in solution (PDB ID: 2JUT) (Ellison et al., 2008). This difference is mainly attributed to the C-terminal Arg13, which upon superposition of the two RgIA structures shows >5 Å distance between their Cα atoms, revealing the intrinsic flexibility of this residue (**Figure 1C**). Another notable difference is the α-helical domain in the middle of the crystallized RgIA molecule, which is missing in the NMR structure of RgIA (**Figure 1C**). In addition, in the crystal structure of RgIA, an intramolecular salt bridge between Asp5 and Arg7 was observed (**Figure 1D**), also missing from its NMR structure.

To investigate whether these observed conformational changes of RgIA upon binding to α9-ECD have been reported in other cases, we sought for examples involving α-Ctxs. When

[1] http://www.pymol.org/

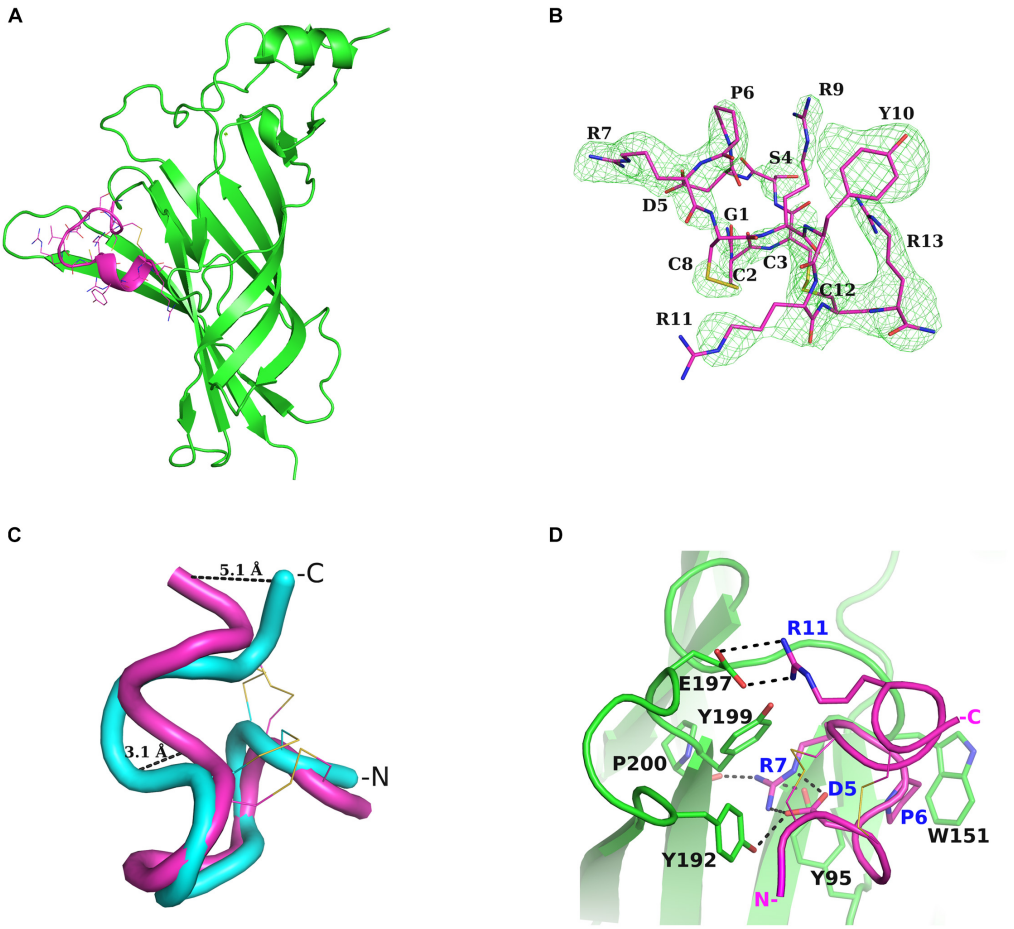

FIGURE 1 | Structure of α-Ctx RgIA bound to nAChR α9-ECD and interactions. **(A)** Overall structure of the complex of monomeric α9-ECD (in green) with α-Ctx RgIA (in magenta). **(B)** Simulated annealing omit map of the region of the bound RgIA, contoured at 3σ. **(C)** Superposition of the NMR structure of RgIA (in cyan) with its crystal structure (in magenta) when bound to α9-ECD, determined in the present study. The highly diverging regions, at the middle helical domain and at the C-terminus, are shown. **(D)** Interaction scheme of RgIA with the (+) side of α9-ECD. The interacting residues are drawn in sticks and the polar or charged interactions are shown in dashed lines. Blue labels account for the RgIA-interacting residues and black labels for the α9-ECD-interacting residues.

comparing the NMR structures of PnIA (PDB ID: 1PEN) (Hu et al., 1996), GIC (PDB ID: 1UL2) (Chi et al., 2004), BuIA (PDB ID: 2I28) (Chi et al., 2006) and LvIA (PDB ID: 2MDQ) (Luo et al., 2014) to their crystal complexes with AChBP (PDB IDs: 2BR8 for PnIA; 5CO5 for GIC; 4EZ1 for BuIA; 5XGL for LvIA) (Celie et al., 2005; Lin et al., 2016; Xu et al., 2017), no differences were noticed regarding their backbone conformations. However, in the case of ImI, which is the most similar α-Ctx to RgIA (**Figure 2B**), two clusters of NMR structures are available; one lacking the α-helical domain in the middle of the toxin (PDB ID: 1CNL) (Gehrmann et al., 1999), similarly to the sole NMR structure of RgIA (PDB ID: 2JUT) (Ellison et al., 2008), and another where the helical domain is present (PDB ID: 1IMI) (Maslennikov et al., 1999) (**Supplementary Figure S2**), as in its crystal complex with AChBP (PDB ID: 2C9T) (Ulens et al., 2006). Thus, it is not clear whether the observed backbone conformational differences between the crystallized RgIA bound to α9-ECD and its NMR structure are induced by its interactions with α9-ECD or could be due to varying in-solution NMR conformational states (as in the case of ImI). Instead, the salt bridge between Asp5 and Arg7 of RgIA is most probably induced by its binding to α9-ECD, since this is also apparent in the crystal complex of ImI with AChBP, while lacking from its varying NMR structures (**Supplementary Figure S2**).

Comparing the α9-ECD/RgIA complex with the structures of AChBPs in their complexes with other α-Ctxs, a strikingly high structural similarity was observed for the bound toxins (**Figure 2A**), despite their differences in sequence composition and length (**Figure 2B**). Specifically, upon superposition of the α9-ECD bound to RgIA with the protomers of AChBPs bound to other α-Ctxs, it was revealed that RgIA has an RMSD value for all paired Cα atoms of 0.773 Å with PnIA (PDB ID: 2BR8) (Celie et al., 2005), 0.778 Å with PeIA (PDB ID: 5JME) (Hone et al., 2018), 0.702 Å with ImI (PDB ID: 2C9T) (Ulens et al., 2006), 0.865 Å with TxIA (PDB ID: 2UZ6) (Dutertre et al., 2007), 1.013 Å with BuIA (PDB ID: 4EZ1), 1.059 Å with GIC (PDB ID: 5CO5) (Lin et al., 2016) and of 1.321 or 0.979 Å with LsIA

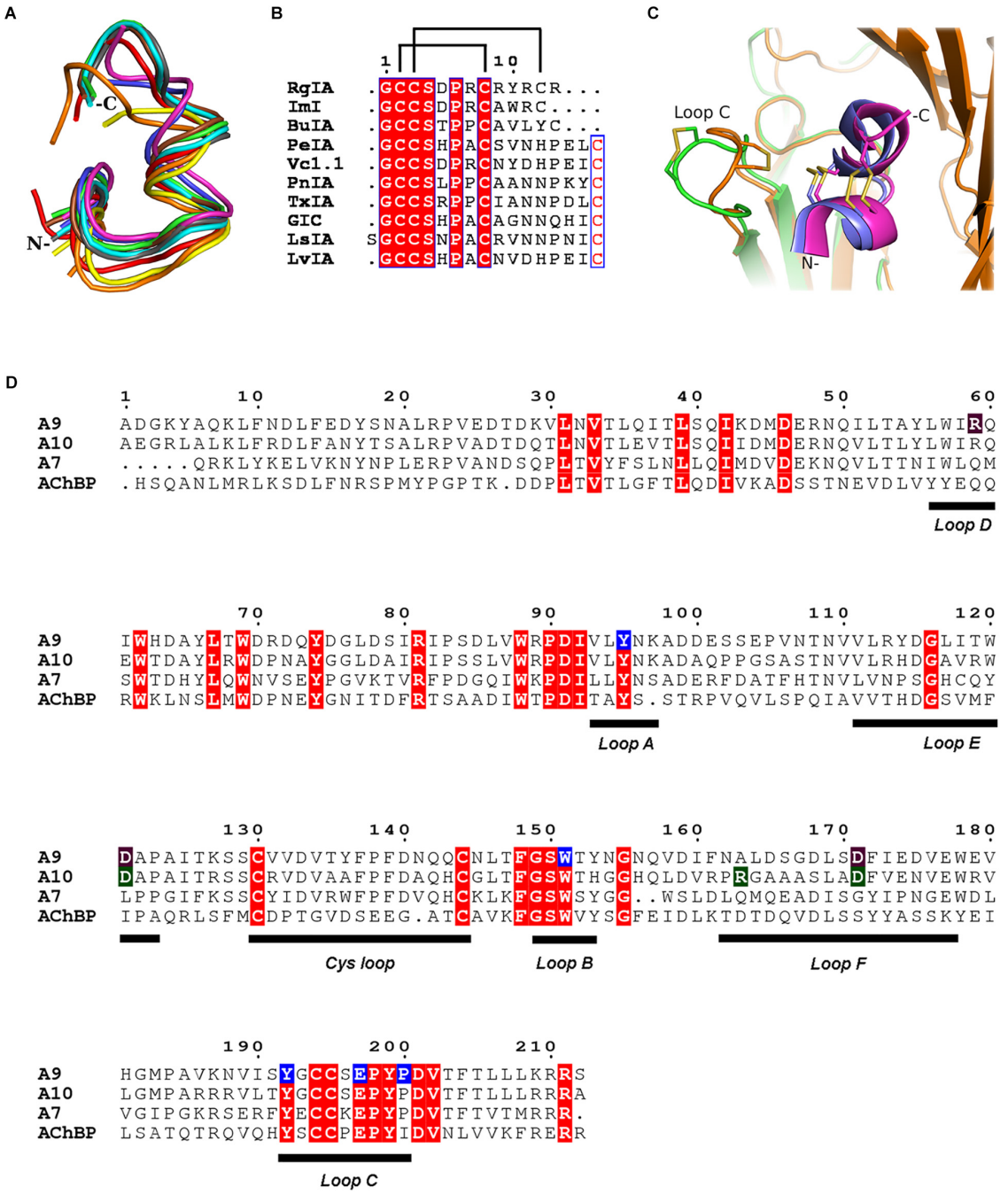

FIGURE 2 | α-Ctxs bound to α9-ECD and homologous proteins. **(A)** Overlay of all crystallized α-Ctxs bound to AChBPs and of RgIA bound to α9-ECD, as a result of the superposition of the protomers of AChBPs to the monomeric α9-ECD (RgIA in magenta, ImI in blue, PeIA in cyan, GIC in green, PnIA in gray, LsIA in red, LvIA in brown, BuIA in yellow, and TxIA in orange). **(B)** Sequence alignment of crystallized α-Ctxs with AChBPs or α9-ECD. Disulfide bridges in RgIA are indicated by lines on top of the alignment. **(C)** Comparison between the AChBP/ImI and α9-ECD/RgIA complexes. AChBP in orange, α9-ECD in green, ImI in blue, and RgIA in magenta. **(D)** Sequence alignment of human α9, α10, α7 nAChR-ECDs and *Lymnaea stagnalis* AChBP. α9(+) side-interacting residues with RgIA, as shown in the crystal structure, in blue boxes; α9(–) and α10(–) interacting residues with RgIA, as shown in the MD studies, in purple and green, respectively.

(PDB ID: 5T90) (Abraham et al., 2017) or LvIA (PDB ID: 5XGL) (Xu et al., 2017), respectively.

Thus, all α-Ctxs in the above complexes adopt similar orientations, but they may be further grouped into three distinct clusters, regarding their backbone trajectories in the above complexes. The α4/3-Ctxs ImI and RgIA comprise the first group, the α4/7-Ctxs GIC, LsIA, LvIA, PeIA, and PnIA fall into the second group and the α4/4-Ctx BuIA is grouped together with the

α4/7-Ctx TxIA (**Supplementary Figure S3**). The members of the first and second groups present an apparent spatial coincidence up to their ninth residue, with RgIA and ImI deviating beyond this point from the other toxins, which on the other hand form a two-turn extended α-helical domain (**Supplementary Figure S3**). RgIA and ImI are identical up to their Cys8 residue and differ in two residues at positions 9 and 10 (ImI-Ala9 and ImI-Trp10 vs. RgIA-Arg9 and RgIA-Tyr10) with RgIA being longer than ImI by a C-terminal Arg residue (**Figure 2B**).

Taken the above into consideration, despite α9-ECD being in a monomeric state, it binds α-Ctx-RgIA in a similar fashion to that of binding of other α-Ctxs to the pentameric AChBPs (**Figure 2A**), as previously shown for the complexes of α9-ECD with α-Bgtx and MLA (Zouridakis et al., 2014). This becomes more evident in **Figure 2C**, which shows the overall very good superposition between the complexes of α9-ECD with RgIA and of AChBP with ImI (Ulens et al., 2006). The above observations suggest that the resolved structure presented here depicts accurately the orientation of RgIA in the binding sites of pentameric α9α10 nAChRs where α9 contributes its (+) side. It should be mentioned that the crystal packing contacts between the bound RgIA and an adjacent symmetric α9-ECD, contributing to the stabilization of the α9-ECD/RgIA complex, affected only the orientation of the side chain of RgIA-Tyr10, as revealed after comparison to its counterpart ImI-Trp10 in the crystal structure of ImI bound to AChBP (**Supplementary Figure S4**).

Interactions of RgIA With α9-ECD

Upon binding, RgIA is buried in the (+) side of α9-ECD (**Figure 1A**) and shares a common orientation with other previously determined α-Ctxs bound to AChBPs (**Figures 2A,C**). Its central helical domain protrudes toward the binding site, while its N- and C-termini are located at the bottom and top of the binding site, respectively (**Figures 1A**, **2C**).

The most profound interactions of RgIA with the (+) side of α9-ECD involve its aspartic residue at position 5 and its arginine residues at positions 7 and 11 (**Figures 1D**, **2B**). RgIA-Asp5 forms a H-bond with loop-C α9-Tyr192, RgIA-Arg7 forms H-bonds with the carbonyl oxygen of loop-C Pro200 and the hydroxyl group of loop-A Tyr95, while RgIA-Arg11 makes a salt bridge with loop-C Glu197 (**Figure 1D**). Additionally, RgIA-Pro6 makes van der Waals interactions with the loop-B Trp151. Notably, the similar α4/3-Ctx ImI makes identical interactions with the (+) side of the binding site of AChBP (Hansen et al., 2005; Ulens et al., 2006), which nevertheless involve highly conserved residues among AChBPs and nAChR α subunits.

Radio-Ligand Competition Experiments

The binding affinity of α-Ctx RgIA to α9-ECD was determined via competition experiments, using the monomeric glycosylated or deglycosylated α9-ECD and radiolabeled [^{125}I]-α-Bgtx (**Figure 3**). The K_i values for the two α9-ECDs, differing in their glycosylation state, were slightly different, with the deglycosylated α9-ECD (the one co-crystallized with RgIA) having 2.7 ± 0.3 μM, and the glycosylated one having 13.3 ± 1.5 μM. Therefore, one could suggest that the interactions presented in the obtained crystal structure with the deglycosylated α9-ECD, depict those occurring in the case of the glycosylated native α9α10 nAChRs, concerning the α9(+) side. Also, these K_i values are in the low micromolar range, as the calculated IC_{50} values for RgIA in human α9α10 nAChRs (Azam and McIntosh, 2012).

Molecular Modeling and MD Simulations of Pentameric Human α9α10 ECDs

With the aim to gain more information about the potential interactions between α-Ctx RgIA and the ligand-binding sites of human α9α10 nAChR, we modeled both possible stoichiometries of the α9α10 nAChR ECD (Indurthi et al., 2014), namely $(\alpha9)_2(\alpha10)_3$ and $(\alpha9)_3(\alpha10)_2$ (**Figure 4**), based on the crystal structures of the complexes α9-ECD/RgIA (**Figure 1A**) and AChBP/ImI (Ulens et al., 2006). In the case of the $(\alpha9)_3(\alpha10)_2$, an additional binding site is formed between α9 ECDs (Indurthi et al., 2014), apart from that between α9 and α10 ECDs in the $(\alpha9)_2(\alpha10)_3$ stoichiometry (Plazas et al., 2005). One RgIA molecule was modeled in the α9(+)/α9(−) or in the α9(+)/α10(−) binding site in the $(\alpha9)_3(\alpha10)_2$ ECD model (**Figures 4A,C**), or in the α10(+)/α9(−) binding site in

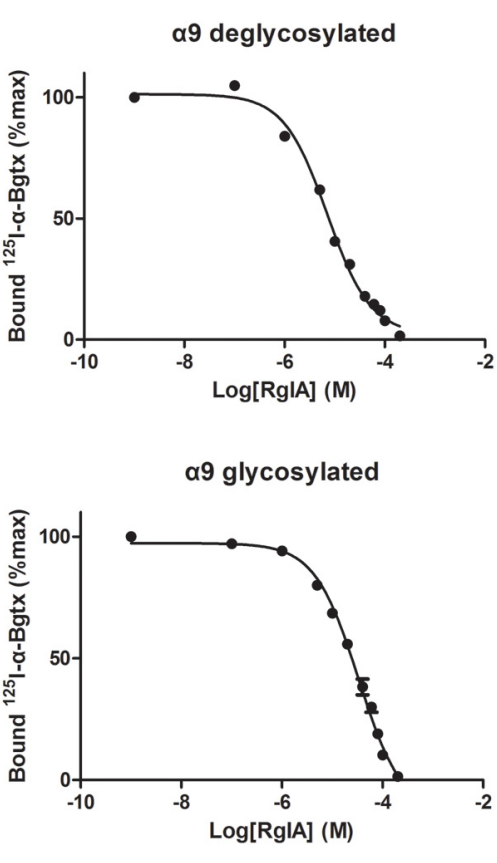

FIGURE 3 | Competition of radiolabeled α-Bgtx by RgIA. **(A)** On deglycosylated α9-ECD **(B)** On glycosylated α9-ECD. Each graph is from four experiments and standard errors are presented with bars.

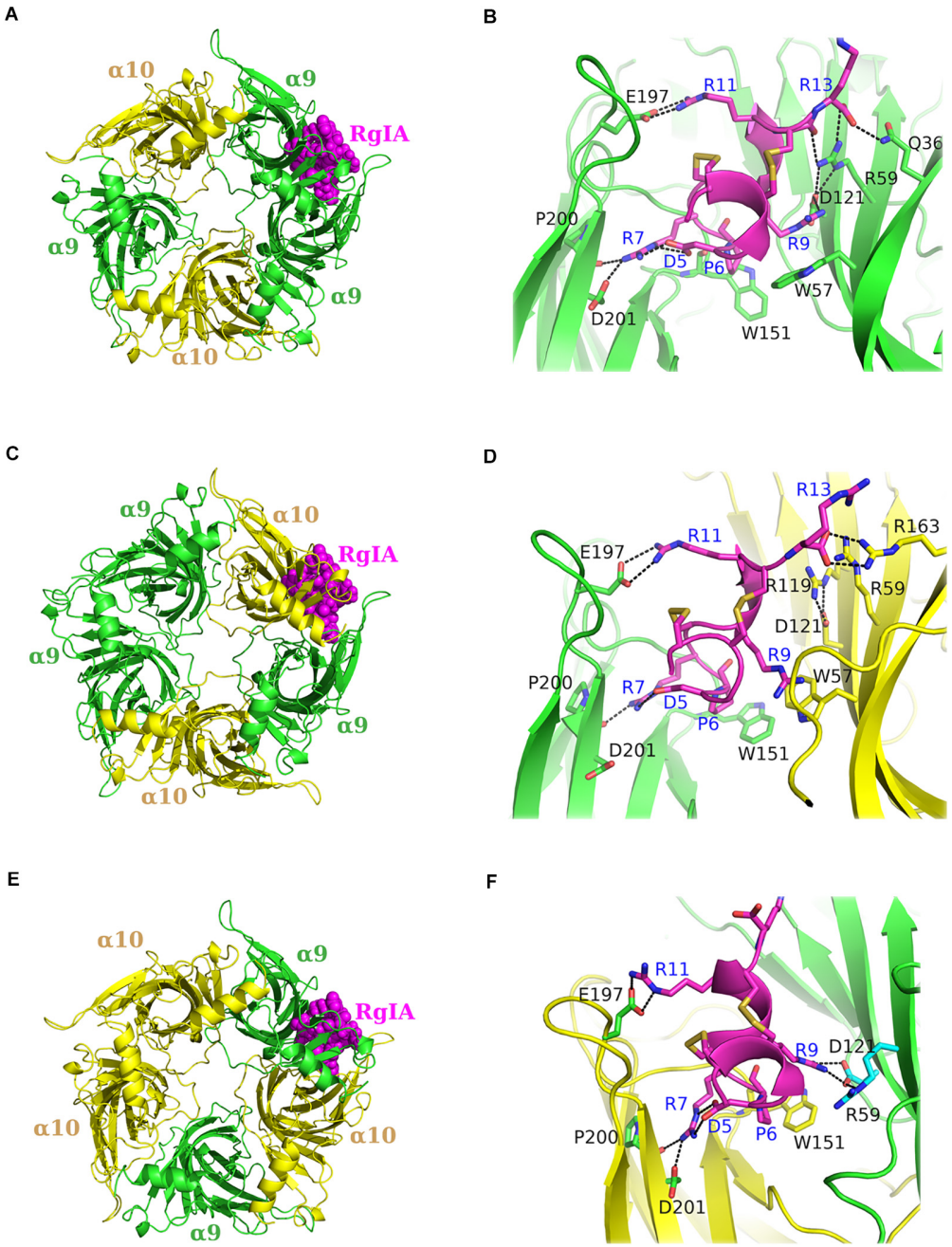

FIGURE 4 | Molecular dynamics (MD) models of α9α10 nAChR-ECDs. **(A,B)** RgIA bound to the α9(+)/α9(−) interface and close view of interactions. **(C,D)** RgIA bound to the α9(+)/α10(−) interface and close view of interactions. **(E,F)** RgIA bound to the α10(+)/α9(−) interface and close view of interactions. α9-ECD in green, α10-ECD in yellow and RgIA in magenta. Labeled in blue are the RgIA-interacting residues and in black the interacting residues of α9 or α10-ECDs.

the model of $(\alpha9)_2(\alpha10)_3$ ECD (**Figure 4E**) (all constructed models are provided as **Supplementary Material** in pdb format). Subsequently, we employed MD simulations for the modeled complexes.

Our MDs revealed that the interactions of RgIA at the (+) sides of the binding sites conferred by α9 or α10 ECDs were almost identical, given the high sequence similarity (77%) between these ECDs (**Figure 2D**). More specifically, the conserved residues Tyr95 and Glu197 formed a hydrogen bond and a salt bridge with RgIA Arg7 and Arg11, respectively, while the conserved Pro200 interacted with a strong hydrogen bond with RgIA-Arg7 (**Figures 4B,D,F**). These interactions were retained throughout the MD simulations (**Figures 5A–C**) and were essentially identical to those shown in the crystal structure of α9-ECD with RgIA (**Figure 1D**). In addition, similarly to the

crystal structure, RgIA-Pro6 interacts favorably with the loop-B Trp151 of both α9(+) and α10(+) sides via CH_2-π interactions (**Figures 4B,D,F**).

At the α9(−) side of either α9(+)/α9(−) or α10(+)/α9(−) binding sites (**Figures 4A,E**), Asp121 and RgIA-Arg9 formed a salt bridge (**Figures 4B,F**), which was stable throughout the course of MD simulations (**Figure 5D**). At both binding sites, α9-Asp121 formed a stable intramolecular interaction with α9-Arg59 (**Figures 4B,F**, **5E**), an interaction present in all previous α9-ECD crystal structures (Zouridakis et al., 2014), as well as in the α9-ECD/RgIA structure, presented here. In the α9(+)/α9(−) binding site, distinctly to the α10(+)/α9(−) binding site, the MD simulations revealed interactions between α9-Gln36 and α9-Arg59 with the carboxylate group of the RgIA C-terminus (**Figure 4B**), which however were short-lived (**Figures 5F,G**), probably due to the high mobility of the RgIA C-terminus, and thus should be considered only transient.

At the α10(−) side of the α9(+)/α10(−) binding site (**Figures 4C,D**), a complete different motif of interactions with RgIA was revealed, probably due to the high accumulation of arginine residues at the α10(−) side (**Figure 4D**). Interestingly, α10-ECD bears two additional arginine residues at positions 119 and 163 of its −) side compared to α9-ECD (**Figures 2D**, **4D**). The stable interaction observed between Asp121 and RgIA-Arg9, when α9 is involved in the (−) side, is no longer present, nor is the intramolecular bond between Asp121 and Arg59 (**Figures 4D**, **5D,E**). Instead, other intramolecular interactions, such as those between Asp121 and Arg119 or between Arg59 and Glu61, stabilize the α10(−) side, but its interactions with RgIA are rather aberrant and transient, apart from the cation-π interaction between α10-Trp57 and RgIA-Arg9 (**Figures 4D**, **5H**).

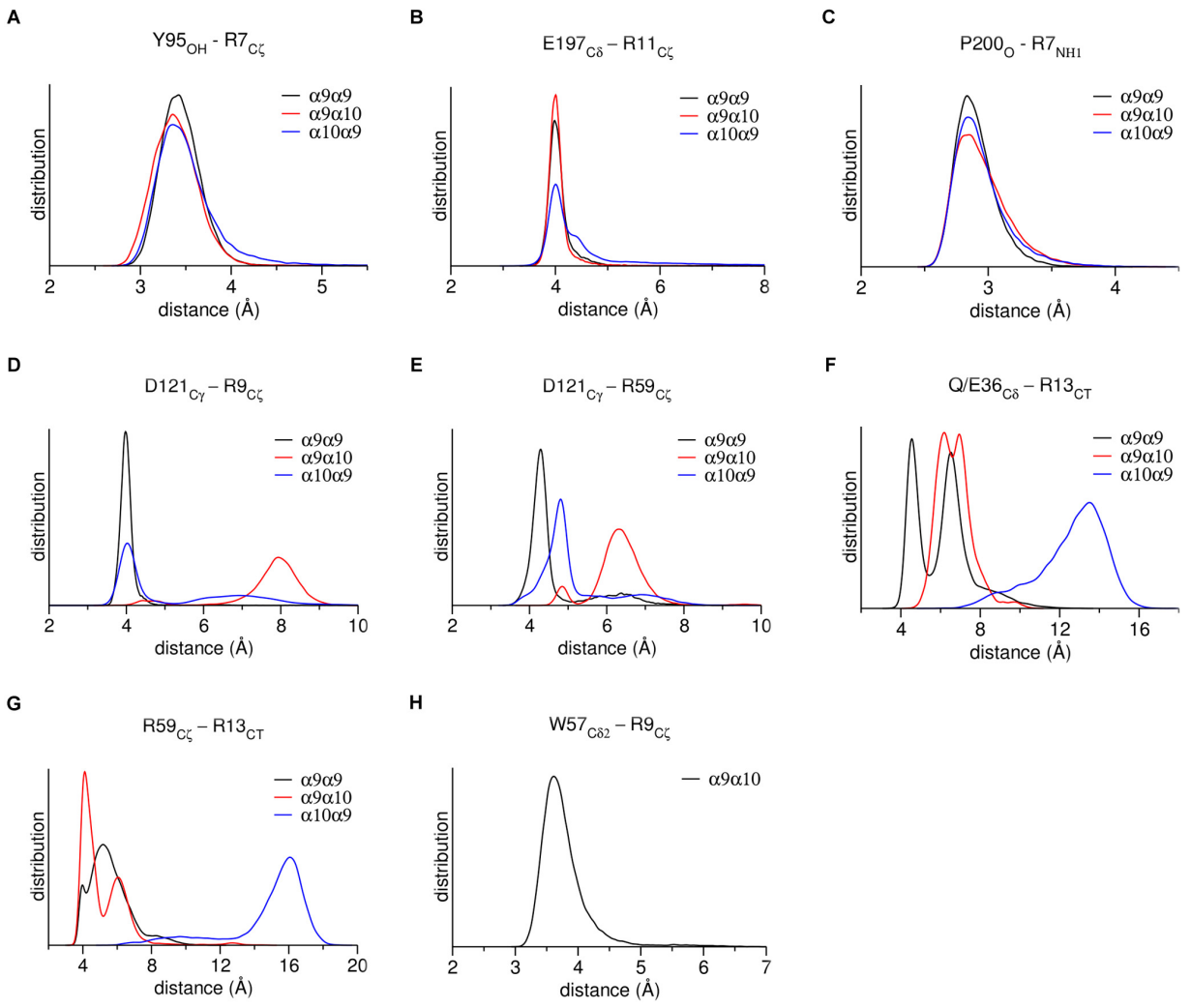

FIGURE 5 | Distribution of distances between characteristic residues, throughout MD simulations. **(A)** α9 or α10 loop-A Tyr95 with RgIA-Arg9. **(B)** α9 or α10 loop-C Glu197 with RgIA-Arg11. **(C)** α9 or α10 loop-C Pro200 with RgIA-Arg7. **(D)** α9 or α10 loop-E Asp121 with RgIA-Arg9. **(E)** Loop-E Asp121 with loop-D Arg59 in α9 or α10 subunits. **(F)** α9-Gln36 or α10-Glu36 with RgIA-Arg13. **(G)** α9 loop-D Arg59 with RgIA-Arg13. **(H)** α10 loop-D Trp57 with RgIA-Arg9.

DISCUSSION

In this study, we determined the crystal structure of the complex of human neuronal nAChR α9-ECD with α-Ctx RgIA, revealing the interactions of RgIA with the α9(+) side (**Figures 1A,D**). The interaction motif of RgIA with α9-ECD is identical to that of α-Ctx ImI with AChBP (Hansen et al., 2005; Ulens et al., 2006), since the involved residues of the two α-Ctxs are identical and the interacting residues of both proteins are highly conserved. Both α-Ctxs interact with α9(+) or AChBP(+) sides through their Asp-Pro-Arg triad of loop 1 and a conserved Arg at position 11 (**Figure 2B**). These observations comply with previous mutational studies, which had shown the critical role of the Asp-Pro-Arg triad to the inhibitory potency of RgIA on α9α10 nAChRs (Ellison et al., 2006, 2008).

Moreover, since the complex of the monomeric α9-ECD with RgIA superimposed very well with the complexes of the pentameric AChBPs with ImI (**Figure 2C**) and other α-Ctxs (**Figure 2A**), this study showed that the (+) side of the α9-ECD alone is adequate to determine the orientation of the bound RgIA. This is similar to previous observations for the complexes of the monomeric α9-ECD with the antagonists MLA and α-Bgtx (Zouridakis et al., 2014). The K_i value of RgIA binding to the deglycosylated α9-ECD was calculated to be 2.7 μM, similar to that for the glycosylated protein (13 μM), which is the form more close to the native α9 subunit (**Figure 3**). Taking also into account that the IC_{50} value of RgIA to human α9α10 nAChRs is also at the low micromolar range (∼0.5 μM) (Azam and McIntosh, 2012), the interactions revealed in the structure of the deglycosylated α9-ECD with RgIA are very likely to depict the ones occurring in the α9(+) side-containing binding sites of native human α9α10 nAChRs.

Notably, α9 and α10 ECDs have a remarkable sequence similarity of 77%, which is even higher for the regions participating in the (+) side (loops A, B, and C) of the binding site (**Figure 2D**). In particular, the (+) sides of the two ECDs differ only in one residue at position 153; α10 has a histidine residue in contrast to tyrosine in α9 and all other nAChR α-subunits. However, this highly conserved tyrosine, as shown in the crystal structures of α9-ECD and other homologous proteins (e.g., Brejc et al., 2001; Kouvatsos et al., 2016; Morales-Perez et al., 2016), faces toward the interior of the protein and has not been considered a binding determinant in nAChRs (Hansen et al., 2005; Ulens et al., 2006). Thus, since the α9(+) and α10(+) sides are almost identical, one can expect that the α10(+) side could also bind RgIA similarly.

Given that α9α10 nAChRs may contain three putative binding sites, namely the α9(+)/α9(−), α9(+)/α10(−), and the α10(+)/α9(−) (Plazas et al., 2005; Ellison et al., 2008; Azam and McIntosh, 2012; Indurthi et al., 2014; Azam et al., 2015; Boffi et al., 2017), we performed MD simulations in order to assess possible preference of RgIA for any of these sites, conferred by the non-conserved (−) sides of α9 or α10 ECDs. Previous attempts of modeling the complex of RgIA with the ECD of α9α10 nAChR have yielded controversial results: Perez et al. (2009) suggested that the favorable binding site for RgIA is the α9(+)/α10(−), whereas Azam et al. (2015) proposed the α10(+)/α9(−), complying with their mutational and electrophysiological data. However, these models were based on the X-ray crystal structures of either the AChBP/ImI complex alone (Ulens et al., 2006), or on the α9-ECD apo structure (Zouridakis et al., 2014) and AChBP/ImI complex. In the current study, the X-ray structure of α9-ECD in complex with RgIA was used as a template together with the AChBP/ImI complex for modeling of the binding sites of the human α9α10 nAChR.

As expected, due to the substantial similarity of the (+) sides of α9 and α10 ECDs, the MD studies showed that RgIA forms similar interactions with them (**Figures 4B,D,F**), some of which have been previously evaluated by mutational studies. The mutation α9-Trp151 to threonine has led to a ∼10-fold increase of the IC_{50} value of RgIA to α9α10 nAChRs (Ellison et al., 2008), while the single-point mutations Glu197Gln or Pro200Gln at the α10(+) side have shown a ∼20- or ∼400-fold decrease in the potency of RgIA to α9α10 nAChRs (Azam et al., 2015).

Instead, the interactions formed between RgIA and the non-conserved (−) sides of α9 or α10 ECDs are significantly different:

(a) At the α9(+)/α9(−) and α10(+)/α9(−) interfaces, the (−) side of α9-ECD forms a critical salt bridge between α9-Asp121 and RgIA-Arg9 (**Figures 4B,F**, **5D**). This interaction was previously shown to be very important for the potency of both ACh and RgIA on α9α10 nAChRs, since mutation α9-Asp121Leu increased the corresponding EC_{50} or IC_{50} values by ∼30 times or by three orders of magnitude, respectively (Azam et al., 2015).

(b) At the α9(+)/α10(−) interface, where the (−) side of α10-ECD is densely populated by positively charged residues (**Figures 4D**, **6**), the interaction of Asp121 with RgIA-Arg9, shown at the α9(+)/α9(−) and α10(+)/α9(−) interfaces, is disrupted; instead, α10-Asp121 makes an intramolecular salt bridge with α10-Arg119, whereas RgIA-Arg9 makes a cation-π interaction with the α10-Trp57 (**Figure 4D**). However, this interaction in α9(+)/α10(−) interfaces, if applicable in nature, could not justify the selectivity of RgIA on α9α10 nAChRs, since this loop-D tryptophan residue is invariant among all nAChR subunits. The observations for the modeled α9(+)/α10(−) interface comply with previous functional data which showed that the mutation α10-Asp121Leu did not affect the inhibitory potency of RgIA on α9α10 nAChRs (Azam et al., 2015).

The differences in the binding motif of RgIA with the α10(−) side compared to the α9(−) side may be attributed to repulsive

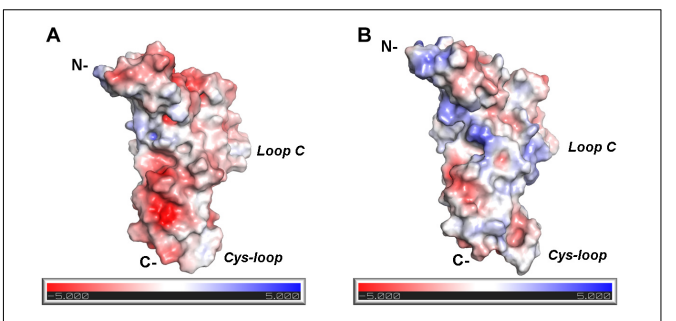

FIGURE 6 | Electrostatic potential distribution at the (–) sides of α9 and α10 nAChR-ECDs. **(A)** α9-ECD. **(B)** α10-ECD.

forces between the profoundly more positively charged α10(−) side (**Figure 6**) and the positively charged RgIA. A first indication supporting the role of electrostatics in the binding of RgIA is the calculated non-bonded interaction energies extracted from the MD simulations of each pentameric assembly. The electrostatic term of the interaction energy (E_{elec}) was calculated to be −743 ± 37 kcal/mol for α9(+)α9(−), −620 ± 87 kcal/mol for α10(+)α9(−), and −498 ± 86 kcal/mol for α9(−)α10(+). The corresponding van der Waals interaction energy terms (E_{vdW}) are calculated to be −95 ± 11 kcal/mol α9(+)α9(−), −74 ± 10 kcal/mol for α10(+)α9(−), and −69 ± 17 kcal/mol for α9(+)α10(−). In addition, the interface areas formed by two adjacent subunits with bound RgIA, in the cases of α9(+)/α9(−) and α10(+)/α9(−) are 1084 ± 121 Å^2 and 1050 ± 80 Å^2, respectively, close to the experimentally determined one (1194 ± 33 Å^2) from the structure of AChBP with α-Ctx ImI (Ulens et al., 2006). Instead, in the case of α9(+)/α10(−), the interface area is significantly lower (685 ± 79 Å^2), indicating a rather aberrant assembly between these two subunits in the presence of α-Ctx RgIA. Taken together, our results indicate the lower affinity of RgIA binding at the α9(+)α10(−) site with respect to the α9(+)α9(−) and α10(+)α9(−), in well agreement with previous mutational and functional data, which have shown that the (+) side of RgIA binding is conferred by either α9 or α10 subunits (Ellison et al., 2008; Azam et al., 2015) and the (−) side by α9 rather than α10 (Azam and McIntosh, 2012; Azam et al., 2015). It seems plausible that the arginine residues at positions 119 and 163 at the (−) side of α10-ECD, which in the case of α9 correspond to threonine and alanine, respectively (**Figure 2D**), contribute critically to the repulsion of α-Ctx RgIA in α10(−) side-containing binding sites. It is noteworthy that α10 is the only nAChR α-subunit bearing charged residues at these sites.

In the presented crystal structure of the complex of α9-ECD with RgIA, and in the structures of the free α9-ECD and of its complexes with α-Bgtx and MLA (Zouridakis et al., 2014), Asp121 forms a stable salt bridge with the adjacent Arg59. Notably, these charged residues are uniquely present in the α9 and α10 nAChR subunits. Our MD simulations showed that this interaction was retained in the α9(−) side in both α9(+)/α9(−) and α10(+)/α9(−) binding sites, but was disrupted in the α10(−) side throughout the simulations (**Figure 5E**), despite its presence in the initial α10-ECD model. Thus, in the case of the α9(+)/α10(−) binding site, where the (−) side of α10-ECD is more positively charged, structural rearrangements of residues at the α10(−) side occurred in the course of MD simulations, in order to accommodate the also positively charged RgIA, leading to different interactions with RgIA (**Figure 4D**) compared to those with the α9(−) side (**Figures 4B,F**).

Interestingly, other α9α10 selective α-Ctxs are PeIA and Vc1.1, which despite being α4/7-Ctxs, have a potency for the rat α9α10 nAChR (IC_{50} of 7 or 19 nM, respectively) comparable with that of RgIA (IC_{50} = 4.5 nM) (McIntosh et al., 2005; Clark et al., 2006; Vincler et al., 2006). PeIA and Vc1.1 have almost identical loop-2 compositions, but completely different than that of RgIA (**Figure 2B**). In addition, PeIA lacks the loop-1 Asp-Pro-Arg triad, shown to make critical interactions with the α9(+) side in the α9-ECD/RgIA crystal structure and with the (+) sides of the presented α9α10 nAChR-ECD models. Thus, the selectivity of these α-Ctxs to α9α10 nAChRs has to deal with other interactions than those between RgIA and the receptor.

Several models of pain and inflammation have demonstrated that α9α10 nAChRs play a role in modulating the pathophysiology associated with neuropathic pain (Di Cesare Mannelli et al., 2014; Pacini et al., 2016). The analgesic and anti-inflammatory effects of RgIA and Vc1.1 via inhibition of the α9α10 nAChR have also been demonstrated (Satkunanathan et al., 2005; Vincler et al., 2006). However, it has been proposed that the effects of these α-Ctxs can also be transmitted via inhibition of $GABA_β$ receptors (Callaghan et al., 2008; Sadeghi et al., 2017). Vc1.1 was tested as the first nAChR-targeting α-Ctx for the treatment of neuropathic pain, but since it was demonstrated that, similarly to RgIA (Azam and McIntosh, 2012), Vc1.1 was several orders of magnitude less potent in humans than in rats (Terlau and Olivera, 2004; Halai et al., 2009), clinical trials were discontinued. The difference in potency of RgIA between human and rat α9α10 nAChRs has been attributed to a specific residue located at position 61 of α9 (Ile in humans vs. Thr in rats), at its (−) side (Azam and McIntosh, 2012). Previous MD studies indicated that this threonine residue in rat α9α10 nAChRs coordinates a network of interactions within α9 (−) side, facilitating the binding of RgIA to these receptors (Azam et al., 2015). Efforts to improve the potency of RgIA in human α9α10 nAChRs have led to an over 1000-fold more potent analog (RgIA4) (Romero et al., 2017), shown to be an effective analgesic in a model of neuropathic pain (Christensen et al., 2017; Romero et al., 2017), while being highly selective for α9α10 nAChRs over $GABA_β$ receptors. Notably, in this analog, among other drastic changes, the positively charged Arg residues at positions 9, 11, and 13 were replaced by the neutral citrulline, Qln, and Tyr residues, respectively. These replacements have probably alleviated the repulsive forces between RgIA and (−) sides of α9α10 nAChRs, while maintaining the ability of RgIA to make interactions with α9α10 nAChRs, but via H-bonding. However, in order to deeply understand the interactions of RgIA4 with α9α10 nAChRs, additional detailed structural studies involving RgIA4 are needed. The findings of the present study, showing the actual interactions of RgIA with the (+) side of the human α9-ECD and the indicative interactions in the fully assembled binding sites of the human α9α10 nAChR ECD, may be helpful for the design of improved therapeutic analogs.

CONCLUSION

The first crystal structure of a human nAChR domain with an α-Ctx is presented. The structure revealed the interactions between α-Ctx RgIA and the (+) side of neuronal nAChR α9-ECD in high detail. Based on the structure of this complex, models of human α9α10 nAChR ECD with fully formed binding sites were constructed with RgIA bound to each of them. Our MD simulations suggest that the favorable binding site of RgIA in the human α9α10 nAChR ECD consists of either α9 or

α10 subunits as the (+) side and of an adjacent α9 rather than α10 subunit as the (−) side. The results of this study may be helpful to medicinal chemists for design of improved RgIA analogs targeting the human α9α10 nAChR against auditory diseases and neuropathic pain.

AUTHOR CONTRIBUTIONS

MZ and PG conceived the project, expressed and purified α9-ECD, conducted the competition experiments, crystallized the complex of α9-ECD with α-Ctx RgIA and solved the crystal structure. PG, MZ, and IK designed the experiments. II and IK synthesized and purified the α-Ctx RgIA and AP performed and analyzed the MD simulations. PG, MZ, and AP wrote the manuscript. ST and VT contributed to management of the project and edited the manuscript. All authors reviewed and approved the manuscript.

FUNDING

This work was supported by a grant from Stavros Niarchos Foundation (ST and MZ), by RSF (Grant No. 16-14-00215) (VT and II), by RFBR (Grant No. 18-04-01366) (IK) and by BioStruct-X (Contract No. 283570/3521).

SUPPLEMENTARY MATERIAL

The Supplementary Material for this article can be found online at: https://www.frontiersin.org/articles/10.3389/fphar.2019.00474/full#supplementary-material

REFERENCES

Abraham, N., Healy, M., Ragnarsson, L., Brust, A., Alewood, P. F., and Lewis, R. J. (2017). Structural mechanisms for alpha-conotoxin activity at the human alpha3beta4 nicotinic acetylcholine receptor. *Sci. Rep.* 7:45466. doi: 10.1038/srep45466

Afonine, P. V., Grosse-Kunstleve, R. W., Echols, N., Headd, J. J., Moriarty, N. W., Mustyakimov, M., et al. (2012). Towards automated crystallographic structure refinement with phenix.refine. *Acta Crystallogr. D Biol. Crystallogr.* 68(Pt 4), 352–367. doi: 10.1107/S0907444912001308

Albuquerque, E. X., Pereira, E. F., Alkondon, M., and Rogers, S. W. (2009). Mammalian nicotinic acetylcholine receptors: from structure to function. *Physiol. Rev.* 89, 73–120. doi: 10.1152/physrev.00015.2008

Azam, L., and McIntosh, J. M. (2009). Alpha-conotoxins as pharmacological probes of nicotinic acetylcholine receptors. *Acta Pharmacol. Sin.* 30, 771–783. doi: 10.1038/aps.2009.47

Azam, L., and McIntosh, J. M. (2012). Molecular basis for the differential sensitivity of rat and human alpha9alpha10 nAChRs to alpha-conotoxin RgIA. *J. Neurochem.* 122, 1137–1144. doi: 10.1111/j.1471-4159.2012.07867.x

Azam, L., Papakyriakou, A., Zouridakis, M., Giastas, P., Tzartos, S. J., and McIntosh, J. M. (2015). Molecular interaction of alpha-conotoxin RgIA with the rat alpha9alpha10 nicotinic acetylcholine receptor. *Mol. Pharmacol.* 87, 855–864. doi: 10.1124/mol.114.096511

Beckmann, J., and Lips, K. S. (2013). The non-neuronal cholinergic system in health and disease. *Pharmacology* 92, 286–302. doi: 10.1159/000355835

Boffi, J. C., Marcovich, I., Gill-Thind, J. K., Corradi, J., Collins, T., Lipovsek, M. M., et al. (2017). Differential contribution of subunit interfaces to alpha9alpha10 nicotinic acetylcholine receptor function. *Mol. Pharmacol.* 91, 250–262. doi: 10.1124/mol.116.107482

Bourne, Y., Sulzenbacher, G., Radic, Z., Araoz, R., Reynaud, M., Benoit, E., et al. (2015). Marine macrocyclic imines, pinnatoxins A and G: structural determinants and functional properties to distinguish neuronal alpha7 from muscle alpha1(2)betagammadelta nAChRs. *Structure* 23, 1106–1115. doi: 10.1016/j.str.2015.04.009

Brejc, K., van Dijk, W. J., Klaassen, R. V., Schuurmans, M., van Der Oost, J., Smit, A. B., et al. (2001). Crystal structure of an ACh-binding protein reveals the ligand-binding domain of nicotinic receptors. *Nature* 411, 269–276. doi: 10.1038/35077011

Callaghan, B., Haythornthwaite, A., Berecki, G., Clark, R. J., Craik, D. J., and Adams, D. J. (2008). Analgesic alpha-conotoxins Vc1.1 and Rg1A inhibit N-type calcium channels in rat sensory neurons via GABAB receptor activation. *J. Neurosci.* 28, 10943–10951. doi: 10.1523/JNEUROSCI.3594-08.2008

Case, D. A., Cheatham, T. E. III, Darden, T., Gohlke, H., Luo, R., Merz, K. M., et al. (2005). The Amber biomolecular simulation programs. *J. Comput. Chem.* 26, 1668–1688. doi: 10.1002/jcc.20290

Celie, P. H., Kasheverov, I. E., Mordvintsev, D. Y., Hogg, R. C., van Nierop, P., van Elk, R., et al. (2005). Crystal structure of nicotinic acetylcholine receptor homolog AChBP in complex with an alpha-conotoxin PnIA variant. *Nat. Struct. Mol. Biol.* 12, 582–588. doi: 10.1038/nsmb951

Celie, P. H., van Rossum-Fikkert, S. E., van Dijk, W. J., Brejc, K., Smit, A. B., and Sixma, T. K. (2004). Nicotine and carbamylcholine binding to nicotinic acetylcholine receptors as studied in AChBP crystal structures. *Neuron* 41, 907–914. doi: 10.1016/s0896-6273(04)00115-1

Chi, S. W., Kim, D. H., Olivera, B. M., McIntosh, J. M., and Han, K. H. (2004). Solution conformation of alpha-conotoxin GIC, a novel potent antagonist of alpha3beta2 nicotinic acetylcholine receptors. *Biochem. J.* 380(Pt 2), 347–352. doi: 10.1042/BJ20031792

Chi, S. W., Kim, D. H., Olivera, B. M., McIntosh, J. M., and Han, K. H. (2006). NMR structure determination of alpha-conotoxin BuIA, a novel neuronal nicotinic acetylcholine receptor antagonist with an unusual 4/4 disulfide scaffold. *Biochem. Biophys. Res. Commun.* 349, 1228–1234. doi: 10.1016/j.bbrc.2006.08.164

Christensen, S. B., Hone, A. J., Roux, I., Kniazeff, J., Pin, J. P., Upert, G., et al. (2017). RgIA4 potently blocks mouse alpha9alpha10 nAChRs and provides long lasting protection against oxaliplatin-induced cold allodynia. *Front. Cell. Neurosci.* 11:219. doi: 10.3389/fncel.2017.00219

Clark, R. J., Daly, N. L., Halai, R., Nevin, S. T., Adams, D. J., and Craik, D. J. (2008). The three-dimensional structure of the analgesic alpha-conotoxin, RgIA. *FEBS Lett.* 582, 597–602. doi: 10.1016/j.febslet.2008.01.027

Clark, R. J., Fischer, H., Nevin, S. T., Adams, D. J., and Craik, D. J. (2006). The synthesis, structural characterization, and receptor specificity of the alpha-conotoxin Vc1.1. *J. Biol. Chem.* 281, 23254–23263. doi: 10.1074/jbc.M604550200

Dellisanti, C. D., Yao, Y., Stroud, J. C., Wang, Z. Z., and Chen, L. (2007). Crystal structure of the extracellular domain of nAChR alpha1 bound to alpha-bungarotoxin at 1.94 A resolution. *Nat. Neurosci.* 10, 953–962. doi: 10.1038/nn1942

Di Cesare Mannelli, L., Cinci, L., Micheli, L., Zanardelli, M., Pacini, A., McIntosh, J. M., et al. (2014). alpha-conotoxin RgIA protects against the development of nerve injury-induced chronic pain and prevents both neuronal and glial derangement. *Pain* 155, 1986–1995. doi: 10.1016/j.pain.2014.06.023

Dineley, K. T., Pandya, A. A., and Yakel, J. L. (2015). Nicotinic ACh receptors as therapeutic targets in CNS disorders. *Trends Pharmacol. Sci.* 36, 96–108. doi: 10.1016/j.tips.2014.12.002

Dutertre, S., Ulens, C., Buttner, R., Fish, A., van Elk, R., Kendel, Y., et al. (2007). AChBP-targeted alpha-conotoxin correlates distinct binding orientations with nAChR subtype selectivity. *EMBO J.* 26, 3858–3867. doi: 10.1038/sj.emboj.7601785

Elgoyhen, A. B., Johnson, D. S., Boulter, J., Vetter, D. E., and Heinemann, S. (1994). Alpha 9: an acetylcholine receptor with novel pharmacological properties

expressed in rat cochlear hair cells. *Cell* 79, 705–715. doi: 10.1016/0092-8674(94)90555-X

Elgoyhen, A. B., Katz, E., and Fuchs, P. A. (2009). The nicotinic receptor of cochlear hair cells: a possible pharmacotherapeutic target? *Biochem. Pharmacol.* 78, 712–719. doi: 10.1016/j.bcp.2009.05.023

Elgoyhen, A. B., and Langguth, B. (2010). Pharmacological approaches to the treatment of tinnitus. *Drug Discov. Today* 15, 300–305. doi: 10.1016/j.drudis.2009.11.003

Elgoyhen, A. B., Vetter, D. E., Katz, E., Rothlin, C. V., Heinemann, S. F., and Boulter, J. (2001). alpha10: a determinant of nicotinic cholinergic receptor function in mammalian vestibular and cochlear mechanosensory hair cells. *Proc. Natl. Acad. Sci. U.S.A.* 98, 3501–3506. doi: 10.1073/pnas.051622798

Ellison, M., Feng, Z. P., Park, A. J., Zhang, X., Olivera, B. M., McIntosh, J. M., et al. (2008). Alpha-RgIA, a novel conotoxin that blocks the alpha9alpha10 nAChR: structure and identification of key receptor-binding residues. *J. Mol. Biol.* 377, 1216–1227. doi: 10.1016/j.jmb.2008.01.082

Ellison, M., Haberlandt, C., Gomez-Casati, M. E., Watkins, M., Elgoyhen, A. B., McIntosh, J. M., et al. (2006). Alpha-RgIA: a novel conotoxin that specifically and potently blocks the alpha9alpha10 nAChR. *Biochemistry* 45, 1511–1517. doi: 10.1021/bi0520129

Emsley, P., Lohkamp, B., Scott, W. G., and Cowtan, K. (2010). Features and development of coot. *Acta Crystallogr. D Biol. Crystallogr.* 66(Pt 4), 486–501. doi: 10.1107/S0907444910007493

Engel, A. G., Shen, X. M., Selcen, D., and Sine, S. M. (2015). Congenital myasthenic syndromes: pathogenesis, diagnosis, and treatment. *Lancet Neurol.* 14, 420–434. doi: 10.1016/s1474-4422(14)70201-7

Evans, P. (2006). Scaling and assessment of data quality. *Acta Crystallogr. D Biol. Crystallogr.* 62(Pt 1), 72–82. doi: 10.1107/S0907444905036693

Evans, P. R. (2011). An introduction to data reduction: space-group determination, scaling and intensity statistics. *Acta Crystallogr. D Biol. Crystallogr.* 67(Pt 4), 282–292. doi: 10.1107/S090744491003982X

Fiser, A., and Sali, A. (2003). Modeller: generation and refinement of homology-based protein structure models. *Methods Enzymol.* 374, 461–491. doi: 10.1016/S0076-6879(03)74020-8

Gehrmann, J., Daly, N. L., Alewood, P. F., and Craik, D. J. (1999). Solution structure of alpha-conotoxin ImI by 1H nuclear magnetic resonance. *J. Med. Chem.* 42, 2364–2372. doi: 10.1021/jm990114p

Giastas, P., Zouridakis, M., and Tzartos, S. J. (2018). Understanding structure-function relationships of the human neuronal acetylcholine receptor: insights from the first crystal structures of neuronal subunits. *Br. J. Pharmacol.* 175, 1880–1891. doi: 10.1111/bph.13838

Gotti, C., Moretti, M., Gaimarri, A., Zanardi, A., Clementi, F., and Zoli, M. (2007). Heterogeneity and complexity of native brain nicotinic receptors. *Biochem. Pharmacol.* 74, 1102–1111. doi: 10.1016/j.bcp.2007.05.023

Gotti, C., Zoli, M., and Clementi, F. (2006). Brain nicotinic acetylcholine receptors: native subtypes and their relevance. *Trends Pharmacol. Sci.* 27, 482–491. doi: 10.1016/j.tips.2006.07.004

Halai, R., Clark, R. J., Nevin, S. T., Jensen, J. E., Adams, D. J., and Craik, D. J. (2009). Scanning mutagenesis of alpha-conotoxin Vc1.1 reveals residues crucial for activity at the alpha9alpha10 nicotinic acetylcholine receptor. *J. Biol. Chem.* 284, 20275–20284. doi: 10.1074/jbc.M109.015339

Hansen, S. B., Sulzenbacher, G., Huxford, T., Marchot, P., Taylor, P., and Bourne, Y. (2005). Structures of Aplysia AChBP complexes with nicotinic agonists and antagonists reveal distinctive binding interfaces and conformations. *EMBO J.* 24, 3635–3646. doi: 10.1038/sj.emboj.7600828

Hecker, A., Kullmar, M., Wilker, S., Richter, K., Zakrzewicz, A., Atanasova, S., et al. (2015). Phosphocholine-modified macromolecules and canonical nicotinic agonists inhibit ATP-induced IL-1beta release. *J. Immunol.* 195, 2325–2334. doi: 10.4049/jimmunol.1400974

Hone, A. J., and McIntosh, J. M. (2018). Nicotinic acetylcholine receptors in neuropathic and inflammatory pain. *FEBS Lett.* 592, 1045–1062. doi: 10.1002/1873-3468.12884

Hone, A. J., Talley, T. T., Bobango, J., Huidobro Melo, C., Hararah, F., Gajewiak, J. B., et al. (2018). Molecular determinants of alpha-conotoxin potency for inhibition of human and rat alpha6beta4 nicotinic acetylcholine receptors. *J. Biol. Chem.* 293, 17838–17852. doi: 10.1074/jbc.RA118.005649

Hopkins, C. W., Le Grand, S., Walker, R. C., and Roitberg, A. E. (2015). Long-time-step molecular dynamics through hydrogen mass repartitioning. *J. Chem. Theory Comput.* 11, 1864–1874. doi: 10.1021/ct5010406

Hu, S. H., Gehrmann, J., Guddat, L. W., Alewood, P. F., Craik, D. J., and Martin, J. L. (1996). The 1.1 A crystal structure of the neuronal acetylcholine receptor antagonist, alpha-conotoxin PnIA from *Conus pennaceus*. *Structure* 4, 417–423. doi: 10.1016/s0969-2126(96)00047-0

Humphrey, W., Dalke, A., and Schulten, K. (1996). VMD: visual molecular dynamics. *J. Mol. Graph.* 14, 33–38, 27–28.

Indurthi, D. C., Pera, E., Kim, H. L., Chu, C., McLeod, M. D., McIntosh, J. M., et al. (2014). Presence of multiple binding sites on alpha9alpha10 nAChR receptors alludes to stoichiometric-dependent action of the alpha-conotoxin, Vc1.1. *Biochem. Pharmacol.* 89, 131–140. doi: 10.1016/j.bcp.2014.02.002

Janes, R. W. (2005). alpha-Conotoxins as selective probes for nicotinic acetylcholine receptor subclasses. *Curr. Opin. Pharmacol.* 5, 280–292. doi: 10.1016/j.coph.2005.01.013

Kabsch, W. (2010). Xds. *Acta Crystallogr. D Biol. Crystallogr.* 66(Pt 2), 125–132. doi: 10.1107/S0907444909047337

Karplus, P. A., and Diederichs, K. (2012). Linking crystallographic model and data quality. *Science* 336, 1030–1033. doi: 10.1126/science.1218231

Kouvatsos, N., Giastas, P., Chroni-Tzartou, D., Poulopoulou, C., and Tzartos, S. J. (2016). Crystal structure of a human neuronal nAChR extracellular domain in pentameric assembly: ligand-bound alpha2 homopentamer. *Proc. Natl. Acad. Sci. U.S.A.* 113, 9635–9640. doi: 10.1073/pnas.1602619113

Lester, H. A., Dibas, M. I., Dahan, D. S., Leite, J. F., and Dougherty, D. A. (2004). Cys-loop receptors: new twists and turns. *Trends Neurosci.* 27, 329–336. doi: 10.1016/j.tins.2004.04.002

Li, S. X., Huang, S., Bren, N., Noridomi, K., Dellisanti, C. D., Sine, S. M., et al. (2011). Ligand-binding domain of an alpha7-nicotinic receptor chimera and its complex with agonist. *Nat. Neurosci.* 14, 1253–1259. doi: 10.1038/nn.2908

Lin, B., Xu, M., Zhu, X., Wu, Y., Liu, X., Zhangsun, D., et al. (2016). From crystal structure of alpha-conotoxin GIC in complex with Ac-AChBP to molecular determinants of its high selectivity for alpha3beta2 nAChR. *Sci. Rep.* 6:22349. doi: 10.1038/srep22349

Luo, S., Zhangsun, D., Schroeder, C. I., Zhu, X., Hu, Y., Wu, Y., et al. (2014). A novel alpha4/7-conotoxin LvIA from Conus lividus that selectively blocks alpha3beta2 vs. alpha6/alpha3beta2beta3 nicotinic acetylcholine receptors. *FASEB J.* 28, 1842–1853. doi: 10.1096/fj.13-244103

Lustig, L. R., Peng, H., Hiel, H., Yamamoto, T., and Fuchs, P. A. (2001). Molecular cloning and mapping of the human nicotinic acetylcholine receptor alpha10 (CHRNA10). *Genomics* 73, 272–283. doi: 10.1006/geno.2000.6503

Maier, J. A., Martinez, C., Kasavajhala, K., Wickstrom, L., Hauser, K. E., and Simmerling, C. (2015). ff14SB: improving the accuracy of protein side chain and backbone parameters from ff99SB. *J. Chem. Theory Comput.* 11, 3696–3713. doi: 10.1021/acs.jctc.5b00255

Maslennikov, I. V., Shenkarev, Z. O., Zhmak, M. N., Ivanov, V. T., Methfessel, C., Tsetlin, V. I., et al. (1999). NMR spatial structure of alpha-conotoxin ImI reveals a common scaffold in snail and snake toxins recognizing neuronal nicotinic acetylcholine receptors. *FEBS Lett.* 444, 275–280. doi: 10.1016/s0014-5793(99)00069-1

McCoy, A. J., Grosse-Kunstleve, R. W., Adams, P. D., Winn, M. D., Storoni, L. C., and Read, R. J. (2007). Phaser crystallographic software. *J. Appl. Crystallogr.* 40(Pt 4), 658–674. doi: 10.1107/S0021889807021206

McIntosh, J. M., Plazas, P. V., Watkins, M., Gomez-Casati, M. E., Olivera, B. M., and Elgoyhen, A. B. (2005). A novel alpha-conotoxin, PeIA, cloned from *Conus pergrandis*, discriminates between rat alpha9alpha10 and alpha7 nicotinic cholinergic receptors. *J. Biol. Chem.* 280, 30107–30112. doi: 10.1074/jbc.M504102200

Millar, N. S., and Gotti, C. (2009). Diversity of vertebrate nicotinic acetylcholine receptors. *Neuropharmacology* 56, 237–246. doi: 10.1016/j.neuropharm.2008.07.041

Morales-Perez, C. L., Noviello, C. M., and Hibbs, R. E. (2016). X-ray structure of the human alpha4beta2 nicotinic receptor. *Nature* 538, 411–415. doi: 10.1038/nature19785

Nemecz, A., Prevost, M. S., Menny, A., and Corringer, P. J. (2016). Emerging molecular mechanisms of signal transduction in pentameric ligand-gated ion channels. *Neuron* 90, 452–470. doi: 10.1016/j.neuron.2016.03.032

Nemecz, A., and Taylor, P. (2011). Creating an alpha7 nicotinic acetylcholine recognition domain from the acetylcholine-binding protein: crystallographic and ligand selectivity analyses. *J. Biol. Chem.* 286, 42555–42565. doi: 10.1074/jbc.M111.286583

Nicke, A., Wonnacott, S., and Lewis, R. J. (2004). Alpha-conotoxins as tools for the elucidation of structure and function of neuronal nicotinic acetylcholine receptor subtypes. *Eur. J. Biochem.* 271, 2305–2319. doi: 10.1111/j.1432-1033.2004.04145.x

Pacini, A., Micheli, L., Maresca, M., Branca, J. J., McIntosh, J. M., Ghelardini, C., et al. (2016). The alpha9alpha10 nicotinic receptor antagonist alpha-conotoxin RgIA prevents neuropathic pain induced by oxaliplatin treatment. *Exp. Neurol.* 282, 37–48. doi: 10.1016/j.expneurol.2016.04.022

Peng, H., Ferris, R. L., Matthews, T., Hiel, H., Lopez-Albaitero, A., and Lustig, L. R. (2004). Characterization of the human nicotinic acetylcholine receptor subunit alpha (alpha) 9 (CHRNA9) and alpha (alpha) 10 (CHRNA10) in lymphocytes. *Life Sci.* 76, 263–280. doi: 10.1016/j.lfs.2004.05.031

Perez, E. G., Cassels, B. K., and Zapata-Torres, G. (2009). Molecular modeling of the alpha9alpha10 nicotinic acetylcholine receptor subtype. *Bioorg. Med. Chem. Lett.* 19, 251–254. doi: 10.1016/j.bmcl.2008.10.094

Plazas, P. V., Katz, E., Gomez-Casati, M. E., Bouzat, C., and Elgoyhen, A. B. (2005). Stoichiometry of the alpha9alpha10 nicotinic cholinergic receptor. *J. Neurosci.* 25, 10905–10912. doi: 10.1523/JNEUROSCI.3805-05.2005

Quik, M., Bordia, T., Huang, L., and Perez, X. (2011). Targeting nicotinic receptors for Parkinson's disease therapy. *CNS Neurol. Disord. Drug Targets* 10, 651–658. doi: 10.2174/187152711797247849

Romero, H. K., Christensen, S. B., Di Cesare Mannelli, L., Gajewiak, J., Ramachandra, R., Elmslie, K. S., et al. (2017). Inhibition of alpha9alpha10 nicotinic acetylcholine receptors prevents chemotherapy-induced neuropathic pain. *Proc. Natl. Acad. Sci. U.S.A.* 114, E1825–E1832. doi: 10.1073/pnas.1621433114

Rucktooa, P., Smit, A. B., and Sixma, T. K. (2009). Insight in nAChR subtype selectivity from AChBP crystal structures. *Biochem. Pharmacol.* 78, 777–787. doi: 10.1016/j.bcp.2009.06.098

Sadeghi, M., McArthur, J. R., Finol-Urdaneta, R. K., and Adams, D. J. (2017). Analgesic conopeptides targeting G protein-coupled receptors reduce excitability of sensory neurons. *Neuropharmacology* 127, 116–123. doi: 10.1016/j.neuropharm.2017.05.020

Salomon-Ferrer, R., Gotz, A. W., Poole, D., Le Grand, S., and Walker, R. C. (2013). Routine microsecond molecular dynamics simulations with AMBER on GPUs. 2. Explicit solvent particle mesh Ewald. *J. Chem. Theory Comput.* 9, 3878–3888. doi: 10.1021/ct400314y

Satkunanathan, N., Livett, B., Gayler, K., Sandall, D., Down, J., and Khalil, Z. (2005). Alpha-conotoxin Vc1.1 alleviates neuropathic pain and accelerates functional recovery of injured neurones. *Brain Res.* 1059, 149–158. doi: 10.1016/j.brainres.2005.08.009

Shahsavar, A., Ahring, P. K., Olsen, J. A., Krintel, C., Kastrup, J. S., Balle, T., et al. (2015). Acetylcholine-binding protein engineered to Mimic the alpha4-alpha4 binding pocket in alpha4beta2 nicotinic acetylcholine receptors reveals interface specific interactions important for binding and activity. *Mol. Pharmacol.* 88, 697–707. doi: 10.1124/mol.115.098061

Sine, S. M., and Engel, A. G. (2006). Recent advances in Cys-loop receptor structure and function. *Nature* 440, 448–455. doi: 10.1038/nature04708

Taly, A., Corringer, P. J., Guedin, D., Lestage, P., and Changeux, J. P. (2009). Nicotinic receptors: allosteric transitions and therapeutic targets in the nervous system. *Nat. Rev. Drug Discov.* 8, 733–750. doi: 10.1038/nrd2927

Terlau, H., and Olivera, B. M. (2004). Conus venoms: a rich source of novel ion channel-targeted peptides. *Physiol. Rev.* 84, 41–68. doi: 10.1152/physrev.00020.2003

Tsetlin, V., Utkin, Y., and Kasheverov, I. (2009). Polypeptide and peptide toxins, magnifying lenses for binding sites in nicotinic acetylcholine receptors. *Biochem. Pharmacol.* 78, 720–731. doi: 10.1016/j.bcp.2009.05.032

Ulens, C., Hogg, R. C., Celie, P. H., Bertrand, D., Tsetlin, V., Smit, A. B., et al. (2006). Structural determinants of selective alpha-conotoxin binding to a nicotinic acetylcholine receptor homolog AChBP. *Proc. Natl. Acad. Sci. U.S.A.* 103, 3615–3620. doi: 10.1073/pnas.0507889103

Unwin, N. (1995). Acetylcholine receptor channel imaged in the open state. *Nature* 373, 37–43. doi: 10.1038/373037a0

Unwin, N. (2005). Refined structure of the nicotinic acetylcholine receptor at 4A resolution. *J. Mol. Biol.* 346, 967–989. doi: 10.1016/j.jmb.2004.12.031

Vincler, M., Wittenauer, S., Parker, R., Ellison, M., Olivera, B. M., and McIntosh, J. M. (2006). Molecular mechanism for analgesia involving specific antagonism of alpha9alpha10 nicotinic acetylcholine receptors. *Proc. Natl. Acad. Sci. U.S.A.* 103, 17880–17884. doi: 10.1073/pnas.0608715103

Walsh, R. M. Jr., Roh, S. H., Gharpure, A., Morales-Perez, C. L., Teng, J., and Hibbs, R. E. (2018). Structural principles of distinct assemblies of the human alpha4beta2 nicotinic receptor. *Nature* 557, 261–265. doi: 10.1038/s41586-018-0081-7

Wessler, I., and Kirkpatrick, C. J. (2008). Acetylcholine beyond neurons: the non-neuronal cholinergic system in humans. *Br. J. Pharmacol.* 154, 1558–1571. doi: 10.1038/bjp.2008.185

Winn, M. D., Ballard, C. C., Cowtan, K. D., Dodson, E. J., Emsley, P., Evans, P. R., et al. (2011). Overview of the CCP4 suite and current developments. *Acta Crystallogr. D Biol. Crystallogr.* 67(Pt 4), 235–242. doi: 10.1107/S0907444910045749

Xu, M., Zhu, X., Yu, J., Luo, S., and Wang, X. (2017). The crystal structure of Ac-AChBP in complex with alpha-conotoxin LvIA reveals the mechanism of its selectivity towards different nAChR subtypes. *Protein Cell* 8, 675–685. doi: 10.1007/s13238-017-0426-2

Zouridakis, M., Giastas, P., Zarkadas, E., Chroni-Tzartou, D., Bregestovski, P., and Tzartos, S. J. (2014). Crystal structures of free and antagonist-bound states of human alpha9 nicotinic receptor extracellular domain. *Nat. Struct. Mol. Biol.* 21, 976–980. doi: 10.1038/nsmb.2900

Conflict of Interest Statement: The authors declare that the research was conducted in the absence of any commercial or financial relationships that could be construed as a potential conflict of interest.

frontiers in Pharmacology

ORIGINAL RESEARCH
published: 31 May 2019
doi: 10.3389/fphar.2019.00577

Periplasmic Expression of 4/7 α-Conotoxin TxIA Analogs in *E. coli* Favors Ribbon Isomer Formation – Suggestion of a Binding Mode at the α7 nAChR

Yamina El Hamdaoui[1†‡], Xiaosa Wu[2‡], Richard J. Clark[3], Julien Giribaldi[4], Raveendra Anangi[2], David J. Craik[2], Glenn F. King[2], Sebastien Dutertre[4], Quentin Kaas[2‡], Volker Herzig[2*‡] and Annette Nicke[1*‡]*

[1] Walther Straub Institute of Pharmacology and Toxicology, Faculty of Medicine, Ludwig-Maximilians-Universität München, Munich, Germany, [2] Institute for Molecular Bioscience, The University of Queensland, Brisbane, QLD, Australia, [3] School of Biomedical Sciences, The University of Queensland, Brisbane, QLD, Australia, [4] CNRS, Institut des Biomolécules Max Mousseron, UMR 5247, Université de Montpellier, Montpellier, France

Peptides derived from animal venoms provide important research tools for biochemical and pharmacological characterization of receptors, ion channels, and transporters. Some venom peptides have been developed into drugs (such as the synthetic ω-conotoxin MVIIA, ziconotide) and several are currently undergoing clinical trials for various clinical indications. Challenges in the development of peptides include their usually limited supply from natural sources, cost-intensive chemical synthesis, and potentially complicated stereoselective disulfide-bond formation in the case of disulfide-rich peptides. In particular, if extended structure–function analysis is performed or incorporation of stable isotopes for NMR studies is required, the comparatively low yields and high costs of synthesized peptides might constitute a limiting factor. Here we investigated the expression of the 4/7 α-conotoxin TxIA, a potent blocker at α3β2 and α7 nicotinic acetylcholine receptors (nAChRs), and three analogs in the form of maltose binding protein fusion proteins in *Escherichia coli*. Upon purification via nickel affinity chromatography and release of the toxins by protease cleavage, HPLC analysis revealed one major peak with the correct mass for all peptides. The final yield was 1–2 mg of recombinant peptide per liter of bacterial culture. Two-electrode voltage clamp analysis on oocyte-expressed nAChR subtypes demonstrated the functionality of these peptides but also revealed a 30 to 100-fold potency decrease of expressed TxIA compared to chemically synthesized TxIA. NMR spectroscopy analysis of TxIA and two of its analogs confirmed that the decreased activity was due to an alternative disulfide linkage rather than the missing C-terminal amidation, a post-translational modification that is common in α-conotoxins. All peptides preferentially formed in the ribbon conformation rather than the native globular conformation. Interestingly, in the case of the α7 nAChR, but not the α3β2 subtype, the loss of potency could be rescued by an R5D substitution. In conclusion, we demonstrate efficient expression of functional but alternatively folded

OPEN ACCESS

Edited by:
Yasuo Mori,
Kyoto University, Japan

Reviewed by:
Shigeki Kiyonaka,
Kyoto University, Japan
Oscar Moran,
Istituto di Biofisica (IBF), Italy

***Correspondence:**
Quentin Kaas
q.kaas@imb.uq.edu.au
orcid.org/0000-0001-9988-6152
Volker Herzig
v.herzig@imb.uq.edu.au
Annette Nicke
annette.nicke@lrz.uni-muenchen.de

†Present address:
Yamina El Hamdaoui,
Institute of Pharmacy and Biochemistry, Johannes Gutenberg University Mainz, Mainz, Germany

‡*These authors have contributed equally to this work*

Specialty section:
This article was submitted to Pharmacology of Ion Channels and Channelopathies, a section of the journal Frontiers in Pharmacology

Received: *08 February 2019*
Accepted: *06 May 2019*
Published: *31 May 2019*

Citation:
El Hamdaoui Y, Wu X, Clark RJ, Giribaldi J, Anangi R, Craik DJ, King GF, Dutertre S, Kaas Q, Herzig V and Nicke A (2019) Periplasmic Expression of 4/7 α-Conotoxin TxIA Analogs in E. coli Favors Ribbon Isomer Formation – Suggestion of a Binding Mode at the α7 nAChR. Front. Pharmacol. 10:577. doi: 10.3389/fphar.2019.00577

ribbon TxIA variants in *E. coli* and provide the first structure–function analysis for a ribbon 4/7-α-conotoxin at α7 and α3β2 nAChRs. Computational analysis based on these data provide evidence for a ribbon α-conotoxin binding mode that might be exploited to design ligands with optimized selectivity.

Keywords: *E. coli*, recombinant expression, 4/7 α-conotoxin, ribbon isomer, molecular modeling, NMR spectroscopy

INTRODUCTION

Nicotinic acetylcholine receptors (nAChRs) are members of the Cys-loop superfamily of pentameric ligand-gated ion channels. Whereas the muscle-type receptors consist of four different subunits (α1,β1,γ/ε,δ), the assembly and stoichiometry of the 11 cloned neuronal subunits (α2–α7, α9, α10, and β2–β4) into nAChR subtypes is considerably more diverse and not well-defined. These neuronal nAChRs represent important drug targets such as for the treatment of pain, Alzheimer's disease, and nicotine addiction (Dineley et al., 2015; Lombardo and Maskos, 2015; Mohamed et al., 2015; Giribaldi and Dutertre, 2018; Hone and McIntosh, 2018). Deciphering their specific compositions and location in nervous system tissues as well as their respective physiological roles requires highly selective ligands.

Venoms from animals contain complex mixtures of small proteins and peptides that are often structurally constrained by disulfide bridges. Some of these peptides show high potency and specificity for certain ion channel subtypes. Cone snails are predatory marine animals that have evolved numerous peptide families that target various ligand- and voltage-gated ion channels (Akondi et al., 2014). The best-studied conotoxin family from a pharmacological perspective is the α-conotoxins, members of which are competitive antagonists of nAChRs (Dutertre et al., 2017). Some of these peptides have analgesic activity *in vivo* and thus are important lead structures for drug development (Akondi et al., 2014; Mohammadi and Christie, 2015).

The majority of α-conotoxins are composed of 12–19 amino acid residues including four cysteine residues that form two disulfide bonds. The cysteines are arranged in a CC–C–C pattern that defines the conotoxin Cysteine Framework I (Kaas et al., 2010). This framework is characterized by vicinal Cys1 and Cys2 residues and two loops formed by Cys1–Cys3 and Cys2–Cys4 disulfide bridges (referred to as the "globular" conformation). Based on the number of amino acid residues within the two loops, the currently characterized α-conotoxins are further classified into 3/4, 4/4, 3/5, 4/6, and 4/7 α-conotoxin subfamilies. These subfamilies show some common specificity for certain nAChR subtypes, with for example, the 3/5 α-conotoxins targeting the muscle-type nAChR and most identified 4/7 α-conotoxins preferentially targeting α7 and/or α3β2* neuronal nAChRs (* indicates the potential presence of further subunits) (Dutertre et al., 2017). Understanding the structure-activity relationships of conotoxins might aid in the development of optimized peptides with tailored selectivity. Usually, such studies employ chemical synthesis for the production of modified versions of the toxins. However, the production of multiple analogs or large quantities for automated application systems or preclinical treatment studies is costly, as is the production of large quantities of isotopically enriched samples for high resolution NMR spectroscopy studies or metabolic flux analysis (Antoniewicz, 2015). Chemical synthesis is also tedious if done manually and requires special equipment and experience that is not typically found in molecular biology laboratories. More generally, in the case of larger peptides (>40 aa), the yield from chemical synthesis is typically low. Finally, certain native peptides are inherently difficult to produce synthetically.

Venom-peptide production in heterologous expression systems might provide an efficient and economical alternative to chemical synthesis for molecular biology laboratories (Klint et al., 2013). It might also be suitable for large scale commercial toxin production. In the current study, we adapted an *Escherichia coli* periplasmic expression system (Klint et al., 2013) for the production of 4/7 α-conotoxin TxIA and three analogs. Unexpectedly, the functional and structural characterization of the expressed analogs indicated that they adopt a fold different from the native peptide (i.e., a 1–4, 2–3 "ribbon" rather than a 1–3, 2–4 "globular" disulfide conformation). These data demonstrate the need for careful structural analysis and confirm earlier findings that non-native folds could still be active. As an explanation for this activity and a basis for future structural studies, we provide the first NMR solution structure of a 4/7 α-conotoxin ribbon isomer and propose a binding mode for this peptide at the α7 nAChR. This information might be useful for the design of new lead structures based on the ribbon α-conotoxin scaffold.

MATERIALS AND METHODS

Preparation of Plasmids

A nucleotide sequence encoding a tobacco etch virus (TEV) protease recognition site (ENLYFQG) followed by [R5N,I9H] TxIA and including *KpnI* and *SacI* restrictions sites at the 5′ and 3′ ends, respectively, was optimized for expression in *E. coli* and assembled from synthetic oligonucleotides (Life Technologies). This construct was cloned in-frame to an 5′ His_6-maltose binding protein (MBP) sequence into the pLICC_D168 vector (Anangi et al., 2012) using *KpnI* and *SacI* cloning sites. The conserved N-terminal glycine residue of the conotoxin sequence forms the last amino acid of the TEV protease recognition site and thus, upon cleavage, produces a native N-terminus in the conotoxin. Plasmids for production of TxIA as well as single mutated R5D and R5N analogs were obtained from this construct by site-directed mutagenesis. The sequences of all plasmids were confirmed by Sanger sequencing.

Recombinant Expression of TxIA Analogs in *E. coli*

α-Conotoxin expression in *E. coli* was performed using a previously described method (Anangi et al., 2012; Klint et al., 2013). BL21 strains of *E. coli* were transformed with the respective plasmids using a standard heat shock protocol. Five colonies were selected to inoculate 5 ml culture medium (Luria-Bertani plus ampicillin) and grown at 37°C until the optical density (OD_{600}) reached 1.0. To determine optimal conditions for toxin expression, 4 ml × 1 ml samples of each culture were then diluted and grown again in 5 ml cultures until an OD of 0.6–0.8 was reached. Then heterologous protein expression was induced with IPTG. In doing so, culturing at 16°C and 37°C and induction with 0.5 and 1.0 mM IPTG were performed and protein expression in induced and non-induced cultures was compared after 4 or 12 h by SDS-PAGE analysis of a cell pellet from 500 μl of culture medium. The clone with the highest protein expression was selected and used to start 1–2 l cultures (from 50 to 100 ml precultures), which were then grown at 37°C with shaking at ∼220 rpm. After reaching an OD of 0.6–0.8, toxin expression was induced with 1 mM IPTG and cultures were grown overnight at 16°C. Cultures were then centrifuged (15 min at 10,500 *g*) and bacterial pellets frozen at −80°C.

SDS-PAGE Analysis

500 μl of culture was centrifuged [5 min, 3,381 *g* (6,000 rpm) in a desktop centrifuge] and cell pellets were supplemented with 30 μl SDS running buffer and 30 μl 3× loading buffer. After heating (10 min at 95–100°C), 30 μl of the solubilized cells were separated on a 10% SDS-PAGE gel under reducing conditions (5% β-mercaptoethanol in the sample). To control the purification and cleavage process, equivalent volumes (30–200 μl) of lysate, flow-through, eluate, and cleaved sample were supplemented with SDS running buffer to obtain 200 μl. After addition of 200 μl 3× SDS running buffer, 50 μl of each sample were separated using SDS-PAGE.

Recombinant Peptide Purification and Cleavage

Cell pellets were resuspended in 50 ml equilibration buffer (TN: 25 mM Tris-HCl, 300 mM NaCl, pH 7.0) and lysed in a constant-pressure cell disrupter (27 kpsi, TS Series Cell Disrupter, ConstantSystems, Ltd., Daventry, United Kingdom). After centrifugation (4°C, 30 min, 44,267 *g*), the supernatant was diluted with an equal volume of modified TN buffer (40 mM Tris-HCl, 400 mM NaCl, pH 8.0), supplemented with DNAse (1 μg/ml lysate) and incubated for 30 min with 5 ml Ni-NTA Superflow resin (Qiagen Pty, Ltd., Chadstone, VIC, Australia) in a gravity-fed column. The column was washed with 50 ml TN buffer containing 15 mM imidazole and then the His_6-MBP-TxIA fusion protein was eluted with 3 × 10 ml (each time 30 min) TN buffer containing 400 mM imidazole. The flow-through was concentrated to 5 ml (Amicon Ultra 30K filter) and diluted with 5 ml TN buffer. TxIA peptide was liberated from the fusion protein by cleavage overnight at room temperature using ∼100 μg TEV protease. In order to maintain TEV protease activity, reduced/oxidized glutathione were added at a ratio of 1:5 w/w.

Recombinant Peptide Purification by HPLC

The protease-cleaved samples were acidified with trifluoracetic acid (TFA), centrifuged (10 min at 6,762 *g*) and filtered (Millipore ultrafree MC 0.2 μm) to remove protein precipitates. Then 50% acetonitrile (ACN) was added to a final concentration of 5% ACN and the peptides were separated on a C18 semi-preparative reversed-phase (RP) HPLC column (Vydac protein/peptide C18 column Cat# 218TP1010) on a Shimadzu Prominence HPLC system (Shimadzu, Rydalmere, NSW, Australia). The following linear gradients of solvent B (90% ACN, 0.043% TFA in water) in solvent A (0.5% TFA in water) were used at a flow rate of 3 ml/min: 5% B for 10 min, then 5–35% B for 30 min followed by 35–80% B over 5 min and 80% B for another 7 min. Absorbance was determined at 214 and 280 nm and collected fractions were lyophilized and stored at −20°C. The fractions containing the correct peptide masses as determined by matrix-assisted laser desorption/ionization mass spectrometry (MALDI MS) were then subjected to another HPLC fractionation using a hydrophilic interaction liquid chromatography (HILIC) column. Samples were dissolved in 95% solvent B and injected into a VisionHT HILIC column (5 μm particle size, 150 mm × 4.6 mm; Grace, Columbia, MD, United States) at a flow rate of 1 ml/min. The same solvents as during the RP-HPLC fractionation were used with the following linear gradients: 95% solvent B for the first 3 min, then 95–75% B over 20 min. Absorbance was determined at 214 and 280 nm and the molecular masses of the peptides determined using MALDI MS.

Analysis by Liquid Chromatography/Mass Spectrometry

Solvents used for LC/MS were of HPLC-grade. Recombinant peptide masses were determined by MALDI time-of-flight (TOF) MS using a 4700 Proteomics Bioanalyzer model (Applied Biosystems, Carlsbad, CA, United States). Peptides were dissolved in water and mixed 1:1 (v/v) with α-cyano-4-hydroxycinnamic acid matrix (7 mg/ml in 50% ACN, 5% formic acid) and mass spectra acquired in positive reflector mode. All reported masses are for the monoisotopic $[M+H^+]$ ions.

For analysis of the synthetic TxIA ribbon analog, the LC/MS system consisted of an Waters Alliance 2695 HPLC (Milford, OH, United States) coupled to a Micromass ZQ mass spectrometer (electrospray ionization mode, ESI+). All analyses were carried out using a Chromolith (Fontenay-sous-Bois, France) HighResolution RP-18e column (4.6 mm × 25 mm, 15 nm–1.15 μm particle size). A flow rate of 3 ml/min and a gradient of 0–100% solvent B over 2.5 min were used. Eluent A was water/0.1% formic acid while eluent B was ACN/0.1% formic acid. UV detection was performed at 214 nm. ESI mass spectra were acquired using a solvent flow rate of 200 μl/min. Nitrogen was used for both the nebulizing and drying gas. Data were obtained in a scan mode over the m/z range 100–1000 or 250–1500 in 0.7 s intervals. Fully folded synthetic ribbon TxIA

was characterized using a Synapt G2-S high-definition MS system (Waters, Corp., Milford, MA, United States) equipped with an ESI source. Chromatographic separation was carried out at a flow rate of 0.4 ml/min on a Acquity H-Class ultrahigh performance liquid chromatography (UPLC) system (Waters, Corp., Milford, MA, United States), equipped with a Kinetex C18 100A column (100 mm × 2.1 mm, 2.6 μm particle size) from Phenomenex (France). The mobile phase consisted of water (solvent A) and ACN (solvent B) with both phases acidified by 0.1% (v/v) formic acid. Mass spectra were acquired in the positive ionization mode.

Two-Electrode Voltage Clamp (TEVC) Electrophysiology

cDNAs encoding rat nAChR subunits were provided by J. Patrick (Baylor College of Medicine, Houston, TX, United States) and subcloned into the oocyte expression vector pNKS2 (Gloor et al., 1995). cRNA was synthesized with the SP6 mMessage mMachine Kit (Ambion, Austin, TX, United States) and adjusted to a concentration of 0.5 μg/μl. nAChR subunit RNAs were mixed in the ratios 1:1 (α3/β2) or 5:1 (α4/β2). *Xenopus laevis* (Nasco International, Fort Atkinson, WI, United States) oocytes were injected with 50 nl aliquots of cRNA (Nanoject automatic oocyte injector, Drummond Scientific, Broomall, PA, United States). Antagonist concentration-response curves were measured as described previously (Dutertre et al., 2005; Beissner et al., 2012) in ND96 (96 mM NaCl, 2 mM KCl, 1 mM $CaCl_2$, 1 mM $MgCl_2$, and 5 mM HEPES at pH 7.4). In brief, current responses to acetylcholine were measured at room temperature 1–6 days after cRNA injection and recorded at −70 mV using a Turbo Tec 05X Amplifier (NPI Electronic, Tamm, Germany) and Cell Works software. A standard concentration of 100 μM ACh or nicotine was used to activate the αβ combinations and the α7 nAChR, respectively. A fast and reproducible solution exchange (<300 ms) was achieved with a 50-μl funnel-shaped oocyte chamber combined with a fast vertical solution flow fed through a custom-made manifold mounted immediately above the oocyte. Agonist pulses were applied for 2 s at 4-min intervals. Following 1 min of perfusion directly after the agonist application, peptides were applied in a static bath for 3 min. IC_{50} values were calculated from a non-linear fit of the Hill equation to the data (Prism version 6.0; GraphPad Software, Inc., San Diego, CA, United States). Data are presented as means ± SEM from at least three oocytes.

Chemical Synthesis of Ribbon and Native α-TxIA

ACN, TFA, dimethylformamide (DMF), *N*,*N*-diisopropylethylamine (DIEA), triisopropylsilane (TIS), dichloromethane (DCM), piperidine and other reagents were obtained from Sigma-Aldrich (St. Louis, MI, United States) or Merck (Darmstadt, Germany) and used as supplied. Fmoc L-amino acid derivatives and 1[*bis*(dimethylamino)methylene]-1H-1,2,3-triazolo[4,5-b]pyridinium 3-oxid hexafluorophosphate (HATU) were purchased from Iris Biotech (Marktredwitz, Germany). AmphiSpheres 20 HMP resin (0.6 mmol/g) was purchased from Agilent Technologies (Les Ulis, France). The side chain protecting groups for amino acids are t-Bu for Asp and Ser; Acm for $Cys_{9,14}$; Trt for $Cys_{1,15}$ and Asn; Pbf for Arg. Ribbon α-TxIA was manually synthesized using the Fmoc-based solid-phase peptide synthesis technique on a VWR (Radnor, PA, United States) microplate shaker. All Fmoc amino acids and HATU were dissolved in DMF to reach 0.5 M. Chain elongation was performed step by step using 0.2 mmol of AmphiSpheres 20 HMP resin. Fmoc deprotection was performed with 20% piperidine in DMF two times, each for 1 min at room temperature, then the resin was washed three times with DMF. Each Fmoc-protected amino acid (5 eq.) was coupled twice in the presence of HATU (5 eq.) and DIEA (10 eq.) in DMF at room temperature for 2 min. After completion of the coupling reaction, the resin was sequentially washed twice with DMF. Cleavage of peptide from the resin and removal of side-chain protecting groups were carried out using 20 ml of a solution containing TFA/TIS/H_2O (95:2.5:2.5, v/v/v) for 3 h at room temperature. After the resin was removed by filtration and washed with DCM, the DCM and TFA were removed under vacuum and cold diethyl ether was added to precipitate the peptide. Crude peptide was purified by preparative RP-HPLC, and its purity determined using LC/ESI-MS. Trt groups were removed during the cleavage step while the Acm protective groups are resistant to cleavage conditions. A two-step oxidation procedure was then carried out. Briefly, the first disulfide bridge was formed from free cysteines with the use of 2,2′-dithiopyridine (DTP) (Maruyama et al., 1999; Giribaldi et al., 2018) and then the second disulfide bridge was formed by concomitant deprotection and oxidation of the Acm groups with the use of iodine (Gyanda et al., 2013). The fully folded peptide was purified by analytical RP-HPLC and purity confirmed by high-resolution mass spectrometry During the purification process, the ribbon form of α-TxIA appears as a broad peak on analytical RP-HPLC (containing unseparable major and a minor peaks), which is possibly due to slow *cis–trans* interconversion of the proline residues.

Globular TxIA was synthesized as described (Dutertre et al., 2007).

Synthetic Peptide Purification

Preparative RP-HPLC was run on a Gilson PLC 2250 HPLC system (Villiers le Bel, France) using a preparative column (Waters DeltaPak C18 Radial-Pak Cartridge, 100 Å, 40 mm × 100 mm, 15 μm particle size, flow rate 50.0 mL/min). Buffer A was 0.1% TFA in water, and buffer B was 0.1% TFA in ACN. Fully folded synthetic TxIA ribbon was purified on a UltiMate 3000 UHPLC system (Thermo Fischer Scientific) using an Kinetex C18 100 A column (100 mm × 2.1 mm, 2.6 μm particle size) from Phenomenex (France). Buffer A was 0.1% formic acid in water, and buffer B was 0.1% formic acid in ACN.

NMR Spectroscopy Analysis

Secondary Shifts of Recombinant Peptides

Peptides were dissolved in 90% H_2O/10% D_2O (Cambridge Isotope Laboratories) at a concentration of 1 mg/ml and pH ∼3.6. Spectra were recorded on a Bruker Avance 600 MHz spectrometer at 7°C and referenced to 4,4-dimethyl-4-silapentane-1-sulfonic acid (DSS) at 0 ppm. Standard Bruker

pulse programs were used for all two-dimensional spectra. Excitation sculpting with gradients was used to achieve water suppression for TOCSY and NOESY experiments (Hwang and Shaka, 1995). NMR experiments included TOCSY (Braunschweiler and Ernst, 1983) using a MLEV-17 spin lock sequence with a 80 ms mixing time, NOESY (Jeener et al., 1979) with a 200 ms mixing time, ^{1}H- ^{13}C HSQC (Palmer et al., 1991) and ^{1}H-^{15}N HSQC (Palmer et al., 1991). Spectra were recorded with 4096 data points in the F2 dimension and 512 increments in the F1 dimension for TOCSY, and NOESY experiments, 2048 × 240 for ^{1}H-^{13}C HSQC and 2048 × 128 for ^{1}H-^{15}N HSQC data points in the F2 dimension and increments in the F1 dimension, respectively. The t1 dimension was zero-filled to 1024 real data points, and the F1 and F2 dimensions were multiplied by a sine-squared function prior to Fourier transformation. All spectra were processed using TopSpin 2.1 (Bruker) and assigned with CcpNmr Analysis (Vranken et al., 2005) using the sequential assignment protocol (Wüthrich, 1986). Secondary shifts were calculated using the random coil values reported by Wishart et al. (1995).

Structure of Synthesized Ribbon TxIA

A 2D NOESY spectrum was acquired with a mixing time of 200 ms at 7°C and interproton distance constraints were calculated from the relative intensities of NOE cross-peaks. Predictions of ϕ and ψ backbone angles were performed with TALOS-N (Shen and Bax, 2013). Distance restraints for the disulfide bonds defined by the regioselective synthesis were used in the structure calculations. The ANNEAL function in CYANA was used to perform 10,000 steps of torsion angle dynamics to generate an initial ensemble of 100 structures from which the 20 structures with the lowest penalty function values were chosen for analysis. Several rounds of structure calculations were performed to resolve distance and angle constraint violations. Using protocols from the RECOORD database (Nederveen et al., 2005), an ensemble of 100 structures was subsequently calculated with CNS (Brünger et al., 1998) using the force field distributed with Haddock 2.0 (Dominguez et al., 2003) and further refined in a water shell (Linge and Nilges, 1999). A set of 20 structures with the lowest energy and no NOE violations greater than 0.2 Å or dihedral-angle violations greater than 3° was selected for MolProbity analysis (Williams et al., 2018). The structures were visualized and figures generated using MOLMOL (Koradi et al., 1996).

Molecular Modeling

Molecular models of the complexes between the ligand-binding domain of α7 nAChR and conotoxins were prepared by homology modeling and then refined using either molecular dynamics (MD) simulations or the ToxDock method (Leffler et al., 2017). The molecular models are provided along the manuscript in **Supplementary Material Data Sheet 1**. Homology models were constructed using Modeler 9v18 (Sali and Blundell, 1993) using three templates: (i) the NMR solution structure of ribbon TxIA (this study); (ii) the α4/α4 interface of the cryo-electron microscopy structure of the human α4β2 nAChR (PDB 6CNK) (Walsh et al., 2018); and (iii) the crystal structure of the complex between globular conotoxin [A10L]TxIA and the *Aplysia californica* acetylcholine binding protein (AChBP, PDB 2UZ6) (Dutertre et al., 2007). A 100 models were generated for each system and the model with the lowest DOPE score (Shen and Sali, 2006) was selected for further refinement.

Refinement With MD Simulations

Homology models of the interaction of ribbon deamidated TxIA, [R5D] ribbon TxIA, and [R5N] ribbon TxIA with rat α7 nAChR were obtained by homology modeling as described above. These initial models were then minimized and subjected to MD simulations in Gromacs 2018 using the Ambr99SB-ILDN forcefield (Lindorff-Larsen et al., 2010). The systems were embedded in a cubic box of 11 nm × 11 nm × 9 nm and solvated with ∼32,000 water molecules and several sodium ions to neutralize the systems. The system was then energy minimized using 10,000 steps of steepest gradient and submitted to an equilibration protocol during which position restraints on the receptor and toxin were progressively released; the constraints on the toxin atoms were released first over 6 ns, and the constraints on the receptor then over 2.4 ns. The systems were then simulated unrestrained for 50 ns. Long-range electrostatic interactions were computed using particle mesh Ewald with default parameters in Gromacs. All bonds involving hydrogens were constrained with the LINCS algorithm, and the time step of the simulation was set to 2 fs. The V-rescale thermostat (Bussi et al., 2007) was used to maintain the temperature at 27°C and the pressure was maintained at one atmosphere using the Berendsen isotropic pressure coupling. The short range electrostatic and Van der Waals cutoffs were both set at 1 nm. The binding free energy of each system was then computed using the MMPB/SA method (Miller et al., 2012) as implemented in Amber18 by analyzing 10 frames extracted every ns from the last 10 ns of the unrestrained simulation.

ToxDock Refinement

The ToxDock (Leffler et al., 2017) refinement and energy computations were carried out using the online server Rosie (Lyskov et al., 2013). Briefly, the Rosetta fast relax protocol (Tyka et al., 2011) was used to generate 200 alternative models representing small structural fluctuation of the complex. The 50 models with lowest Rosetta total score were submitted for a FlexPepDock refinement (Raveh et al., 2010), generating 500 alternative binding modes of the peptide bound to the receptor and computing the reweighted docking Rosetta score. The average of the 25 lowest reweighted score was taken as the relevant to the binding score of the complex, as previously described (Leffler et al., 2017). The Talaris2013 energy function was used for all Rosetta computations (Leaver-Fay et al., 2013).

RESULTS

Efficient Production of Recombinant TxIA Analogs

Like most characterized 4/7 α-conotoxins, TxIA preferentially targets α7 and α3β2 nAChRs with nanomolar potency but has no detectable activity at the α4β2 subtype (Dutertre et al.,

2007). Whereas some α3β2-selective conotoxins such as MII (Azam and McIntosh, 2009) also have high potency at the closely related α6β2 receptor, no conotoxin that selectively targets the α4β2 nAChR has been yet identified, and only a few 4/7 α-conotoxins, such as MII (Cartier et al., 1996), GID (Nicke et al., 2003), and GIC (McIntosh et al., 2002) have been shown to block this receptor, albeit at high nanomolar or micromolar concentrations. Therefore, one aim of this study was to identify amino acid side chains that could prevent conotoxin binding to α4β2 receptors by investigating if TxIA could be modified to obtain a conotoxin with at least weak activity at α4β2. To this end, we compared the amino acid sequence of TxIA with those of MII, and GID and selected two positions, 5 and 9, in which we substituted the amino acid side chains (**Figure 1A**). Position 5 was previously shown to be important for MII binding to α3β2 nAChRs (Everhart et al., 2004).

The DNA sequences corresponding to TxIA and analogs were optimized for expression in *E. coli* and fused N-terminally via a TEV protease cleavage site to MBP (**Figure 1B**). Although the consensus TEV protease cleavage site is ENLYFQ/S, the protease also efficiently cleaves at ENLYFQ/G (Kapust et al., 2002), which has the advantage that the N-terminal glycine residue that is present in most α-conotoxins can be used and remains after cleavage. Expression of the TxIA analogs in form of a His_6-MBP fusion protein was done to target the construct to the *E. coli* periplasmic space where the disulfide bond folding machinery of the bacterium (i.e., the Dsb proteins) is located and the oxidative environment is favorable for conotoxin folding and disulfide bond formation. Upon transformation of *E. coli* with these constructs and induction with IPTG, the respective fusion proteins represented the dominant proteins produced and they could be successfully purified and cleaved as indicated by the size shift of the MBP fusion construct (**Figure 1C** and **Supplementary Figure S1A**). Further purification by RP-HPLC revealed one dominant peak for each of the TxIA analogs (**Figure 2A** and **Supplementary Figure S1B**). The corresponding fractions contained the calculated mass of the fully oxidized peptides (**Figure 2C**) and turned out to represent the sole functional fractions when tested by TEVC electrophysiological analysis on α3β2 nAChRs expressed in *Xenopus laevis* oocytes (**Figure 2B** and **Supplementary Figure S1C**). The obtained yields were 1–2 mg of conotoxin per liter of culture. An additional HILIC-HPLC purification step was employed (**Supplementary Figure S2**) to obtain pure recombinant peptides as determined using MALDI-MS (**Figure 2C** and **Supplementary Figure S2**). These purified peptides were then used for preparation of concentration response curves (see below). The double mutant [R5N,I9H] was not further analyzed.

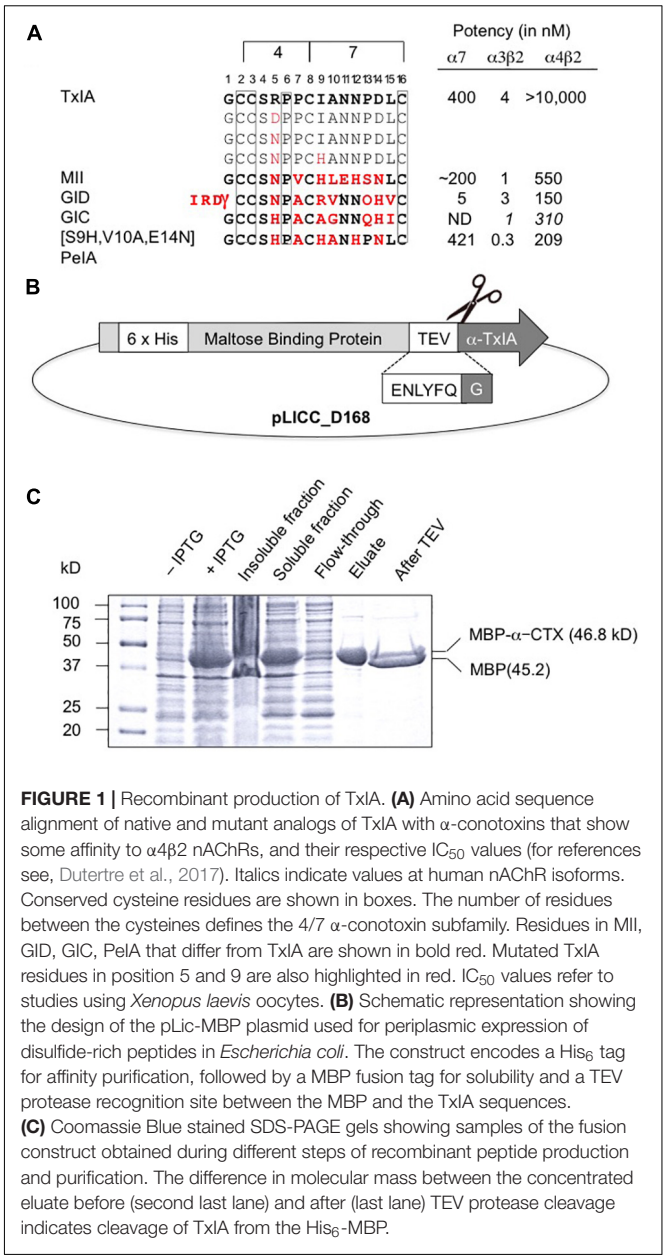

FIGURE 1 | Recombinant production of TxIA. **(A)** Amino acid sequence alignment of native and mutant analogs of TxIA with α-conotoxins that show some affinity to α4β2 nAChRs, and their respective IC_{50} values (for references see, Dutertre et al., 2017). Italics indicate values at human nAChR isoforms. Conserved cysteine residues are shown in boxes. The number of residues between the cysteines defines the 4/7 α-conotoxin subfamily. Residues in MII, GID, GIC, PeIA that differ from TxIA are shown in bold red. Mutated TxIA residues in position 5 and 9 are also highlighted in red. IC_{50} values refer to studies using *Xenopus laevis* oocytes. **(B)** Schematic representation showing the design of the pLic-MBP plasmid used for periplasmic expression of disulfide-rich peptides in *Escherichia coli*. The construct encodes a His_6 tag for affinity purification, followed by a MBP fusion tag for solubility and a TEV protease recognition site between the MBP and the TxIA sequences. **(C)** Coomassie Blue stained SDS-PAGE gels showing samples of the fusion construct obtained during different steps of recombinant peptide production and purification. The difference in molecular mass between the concentrated eluate before (second last lane) and after (last lane) TEV protease cleavage indicates cleavage of TxIA from the His_6-MBP.

Electrophysiological Analysis of Recombinant TxIA Analogs Reveals Strongly Reduced Potency

We compared the potencies of the repurified expressed peptides TxIA, [R5D]TxIA, and [R5N]TxIA with synthetic TxIA at oocyte-expressed α3β2, α4β2, and α7 nAChRs. Unlike the *E. coli*-expressed α-conotoxins, but like native TxIA, the synthetic TxIA was C-terminally amidated. Not only were none of the analogs active at the α4β2 nAChR but all recombinant peptides showed a marked drop in potency compared to synthetic TxIA (**Figure 3A**). Preparation of full concentration-response curves revealed that in comparison to synthetic TxIA, which yielded IC_{50} values of ∼5 nM and 2 μM at α3β2 and α7 nAChRs, respectively, the recombinant TxIA was about 100- and 50-fold less active at α3β2 and α7 nAChRs (**Figure 3B** and **Table 1**). Interestingly, the potency decrease at the α7 receptor was almost completely reversed when the arginine residue in position 5 was substituted by an aspartic acid residue, but not when an asparagine residue was introduced in this position.

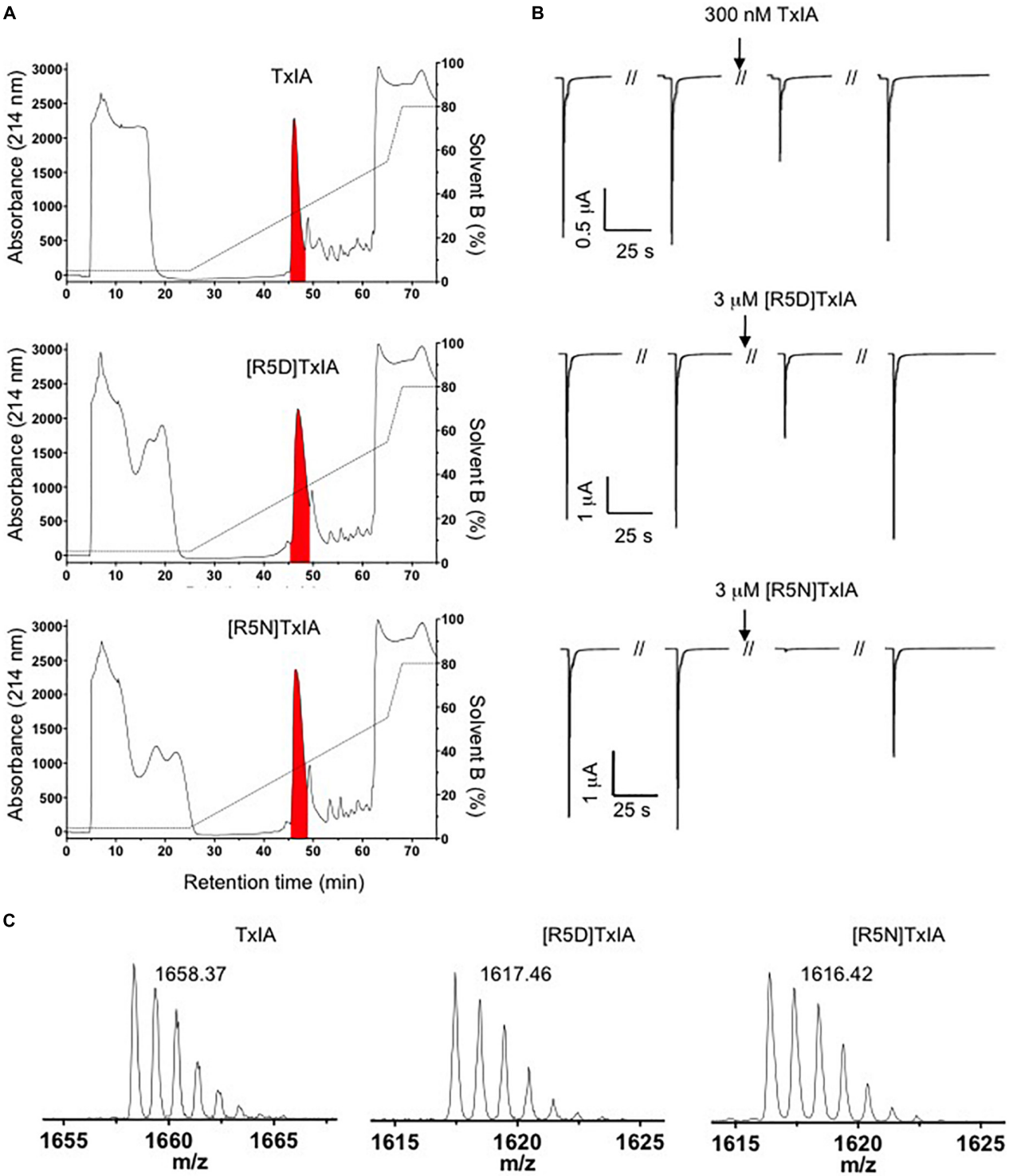

FIGURE 2 | Purification of TxIA and mutant (R5D, R5N) analogs. **(A)** RP-HPLC chromatograms showing first step RP-HPLC fractionation with the peaks highlighted in red containing the correct molecular mass as determined by MALDI MS. **(B)** Antagonistic activity of the purified toxin peak (i.e., the red peak from **A**) at α3β2 nAChRs. Oocytes were clamped at –70 mV and 100 mM ACh were used to activate α3β2 nAChRs. **(C)** MALDI MS traces after second step HILIC fractionation of the purified TxIA and analogs (red colored fractions in **Supplementary Figure S2**) indicate the monoisotopic molecular masses of the purified toxins. All reported masses are for $[M + H]^+$ ions.

Consequently, whatever caused the decrease in activity of the recombinant TxIA, lack of amidation, proline isomerization, and/or misfolding of the peptide, could be compensated by changes in the primary structure.

Structural Analysis of Recombinant TxIA Analogs Confirms the Preferential Formation of Ribbon Isomers

Because all of the recombinant peptides showed at least some potency at α3β2 nAChRs and peptides in the other fractions turned out to be inactive or less active, we assumed that the dominant peaks corresponded to the native (i.e., globular) conformation of the peptides. However, because of the strong potency decrease that is clearly higher than the 2- or 5-fold potency reduction of non-amidated AnIB analogs at α3β2 and α7 nAChRs, respectively (Loughnan et al., 2004) we considered the possibility of non-native disulfide linkage in the *E. coli*-expressed TxIA analogs. To test this hypothesis, NMR structural analysis was performed. The three expressed TxIA analogs yielded well-dispersed ^{1}H NMR resonances, implying that they adopt ordered structures in solution. These peptides were further analyzed using two-dimensional NMR so that the data could be compared to published data for Pn1.2, which has a related sequence and where NMR data for each of the disulfide isomers is available (Carstens et al., 2016). To assign the spectra, Hα-NH_{i+1} connectivities obtained from NOESY spectra were used in the sequential assignment of individual spin systems determined from the TOCSY spectra. For all of the TxIA analogs, sequential Hα-NH_{i+1} connectivities were observed for the entire peptide chain, except at the Pro residues that lack backbone amide protons. Analysis of the NOE data and the Cδ chemical shifts of Pro7 indicated that this proline is in the *cis* confirmation (Schubert et al., 2002). Analysis of secondary shift data can supply information on secondary structural elements of peptides (Wishart et al., 1991), and is useful for comparing structural frameworks in disulfide-rich peptides. **Figure 4B** shows the Hα secondary shifts for TxIA and compares these values with previously published secondary shifts for the three possible disulfide isomers of Pn1.2. The Hα secondary shifts for the TxIA most closely resemble those of the ribbon isomer of Pn1.2, especially in the N-terminal region, which suggests that the expressed TxIA is in the ribbon form. Furthermore, a comparison of the secondary shifts for each expressed TxIA analog (**Figure 4A**) and synthetic ribbon TxIA (see below and **Supplementary Figure S3C**) reveals that they are almost identical and all four peptides form the same disulfide isomer. Most of the secondary shifts for the TxIA analogs vary within the ± 0.1 ppm range that is consistent with a random coil structure, however residues 9–11 have secondary shift values more negative than −0.1 ppm, suggesting this region has some helical character. Our structural and functional characterization of the TxIA analogs is in agreement with data from Wu et al. (2014), where an 80-fold potency reduction (IC_{50} of 5.4 to 430 nM) of synthesized ribbon TxIA was observed at α3β2 nAChRs, which corresponds well to the 100-fold reduction found in our study. Importantly, this analysis further confirmed the purity of the expressed toxins as similar retention times for globular and ribbon TxIA have been described (Wu et al., 2014).

Solution Structure and Potential Binding Mode of the Ribbon Isomer of TxIA

α-Conotoxins are generally considered to be weakly active or inactive if they are folded in non-native conformations such as "ribbon" or "bead" disulfide isomers. However, in case of the 4/6 conotoxin AuIB, the ribbon isomer turned out to be more potent at α3β4 nAChRs than the globular form and seemed to bind to the orthosteric binding site (Grishin et al., 2010). Likewise, the ribbon form of the 4/3 α-conotoxin ImII was found to compete with binding of its natively folded isomer at α7 nAChRs and also bound to an additional binding site at *Torpedo* nAChRs (Kasheverov et al., 2009). For AuIB, a binding mode has recently been defined in detail (Wu et al., 2018). However, no ribbon 4/7 α-conotoxin structure has been determined to date (Kaas et al., 2012). Inspired by the fact that ribbon isomers of some conotoxins can competitively block ACh binding and that TxIA potency at the α7 nAChR could be improved by the substitution R5D, we set out to determine the structure of the ribbon conformer of TxIA and its binding mode at α7 nAChR. To this end, a non-amidated ribbon isomer of TxIA was synthesized (**Supplementary Figure S3**) by a two-step oxidation method and its NMR structure calculated using CYANA 3.0 (Güntert et al., 1997) and refined in CNS (Brünger et al., 1998) using TALOS-N (Shen et al., 2009) derived dihedral angle restraints, and hydrogen bond restraints derived from D_2O exchange experiments.

The structural statistics for the ensemble of the 20 lowest energy structures for each isomer are shown in **Table 2**, and the structural ensemble of the 20 representative structures are shown in **Figure 4C** (left). The mean structure of the ribbon isomer of TxIA (**Figure 4C**, right), although well-defined (backbone RMSD = 0.58 ± 0.3 Å), possesses no defined secondary structure elements. However, several of the structures in the ensemble have a 3_{10}-helical segment spanning residues Cys8 to Asn11, which is generally consistent with the Hα secondary shift data. Furthermore, loop 1 of ribbon TxIA (Cys2–Cys8) is well-defined (backbone RMSD = 0.21 ± 0.07 Å) and resembles loop 1 of globular TxIA, but loop 2 (Cys8–Cys16) is less well-defined (backbone RMSD = 0.48 ± 0.29 Å) and adopts a conformation that is distinct from loop 2 of globular TxIA. Analysis of the electrostatic surface features in MOLMOL reveals negatively charged regions on opposite faces, corresponding to the C-terminal acid and the sidechain of Asp14, and a positively charged region due to the sidechain of Arg5 and N-terminus (**Figure 4D**). This structure was subsequently used to probe the binding mode in a MD-refined model and a model based on the recently defined ToxDoc application.

Molecular Modeling

Binding Modes in the ToxDock- and MD-Refined Models

The binding modes of ribbon TxIA at the α7 nAChR generated by MD simulations and by ToxDock are globally similar in

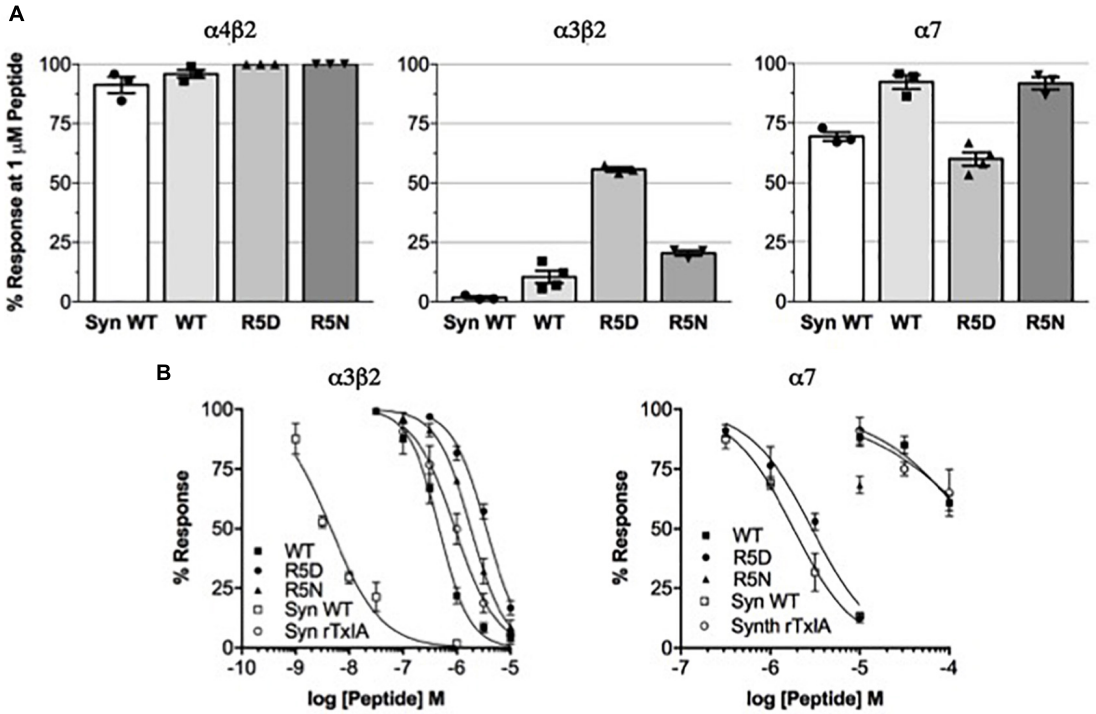

FIGURE 3 | Potency comparison of synthesized amidated and expressed non-amidated TxIA on nAChR subtypes. **(A)** Reduction of control responses activated by 100 μM ACh or nicotine (in case of α7 nAChR) by 1 μM synthetic (syn) or recombinant TxIA (rec = wild type; R5D and R5N amino acid substitutions) at the indicated nAChR subtypes expressed in *Xenopus* oocytes and measured using TEVC electrophysiology. **(B)** Concentration-response curves for synthetic and recombinant TxIA at α3β2 (left) and α7 (right) nAChRs. Error bars represent the SEM from at least three recordings [except for high (>10 μM) concentrations of synthetic peptides, where not enough material was available]. Oocytes were clamped at –70 mV. 100 μM ACh or 100 μM nicotine were used to activate α3β2 and α7 receptors, respectively.

TABLE 1 | IC_{50} values and Hill coefficients (n_H) for synthetic TxIA and recombinant TxIA, [R5D]TxIA, and [R5N]TxIA at rat α3β2 and α7 nAChRs.

	α3β2		α7	
	IC_{50} (nM)	**n_H**	**IC_{50} (nM)**	**n_H**
Synthetic TxIA	4.6 (3.6 to 5.8)	−0.93 (−1.15 to −0.71)	1812 (1555 to 2111)	−1,23 (−1,52 to −0,99)
Synthetic rTxIA	928 (810 to 1064)	−1.14 (−1.3 to −0.98)	*≈ 200.000*	ND
Recombinant TxIA	470 (432 to 512)	−1.54 (−1.73 to −1.35)	*≈ 200.000*	ND
Recombinant [R5D]TxIA	3543 (3166 to 3965)	−1.38 (−1.58 to −1.17)	2915 (2406 to 3532)	−1.24 (−1.53 to −0.96)
Recombinant [R5N]TxIA	1834 (1704 to 1974)	−1.36 (−1.49 to −1.24)	ND	ND

Numbers in brackets are 95% confidence intervals. ND means not determined. Italic numbers are estimates.

terms of the orientation of the toxin in the binding site, with some molecular interactions shared between the two models but also a range of interactions that are different (**Figures 5A,B**). Pro6 in Loop 1 of wild-type or variant ribbon TxIA occupies a similar position in the models as P6 of the globular TxIA in the TxIA/AChBP experimental structure. P6 is an important determinant of the interaction of α-conotoxins as it is embedded in the aromatic box, which is at the bottom of the orthosteric binding site and is recognized by acetylcholine. Another important conserved feature of the interaction of globular α-conotoxin with AChBP is the stacking between the vicinal disulfide bridge of the C-loop with the first disulfide bond of the α-conotoxin. The MD-refined model displays this interaction but not the ToxDock-refined model in which the side chain of D14 stacks between the two disulfide bonds. This is interesting because the conformation of toxin in the two models is globally preserved (the backbone RMSD of the toxins in the two models is only 1.5 Å). The binding mode in the ToxDock

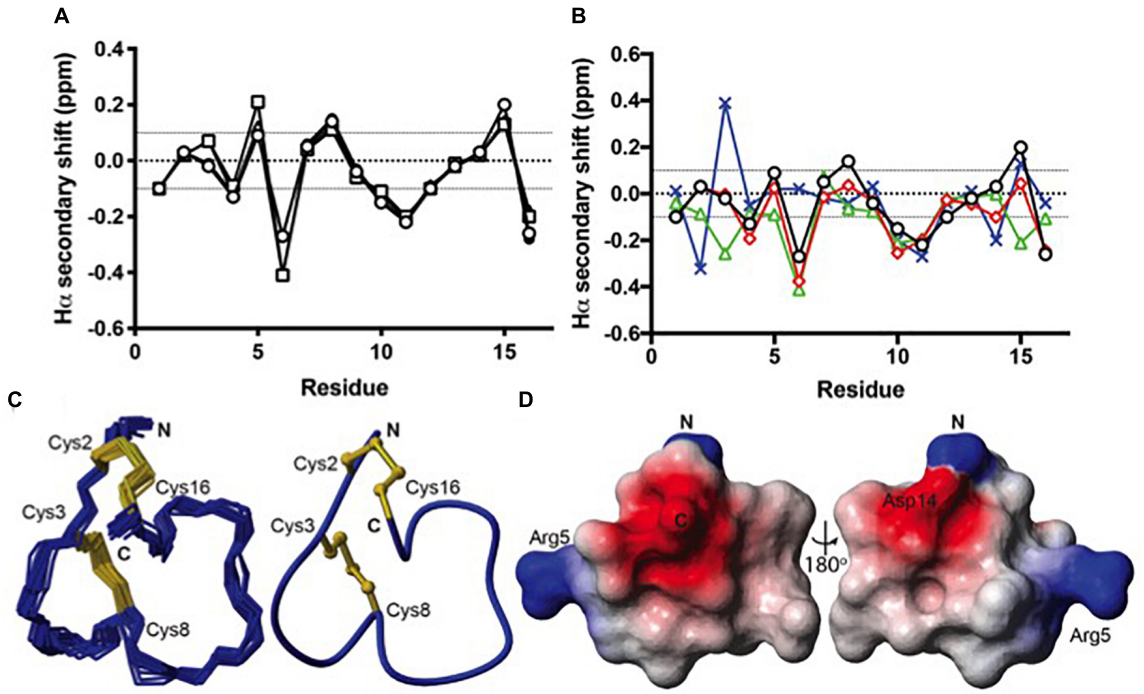

FIGURE 4 | Structural analysis of the ribbon disulfide isomers of TxIA and analogs. **(A)** Hα secondary shift values for recombinant TxIA (open circles), [R5D]TxIA (squares), [R5N]TxIA (triangles), and synthetic ribbon TxIA (closed circles) at 7°C. Please note that due to the identity of the peptides, the secondary shifts overlap and most data points (filled circles) are hardly visible **(B)** A comparison of the Hα secondary shifts for ribbon TxIA (black) with the Hα secondary shifts of ribbon (red), globular (green) and beads (blue) isomers of Pn1.2. The values for ribbon TxIA most closely match those of ribbon Pn1.2, especially in the N-terminal region. **(C)** Left panel: ensemble of the 20 lowest energy structures for ribbon TxIA. The peptide backbone is in blue and the disulfides are in gold. Right panel: the mean structure of ribbon TxIA calculated from the ensemble. The structure is shown in ribbon format with disulfide bonds in ball and stick. The N- and C-termini are indicated and the cysteines are labeled. **(D)** Electrostatic surface of ribbon TxIA (PDB ID 6OTA) highlighting the negatively charged regions (red) corresponding to the C-terminal acid and Asp14, and the positively charged regions (blue) corresponding to the N-terminus and the side chain of Arg5.

model is slightly tilted compared to the MD model, and this leads to a change in reorientation of the N-terminus (from G1 to S4) and of Loop 2 in general. The conformation of the wild-type and variants in the context of the binding site was highly stable, with a backbone RMSD < 1.5 Å and on average 1 Å from the initial homology model. The binding modes of the toxins were also similarly stable, with Loop 1 being highly rigid and Loop 2 undergoing larger, albeit small, conformational fluctuation. The binding mode of the ToxDock model was not sampled during the MD refinement, and they should therefore be considered as two hypothetical binding modes. The location and interaction of position 5 in the models of the wild-type TxIA are similar, and the interactions of this position in TxIA and variants will now be described using the MD-refined models (**Figures 5C–E**). **Supplementary Figure S4** describes the interaction as suggested in the ToxDock-refined models.

Molecular Interactions of Position 5

TxIA R5 is located in Loop 1 and establishes a salt-bridge with α7 D196 in the wild-type model, similar to the interaction of globular TxIA R5 with AChBP D197 in the TxIA/AChBP crystal structure. The model also suggests the proximity of two principal subunit basic residues, α7 R185 and K144, which could create an unfavorable electrostatic environment for Arg 5. In contrast, the model of ribbon [R5D]TxIA shows that D5 establishes a salt bridge with α7 R185. In the ToxDock model of [R5D]TxIA, D5 also forms a salt-bridge but with α7 K144. Position 5 therefore seems to be better suited for a negatively charged residue than a basic residue. Asn and Asp are isosteric, but Asn is neutral whereas Asp is negatively charged. In contrast to [R5D]TxIA, the mutant displaying an Asn at position 5, i.e., [R5N]TxIA, has similar activity to the parent peptide, strongly suggesting that the charge of the side chain at position 5 drives the increase in activity at the α7 nAChR (**Figures 5D,E**). This observation also suggests that the charge interactions of TxIA R5 with the complementary subunit balanced out and do not contribute to affinity. Interestingly, this analysis suggests that an R5D substitution of the globular TxIA would increase affinity for the α7 nAChR.

Mutational Energy Predictions

The interaction energies predicted by ToxDock were similar for the three complexes, with the interaction energy of wild-type ribbon TxIA in Rosetta units (RUs) being −592 for TxIA, −594 for [R5D]TxIA, and −595 for [R5N] TxIA. The mutational energies predicted by MMPB/SA suggest that the [R5N] mutant should have increased affinity by −4 kcal/mol compared to the parent peptide, while the [R5D] substitution

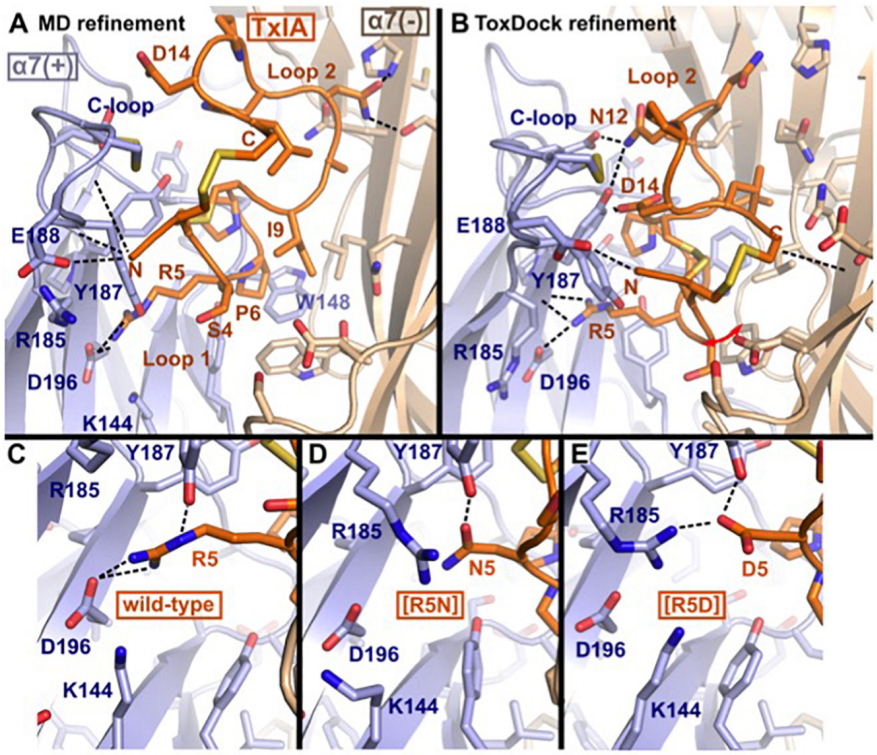

FIGURE 5 | Molecular models of the binding modes of ribbon TxIA at the α7 nAChR: **(A)** MD-refined molecular model, **(B)** ToxDock refined molecular model, and interaction of position 5 in the MD-refined model of **(C)** ribbon TxIA, **(D)** ribbon [R5N]TxIA, or **(E)** ribbon [R5D]TxIA. The last frame of the 50 ns MD simulation is shown in **(A)**. The model with the lowest re-weighted Rosetta score is shown in **(B)**. The backbone of the receptor and peptides are shown using cartoon representation [blue and wheat color for the principal (+) and complementary (–) subunits, respectively], the side chains of the toxins are shown as sticks (orange) and the side chain of receptor residues located at less than 5 Å from the toxin are shown in stick representation. Hydrogen bonds are indicated by dashed black lines.

was predicted to decrease affinity by 13 kcal/mol. None of the energy predictions therefore correlated with the experimental IC_{50} values, possibly because the main determinants of the affinity change involve evaluating the interaction of salt bridges in a partially solvated environment in the vicinity of several oppositely charged residues, which is challenging. Current force fields still have difficulty in reproducing the strength of solvated salt bridges (Ahmed et al., 2018). In addition, the estimation of binding energy is highly dependent on the accuracy of the three-dimensional structures of the complex. The incomplete consensus between the ToxDock- and MD-refined models suggest that these binding modes of ribbon α-conotoxins are not accurate enough for predicting the impact of mutations using score or energy computations. The determination of an experimental structure of a ribbon conotoxin bound to either AChBP or a nAChR should dramatically increase our ability to predict the interaction of ribbon conotoxins and the impact of mutations.

DISCUSSION

Here we describe for the first time the production of a recombinant α-conotoxin (4/7 α-conotoxin TxIA and three analogs) by expression in the periplasm of *E. coli*. We characterized the structure of three of these recombinant toxins and determined that, contrary to expectation, they adopt a ribbon conformation, which is not the dominant disulfide connectivity obtained during random oxidation of synthetically produced α-conotoxins. Ribbon TxIA experienced a significant decrease in activity at the α3β2 and α7 nAChRs, and we discovered that the mutant [R5D]TxIA could rescue the activity at the α7 nAChR at a similar level to that of globular TxIA, possibly because the location of position 5 in the α7 binding site is more electropositive.

Expression of α-Conotoxins in Bacteria

So far, three α-conotoxins, the 4/7 α-conotoxins Vc1.1, LvIA, and TxIB, have been recombinantly expressed (Singer et al., 2012; Zhu et al., 2016; Yu et al., 2018). Vc1.1 was expressed in the non-pathogenic *Salmonella enterica* serovar Typhimurium strain LT2. It was fused via a TEV protease cleavage site to a flagellar secretion substrate FlgM, enabling export of recombinant non-flagellar peptides through the flagellum and into the surrounding medium (Singer et al., 2012). No functional or structural data of *Salmonella*-expressed Vc1.1 were provided in that study.

LvIA was expressed in tandem repeats of various lengths in *E. coli* and purified from inclusion bodies which are

TABLE 2 | Structural statistics for the final ensemble of 20 structures for the ribbon isomer of TxIA with the highest overall MolProbity score.

Energies (kcal/mol)	
Overall	−475.3 ± 3.1
Bonds	6.51 ± 0.67
Angles	20.11 ± 2.48
Improper	9.21 ± 2.26
Van der Waals	−36.82 ± 3.04
NOE	0.02 ± 0.01
cDih	0.98 ± 0.67
Dihedral	65.78 ± 0.89
Electrostatic	−541 ± 6.3
MolProbity statistics	
Clashes (>0.4 Å/1000 atoms)	14.3 ± 4.66
Poor rotamers	0.05 ± 0.22
Ramachandran outliers (%)	0.0 ± 0.0
Ramachandran favored (%)	85.5 ± 6.19
MolProbity score	2.29 ± 0.31
Residues with bad bonds	0.00 ± 0.00
Residues with bad angles	0.00 ± 0.00
Atomic RMSD (Å)	
Mean global backbone	0.58 ± 0.26 (residues 1–16)
Mean global heavy	1.19 ± 0.37 (residues 1–16)
Distance Restraints	
Intraresidue (| i-j| = 0)	35
Sequential (| i-j| = 1)	44
Medium range (1 < | i-j| < 5)	16
Long range (| i-j| > 5)	8
Hydrogen bonds	3
Total	106
Dihedral angle restraints	
ϕ	11
ψ	8
χ^1	9
Total	28
Violations from experimental restraints	
Total NOE violations exceeding 0.3 Å	0
Total dihedral violations exceeding 3.0^0	0

generated during conventional recombinant protein expression in *E. coli* (Zhu et al., 2016). To allow chemical cleavage with cyanogen bromide, the individual peptide sequences were linked by methionine residues, which resulted in the N-terminal addition of a methionine residue to the cleaved peptides. Using this procedure and folding by air oxidation, a 18-fold decrease in activity from 9 to 160 nM was observed for the recombinant peptide compared to synthetic LvIA (Luo et al., 2014; Zhu et al., 2016). This decrease in activity was suggested to be due to the additional N-terminal methionine and/or the missing C-terminal amidation. The latter would be in agreement with the 2- and 5-fold potency reduction of non-amidated AnIB analogs at α3β2 and α7 subtypes respectively (Loughnan et al., 2004). However, the disulfide connectivity of the *E. coli*-expressed LvIA was not determined and our study of recombinant TxIA suggests that alternative disulfide connectivity could also explain the activity change.

In a more recent study from the same group (Yu et al., 2018), monomeric TxIB was expressed in *E. coli* as a ketosteroid isomerase (KSI)–TxIB(M)–His_6–fusion protein. KSI was used to help stabilize the peptide in inclusion bodies and the insoluble KSI could be easily separated upon cleavage from the peptide. A C-terminal methionine residue (M) had to be added to allow subsequent release of the peptide from KSI and the His_6-tag by cleavage with cyanogen bromide. Interestingly, the recombinant TxIB retained selectivity for α6β2 receptors and showed only a moderate twofold decrease in potency. Based on these properties, a globular fold was inferred because ribbon and bead isomers of TxIB were reported to be inactive.

Encouraged by reports on bacterial expression of other toxins and in an attempt to bypass the problem of aggregation in inclusion bodies, we exploited a system that allows expression of venom peptides in the form of periplasmic MBP fusion proteins. The idea of using periplasmic expression is to hijack the disulfide-bonding machinery in *E. coli* for producing natively folded heterologous peptides (Klint et al., 2013). Here, intramolecular disulfide bonds should form as the polypeptide chain exits the reductive environment of the bacterial cytoplasm and enters the oxidizing periplasmic environment. With a success rate of 75% based on the expression of 31 venom peptides (ranging from 17 to 76 residues in length with 2–6 disulfide bonds) from spiders, scorpions, sea anemone, and cone snails, this method mostly produces correctly folded peptides (Klint et al., 2013). However, the 25% of peptides that failed to express using this method indicate that the folding machinery in *E. coli* is not always a good surrogate for the mechanisms found in the venomous organisms from which the respective peptides were sourced. In the case of venom peptides from cone snails, the only other peptide that was tried (and failed) in this expression system was MVIA (Klint et al., 2013). In regard to TxIA, we could also not produce any native (globular) isomer, as all of the recombinant TxIA formed the ribbon isomer. In summary, for the only two *Conus* venom peptides that have been investigated so far, periplasmic expression in *E. coli* failed to produce the native disulfide-bond isomer. However, additional data with other *Conus* peptides is required to make a conclusion about the general suitability of this system for producing natively-folded cone snail venom peptides.

Does the Primary Structure Affect the Folding?

One surprising finding was that all expressed variants eluted in one dominant peak. In contrast to the present results and in agreement with data on other α-conotoxins, chemically synthesized and randomly oxidized α-conotoxin TxIA folds in all three possible conformations, globular, ribbon, and beads (Wu et al., 2014). This suggests the presence of factors that aid the formation of ribbon isomers in the periplasm of *E. coli* in contrast to the venom gland of the cone snail, in which the globular isomer is formed. In that case, misfolding could be a general problem for *E. coli* expression of α-conotoxins. Alternatively, TxIA could

have features in its amino acid sequence that favor formation of the ribbon fold, such as non-covalent interactions that stabilize the respective cysteine positioning. For example, a study by Kang et al. (2005) found that C-terminal amidation can cause a preferential (but not absolute) formation of the globular form of the 4/3-α-conotoxin ImI, supposedly by different hydrogen bonding interactions of the C-terminus. In this context, the potential effect of a Pro-Pro motif present in the first loop of TxIA instead of the more common Pro-Ala motif might also be important due to the structural constraints induced by proline residues. However, TxIB, which appeared to fold preferentially in the globular fold (Yu et al., 2018) has a first loop with amino acid sequence identical to [R5D]TxIA, which favored the ribbon conformation in our study. Thus, factors in loop 2 of 4/7 α-conotoxins would be more likely to affect the disulfide formation.

The inability to create post-translational modifications of α-conotoxins in *E. coli* (besides disulfide bonds) is potentially a problem as some of these modifications are important for activity in some conotoxins. Nevertheless, certain modifications such as tyrosine sulfation, glutamate carboxylation or C-terminal amidation had relatively minor effects in previous studies and might be dispensable for some toxins (Nicke et al., 2003; Loughnan et al., 2004). *In vitro* modifications such as C-terminal amidation, might also be feasible on purified recombinantly expressed toxins (Ul-Hasan et al., 2013; Zielinski et al., 2016).

Structural Comparison of 4/7 α-Conotoxin Ribbon and Globular Isomers

The solution structures of four ribbon α-conotoxins have been determined and are publicly available; these include the 3/5 α-conotoxin GI (PDB 1XGB) (Gehrmann et al., 1998), the 4/4 α-conotoxin BuIA (PDB 2NS3) (Jin et al., 2007), the 4/6 α-conotoxin AuIB (PDB 1MXP) (Dutton et al., 2002), and the 4/6 α-conotoxin Pu1.2 (Carstens et al., 2016). The structures of ribbon conotoxins are typically less well-defined than that of the corresponding globular isomers, with Loop 1 being relatively rigid whereas Loop 2 adopts multiple conformations, presumably indicating a greater flexibility (**Figure 6**). The four ribbon conotoxins with four residues in Loop 1, i.e., BuIA, rAuIB, Pu1.2, and TxIA, have a very similar conformation of Loop 1. Their Loop 2 conformations are different, reflecting the larger structural variability of Loop 2 in globular conotoxins (Akondi et al., 2014).

The ribbon isomers of α-conotoxins have naturally occurring structural analogs, the cysteine Framework X, with which they share two disulfide bridges in a ribbon isomer connectivity, a similar size, and four cysteine residues in similar pattern along the amino acid sequence (i.e., CC-C-C) (McIntosh et al., 2000). Loop 2 of cysteine framework X conotoxins contains only two amino acids, with the second residue of this loop being a hydroxyproline. The Loop 1 of framework X toxins has four residues, similar to the cysteine Framework I α-conotoxins, but it does not contain the Pro residue that is conserved in the α-conotoxins, and which occupies the orthosteric binding site of nAChRs as suggested by the crystal structures of complexes between α-conotoxins and AChBP (Lin et al., 2016). Framework X conotoxins are not active at nAChRs but rather target the neuronal noradrenaline transporter, and hence they are classified in the χ pharmacological family (Sharpe et al., 2001). Interestingly, the ribbon isomer of an α-conotoxin was even identified in a cone snail venom, indicating that for some α-conotoxins the ribbon isomer is also native (Safavi-Hemami et al., 2012).

Comparison of Proposed Binding Mode of Ribbon and Globular α-Conotoxins

A binding mode was recently proposed for the ribbon α-conotoxin AuIB at the α3β4 nAChR (Wu et al., 2018), and this binding mode is similar to the MD-refined binding mode of ribbon TxIA, as illustrated in **Figure 7**. It was demonstrated that the sole binding site of ribbon AuIB is at the α3(+)α3(−) interface based on its subunit stoichiometry-dependent activity at α3β4 nAChR (Grishin et al., 2010). Ribbon AuIB was recently suggested to adopt a similar binding mode to that of the globular α-conotoxin on the basis of an Ala scan which revealed that

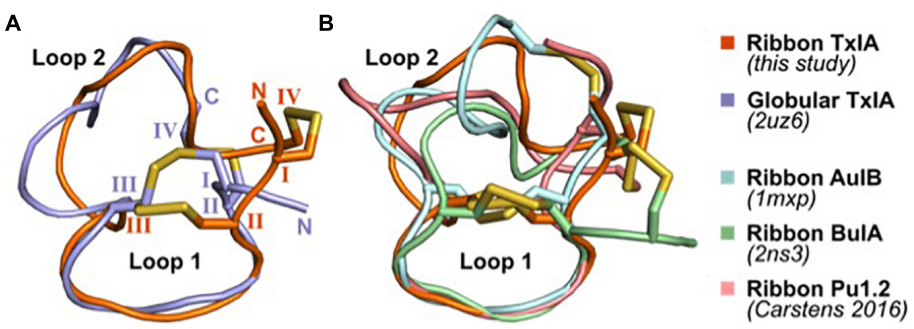

FIGURE 6 | Comparison of the NMR solution structure of ribbon TxIA with **(A)** globular TxIA and **(B)** other ribbon contoxin structures. The first model from the NMR ensemble was used in this figure, with the caveat that the 20 models of ribbon AuIB display a high conformational variability of Loop 2. The peptides are shown in cartoon representations and the disulfide bonds are indicated as yellow sticks. The N- and C-termini are indicated in **(A)**, and the hemi-cystine residues are numbered using Roman numerals. The PDB identifier of the experimentally determined three-dimensional structures is indicated where available.

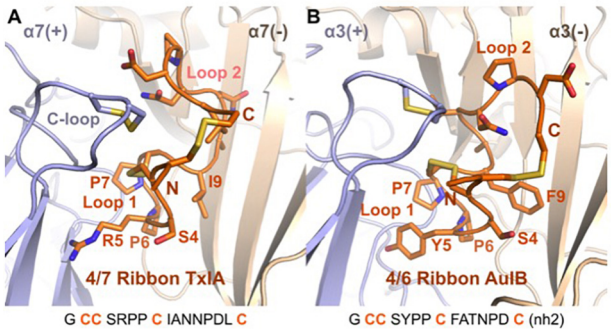

FIGURE 7 | Comparison of the binding mode of ribbon TxIA **(A)** and ribbon AuIB **(B)** at the interface between two α7 or α3 subunits, respectively. The toxins are in orange, with their backbone in cartoon representation and their side chains in stick representation. The binding site principal (+) and complementary (–) subunits are shown in blue and wheat color, respectively. The vicinal disulfide bond of the C-loop is shown in stick representation. The two binding sites have been oriented similarly for convenient comparison. The sequence of the two toxins is shown at the bottom of the figure.

most of the residues that are important for the activity of the globular isomer are also important for the ribbon isomer (Wu et al., 2018). Crystal structures of α-conotoxin/AChBP complexes showed that the first loops of the globular α-conotoxins overlap well, whereas the second loops adopt different conformations and interactions (Dutertre et al., 2007). Like the structures of globular α-conotoxins belonging to different loop-length subgroups bound to the AChBPs, the conformations of the Loop 1 of ribbon 4/7 TxIA and 4/6 AuIB overlay well in the binding sites but their second loop adopts different conformations. We have previously been able to explain the impact of more than 30 mutants of the complex between globular α-conotoxin ImI and the rat α7 nAChR, suggesting that our method can generate a reasonably accurate model of the receptor (Yu et al., 2011; Yu et al., 2012). The differences of binding modes observed after the two refinement methods seem therefore to originate from modeling the flexibility and interaction of the peptide. Interestingly, ribbon [P7A]AuIB has a structure similar to globular AuIB, but despite this change of conformation this mutation is innocuous (Wu et al., 2018), suggesting that ribbon AuIB would adopt a helical conformation by conformational selection. Similarly, ribbon TxIA also becomes more helical in both the MD- and ToxDock-refined models, suggesting that a helical conformation is optimal for interaction. The orientations of the loop 2 of ribbon TxIA and AuIB are different in the binding site, although position 9 (I9 of ribbon TxIA and Y9 of ribbon AuIB) was suggested to be buried at the interface with the complementary subunit for both peptides. Position 9 has been identified as a key determinant that modulates the activity of ribbon AuIB and it could also be involved in modulation of the activity of ribbon TxIA.

Because of their exceptional selectivity for certain ion channel or receptor subtypes, many conopeptides are used as tools in neuroscience and pharmacological research. Some of them have even been developed for clinical applications such as ω-conotoxin MVIIA (ziconitide), which is an FDA-approved analgesic for the treatment of intractable pain (Livett et al., 2004; Essack et al., 2012). In the case of α-conotoxins, the 4/7 α-conotoxins Vc1.1 and MII, the 4/3 α-conotoxin RgIA, and the 4/6 α-conotoxin AuIB, were found to have potent analgesic properties. Although there still exists some controversy regarding their physiological target (for a recent review see, Dutertre et al., 2017) these conotoxins are important lead structures. New methods for large-scale production of these conotoxins and development of a deeper understanding of their structure-activity relationships will accelerate their development into optimized tools and, hopefully, novel drugs.

AUTHOR CONTRIBUTIONS

AN: study design. YH, XW, RC, JG, RA, SD, QK, VH, and AN: experiments. YH, XW, RC, RA, DC, SD, QK, VH, and AN: data analysis. QK and AN: manuscript preparation. YH, DC, GK, and VH: manuscript editing. GK, VH, and AN: funding acquisition. All authors revised and approved the manuscript.

FUNDING

This work was supported by a DAAD-Group of Eight (Go8) travel grant (to AN, VH, and GK), The DFG (GRK 2338 TP1 to AN) and a Principal Research Fellowship APP1044414 to GK from the Australian National Health and Medical Research Council.

ACKNOWLEDGMENTS

We thank Prof. Walther Stühmer for generous support and Annett Sporning for technical assistance.

SUPPLEMENTARY MATERIAL

The Supplementary Material for this article can be found online at: https://www.frontiersin.org/articles/10.3389/fphar.2019.00577/full#supplementary-material

FIGURE S1 | Expression **(A)**, purification **(B)**, and analysis of antagonistic potency **(C)** at α3β2 nAChR of the [R5N,I9H]TxIA double mutant.

FIGURE S2 | Second step HILIC fractionation of purified expressed TxIA analogs and synthetic globular and ribbon TxIA isomers. Fractions containing the correct molecular mass are highlighted in color. The red colored fractions were generally used for all further experiments, orange colored fractions contained additional salt ions. The dashed line indicates the gradient of solvent B (90% ACN/0.043% TFA). MALDI MS traces indicate the monoisotopic molecular masses of the synthesized toxins. All reported masses are for $[M + H]^+$ ions. Note that the synthetic globular TxIA was C-terminally amidated, explaining the difference in molecular mass to the synthetic ribbon and recombinant TxIA (**Figure 2C**).

FIGURE S3 | Characterization of chemically synthesized ribbon TxIA. **(A)** UV absorbance chromatogram at 214 nm of synthetic TxIA ribbon. The minor peak is probably due to conformational exchange since the merging of the two peaks is observed at 55°C. ACN gradient from 0 to 100% in 2.5 min. **(B)** ESI-MS of synthethic TxIA ribbon. **(C)** Overlay of the amide region of the TOCSY spectra for

recombinantly expressed TxIA (red) and synthetic ribbon TxIA (blue). Small differences in chemical shift for the H_N protons are observed for Cys3 and Cys16 between samples presumably due to a slight variation in pH between samples.

FIGURE S4 | Comparison of the interactions between the position 5 of ribbon TxIA **(A)** and R5N **(B)** and R5D **(C)** variants at the α7 nAChR in the ToxDock-refined molecular models. The α7 nAChR is in blue and the toxins in orange. Hydrogen bonds are represented using dashed lines.

DATA SHEET S1 | Atomic coordinates files in PDB format of the molecular models of the interaction between ribbon TxIA and the α7 nAChR. Two models are provided, one refined using a molecular dynamics simulation and the other refined using the ToxDock protocol.

REFERENCES

Ahmed, M. C., Papaleo, E., and Lindorff-Larsen, K. (2018). How well do force fields capture the strength of salt bridges in proteins? *PeerJ* 6:e4967. doi: 10.7717/peerj.4967

Akondi, K. B., Muttenthaler, M., Dutertre, S., Kaas, Q., Craik, D. J., Lewis, R. J., et al. (2014). Discovery, synthesis, and structure-activity relationships of conotoxins. *Chem. Rev.* 114, 5815–5847. doi: 10.1021/cr400401e

Anangi, R., Rash, L. D., Mobli, M., and King, G. F. (2012). Functional expression in *Escherichia coli* of the disulfide-rich sea anemone peptide APETx2, a potent blocker of acid-sensing ion channel 3. *Mar. Drugs* 10, 1605–1618. doi: 10.3390/md10071605

Antoniewicz, M. R. (2015). Methods and advances in metabolic flux analysis: a mini-review. *J. Ind. Microbiol. Biotechnol.* 42, 317–325. doi: 10.1007/s10295-015-1585-x

Azam, L., and McIntosh, J. M. (2009). α-Conotoxins as pharmacological probes of nicotinic acetylcholine receptors. *Acta Pharmacol. Sin.* 30, 771–783. doi: 10.1038/aps.2009.47

Beissner, M., Dutertre, S., Schemm, R., Danker, T., Sporning, A., Grubmuller, H., et al. (2012). Efficient binding of 4/7 α-conotoxins to nicotinic α4β2 receptors is prevented by Arg185 and Pro195 in the α4 subunit. *Mol. Pharmacol.* 82, 711–718. doi: 10.1124/mol.112.078683

Braunschweiler, L., and Ernst, R. R. (1983). Coherence transfer by isotropic mixing: application to proton correlation spectroscopy. *J. Magn. Reson.* 53, 521–528. doi: 10.1016/0022-2364(83)90226-3

Brünger, A. T., Adams, P. D., Clore, G. M., DeLano, W. L., Gros, P., Grosse-Kunstleve, R. W., et al. (1998). Crystallography & NMR system: a new software suite for macromolecular structure determination. *Acta Crystallogr. D Biol. Crystallogr.* 54, 905–921. doi: 10.1107/S0907444998003254

Bussi, G., Donadio, D., and Parrinello, M. (2007). Canonical sampling through velocity rescaling. *J. Chem. Phys.* 126, 014101. doi: 10.1063/1.2408420

Carstens, B. B., Berecki, G., Daniel, J. T., Lee, H. S., Jackson, K. A., Tae, H. S., et al. (2016). Structure-Activity Studies of Cysteine-Rich α-Conotoxins that inhibit high-voltage-activated calcium channels via GABAB receptor activation reveal a minimal functional motif. *Angew. Chem. Int. Ed. Engl.* 55, 4692–4696. doi: 10.1002/anie.201600297

Cartier, G. E., Yoshikami, D., Gray, W. R., Luo, S., Olivera, B. M., and McIntosh, J. M. (1996). A new α-conotoxin which targets α3β2 nicotinic acetylcholine receptors. *J. Biol. Chem.* 271, 7522–7528. doi: 10.1074/jbc.271.13.7522

Dineley, K. T., Pandya, A. A., and Yakel, J. L. (2015). Nicotinic ACh receptors as therapeutic targets in CNS disorders. *Trends Pharmacol. Sci.* 36, 96–108. doi: 10.1016/j.tips.2014.12.002

Dominguez, C., Boelens, R., and Bonvin, A. M. (2003). HADDOCK: a protein-protein docking approach based on biochemical or biophysical information. *J. Am. Chem. Soc.* 125, 1731–1737. doi: 10.1021/ja026939x

Dutertre, S., Nicke, A., and Lewis, R. J. (2005). β2 subunit contribution to 4/7 α-conotoxin binding to the nicotinic acetylcholine receptor. *J. Biol. Chem.* 280, 30460–30468. doi: 10.1074/jbc.M504229200

Dutertre, S., Nicke, A., and Tsetlin, V. I. (2017). Nicotinic acetylcholine receptor inhibitors derived from snake and snail venoms. *Neuropharmacology* 127, 196–223. doi: 10.1016/j.neuropharm.2017.06.011

Dutertre, S., Ulens, C., Buttner, R., Fish, A., van Elk, R., Kendel, Y., et al. (2007). AChBP-targeted α-conotoxin correlates distinct binding orientations with nAChR subtype selectivity. *EMBO J.* 26, 3858–3867. doi: 10.1038/sj.emboj.7601785

Dutton, J. L., Bansal, P. S., Hogg, R. C., Adams, D. J., Alewood, P. F., and Craik, D. J. (2002). A new level of conotoxin diversity, a non-native disulfide bond connectivity in α-conotoxin AuIB reduces structural definition but increases biological activity. *J. Biol. Chem.* 277, 48849–48857. doi: 10.1074/jbc.M208842200

Essack, M., Bajic, V. B., and Archer, J. A. (2012). Conotoxins that confer therapeutic possibilities. *Mar. Drugs* 10, 1244–1265. doi: 10.3390/md10061244

Everhart, D., Cartier, G. E., Malhotra, A., Gomes, A. V., McIntosh, J. M., and Luetje, C. W. (2004). Determinants of potency on α-conotoxin MII, a peptide antagonist of neuronal nicotinic receptors. *Biochemistry* 43, 2732–2737. doi: 10.1021/bi036180h

Gehrmann, J., Alewood, P. F., and Craik, D. J. (1998). Structure determination of the three disulfide bond isomers of α-conotoxin GI: a model for the role of disulfide bonds in structural stability. *J. Mol. Biol.* 278, 401–415. doi: 10.1006/jmbi.1998.1701

Giribaldi, J., and Dutertre, S. (2018). α-Conotoxins to explore the molecular, physiological and pathophysiological functions of neuronal nicotinic acetylcholine receptors. *Neurosci. Lett.* 679, 24–34. doi: 10.1016/j.neulet.2017.11.063

Giribaldi, J., Wilson, D., Nicke, A., El Hamdaoui, Y., Laconde, G., Faucherre, A., et al. (2018). Synthesis, structure and biological activity of CIA and CIB, two α-conotoxins from the predation-evoked venom of *Conus catus*. *Toxins* 10:222. doi: 10.3390/toxins10060222

Gloor, S., Pongs, O., and Schmalzing, G. (1995). A vector for the synthesis of cRNAs encoding Myc epitope-tagged proteins in *Xenopus laevis* oocytes. *Gene* 160, 213–217. doi: 10.1016/0378-1119(95)00226-v

Grishin, A. A., Wang, C. I., Muttenthaler, M., Alewood, P. F., Lewis, R. J., and Adams, D. J. (2010). α-conotoxin AuIB isomers exhibit distinct inhibitory mechanisms and differential sensitivity to stoichiometry of α3β4 nicotinic acetylcholine receptors. *J. Biol. Chem.* 285, 22254–22263. doi: 10.1074/jbc.M110.111880

Güntert, P., Mumenthaler, C., and Wüthrich, K. (1997). Torsion angle dynamics for NMR structure calculation with the new program DYANA. *J. Mol. Biol.* 273, 283–298. doi: 10.1006/jmbi.1997.1284

Gyanda, R., Banerjee, J., Chang, Y. P., Phillips, A. M., Toll, L., and Armishaw, C. J. (2013). Oxidative folding and preparation of α-conotoxins for use in high-throughput structure-activity relationship studies. *J. Pept. Sci.* 19, 16–24. doi: 10.1002/psc.2467

Hone, A. J., and McIntosh, J. M. (2018). Nicotinic acetylcholine receptors in neuropathic and inflammatory pain. *FEBS Lett.* 592, 1045–1062. doi: 10.1002/1873-3468.12884

Hwang, T. L., and Shaka, A. J. (1995). Water suppression that works - excitation sculpting using arbitrary wave-forms and pulsed-field gradients. *J. Magn. Reson. A* 112, 275–279. doi: 10.1006/Jmra.1995.1047

Jeener, J., Meier, B. H., Bachmann, P., and Ernst, R. R. (1979). Investigation of exchange processes by two-dimensional NMR spectroscopy. *J. Chem. Phys.* 71, 4546–4553. doi: 10.1063/1.438208

Jin, A. H., Brandstaetter, H., Nevin, S. T., Tan, C. C., Clark, R. J., Adams, D. J., et al. (2007). Structure of α-conotoxin BuIA: influences of disulfide connectivity on structural dynamics. *BMC Struct. Biol.* 7:28. doi: 10.1186/1472-6807-7-28

Kaas, Q., Westermann, J. C., and Craik, D. J. (2010). Conopeptide characterization and classifications: an analysis using ConoServer. *Toxicon* 55, 1491–1509. doi: 10.1016/j.toxicon.2010.03.002

Kaas, Q., Yu, R., Jin, A. H., Dutertre, S., and Craik, D. J. (2012). ConoServer: updated content, knowledge, and discovery tools in the conopeptide database. *Nucleic Acids Res.* 40, D325–D330. doi: 10.1093/nar/gkr886

Kang, T. S., Vivekanandan, S., Jois, S. D., and Kini, R. M. (2005). Effect of C-terminal amidation on folding and disulfide-pairing of α-conotoxin ImI. *Angew. Chem. Int. Ed. Engl.* 44, 6333–6337. doi: 10.1002/anie.200502300

Kapust, R. B., Tozser, J., Copeland, T. D., and Waugh, D. S. (2002). The P1′ specificity of tobacco etch virus protease. *Biochem. Biophys. Res. Commun.* 294, 949–955. doi: 10.1016/S0006-291X(02)00574-0

Kasheverov, I. E., Zhmak, M. N., Fish, A., Rucktooa, P., Khruschov, A. Y., Osipov, A. V., et al. (2009). Interaction of α-conotoxin ImII and its analogs with nicotinic receptors and acetylcholine-binding proteins: additional binding sites on *Torpedo* receptor. *J. Neurochem.* 111, 934–944. doi: 10.1111/j.1471-4159.2009.06359.x

Klint, J. K., Senff, S., Saez, N. J., Seshadri, R., Lau, H. Y., Bende, N. S., et al. (2013). Production of recombinant disulfide-rich venom peptides for structural and functional analysis via expression in the periplasm of *E. coli*. *PLoS One* 8:e63865. doi: 10.1371/journal.pone.0063865

Koradi, R., Billeter, M., and Wüthrich, K. (1996). MOLMOL: a program for display and analysis of macromolecular structures. *J. Mol. Graph.* 14, 51–55. doi: 10.1016/0263-7855(96)00009-4

Leaver-Fay, A., O'Meara, M. J., Tyka, M., Jacak, R., Song, Y., Kellogg, E. H., et al. (2013). Scientific benchmarks for guiding macromolecular energy function improvement. *Methods Enzymol.* 523, 109–143. doi: 10.1016/B978-0-12-394292-0.00006-0

Leffler, A. E., Kuryatov, A., Zebroski, H. A., Powell, S. R., Filipenko, P., Hussein, A. K., et al. (2017). Discovery of peptide ligands through docking and virtual screening at nicotinic acetylcholine receptor homology models. *Proc. Natl. Acad. Sci. U.S.A.* 114, E8100–E8109. doi: 10.1073/pnas.1703952114

Lin, B., Xiang, S., and Li, M. (2016). Residues responsible for the selectivity of α-conotoxins for Ac-AChBP or nAChRs. *Mar. Drugs* 14, E173. doi: 10.3390/md14100173

Lindorff-Larsen, K., Piana, S., Palmo, K., Maragakis, P., Klepeis, J. L., Dror, R. O., et al. (2010). Improved side-chain torsion potentials for the Amber ff99SB protein force field. *Proteins* 78, 1950–1958. doi: 10.1002/prot.22711

Linge, J. P., and Nilges, M. (1999). Influence of non-bonded parameters on the quality of NMR structures: a new force field for NMR structure calculation. *J. Biomol. NMR* 13, 51–59.

Livett, B. G., Gayler, K. R., and Khalil, Z. (2004). Drugs from the sea: conopeptides as potential therapeutics. *Curr. Med. Chem.* 11, 1715–1723. doi: 10.2174/0929867043364928

Lombardo, S., and Maskos, U. (2015). Role of the nicotinic acetylcholine receptor in Alzheimer's disease pathology and treatment. *Neuropharmacology* 96(Pt. B), 255–262. doi: 10.1016/j.neuropharm.2014.11.018

Loughnan, M. L., Nicke, A., Jones, A., Adams, D. J., Alewood, P. F., and Lewis, R. J. (2004). Chemical and functional identification and characterization of novel sulfated α-conotoxins from the cone snail *Conus anemone*. *J. Med. Chem.* 47, 1234–1241. doi: 10.1021/jm031010o

Luo, S., Zhangsun, D., Schroeder, C. I., Zhu, X., Hu, Y., Wu, Y., et al. (2014). A novel α4/7-conotoxin LvIA from *Conus lividus* that selectively blocks α3β2 vs. α6/α3β2β3 nicotinic acetylcholine receptors. *FASEB J.* 28, 1842–1853. doi: 10.1096/fj.13-244103

Lyskov, S., Chou, F. C., Conchuir, S. O., Der, B. S., Drew, K., Kuroda, D., et al. (2013). Serverification of molecular modeling applications: the Rosetta Online Server that Includes Everyone (ROSIE). *PLoS One* 8:e63906. doi: 10.1371/journal.pone.0063906

Maruyama, K., Nagasawa, H., and Suzuki, A. (1999). 2,2′-Bispyridyl disulfide rapidly induces intramolecular disulfide bonds in peptides. *Peptides* 20, 881–884. doi: 10.1016/s0196-9781(99)00076-5

McIntosh, J. M., Corpuz, G. O., Layer, R. T., Garrett, J. E., Wagstaff, J. D., Bulaj, G., et al. (2000). Isolation and characterization of a novel conus peptide with apparent antinociceptive activity. *J. Biol. Chem.* 275, 32391–32397. doi: 10.1074/jbc.M003619200

McIntosh, J. M., Dowell, C., Watkins, M., Garrett, J. E., Yoshikami, D., and Olivera, B. M. (2002). α-Conotoxin GIC from *Conus geographus*, a novel peptide antagonist of nicotinic acetylcholine receptors. *J. Biol. Chem.* 277, 33610–33615. doi: 10.1074/jbc.M205102200

Miller, B. R. III, McGee, T. D. Jr., Swails, J. M., Homeyer, N., Gohlke, H., Roitberg, A. E., et al. (2012). MMPBSA.py: an efficient program for end-state free energy calculations. *J. Chem. Theory Comput.* 8, 3314–3321. doi: 10.1021/ct300418h

Mohamed, T. S., Jayakar, S. S., and Hamouda, A. K. (2015). Orthosteric and Allosteric Ligands of nicotinic acetylcholine receptors for smoking cessation. *Front. Mol. Neurosci.* 8:71. doi: 10.3389/fnmol.2015.00071

Mohammadi, S. A., and Christie, M. J. (2015). Conotoxin Interactions with α9α10-nAChRs: Is the α9α10-nicotinic acetylcholine receptor an important therapeutic target for pain management? *Toxins* 7, 3916–3932. doi: 10.3390/toxins7103916

Nederveen, A. J., Doreleijers, J. F., Vranken, W., Miller, Z., Spronk, C. A. E. M., Nabuurs, S. B., et al. (2005). RECOORD: a recalculated coordinate database of 500+proteins from the PDB using restraints from the BioMagResBank. *Proteins* 59, 662–672. doi: 10.1002/Prot.20408

Nicke, A., Loughnan, M. L., Millard, E. L., Alewood, P. F., Adams, D. J., Daly, N. L., et al. (2003). Isolation, structure, and activity of GID, a novel α 4/7-conotoxin with an extended N-terminal sequence. *J. Biol. Chem.* 278, 3137–3144. doi: 10.1074/jbc.M210280200

Palmer, A. G., Cavanagh, J., Wright, P. E., and Rance, M. (1991). Sensitivity improvement in proton-detected 2-dimensional heteronuclear correlation NMR-spectroscopy. *J. Magn. Reson.* 93, 151–170. doi: 10.1016/0022-2364(91)90036-S

Raveh, B., London, N., and Schueler-Furman, O. (2010). Sub-angstrom modeling of complexes between flexible peptides and globular proteins. *Proteins* 78, 2029–2040. doi: 10.1002/prot.22716

Safavi-Hemami, H., Gorasia, D. G., Steiner, A. M., Williamson, N. A., Karas, J. A., Gajewiak, J., et al. (2012). Modulation of conotoxin structure and function is achieved through a multienzyme complex in the venom glands of cone snails. *J. Biol. Chem.* 287, 34288–34303. doi: 10.1074/jbc.M112.366781

Sali, A., and Blundell, T. L. (1993). Comparative protein modelling by satisfaction of spatial restraints. *J. Mol. Biol.* 234, 779–815. doi: 10.1006/jmbi.1993.1626

Schubert, M., Labudde, D., Oschkinat, H., and Schmieder, P. (2002). A software tool for the prediction of Xaa-Pro peptide bond conformations in proteins based on 13C chemical shift statistics. *J. Biomol. NMR* 24, 149–154.

Sharpe, I. A., Gehrmann, J., Loughnan, M. L., Thomas, L., Adams, D. A., Atkins, A., et al. (2001). Two new classes of conopeptides inhibit the α1-adrenoceptor and noradrenaline transporter. *Nat. Neurosci.* 4, 902–907. doi: 10.1038/nn0901-902

Shen, M. Y., and Sali, A. (2006). Statistical potential for assessment and prediction of protein structures. *Protein Sci.* 15, 2507–2524. doi: 10.1110/ps.062416606

Shen, Y., and Bax, A. (2013). Protein backbone and sidechain torsion angles predicted from NMR chemical shifts using artificial neural networks. *J. Biomol. NMR* 56, 227–241. doi: 10.1007/S10858-013-9741-Y

Shen, Y., Delaglio, F., Cornilescu, G., and Bax, A. (2009). TALOS+: a hybrid method for predicting protein backbone torsion angles from NMR chemical shifts. *J. Biomol. NMR* 44, 213–223. doi: 10.1007/s10858-009-9333-z

Singer, H. M., Erhardt, M., Steiner, A. M., Zhang, M. M., Yoshikami, D., Bulaj, G., et al. (2012). Selective purification of recombinant neuroactive peptides using the flagellar type III secretion system. *mBio* 3:e00115-12. doi: 10.1128/mBio.00115-12

Tyka, M. D., Keedy, D. A., Andre, I., Dimaio, F., Song, Y., Richardson, D. C., et al. (2011). Alternate states of proteins revealed by detailed energy landscape mapping. *J. Mol. Biol.* 405, 607–618. doi: 10.1016/j.jmb.2010.11.008

Ul-Hasan, S., Burgess, D. M., Gajewiak, J., Li, Q., Hu, H., Yandell, M., et al. (2013). Characterization of the peptidylglycine α-amidating monooxygenase (PAM) from the venom ducts of neogastropods, *Conus bullatus* and *Conus geographus*. *Toxicon* 74, 215–224. doi: 10.1016/j.toxicon.2013.08.054

Vranken, W. F., Boucher, W., Stevens, T. J., Fogh, R. H., Pajon, A., Llinas, M., et al. (2005). The CCPN data model for NMR spectroscopy: development of a software pipeline. *Proteins* 59, 687–696. doi: 10.1002/prot.20449

Walsh, RM Jr, Roh, S. H., Gharpure, A., Morales-Perez, C. L., Teng, J., and Hibbs, R. E. (2018). Structural principles of distinct assemblies of the human α4β2 nicotinic receptor. *Nature* 557, 261–265. doi: 10.1038/s41586-018-0081-7

Williams, C. J., Headd, J. J., Moriarty, N. W., Prisant, M. G., Videau, L. L., Deis, L. N., et al. (2018). MolProbity: more and better reference data for improved all-atom structure validation. *Protein Sci.* 27, 293–315. doi: 10.1002/pro.3330

Wishart, D. S., Bigam, C. G., Holm, A., Hodges, R. S., and Sykes, B. D. (1995). 1H, 13C and 15N random coil NMR chemical shifts of the common amino acids. I. Investigations of nearest-neighbor effects. *J. Biomol. NMR* 5, 67–81. doi: 10.1007/bf00227471

Wishart, D. S., Sykes, B. D., and Richards, F. M. (1991). Relationship between nuclear magnetic resonance chemical shift and protein secondary structure. *J. Mol. Biol.* 222, 311–333. doi: 10.1016/0022-2836(91)90214-q

Wu, X., Tae, H. S., Huang, Y. H., Adams, D. J., Craik, D. J., and Kaas, Q. (2018). Stoichiometry dependent inhibition of rat α3β4 nicotinic acetylcholine receptor by the ribbon isomer of α-conotoxin AuIB. *Biochem. Pharmacol.* 155, 288–297. doi: 10.1016/j.bcp.2018.07.007

Wu, Y., Wu, X., Yu, J., Zhu, X., Zhangsun, D., and Luo, S. (2014). Influence of disulfide connectivity on structure and bioactivity of α-conotoxin TxIA. *Molecules* 19, 966–979. doi: 10.3390/molecules19010966

Wüthrich, K. (1986). *NMR of Proteins and Nucleic Acids*. New York, NY: Wiley-Interscience.

Yu, J., Zhu, X., Yang, Y., Luo, S., and Zhangsun, D. (2018). Expression in *Escherichia coli* of fusion protein comprising α-conotoxin TxIB and preservation of selectivity to nicotinic acetylcholine receptors in the purified product. *Chem. Biol. Drug Des.* 91, 349–358. doi: 10.1111/cbdd.13104

Yu, R., Craik, D. J., and Kaas, Q. (2011). Blockade of neuronal α7-nAChR by α-conotoxin ImI explained by computational scanning and energy calculations. *PLoS Comput. Biol.* 7:e1002011. doi: 10.1371/journal.pcbi.1002011

Yu, R., Kaas, Q., and Craik, D. J. (2012). Delineation of the unbinding pathway of α-conotoxin ImI from the α7 nicotinic acetylcholine receptor. *J. Phys. Chem. B* 116, 6097–6105. doi: 10.1021/jp301352d

Zhu, X., Bi, J., Yu, J., Li, X., Zhang, Y., Zhangsun, D., et al. (2016). Recombinant expression and characterization of α-Conotoxin LvIA in *Escherichia coli*. *Mar. Drugs* 14:11. doi: 10.3390/md14010011

Zielinski, M., Wojtowicz-Krawiec, A., Mikiewicz, D., Kesik-Brodacka, M., Cecuda-Adamczewska, V., Marciniak-Rusek, A., et al. (2016). Expression of recombinant human bifunctional peptidylglycine α-amidating monooxygenase in CHO cells and its use for insulin analogue modification. *Protein Expr. Purif.* 119, 102–109. doi: 10.1016/j.pep.2015.11.017

Conflict of Interest Statement: The authors declare that the research was conducted in the absence of any commercial or financial relationships that could be construed as a potential conflict of interest.

frontiers in Pharmacology

ORIGINAL RESEARCH
published: 03 July 2019
doi: 10.3389/fphar.2019.00748

From Synthetic Fragments of Endogenous Three-Finger Proteins to Potential Drugs

*Elena V. Kryukova[1], Natalia S. Egorova[1], Denis S. Kudryavtsev[1], Dmitry S. Lebedev[1], Ekaterina N. Spirova[1], Maxim N. Zhmak[1], Aleksandra I. Garifulina[1], Igor E. Kasheverov[1,2], Yuri N. Utkin[1] and Victor I. Tsetlin[1,3]**

[1] Department of Molecular Neuroimmune Signalling, Shemyakin-Ovchinnikov Institute of Bioorganic Chemistry, Russian Academy of Sciences, Moscow, Russia, [2] Sechenov First Moscow State Medical University, Institute of Molecular Medicine, Moscow, Russia, [3] PhysBio of MEPhI, Moscow, Russia

The proteins of the Ly6 family have a three-finger folding as snake venom α-neurotoxins, targeting nicotinic acetylcholine receptors (nAChRs), and some of them, like mammalian secreted Ly6/uPAR protein (SLURP1) and membrane-attached Ly-6/neurotoxin (Lynx1), also interact with distinct nAChR subtypes. We believed that synthetic fragments of these endogenous proteins might open new ways for drug design because nAChRs are well-known targets for developing analgesics and drugs against neurodegenerative diseases. Since interaction with nAChRs was earlier shown for synthetic fragments of the α-neurotoxin central loop II, we synthesized a 15-membered fragment of human Lynx1, its form with two Cys residues added at the N- and C-termini and forming a disulfide, as well as similar forms of human SLURP1, SLURP2, and of *Drosophila* sleepless protein (SSS). The IC_{50} values measured in competition with radioiodinated α-bungarotoxin for binding to the membrane-bound *Torpedo californica* nAChR were 4.9 and 7.4 μM for Lynx1 and SSS fragments, but over 300 μM for SLURP1 or SLURP2 fragments. The affinity of these compounds for the α7 nAChR in the rat pituitary tumor-derived cell line GH4C1 was different: 13.1 and 147 μM for SSS and Lynx1 fragments, respectively. In competition for the ligand-binding domain of the α9 nAChR subunit, SSS and Lynx1 fragments had IC_{50} values of about 40 μM, which correlates with the value found for the latter with the rat α9α10 nAChR expressed in the *Xenopus* oocytes. Thus, the activity of these synthetic peptides against muscle-type and α9α10 nAChRs indicates that they may be useful in design of novel myorelaxants and analgesics.

Keywords: three-finger proteins, peptide fragments, Ly6 family, nicotinic acetylcholine receptors, nAChRs

OPEN ACCESS

Edited by:
Charles K. Abrams, University of Illinois at Chicago, United States

Reviewed by:
Antonio R. Artalejo, Complutense University of Madrid, Spain
Salvatore Salomone, University of Catania, Italy

***Corresponding author:**
Victor I. Tsetlin
vits@mx.ibch.ru

Specialty section:
This article was submitted to Pharmacology of Ion Channels and Channelopathies, a section of the journal Frontiers in Pharmacology

Received: *24 October 2018*
Accepted: *11 June 2019*
Published: *03 July 2019*

Citation:
Kryukova EV, Egorova NS, Kudryavtsev DS, Lebedev DS, Spirova EN, Zhmak MN, Garifulina AI, Kasheverov IE, Utkin YN and Tsetlin VI (2019) From Synthetic Fragments of Endogenous Three-Finger Proteins to Potential Drugs. Front. Pharmacol. 10:748. doi: 10.3389/fphar.2019.00748

INTRODUCTION

According to proteomic and transcriptomic studies, a dominant family in the venoms of *Elapidae* snakes (cobras, kraits, coral snakes, and some others) are proteins containing about 60–80 amino acid residues, 4–5 disulfide bonds, and having a common type of the compact spatial structure built of three β-structural disulfide-confined loops (Kini and Doley, 2010; Utkin, 2013; Tsetlin, 2015), explaining their

Abbreviations: Ly6, lymphocyte antigen 6; Lynx1, Ly-6/neurotoxin; SLURP, secreted Ly6/uPAR protein; SSS, Drosophila sleepless protein; nAChR, nicotinic acetylcholine receptors; AChBP, acetylcholine-binding protein; LBD, ligand binding domain; α-Bgtx, α-bungarotoxin.

common name of "three-finger proteins" (TFPs). The snake venom TFPs greatly differ in their activity: short- and long-chain α-neurotoxins, as well as certain non-conventional neurotoxins are blocking nicotinic acetylcholine receptors (nAChRs) (Tsetlin, 2015), while another group of TFPs is attacking muscarinic acetylcholine receptors (Karlsson et al., 2000). There are toxins inhibiting β-adrenergic and other G-protein coupled receptors (GPCRs) (Blanchet et al., 2017). Among the recently found snake venom neurotoxins are mambalgins blocking the acid-sensitive ion channels (ASICs) (Brzezicki and Zakowicz, 2018). The targets of the snake venom TFPs are not limited by receptors and ion channels: for example, fasciculins from the *Dendroaspis angusticeps* mamba venom inhibit acetylcholinesterase (Karlsson et al., 1984), while cytotoxins, also known as cardiotoxins, do not have a selective target and penetrate the cell membrane (Dubovskii et al., 2013). It is a long history of using venoms as such for medical purposes (Chan et al., 2016; Estevão-Costa et al., 2018). Some individual components, as α-cobratoxin from the cobra venom and batroxobin from jararaca venom, are tested as possible remedies against pain (Gong et al., 2015) and as defibrinogenating agents (Ding et al., 2018), respectively.

There is no X-ray structure for a snake venom neurotoxin in complex with any whole-size nAChR subtype. However, high-resolution X-ray structures of toxins with the nAChR models are available: α-cobratoxin complex (Bourne et al., 2005) with the acetylcholine-binding protein (AChBP), which is an excellent model for the nAChR ligand-binding domain (LBD) (Smit et al., 2001; Ulens et al., 2006), α-bungarotoxin bound to the chimera of AChBP with the LBD of the α7 nAChR (Huang et al., 2013), as well as to the monomeric LBDs of the α1 and α9 nAChR subunits (Dellisanti et al., 2007; Zouridakis et al., 2014). All these structures, as well as earlier data on chemical modification and mutagenesis of α-neurotoxins, show the important role of the neurotoxin central loop II. Indeed, synthetic fragments of the central loop retained partial activity of the starting toxin and one such peptide was used for production of antisera for native toxin neutralization (de la Rosa et al., 2017).

Thus, synthetic fragments of snake venom toxins look promising for drug design. However, our paper is focusing not on the synthetic fragments of α-neurotoxins, but on the Ly6 proteins. Some of these proteins interact with nAChRs [see reviews (Ibañez-Tallon and Nitabach, 2012; Tsetlin, 2015)] and are considered as potential drugs (Miwa and Walz, 2012; Narumoto et al., 2013; Swamynathan et al., 2017; Lyukmanova et al., 2016a). Among them are mammalian proteins Lynx1 attached to the membrane in the vicinity of nAChRs by the glycosyl phosphoinositide anchor, and a secreted water-soluble protein SLURP1 (Durek et al., 2017). In view of the perspectives shown by synthetic fragments of α-neurotoxins, we synthesized the loop II fragments of these proteins and tested their activity against several nAChR subtypes. In case of positive results, the advantage of such peptides would be their origin from the endogenous proteins, allowing to expect from them only minimal toxicity. We synthesized the fragments of human Lynx1, SLURP1, and SLURP2, as well as a fragment of the a central loop of the *Drosophila* protein SSS, because for this protein [promoting sleep in *Drosophila* by inhibiting its neuronal nAChRs and activating a potassium channel (Wu et al., 2014)] the essential role of its whole loop II was demonstrated by heterologous expression of the protein lacking the N- and C-terminal loops (Wu et al., 2016).

MATERIALS AND METHODS

Solid-Phase Peptide Synthesis of the Central Loop Fragments of the Ly6 Proteins Interacting With nAChRs

The amino-acid sequences of the chosen synthetic fragments and a typical form of the Ly6 protein moiety are presented in **Figure 1**. The peptides were prepared by solid-phase synthesis using Fmoc/t-butyl strategy on tritylchloride-polystyrene resin (Intavis, Cologne, Germany). The disulfides were formed under conventional oxidation conditions: prolonged incubation on air in 50% aqueous acetonitrile at room temperature in the presence N-ethyldiisopropylamine (pH 8.0). All peptides were purified by high-performance liquid chromatography (HPLC) on a 250 × 30 mm C8 column (Dr. Maisch, Ammerbuch-Entringen, Germany) in linear gradient of acetonitrile from 10% to 40% and then lyophilized. The molecular masses determined by electrospray ionization ion trap mass spectrometry (ESI-IT-MS) were very close to theoretically calculated ones (see **Table 1**). The theoretical pI (isoelectric point) computation was done with Compute pI/Mw tool on SIB Bioinformatics Resource Portal (https://web.expasy.org/compute_pi/). The peptides purity (>98%) was confirmed using analytical HPLC. In order to stabilize the spatial structure, Cys residues were added at N- and C-termini to all peptides [except Lynx1 linear (**2**)] and were either left free [as in Lynx1 linear short (**4**)] or formed a disulfide as in Lynx1, Lynx1 short, SSS, SLURP1, and SLURP2 (**1**, **3**, **5**–**7**). In order to prevent formation of disulfides in peptide **4**, it was stored in the lyophilized form and dissolved immediately before the experiment. The structures and characteristics of the synthesized peptides are shown in **Table 1**.

Radioligand Analysis of Peptide Interactions With Various nAChR Subtypes, Ligand-Binding Domain of the α9 Subunit and With the AChBP

The binding capacity (IC_{50} values) was estimated in competition with the radioiodinated α-bungarotoxin [prepared as described in Kryukova et al. (2018) with specific radioactivity of 500 Curies/mmol] for association with the membrane-bound *Torpedo californica* nAChR (Hucho et al., 1978) (kindly provided by Prof. F. Hucho, Institute for Chemistry and Biochemistry, Freie Universität Berlin, Germany), human α7 nAChR stably expressed in the rat pituitary tumor-derived cell line GH4C1 (Virginio et al., 2002) (received from Eli Lilly and Company, London, UK), LBD of the human nAChR α9 subunit (Zouridakis et al., 2014) (prepared in the laboratory of Prof. S. Tzartos, Department of Neurobiology, Hellenic Pasteur Institute, Greece), and AChBP from *Aplysia californica* (Lin et al., 2014) (kindly provided by Prof. S. Luo, Key Laboratory for Marine Drugs of Haikou, Hainan University, China).

The suspensions of membranes from *T. californica* ray electric organ (1.25 nM α-bungarotoxin binding sites) or human

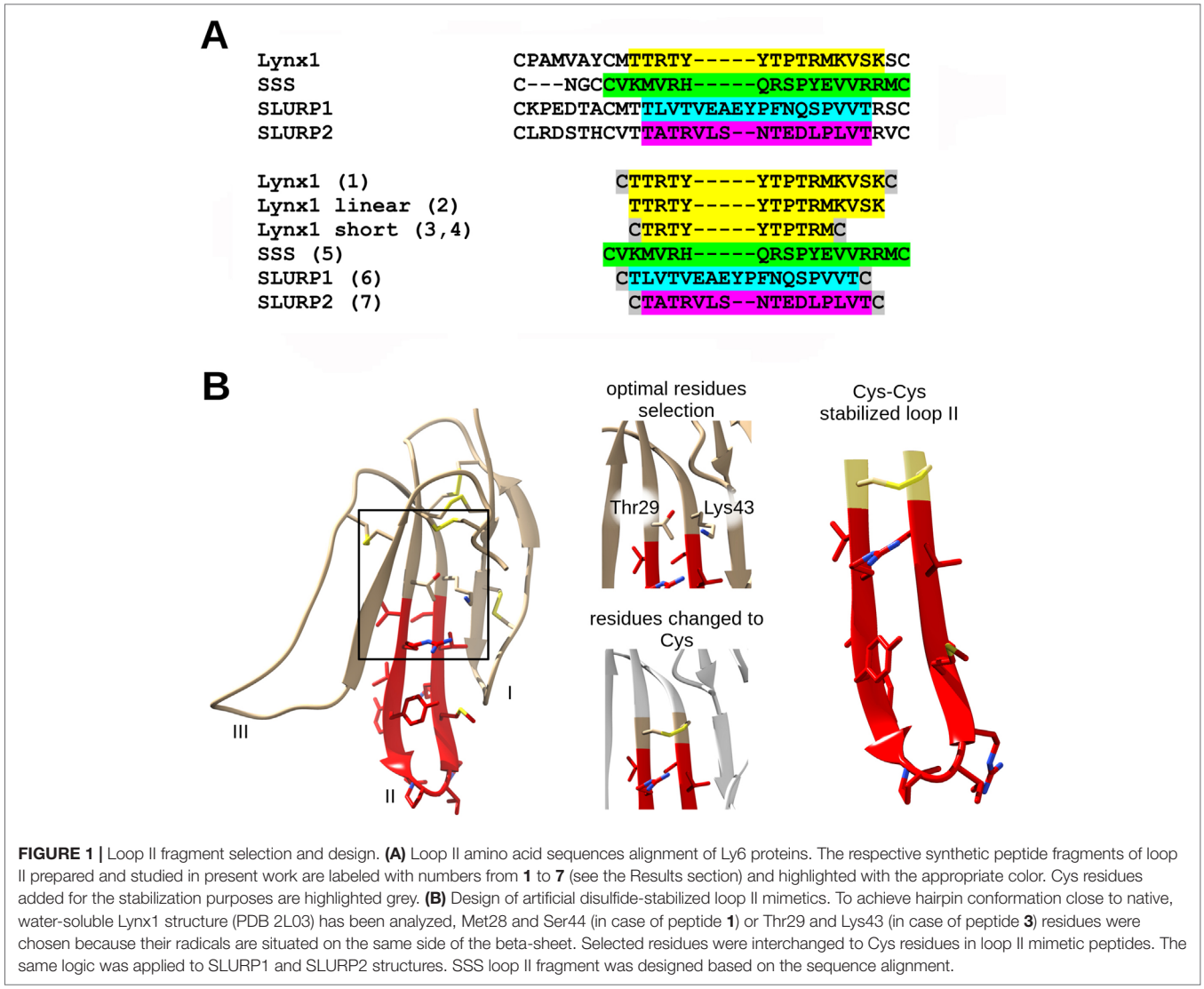

FIGURE 1 | Loop II fragment selection and design. **(A)** Loop II amino acid sequences alignment of Ly6 proteins. The respective synthetic peptide fragments of loop II prepared and studied in present work are labeled with numbers from **1** to **7** (see the Results section) and highlighted with the appropriate color. Cys residues added for the stabilization purposes are highlighted grey. **(B)** Design of artificial disulfide-stabilized loop II mimetics. To achieve hairpin conformation close to native, water-soluble Lynx1 structure (PDB 2L03) has been analyzed, Met28 and Ser44 (in case of peptide **1**) or Thr29 and Lys43 (in case of peptide **3**) residues were chosen because their radicals are situated on the same side of the beta-sheet. Selected residues were interchanged to Cys residues in loop II mimetic peptides. The same logic was applied to SLURP1 and SLURP2 structures. SSS loop II fragment was designed based on the sequence alignment.

TABLE 1 | Structures and characteristics of the synthesized Ly6 peptides.

Ly6 peptide	Peptide sequence	Molecular masses (MH^+)		pI
		Calculated	Measured	
Lynx1 **(1)**	CTTRTYYTPTRMKVSKC	2,036.97	2,036.90	9.70
Lynx1 linear **(2)**	TTRTYYTPTRMKVSK	1,832.96	1,832.85	10.45
Lynx1 short **(3)**	CTRTYYTPTRMC	1,493.63	1,493.60	8.90
Lynx1 short linear **(4)**	CTRTYYTPTRMC	1,495.64	1,495.70	8.90
SSS **(5)**	CKMVRHQRSPYEVVRRMC	2,278.12	2,278.17	10.09
SLURP1 **(6)**	CTLVTVEAEYPFNQSPVVTC	2,200.02	2,200.12	3.80
SLURP2 **(7)**	CTATRVLSNTEDLPLVTC	1,935.94	1,936.00	4.37

α7 nAChR expressed in GH4C1 cells (0.4 nM α-bungarotoxin binding sites) or expressed *A. californica* AChBP (150 nM α-bungarotoxin binding sites) were incubated in 50 µl of binding buffer [20 mM Tris-HCl buffer, pH 8.0, containing 1 mg/ml bovine serum albumin (BSA)] for 90 min with various amounts of the Ly6 peptides, followed by an additional 5-min incubation with 0.1–0.2 nM ^{125}I-labeled α-bungarotoxin (500 Ci/mmol). The membranes and cell suspensions were applied to glass GF/C filters (Whatman, Maidstone, UK) pretreated with 0.3% polyethylenimine. The samples were then washed (3 × 4 ml) with cold 20 mM Tris-HCl buffer, pH 8.0, containing 0.1 mg/ml BSA and bound radioactivity was measured with a Wallac 1470 Wizard Gamma Counter (PerkinElmer, Waltham, MA, USA). The *A. californica* AChBP samples were applied to two layers of DE-81 filters presoaked in phosphate-buffered saline containing 0.1 mg/ml BSA and washed (3 × 4 ml) with the same buffer. For human α9 LBD, the competition assays were carried out with 100 nM α9 LBD and different amounts of the Ly6 peptides. After incubation, 0.1–0.2 nM ^{125}I-labeled α-bungarotoxin (500 Ci/mmol) and 10 µl of Ni^{2+}-NTA agarose beads (Qiagen, Hilden, Germany) prewashed twice with binding buffer and diluted three times with the same buffer were added and after additional 5-min incubation (during this time, ^{125}I-labeled α-bungarotoxin occupies about 50% of binding sites on the *Torpedo* receptor and about 30–40% on the α7 nAChR), suspensions were applied to glass GF/C filters, washed, and bound radioactivity was measured as described above. Nonspecific ^{125}I-α-bungarotoxin binding was determined in the presence of 200-fold excess of α-cobratoxin.

Two-Electrode Voltage Clamp Analysis of Peptides Interaction With the Rat and Human α9α10, Human α3β2, and Human α4β2 nAChRs

Xenopus laevis frogs were fed twice a week and maintained according to supplier recommendations (https://www.enasco.com/page/xen_care).

All experiments were carried out in strict accordance with the World Health Organization's International Guiding Principles for Biomedical Research Involving Animals. The protocol (protocol number: 251/2018 26.02.18) was approved by Institutional Animal Care and Use Committee basing on the Institutional Policy on the Use of Laboratory Animals of the Shemyakin-Ovchinnikov Institute of Bioorganic Chemistry RAS.

Oocytes were removed from mature, anesthetized *Xenopus laevis* by dissecting abdomen and removing necessary amount of ovarium. Stage V–VI *Xenopus laevis* oocytes were defolliculated with 2 mg/ml collagenase type I (Life Technologies, Camarillo, USA) at room temperature (21–24°C) for 2 h in Ca^{2+}-free Barth's solution composed of (in mM) 88 NaCl, 1.1 KCl, 2.4 $NaHCO_3$, 0.8 $MgSO_4$, and 15 HEPES-NaOH at pH 7.6. Oocytes were injected with 9.2 ng of rat or human nAChR α9 and α10 cRNA (in a ratio 1:1) or human α3 and β2 or α4 and β2 cRNA (in a ratio 1:1). Oocytes were incubated at 18°C for 2–4 days before electrophysiological recordings in Barth's solution composed of (in mM) 88 NaCl, 1.1 KCl, 2.4 $NaHCO_3$, 0.3 $Ca(NO_3)_2$, 0.4 $CaCl_2$, 0.8 $MgSO_4$, and 15 HEPES-10NaOH at pH 7.6, supplemented with 40 µg/ml gentamicin and 100 µg/ml ampicillin. Recordings were performed using turbo TEC-03X amplifier (NPI Electronic, Tamm, Germany) and WinWCP recording software (University of Strathclyde, Glasgow, UK). The glass recording electrodes were filled with 3 M KCl and the electrode resistance was 0.1–0.5 MΩ. Membrane potential was clamped at −60 mV. Oocytes were briefly washed with Ba^{2+} Ringer's solution (Fuchs and Murrow, 1992) composed of (in mM) 115 NaCl, 2.5 KCl, 1.8 $BaCl_2$, 10 HEPES at pH 7.2, followed by three applications of 10 µM acetylcholine (ACh). Washout with Ba^{2+} Ringer's was done for 5 min between ACh applications. Oocytes were preincubated with various concentrations of Ly6 peptides for 5 min followed by their co-application with ACh. To induce ion current, we used ACh in the concentration range from 10 to 30 µM. The peak current amplitudes of ACh-induced responses were measured before (ACh alone) and after the preincubation of oocytes with peptides. The ratio between these two measurements was used to assess the activity of the tested compounds. In the experiments with α3β2 and α4β2, the above technique was also used, except that oocytes were washed in Barth`s solution. All control experiments were performed on the same day.

Rat α9 and α10 cDNAs was cloned in a pGEMHE vector; human α9, α10, α3, and β2 cDNAs were derived from pT7TS vector. Human α4 was cloned in pSP64 vector. Plasmid pT7TS constructs of human nAChR α9 and α10 subunits and human α3 and β2 subunits were linearized with *Xba*I restriction enzymes (NEB, Ipswich, USA). pSP64 vector was linearized with BamH1 restriction enzymes (NEB, Ipswich, USA). Rat α9 and α10 plasmids were linearized using *Nhe*I (NEB, Ipswich, USA). All plasmid constructs were sequencing before mRNA synthesis. The indicated restriction enzymes were chosen as their restriction sites are located downstream of the sequence as it is recommended by the manufacturer in mMESSAGE mMACHINE® High Yield Capped RNA Transcription Kit (Thermo Fisher Scientific, Waltham, USA). mRNAs were transcribed *in vitro* using T7 mMESSAGE mMachine™ (Thermo Fisher Scientific, Waltham, USA) and SP6 were prepared using SP6 mMESSAGE mMACHINE® High Yield Capped RNA Transcription Kit (Thermo Fisher Scientific, Waltham, USA). Transcribed mRNA was polyadenylated using the Poly-A-Tailing Kit (Thermo Fisher Scientific, Waltham, USA). The mRNAs were stored up to 6 months at −70°C. Before every use, the degradation levels of mRNAs were checked by gel electrophoresis.

Statistical Analysis

The binding results were analyzed using ORIGIN 8.0 (OriginLab Corporation, Northampton, MA, USA) fitting to a one-site dose-response curve by the equation: % response = $100/\{1+([\text{toxin}]/IC_{50})^n\}$, where IC_{50} is the concentration at which 50% of the binding sites are inhibited and n is the Hill coefficient. Data of the radioligand assay are presented as mean with 95% confidence interval (CI) for the indicated number (n) of independent experiments. Paired Student's t-test was done in ORIGIN 8.0 with the significance level set to $p < 0.05$.

RESULTS

Figure 1 and **Table 1** show that the fragments of several Ly6 proteins were obtained as homogeneous peptides and their structure has been confirmed by mass spectrometry. **Table 1** shows that the synthesized loops of human Lynx1 and *Drosophila* SSS have very close calculated pI values (9.7 and 10.0). They are basic similarly to the respective fragment (with the pI values of 7.9) of a short neurotoxin II [which like Ly6 proteins does not have an additional disulfide in the central loop (Grishin et al., 1973)] and are much closer to pI 10.46 for a weak toxin *Naja kaouthia* respective fragment [which also contains no additional disulfide in the central loop, but similarly to Ly6 proteins possesses additional disulfide in the N-terminal loop (Utkin et al., 2001)]. However, the pI values for SPURP1 and SLURP2 fragments are much lower (3.80 and 4.37, respectively), which might explain a big difference from the Lynx1 and SSS fragments in our biological tests (see below).

Radioligand Analysis of Ly6 Peptides Interaction With nAChR Subtypes and Their Models

Since high-affinity binding of radioiodinated α-bungarotoxin (αBgt) to muscle-type, α7 and α9α10 nAChRs occurs at their orthosteric sites, competition with this radioligand allows to detect binding to such sites also for the compounds of interest. **Figure 2** and **Table 2** show that the most active against the muscle-type receptor from *T. californica* was the fragment of Lynx1 (**1**) (IC_{50} = 4.9 μM), but it had almost a 30-fold lower activity against human α7 nAChR. Interestingly, the SSS fragment (**5**) was slightly less active against *Torpedo* receptor (7.4 μM), but 10-fold more active against α7 nAChR than the Lynx1 fragment (**1**) (IC_{50} 13.1 and 147.7 μM, respectively). Although cyclization was expected to stabilize the spatial structure, a linear form of the Lynx1 fragment (**2**) on the *Torpedo* and α7 nAChRs had the activity quite similar to that of the cyclized form. Linear (**4**) and especially cyclic (**3**) shorter forms of Lynx1 fragment were less active against *Torpedo* nAChR, but twofold more active against α7 nAChR than peptide (**1**).

In competition with ^{125}I-αBgt for the binding to α9 LBD, the SSS fragment (**5**), cyclic and linear Lynx1 fragments (**1** and **2**) revealed very similar affinities, their IC_{50} values being around 40 μM. On the other hand, **Table 2** shows that for SLURP1 and SLURP2 fragments even at concentrations over 300 μM, no inhibition of ^{125}I-αBgt binding was observed either with muscle and α7 nAChRs, or with α9 LBD. The loss of any inhibition at such high concentrations indicates the absence of nonspecific effects of the studied peptides on the binding of the radioligand to the targets. In fact, SLURP1 and SLURP2 fragments act as scrambled peptides in these experiments. Interestingly, although AChBP is known to bind compounds interacting not only with the nAChRs, but also with different Cys-loop receptors (Sixma and Smit, 2003; Brams et al., 2011) at concentration of about 100 μM, none of the compounds given in **Table 2** competed with ^{125}I-αBgt for binding to the *A. californica* AChBP

Two-Electrode Voltage Clamp Analysis

Since, this work was stimulated by the discovery of SLURP1 inhibition of the human and rat α9α10 nAChRs (Durek et al., 2017), we tested the activity of the synthesized peptides by two-electrode voltage clamp against human α9α10 nAChR expressed in the *Xenopus* oocytes. Unfortunately, no inhibition was registered for the SLURP1 or SLURP2 fragments (**6** and **7**) at concentrations as high as 50 μM (data not shown). On the other hand, although α9α10 nAChR was not detected among the targets of Lynx1 or its water-soluble variant (ws-Lynx1), the Lynx1 fragment (**1**) inhibited rat α9α10 nAChR with IC_{50} of 27 μM (**Figure 3A**). A slightly weaker activity was found for the Lynx1 linear fragment (**2**), while only 50% inhibition was detected for SSS fragment (**5**) at 100 μM concentration (**Figure 3B**).

Taking into account that neuronal αβ heteromeric nAChRs were among the targets of Lynx1 (Miwa et al., 1999; Ibañez-Tallon and Nitabach, 2012), ws-Lynx1 (Lyukmanova et al., 2011, Lyukmanova et al., 2013; Thomsen et al., 2014), and SLURP1 (Durek et al., 2017), we also tested the activity of the synthetic fragments against these receptors in electrophysiological experiments. At 30 μM, Lynx1 fragment (**1**) showed a tendency to inhibition of the current in the α3β2 nAChR by 30% (**Figure 4**). Similar effects were exerted by SLURP1 fragment (**6**) (**Figure 4**), whereas Lynx1 linear fragment (**2**), SLURP2 fragment (**7**), and the SSS fragment (**5**) were inactive. Unfortunately no significant activity of the peptides was detected in comparison to the currents recorded in response to 30 μM acetylcholine application. None of the peptides inhibited the ion currents in α4β2 nAChR (data not shown).

DISCUSSION

Historically, Lynx-1 was the first protein of the Ly6 family found co-localized in the mouse brain with the α7 and α4β2 nAChRs and shown to inhibit their activity (Miwa et al., 1999). This protein is of special interest to us because several years ago at the Shemyakin-Ovchinnikov Institute a water-soluble analog of Lynx1, devoid of the GPI anchor, was heterologously expressed in *Escherichia coli.* It inhibited ion currents in several nAChR subtypes and its three-dimensional structure was established by ^{1}H-NMR (Lyukmanova et al., 2011). Moreover, several mutations in its central loop II were shown to affect the activity (Lyukmanova et al., 2013). However, a water-soluble ws-Lynx1 is only a model of the membrane-bound Lynx1 and the differences in behavior were demonstrated in mouse overexpressing *Lynx 1* genes with or without the sequence coding for the GPI anchor (Miwa and Walz, 2012). The advantage of SLURP1 and SLURP2, the solution structures of which are also known (Lyukmanova et al., 2016b; Vasilyeva et al., 2017), is that they are naturally occurring water-soluble proteins and the research can be done on them as such, rather than on their models. Much information is available about the SLURP1/SLURP2 involvement in several diseases, predominantly in the skin disease Mal de Meleda (Perez and Khachemoune, 2016). However, until recently the work was done not on SLURP1 as such, but on various fusion proteins incorporating SLURP1. One publication

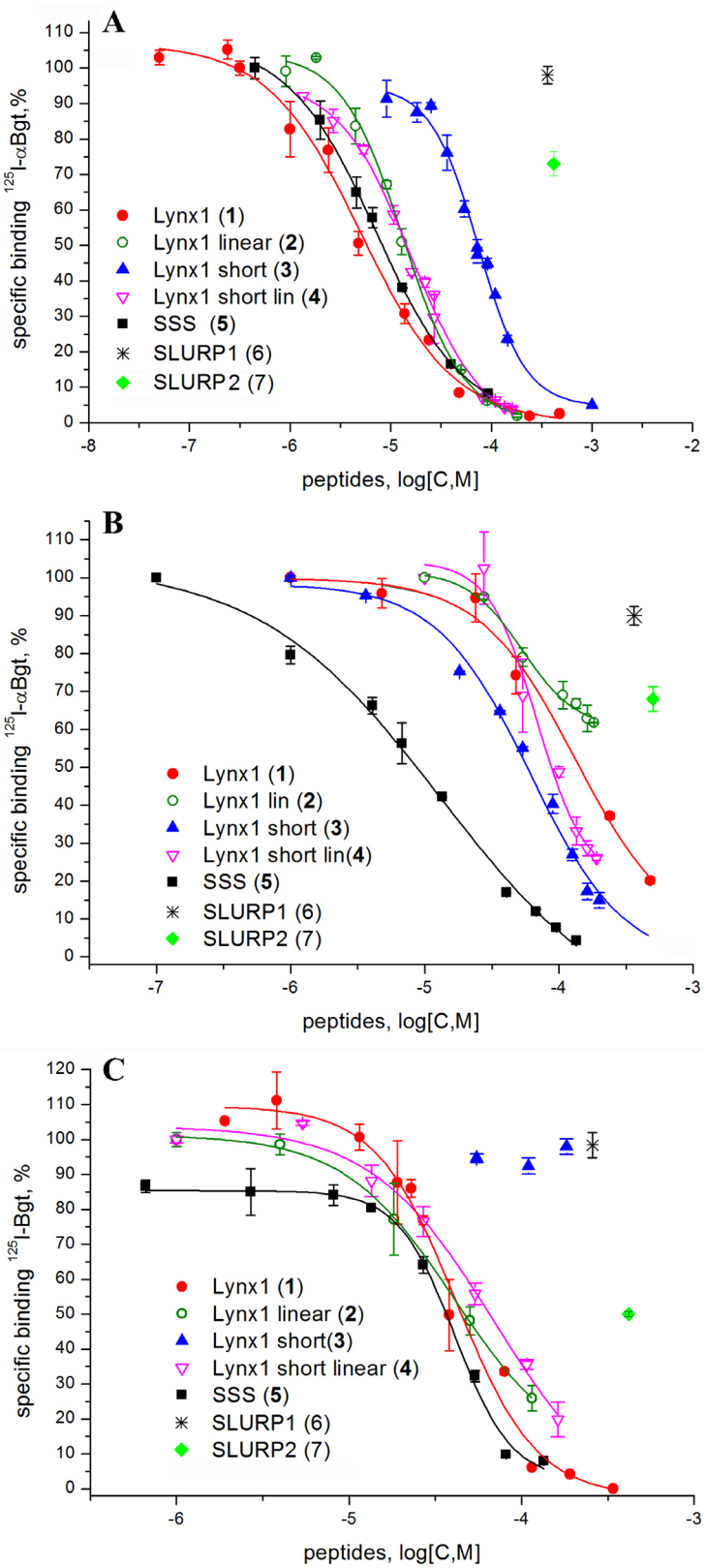

FIGURE 2 | Competition of [^{125}I]-labeled αBgt with Lynx1 peptides and SSS fragment for binding to **(A)** *Torpedo californica* nAChR, **(B)** human α7 nAChR expressed in the GH4C1 cell line, and **(C)** ligand-binding domain (LBD) of the human nAChR α9 subunit. IC_{50} values and 95% confidence interval (CI 95%) for these data are presented in **Table 2**. Each data point represents the mean ± SEM of three to four independent experiments.

TABLE 2 | The binding affinity of synthetic peptides to *T. californica,* human α7 nAChR, human α9 LBD, and *A. californica* AChBP measured by a competitive radioligand assay with ^{125}I-α-Bgt. The IC_{50} values and 95% confidence interval (CI) are presented for three to four independent experiments.

Ly6 peptide	IC_{50}, μM (95%CI)			
	T. californica	α7	α9 LBD	AChBP
Lynx1 **(1)**	4.9 (3.81–6.30)	173 (42.28–415.7)	41.7 (13.18–52.48)	>100
Lynx1 linear **(2)**	13.2 (11.26–15.68)	>180	40.7 (30.76–53.95)	>100
Lynx1 short **(3)**	74.13 (64.53–84.22)	58.9 (50.19–74.43)	>100	>100
Lynx1 short linear **(4)**	15.60 (13.55–18.62)	69.2 (48.98–98.63)	70.8 (25.7–190.5)	>100
SSS **(5)**	7.4 (7.14–7.73)	13.1 (6.60–26.1)	41.7 (38.19–47.86)	>100
SLURP1 **(6)**	>360	>360	>300	>100
SLURP2 **(7)**	>420	>500	~400	>100

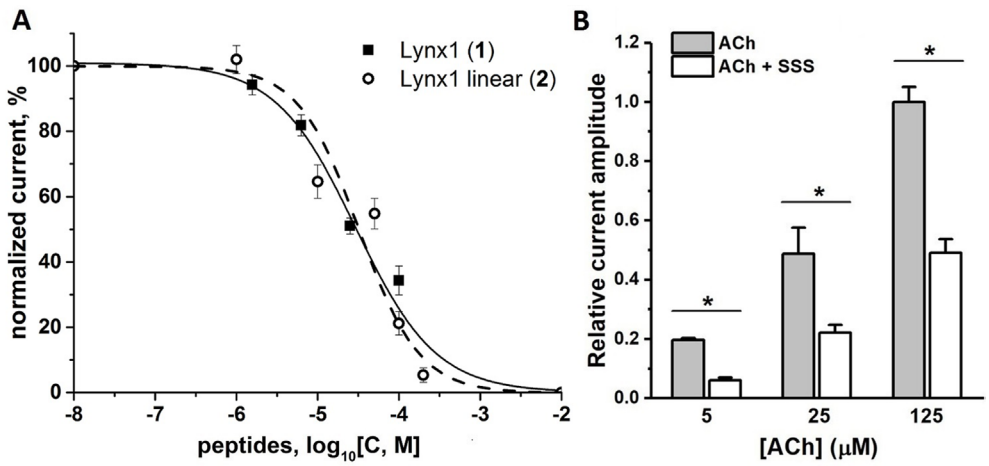

FIGURE 3 | Activity of synthetic Ly6 peptides on human and rat α9α10 nAChRs expressed in *X. laevis* oocytes. **(A)** Inhibition of ion currents induced by 30 μM acetylcholine by Lynx1 **(1)** fragment in the rat (■, solid line) α9α10 nAChRs or by Lynx1 linear fragment **(2)** in the human (○, dashed line) α9α10 nAChRs. The oocytes were pre-incubated with peptides for 5 min. For Lynx1 **(1)** the calculated IC_{50} was 27.00 μM (CI 95% 14.55–41.26 μM), n = 3. For Lynx1 linear fragment **(2)** the calculated IC_{50} was 32.30 μM (CI 95% 14.70–70.99 μM), n = 3. **(B)** Bar graph of 100 μM SSS fragment **(5)** inhibition of ion currents induced by 25 μM acetylcholine (ACh) in the human α9α10 nAChR. Data are presented as mean ± SEM, n = 3. Paired Student's t-test, $p < 0.05$ (*black asterisks*, normalized current evoked by acetylcholine in the presence of SSS *vs* normalized current induced by acetylcholine in the absence of SSS).

revealed potentiation of ion currents in α7 nAChR at nanomolar concentration of the used fusion SLURP1 protein (Chimienti et al., 2003). However, on the human SLURP1, differing from the naturally occurring protein only by the additional N-terminal Met residue, the effect was the opposite: inhibition rather than enhancement of ion current in α7 nAChR and at micromolar, rather than at nanomolar concentration (Lyukmanova et al., 2016b). Moreover, with the SLURP1 prepared by peptide synthesis and having virtually the same primary structure as the native protein, no inhibition of the α7 nAChR took place, but inhibition of several heterooligomeric nAChRs was registered (Durek et al., 2017). Most interestingly, with this SLURP-1 for the first time for an Ly6 protein inhibition of the α9α10 nAChR was observed and binding was proved to occur at an allosteric site (Durek et al., 2017). This finding to a considerable degree stimulated the present work because α9α10 nAChRs are targets for developing new analgesics, as illustrated most convincingly by research on those α-conotoxins, which are selective for this nAChR subtype (Dutertre et al., 2017; Hone and McIntosh, 2018).

As was described in the Introduction, a certain success was achieved in research using mainly the central loop II of three-finger neurotoxins where the structure was additionally stabilized by connecting the N- and C-termini of peptide by the grafted disulfide. We decided to synthesize the appropriate loops of Lynx1, SLURP1, and SLURP 2 and test their possible activities against several nAChR subtypes. We also included the *Drosophila* protein SSS, which affects the sleep processes interacting both with the nAChRs and potassium channels (Wu et al., 2014). Additional importance of this protein for our work, focusing on the central loops II from the TFPs of the Ly6 family, was due to the recently demonstrated functional activity for its heterologically expressed loop II (Wu et al., 2016).

The results in this work show that the synthetic fragments of Lynx1 and SSS demonstrated a low micromolar binding to the muscle-type *Torpedo* nAChR, as detected in competition with radioactive α-Bgt. Similar binding was registered with the SSS fragment (**5**) in case of the α7 nAChR, while Lynx1 fragment (**1**) was over 10-fold less active. A comparison of the cyclized and

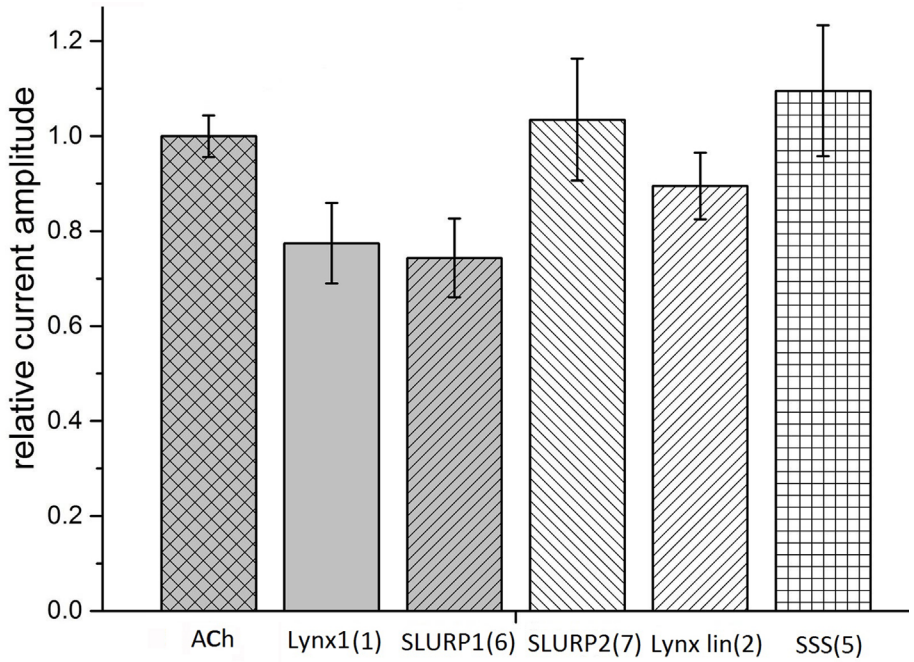

FIGURE 4 | Bar graph of 50 μM Ly6 fragments of Lynx1 **(1)**, SLURP1 **(6)**, SLURP2 **(7)**, Lynx1 linear **(2)**, and SSS **(5)** inhibition of ion currents induced by 30 μM ACh in the human α3β2 nAChR expressed in *X. laevis* oocytes. The current recorded in response to 30 μM ACh application (ACh) is accepted as 1. The current recorded in response to application of acetylcholine in the presence of peptides was compared with the mean between previous and afterwards acetylcholine-induced current. Normalized currents are presented as mean ± SEM, n = 3 [for SLURP2 **(7)**, Lynx1 linear **(2)**, and SSS **(5)**] or n = 5 [for Lynx1 **(1)** and SLURP1 **(6)**]. Ion current values for Lynx1 **(1)** and SLURP1 **(6)** are 0.77 ± 0.08 and 0.74 ± 0.08, respectively.

linear forms of Lynx1 fragment (**1** and **2**) shows that, contrary to expectations, stabilizing the spatial structure due to connecting the N- and C-termini did not cause a marked increase in the activity against certain targets. Surprisingly, shortening of the peptide (**4**) did not diminish its affinity, as compared to peptide (**2**), indicating that both peptides apparently retain the required conformation. Since peptides still should be relatively flexible it is difficult why cyclization of the short peptide (**3**) is weakening its interaction with the muscle-type and α9/α10 nAChRs.

Both for the SSS and Lynx1 fragments, their association with the α9 LBD was relatively weak (IC_{50} on the average of 40 μM); inhibition (IC_{50}) of ion currents in the α9α10 nAChR expressed in *Xenopus* oocytes measured for the Lynx fragment (**1**) was about 30 μM and a slightly less activity was found for the SSS fragment (**5**).

Unfortunately, our hope that the synthetic fragment of SLURP1 will possess at least a part of the activity against α9α10 nAChR found in SLURP1 itself (Durek et al., 2017) was not realized. Neither SLURP1 fragment (**6**) nor that (**7**) of SLURP2 revealed noticeable inhibition of ^{125}I-αBgt binding to *Torpedo* and human α7 nAChRs or to the α9 domain. They also did not compete with ^{125}I-αBgt for binding to *A. californica* AChBP, but none other synthetic fragment (active against several nAChRs) also manifested a competition. This result is not easy to explain because usually AChBPs are not very discriminative and with low affinity can bind diverse compounds capable of interacting with one or another nAChR subtype or with a different Cys-loop receptor (Brejc et al., 2001; Rucktooa et al., 2009; Brams et al., 2011).

Although our work is focusing on the muscle-type, α7, and α9α10 nAChRs, all of which efficiently bind αBgt (which at nanomolar concentrations also blocks ion currents in them), we checked possible effects of our synthetic fragments on the heterooligomeric α3β2 nAChR. The reason for this is that Lynx1 in the very first publication (Miwa et al., 1999) was shown to inhibit α4β2 nAChRs, while its effects on the function of other heteromeric nAChRs (Ibañez-Tallon and Nitabach, 2012) and on the process of their assembly (Parker et al., 2017) were demonstrated later. In addition, SLURP1 not only inhibited α9α10 nAChR, but also (at low micromolar level) diminished the currents in the α3β2 and α3β4 nAChRs (Durek et al., 2017). The SSS protein was earlier shown to inhibit a heteromeric nAChR of *Drosophila* (Wu et al., 2014). As **Figure 4** shows at least with the α3β2 nAChR, the SLURP1 fragment (**6**) had the activity comparable to that shown by other Ly6 synthetic fragments to one or another target.

It should be mentioned that there are many publications on the activity of the synthetic three-finger toxins and of their fragments: synthetic fragments of the central loop II of α-neurotoxins have been already mentioned (Kasheverov and Tsetlin, 2017), there are also full-size synthetic α-neurotoxins (Rey-Suárez et al., 2012), non-conventional neurotoxins (Poh et al., 2002), TFP toxins inhibiting acetylcholinesterase (fasciculins) (Falkenstein and Peña, 1997), synthetic mambalgins, and their

analogs attacking ASICs (Schroeder et al., 2014). Not always in the work on TFP toxins the interest was focused on the central loop: for the synthetic N-terminal loop of cardiotoxin I from the *Naja atra* cobra venom the authors reported antimicrobial activity against Gram-positive and Gram-negative bacteria (Sala et al., 2018). Interestingly, molecular modeling indicates that binding of another cytotoxin I (*Naja mossambica mossambica*) to 20S proteasome (resulting in the inhibition of its chymotryptic activity) is due to the toxin N-terminal loop (Munawar et al., 2015). It is worth to mention that the N-terminal sequence of SIRS (soluble immune response suppressor) has a homology to short α-neurotoxin and its synthetic 21-membered N-terminal fragment was shown to inhibit the development of experimental allergic encephalitis (Webb, 2016).

On the contrary, there is not much work on the synthetic fragments of the Ly6 proteins, and we could not find any publications in scientific literature on the synthetic fragments of those Ly6 proteins which interact with nAChRs or affect their assembly. In the patent database we found one (Walz, 2014) where a series of peptides homologous to Lynx1 fragment (**1**) has been synthesized homologous to Lynx1 fragment (**1**) but devoid of the N- and C-terminal Cys residues. However, the peptides were designed to facilitate penetration of the blood–brain barrier, but their interaction with the nAChRs or any other receptor was not tested. Thus, to best of our knowledge, here are the first data on the interaction of synthetic fragments of the central loop of Ly6 proteins with nAChRs.

In the case of the SLURP1 fragment, we did not manage to register the activity against α9α10 nAChR, which would be comparable to that of the synthetic SLURP1 and thus might prove useful for design of new analgesics. The aforementioned examples of the snake-venom TFPs show that, in the future, a success might come with the fragments not only of the central loop II (see **Figure 1**) but of other loops as well. In particular, mutagenesis of ws-Lynx1 demonstrated the functional role of several residues both in the central loop and in the N-terminal loop (Lyukmanova et al., 2013).

The activity of Lynx1 and SSS synthetic fragments, although being in low μM range, should not be called low. The affinity of α-neurotoxins against the muscle-type and α7 nAChRs is in the nanomolar range, but earlier in radioligand and electrophysiology experiments, it was shown that both ws-Lynx1 and recombinant SLURP1 (bearing an additional N-terminal Met residue) bind to the *Torpedo*, α7, and several heteromeric nAChRs and inhibit their currents at low μM concentrations (Lyukmanova et al., 2016b). The concentration of Lynx1 in the brain was also shown to be in the μM range (Thomsen et al., 2014). With a similar μM affinity synthetic SLURP1 (identical in the amino acid sequence to the naturally occurring protein) inhibits α9α10 and α3β2 nAChRs (but does not inhibit either rat or human α7 nAChRs). The synthetic fragment of Lynx1, at least toward muscle-type *Torpedo* nAChR, reproduces the activity of the full-size ws-Lynx1. This activity might find practical applications—for example, for design of efficient myorelaxants. In this respect, about 30-fold lower affinity of Lynx1 fragment (**1**) toward α7 nAChR can be an advantage: it resembles the case of azemiopsin, a linear peptide from the viper venom, which is considerably more selective to muscle nAChRs than to α7 nAChRs and for which preclinical studies as a myorelaxant have been recently completed (Shelukhina et al., 2018).

AUTHOR CONTRIBUTIONS

VT contributed to the conception and planning of the study. EK contributed to the leadership of the project, planning of experiments, and radioligand assay. NE and MZ contributed to the synthesis and characterization of peptides. IK contributed to the preparation of radioligand. DK, DL, ES, and AG contributed to the analysis of biological activities of the peptides. EK, YU, and VT contributed to the drafting of the manuscript and its editing.

FUNDING

The major support of this work was by RSF grant 16-14-00215. VT was additionally supported by the RFBR grants 18-04-00844 and 17-00-00063 komfi. IK was additionally supported by the RFBR grant 18-04-01366.

ACKNOWLEDGMENTS

The authors are grateful to Prof. S. Tsartos for the α9 LBD, to Prof. F. Hucho for the membrane-bound *T. californica* nAChR, to Eli-Lilly Company (London, UK) for α7 nAChR transfected in the GH4C1 cell line, and to Prof. S. Luo for *A. californica* AChBP.

REFERENCES

Blanchet, G., Alili, D., Protte, A., Upert, G., Gilles, N., Tepshi, L., et al. (2017). Ancestral protein resurrection and engineering opportunities of the mamba aminergic toxins. *Sci. Rep.* 7, 2701. doi: 10.1038/s41598-017-02953-0

Bourne, Y., Talley, T. T., Hansen, S. B., Taylor, P., and Marchot, P. (2005). Crystal structure of a Cbtx-AChBP complex reveals essential interactions between snake alpha-neurotoxins and nicotinic receptors. *EMBO J.* 24, 1512–1522. doi: 10.1038/sj.emboj.7600620

Brams, M., Pandya, A., Kuzmin, D., van Elk, R., Krijnen, L., Yakel, J. L., et al. (2011). A structural and mutagenic blueprint for molecular recognition of strychnine and d-tubocurarine by different cys-loop receptors. *PLoS Biol.* 9, e1001034. doi: 10.1371/journal.pbio.1001034

Brejc, K., van Dijk, W. J., Klaassen, R. V., Schuurmans, M., van der Oost, J., Smit, A. B., et al. (2001). Crystal structure of an ACh-binding protein reveals the ligand-binding domain of nicotinic receptors. *Nature* 411, 269–276. doi: 10.1038/35077011

Brzezicki, M. A., and Zakowicz, P. T. (2018). Mambalgins, the venom-origin peptides as a potentially Novel Group of Analgesics: mini review. *CNS Neurol. Disord. Drug Targets* 17, 87–97. doi: 10.2174/1871527317666171221110419

Chan, Y. S., Cheung, R. C. F., Xia, L., Wong, J. H., Ng, T. B., and Chan, W. Y. (2016). Snake venom toxins: toxicity and medicinal applications. *Appl. Microbiol. Biotechnol.* 100, 6165–6181. doi: 10.1007/s00253-016-7610-9

Chimienti, F., Hogg, R. C., Plantard, L., Lehmann, C., Brakch, N., Fischer, J., et al. (2003). Identification of SLURP-1 as an epidermal neuromodulator explains the clinical phenotype of Mal de Meleda. *Hum. Mol. Genet.* 12, 3017–3024. doi: 10.1093/hmg/ddg320

de la Rosa, G., Pastor, N., Alagón, A., and Corzo, G. (2017). Synthetic peptide antigens derived from long-chain alpha-neurotoxins: Immunogenicity effect against elapid venoms. *Peptides* 88, 80–86. doi: 10.1016/j.peptides.2016.12.006

Dellisanti, C. D., Yao, Y., Stroud, J. C., Wang, Z.-Z., and Chen, L. (2007). Crystal structure of the extracellular domain of nAChR α1 bound to α-bungarotoxin at 1.94 Å resolution. *Nat. Neurosci.* 10, 953–962. doi: 10.1038/nn1942

Ding, J., Zhou, D., Hu, Y., Elmadhoun, O., Pan, L., Ya, J., et al. (2018). The efficacy and safety of Batroxobin in combination with anticoagulation on cerebral venous sinus thrombosis. *J. Thromb. Thrombolysis* 46, 371–378. doi: 10.1007/s11239-018-1718-y

Dubovskii, P. V., Konshina, A. G., and Efremov, R. G. (2013). Cobra cardiotoxins: membrane interactions and pharmacological potential. *Curr. Med. Chem.* 21, 270–287. doi: 10.2174/0929867311320660315

Durek, T., Shelukhina, I. V., Tae, H.-S., Thongyoo, P., Spirova, E. N., Kudryavtsev, D. S., et al. (2017). Interaction of synthetic human SLURP-1 with the nicotinic acetylcholine receptors. *Sci. Rep.* 7, 16606. doi: 10.1038/s41598-017-16809-0

Dutertre, S., Nicke, A., and Tsetlin, V. I. (2017). Nicotinic acetylcholine receptor inhibitors derived from snake and snail venoms. *Neuropharmacology* 127, 196–223. doi: 10.1016/j.neuropharm.2017.06.011

Estevão-Costa, M.-I., Sanz-Soler, R., Johanningmeier, B., and Eble, J. A. (2018). Snake venom components in medicine: from the symbolic rod of Asclepius to tangible medical research and application. *Int. J. Biochem. Cell Biol.* 104, 94–113. doi: 10.1016/j.biocel.2018.09.011

Falkenstein, R. J., and Peña, C. (1997). Synthetic peptides derived from the central loop of fasciculin: structural analysis and evaluation as inhibitors of acetylcholinesterase. *Biochim. Biophys. Acta* 1340, 143–151. doi: 10.1016/S0167-4838(97)00040-X

Fuchs, P. A., and Murrow, B. W. (1992). Cholinergic inhibition of short (outer) hair cells of the chick's cochlea. *J. Neurosci.* 12.3, 800–809. doi: 10.1523/JNEUROSCI.12-03-00800.1992

Gong, S., Liang, Q., Zhu, Q., Ding, D., Yin, Q., Tao, J., et al. (2015). Nicotinic acetylcholine receptor α7 subunit is involved in the cobratoxin-induced antinociception in an animal model of neuropathic pain. *Toxicon* 93, 31–36. doi: 10.1016/j.toxicon.2014.11.222

Grishin, E. V., Sukhikh, A. P., Lukyanchuk, N. N., Slobodyan, L. N., Lipkin, V. M., and Ovchinnikov, Y. A. (1973). Amino acid sequence of neurotoxin II from Naja naja oxiana venom. *FEBS Lett.* 36, 77–78. doi: 10.1016/0014-5793(73)80340-0

Hone, A. J., and McIntosh, J. M. (2018). Nicotinic acetylcholine receptors in neuropathic and inflammatory pain. *FEBS Lett.* 592, 1045–1062. doi: 10.1002/1873-3468.12884

Huang, S., Li, S.-X., Bren, N., Cheng, K., Gomoto, R., Chen, L., et al. (2013). Complex between α-bungarotoxin and an α7 nicotinic receptor ligand-binding domain chimaera. *Biochem. J.* 454, 303–310. doi: 10.1042/BJ20130636

Hucho, F., Bandini, G., and Suarez-Isla, B. A. (1978). The acetylcholine receptor as part of a protein complex in receptor-enriched membrane fragments from Torpedo californica electric tissue. *Eur. J. Biochem.* 83, 335–340. doi: 10.1111/j.1432-1033.1978.tb12099.x

Ibañez-Tallon, I., and Nitabach, M. N. (2012). Tethering toxins and peptide ligands for modulation of neuronal function. *Curr. Opin. Neurobiol.* 22, 72–78. doi: 10.1016/j.conb.2011.11.003

Karlsson, E., Mbugua, P. M., and Rodriguez-Ithurralde, D. (1984). Fasciculins, anticholinesterase toxins from the venom of the green mamba Dendroaspis angusticeps. *J. Physiol. Paris* 79, 232–240.

Karlsson, E., Jolkkonen, M., Mulugeta, E., Onali, P., and Adem, A. (2000). Snake toxins with high selectivity for subtypes of muscarinic acetylcholine receptors. *Biochimie* 82, 793–806. doi: 10.1016/S0300-9084(00)01176-7

Kasheverov, I. E., and Tsetlin, V. I. (2017). "Snake Venom Components as Basis for Biologically Active Synthetic Peptides," in, 103–128. doi: 10.1007/978-94-007-6452-1_23

Kini, R. M., and Doley, R. (2010). Structure, function and evolution of three-finger toxins: mini proteins with multiple targets. *Toxicon* 56, 855–867. doi: 10.1016/j.toxicon.2010.07.010

Kryukova, E. V., Ivanov, I. A., Lebedev, D. S., Spirova, E. N., Egorova, N. S., Zouridakis, M., et al. (2018). Orthosteric and/or allosteric binding of α-conotoxins to nicotinic acetylcholine receptors and their models. *Mar. Drugs* 16, E460. doi: 10.3390/md16120460

Lin, B., Meng, H., Bing, H., Zhangsun, D., and Luo, S. (2014). Efficient expression of acetylcholine-binding protein from Aplysia californica in Bac-to-Bac system. *Biomed. Res. Int.* 2014, 691480. doi: 10.1155/2014/691480

Lyukmanova, E. N., Shenkarev, Z. O., Shulepko, M. A., Mineev, K. S., D'Hoedt, D., Kasheverov, I. E., et al. (2011). NMR structure and action on nicotinic acetylcholine receptors of water-soluble domain of human LYNX1. *J. Biol. Chem.* 286, 10618–10627. doi: 10.1074/jbc.M110.189100

Lyukmanova, E. N., Shulepko, M. A., Buldakova, S. L., Kasheverov, I. E., Shenkarev, Z. O., Reshetnikov, R. V., et al. (2013). Water-soluble LYNX1 residues important for interaction with muscle-type and/or neuronal nicotinic receptors. *J. Biol. Chem.* 288, 15888–15899. doi: 10.1074/jbc.M112.436576

Lyukmanova, E. N., Shulepko, M. A., Kudryavtsev, D., Bychkov, M. L., Kulbatskii, D. S., Kasheverov, I. E., et al. (2016a). Human secreted Ly-6/uPAR related protein-1 (SLURP-1) is a selective allosteric antagonist of α7 nicotinic acetylcholine receptor. *PLoS One* 11, e0149733. doi: 10.1371/journal.pone.0149733

Lyukmanova, E. N., Shulepko, M. A., Shenkarev, Z. O., Bychkov, M. L., Paramonov, A. S., Chugunov, A. O., et al. (2016b). Secreted isoform of human Lynx1 (SLURP-2): spatial structure and pharmacology of interactions with different types of acetylcholine receptors. *Sci. Rep.* 6, 30698. doi: 10.1038/srep30698

Miwa, J. M., and Walz, A. (2012). Enhancement in motor learning through genetic manipulation of the Lynx1 gene. *PLoS One* 7, e43302. doi: 10.1371/journal.pone.0043302

Miwa, J. M., Ibanez-Tallon, I., Crabtree, G. W., Sánchez, R., Sali, A., Role, L. W., et al. (1999). lynx1, an endogenous toxin-like modulator of nicotinic acetylcholine receptors in the mammalian CNS. *Neuron* 23, 105–114. doi: 10.1016/S0896-6273(00)80757-6

Munawar, A., Akrem, A., Hussain, A., Spencer, P., and Betzel, C. (2015). Molecular model of Cytotoxin-1 from Naja mossambica mossambica venom in complex with chymotrypsin. *Theor. Biol. Forum* 108, 89–99.

Narumoto, O., Niikura, Y., Ishii, S., Morihara, H., Okashiro, S., Nakahari, T., et al. (2013). Effect of secreted lymphocyte antigen-6/urokinase-type plasminogen activator receptorrelated peptide-1 (SLURP-1) on airway epithelial cells. *Biochem. Biophys. Res. Commun.* 438, 175–179. doi: 10.1016/j.bbrc.2013.07.048

Parker, R. L., O'Neill, H. C., Henley, B. M., Wageman, C. R., Drenan, R. M., Marks, M. J., et al. (2017). Deletion of lynx1 reduces the function of α6* nicotinic receptors. *PLoS One* 12, e0188715. doi: 10.1371/journal.pone.0188715

Perez, C., and Khachemoune, A. (2016). Mal de Meleda: a focused review. *Am. J. Clin. Dermatol.* 17, 63–70. doi: 10.1007/s40257-015-0157-1

Poh, S. L., Mourier, G., Thai, R., Armugam, A., Molgó, J., Servent, D., et al. (2002). A synthetic weak neurotoxin binds with low affinity to Torpedo and chicken alpha7 nicotinic acetylcholine receptors. *Eur. J. Biochem.* 269, 4247–4256. doi: 10.1046/j.1432-1033.2002.03113.x

Rey-Suárez, P., Floriano, R. S., Rostelato-Ferreira, S., Saldarriaga-Córdoba, M., Núñez, V., Rodrigues-Simioni, L., et al. (2012). Mipartoxin-I, a novel three-finger toxin, is the major neurotoxic component in the venom of the redtail coral snake Micrurus mipartitus (Elapidae). *Toxicon* 60, 851–863. doi: 10.1016/j.toxicon.2012.05.023

Rucktooa, P., Smit, A. B., and Sixma, T. K. (2009). Insight in nAChR subtype selectivity from AChBP crystal structures. *Biochem. Pharmacol.* 78, 777–787. doi: 10.1016/j.bcp.2009.06.098

Sala, A., Cabassi, C. S., Santospirito, D., Polverini, E., Flisi, S., Cavirani, S., et al. (2018). Novel Naja atra cardiotoxin 1 (CTX-1) derived antimicrobial peptides with broad spectrum activity. *PLoS One* 13, e0190778. doi: 10.1371/journal.pone.0190778

Schroeder, C. I., Rash, L. D., Vila-Farrés, X., Rosengren, K. J., Mobli, M., King, G. F., et al. (2014). Chemical synthesis, 3D structure, and ASIC binding site of the toxin mambalgin-2. *Angew. Chem. Int. Ed. Engl.* 53, 1017–1020. doi: 10.1002/anie.201308898

Shelukhina, I. V., Zhmak, M. N., Lobanov, A. V., Ivanov, I. A., Garifulina, A. I., Kravchenko, I. N., et al. (2018). Azemiopsin, a selective peptide antagonist of muscle nicotinic acetylcholine receptor: preclinical evaluation as a local muscle relaxant. *Toxins (Basel)* 10, 34. doi: 10.3390/toxins10010034

Sixma, T. K., and Smit, A. B. (2003). Acetylcholine binding protein (AChBP): a secreted glial protein that provides a high-resolution model for the extracellular domain of pentameric ligand-gated ion channels. *Annu. Rev. Biophys. Biomol. Struct.* 32, 311–334. doi: 10.1146/annurev.biophys.32.110601.142536

Smit, A. B., Syed, N. I., Schaap, D., van Minnen, J., Klumperman, J., Kits, K. S., et al. (2001). A glia-derived acetylcholine-binding protein that modulates synaptic transmission. *Nature* 411, 261–268. doi: 10.1038/35077000

Swamynathan, S., Loughner, C. L., and Swamynathan, S. K. (2017). Inhibition of HUVEC tube formation via suppression of NFκB suggests an anti-angiogenic role for SLURP1 in the transparent cornea. *Exp. Eye Res.* 164, 118–128. doi: 10.1016/j.exer.2017.08.007

Thomsen, M. S., Cinar, B., Jensen, M. M., Lyukmanova, E. N., Shulepko, M. A., Tsetlin, V., et al. (2014). Expression of the Ly-6 family proteins Lynx1 and Ly6H in the rat brain is compartmentalized, cell-type specific, and developmentally regulated. *Brain Struct. Funct.* 219, 1923–1934. doi: 10.1007/s00429-013-0611-x

Tsetlin, V. I. (2015). Three-finger snake neurotoxins and Ly6 proteins targeting nicotinic acetylcholine receptors: pharmacological tools and endogenous modulators. *Trends Pharmacol. Sci.* 36, 109–123. doi: 10.1016/j.tips.2014.11.003

Ulens, C., Hogg, R. C., Celie, P. H., Bertrand, D., Tsetlin, V., Smit, A. B., et al. (2006). Structural determinants of selective -conotoxin binding to a nicotinic acetylcholine receptor homolog AChBP. *Proc. Natl. Acad. Sci. U.S.A.* 103, 3615–3620. doi: 10.1073/pnas.0507889103

Utkin, Y. N. (2013). Three-finger toxins, a deadly weapon of elapid venom–milestones of discovery. *Toxicon* 62, 50–55. doi: 10.1016/j.toxicon.2012.09.007

Utkin, Y. N., Kukhtina, V. V., Kryukova, E. V., Chiodini, F., Bertrand, D., Methfessel, C., et al. (2001). Weak toxin" from Naja kaouthia is a nontoxic antagonist of alpha 7 and muscle-type nicotinic acetylcholine receptors. *J. Biol. Chem.* 276, 15810–15815. doi: 10.1074/jbc.M100788200

Vasilyeva, N. A., Loktyushov, E. V., Bychkov, M. L., Shenkarev, Z. O., and Lyukmanova, E. N. (2017). Three-finger proteins from the Ly6/uPAR family: functional diversity within one structural motif. *Biochemistry (Mosc)* 82, 1702–1715. doi: 10.1134/S0006297917130090

Virginio, C., Giacometti, A., Aldegheri, L., Rimland, J. M., and Terstappen, G. C. (2002). Pharmacological properties of rat alpha 7 nicotinic receptors expressed in native and recombinant cell systems. *Eur. J. Pharmacol.* 445 (3), 153–161. doi: 10.1016/S0014-2999(02)01750-8

Walz, A. (2014). *Compositions and methods for transport across the blood brain barrier*. U.S. Patent No 8,629,114 B2.

Webb, D. R. (2016). Soluble Immune Response Suppressor (SIRS): reassessing the immunosuppressant potential of an elusive peptide. *Biochem. Pharmacol.* 117, 1–9. doi: 10.1016/j.bcp.2016.03.022

Wu, M., Liu, C. Z., and Joiner, W. J. (2016). Structural analysis and deletion mutagenesis define regions of QUIVER/SLEEPLESS that are responsible for interactions with shaker-type potassium channels and nicotinic acetylcholine receptors. *PLoS One* 11, e0148215. doi: 10.1371/journal.pone.0148215

Wu, M., Robinson, J. E., and Joiner, W. J. (2014). SLEEPLESS is a bifunctional regulator of excitability and cholinergic synaptic transmission. *Curr. Biol.* 24, 621–629. doi: 10.1016/j.cub.2014.02.026

Zouridakis, M., Giastas, P., Zarkadas, E., Chroni-Tzartou, D., Bregestovski, P., and Tzartos, S. J. (2014). Crystal structures of free and antagonist-bound states of human α9 nicotinic receptor extracellular domain. *Nat. Struct. Mol. Biol.* 21, 976–980. doi: 10.1038/nsmb.2900

Conflict of Interest Statement: The authors declare that the research was conducted in the absence of any commercial or financial relationships that could be construed as a potential conflict of interest.

frontiers in Pharmacology

ORIGINAL RESEARCH
published: 30 July 2019
doi: 10.3389/fphar.2019.00848

A Decoy-Receptor Approach Using Nicotinic Acetylcholine Receptor Mimics Reveals Their Potential as Novel Therapeutics Against Neurotoxic Snakebite

*Laura-Oana Albulescu[1], Taline Kazandjian[1], Julien Slagboom[2], Ben Bruyneel[2], Stuart Ainsworth[1], Jaffer Alsolaiss[1], Simon C. Wagstaff[3], Gareth Whiteley[1], Robert A. Harrison[1,4], Chris Ulens[5], Jeroen Kool[2] and Nicholas R. Casewell[1,4]**

[1] Centre for Snakebite Research & Interventions, Liverpool School of Tropical Medicine, Liverpool, United Kingdom, [2] AIMMS Division of BioMolecular Analysis, Vrije Universiteit Amsterdam, Amsterdam, Netherlands, [3] Bioinformatics Unit, Liverpool School of Tropical Medicine, Liverpool, United Kingdom, [4] Centre for Drugs and Diagnostics, Liverpool School of Tropical Medicine, Liverpool, United Kingdom, [5] Laboratory of Structural Neurobiology, Department of Cellular and Molecular Medicine, Faculty of Medicine, KU Leuven, Leuven, Belgium

OPEN ACCESS

Edited by:
Victor I. Tsetlin, Institute of Bioorganic Chemistry (RAS), Russia

Reviewed by:
Richard J. Lewis, University of Queensland, Australia
Choo Hock Tan, University of Malaya, Malaysia

***Correspondence:**
Nicholas R. Casewell
Nicholas.casewell@lstmed.ac.uk

Specialty section:
This article was submitted to Pharmacology of Ion Channels and Channelopathies, a section of the journal Frontiers in Pharmacology

Received: *24 January 2019*
Accepted: *02 July 2019*
Published: *30 July 2019*

Citation:
Albulescu L-O, Kazandjian T, Slagboom J, Bruyneel B, Ainsworth S, Alsolaiss J, Wagstaff SC, Whiteley G, Harrison RA, Ulens C, Kool J and Casewell NR (2019) A Decoy-Receptor Approach Using Nicotinic Acetylcholine Receptor Mimics Reveals Their Potential as Novel Therapeutics Against Neurotoxic Snakebite. Front. Pharmacol. 10:848. doi: 10.3389/fphar.2019.00848

Snakebite is a neglected tropical disease that causes 138,000 deaths each year. Neurotoxic snake venoms contain small neurotoxins, including three-finger toxins (3FTxs), which can cause rapid paralysis in snakebite victims by blocking postsynaptic transmission *via* nicotinic acetylcholine receptors (nAChRs). These toxins are typically weakly immunogenic and thus are often not effectively targeted by current polyclonal antivenom therapies. We investigated whether nAChR mimics, also known as acetylcholine binding proteins (AChBPs), could effectively capture 3FTxs and therefore be developed as a novel class of snake-generic therapeutics for combatting neurotoxic envenoming. First, we identified the binding specificities of 3FTx from various medically important elapid snake venoms to nAChR using two recombinant nAChR mimics: the AChBP from *Lymnaea stagnalis* and a humanized neuronal α7 version (α7-AChBP). We next characterized these AChBP-bound and unbound fractions using SDS-PAGE and mass spectrometry. Interestingly, both mimics effectively captured long-chain 3FTxs from multiple snake species but largely failed to capture the highly related short-chain 3FTxs, suggesting a high level of binding specificity. We next investigated whether nAChR mimics could be used as snakebite therapeutics. We showed that while α7-AChBP alone did not protect against *Naja haje* (Egyptian cobra) venom lethality *in vivo*, it significantly prolonged survival times when coadministered with a nonprotective dose of antivenom. Thus, nAChR mimics are capable of neutralizing specific venom toxins and may be useful adjunct therapeutics for improving the safety and affordability of existing snakebite treatments by reducing therapeutic doses. Our findings justify exploring the future development of AChBPs as potential snakebite treatments.

Keywords: nicotinic acetylcholine receptors (nAChR), long-chain three-finger toxins (3FTx), acetylcholine binding proteins (AChBPs), snake venom neurotoxins, envenoming, therapeutics

INTRODUCTION

Snakebite is a neglected tropical disease that results in high mortality (138,000 deaths per annum) and morbidity (~400,000 cases per annum), and it is the rural impoverished people of the tropics who suffer the greatest burden (Gutiérrez et al., 2017). Elapids (family Elapidae) are one of the main groups of medically important snakes responsible for severe envenoming and include the cobras (*Naja* spp.), kraits (*Bungarus* spp.), mambas (*Dendroaspis* spp.), and coral snakes (*Micrurus* spp.). Elapid envenoming often causes postsynaptic neurotoxic effects by blocking neuromuscular transmission that can culminate in respiratory paralysis and death (Gutiérrez et al., 2017). Three-finger toxins (3FTxs) play a key role, with many competitively binding to postsynaptic neuromuscular and neuronal nicotinic acetylcholine receptors (nAChRs) to inhibit the binding of acetylcholine (Chang, 1979). Importantly, ever since the discovery of α-bungarotoxin, snake venom neurotoxins have been extensively employed for characterizing nAChRs and understanding the basis of neurotransmission. Therefore, a comprehensive knowledge of their targets and mechanisms of action remains important for a range of biological disciplines.

Three-finger toxins are one of many snake venom toxin types that are encoded by a multilocus gene family (Casewell et al., 2013). The frequent duplication of toxin-encoding genes coupled with bursts of accelerated evolution results in snake venom composition varying at every taxonomic level, including inter- and intraspecifically (Chippaux et al., 1991; Casewell et al., 2013; Casewell et al., 2014). Moreover, elapid venom proteomes are usually dominated by 3FTxs, which typically consist of numerous isoforms that comprise over 60% of venom proteins (Tasoulis and Isbister, 2017). These are small disulfide-bond rich proteins with a globular core and three β-stranded loops that extend from the core as "fingers" and can be classified into short-chain, long-chain, weak and nonconventional neurotoxins, cardiotoxins, and others (Kessler et al., 2017). Short-chain 3FTxs are small proteins consisting of 60–62 amino acid residues that contain four disulfide bridges, while long-chain α-neurotoxins (long-chain 3FTxs) have 66–74 amino acid residues and display an additional disulfide bond.

The small size (~7–12 kDa) of these potent neurotoxins poses a therapeutic challenge—they are weakly immunogenic (Tan et al., 2016b; Wong et al., 2016), yet all snakebite therapeutics (antivenoms) are manufactured from IgG of venom-immunized animals. The antineurotoxic efficacy of current antivenoms is further compromised because only 10–15% of the resulting IgG binds venom proteins (Casewell et al., 2010), with the remainder generated in response to environmental antigens to which the animals are exposed. Furthermore, antivenom efficacy is highly snake species-specific, resulting in limited cross-reactivity to venom toxins not included in the immunizing mixture (Tan et al., 2016a; Oh et al., 2019)—an inevitable result of venom variation (Williams et al., 2011). To circumvent this challenge, many antivenom manufacturers use mixtures of venoms as immunogens. However, this often results in polyspecific antivenoms requiring much higher therapeutic doses [e.g., 5–10 vials (50–100 ml) of ~50–100 mg/ml antibodies] to effect cure, which, in turn, results in high incidences of foreign protein-related adverse reactions (de Silva et al., 2016) and prohibitively expensive treatment costs for impoverished snakebite victims [e.g., 48–315 USD/vial in Africa (Harrison et al., 2017)]. Therefore, a therapeutic approach providing cross-generic neutralization of snake venom neurotoxins (i.e., irrespective of the snake species responsible for the bite) and, at low therapeutic doses, would be highly valuable.

Acetylcholine binding proteins (AChBPs) are mimics of the extracellular ligand-binding domain of nAChRs and have been used extensively in structural studies of complexes of the receptor with a wide range of nicotinic agonists (Brejc et al., 2001), partial agonists (Hibbs et al., 2009), antagonists (Brams et al., 2011), and allosteric modulators (Spurny et al., 2015). AChBPs form pentameric complexes in which five subunits radially assemble around a central vestibule. The pharmacological properties of AChBPs from the freshwater snail *Lymnaea stagnalis* (Ls-AChBP) most closely resemble the human α7-nAChR (Smit et al., 2001), which is one of the most abundant nAChR subtypes in the brain. Other receptor mimics with different binding specificities have also been described, including a humanized version of the neuronal α7 receptor (α7-AChBP) (Li et al., 2011). In addition to AChBPs, the *Torpedo marmorata* (marbled electric ray) electric organ nAChR (Unwin, 2005) has been extensively studied as a model for the heteropentameric muscle-type nAChR (Miyazawa et al., 2003).

In parallel with structural studies on these nAChR homologues, short- and long-chain 3FTxs from snake venom, such as α-bungarotoxin from *Bungarus multicinctus* (many-banded krait) (Huang et al., 2013), α-cobratoxin from *Naja kaouthia* (monocled cobra) (Bourne et al., 2005), and erabutoxin from *Laticauda semifasciata* (black-banded sea krait) (Servent et al., 1997), have been employed as ligands to characterize the binding interfaces between toxins and nAChRs. In mutagenesis studies using recombinant or purified toxins in combination with the neuronal or the *Torpedo* nAChRs, short-chain 3FTxs were shown to interact with high affinity with the muscle-type receptor (Antil et al., 1999; Servent et al., 2000), while long-chain 3FTxs effectively bound to both the muscle and neuronal α7-nAChRs (Servent et al., 1997; Antil-Delbeke et al., 2000). Nevertheless, these studies employed a limited number of isolated snake toxins and thus did not expose these receptors to all of the various 3FTx isoforms present in a single venom to investigate their interactions. More recently, AChBPs have been utilized for profiling venom neurotoxicity using a microfluidic system, resulting in the detection of low-affinity binders, such as venom phospholipases A_2 (PLA_2), that interact with AChBP, in addition to 3FTxs (Slagboom et al., 2018). Other studies have reported the ability of a *N. kaouthia* PLA_2 to block acetylcholine currents in *Lymnaea stagnalis* neurons or to compete with α-bungarotoxin for binding to *Torpedo* or α7-type receptors (Vulfius et al., 2014). The purified *Torpedo* nAChR has also been employed in *in vitro* assays to assess antivenom efficacy against the venoms

Abbreviations: nAChR, nicotinic acetylcholine receptor; AChBPs, acetylcholine-binding proteins; 3FTx, three-finger toxin; Ls-AChBP, *Lymnaea stagnalis* AChBP; PLA_2, phospholipase A2; vNGF, venom nerve growth factor

of *N. kaouthia* (Thai monocled cobra), *N. naja* (Indian cobra), and *B. candidus* (Malayan krait) (Ratanabanangkoon et al., 2017, Ratanabanangkoon et al., 2018).

In this study, we aimed to assess the nAChR-binding specificities of toxins found in a variety of elapid snake venoms sourced from distinct geographic regions by employing two recombinant neuronal nAChR mimics: the Ls-AChBP and the humanized α7-AChBP. Using a ligand-fishing approach, we characterized the AChBP-bound and AChBP-unbound fractions from seven elapid venoms by SDS-PAGE and mass spectrometry. We find that AChBPs effectively capture long-chain 3FTxs from a variety of snake venoms but have little interaction with short-chain 3FTxs. We also evaluated whether AChBP mimics could be used as therapeutics against envenoming using *Naja haje* (Egyptian cobra) venom in an *in vivo* murine model of venom lethality. Our data suggest that nAChR mimics show potential as cross-species adjunct therapeutics against the life-threatening pathologies caused by certain postsynaptic venom toxins, although future optimization to broaden their specificity against other classes of neurotoxins will likely be required to fully exploit their therapeutic potential.

MATERIALS AND METHODS

AChBP Expression and Purification

The AChBP from *Lymnaea stagnalis* (Ls-AChBP) and α7-AChBP were expressed and purified as previously described (Spurny et al., 2015) with slight modifications. In brief, a C-terminal His-tagged fusion of the protein was expressed in *Sf*9 insect cells (a clonal isolate of *Spodoptera frugiperda* Sf21 cells) using the Bac-to-Bac baculovirus expression system (Invitrogen). AChBPs were purified from the expression medium by adding Ni Sepharose 6 Fast Flow beads (GE Healthcare). The beads were collected on a column, and impurities were washed with buffer containing 20 mM Tris–Cl (pH 8.0), 300 mM NaCl, and 40 mM imidazole. AChBP was eluted with the same buffer containing 300 mM imidazole. Fractions containing AChBP were pooled, concentrated, and further purified using size-exclusion chromatography on a Superdex 200 10/300 GL column (GE Healthcare) and a running buffer containing 20 mM Tris–Cl (pH 8.0) and 150 mM NaCl. Fractions corresponding to the pentameric protein were pooled, concentrated to 6 mg/ml, snap-frozen in liquid nitrogen, and stored at −80°C until further use.

Snake Venoms

Venoms were sourced from either wild-caught specimens maintained in or historical venom samples stored in the Herpetarium of the Liverpool School of Tropical Medicine. The venoms selected were from diverse geographical localities and were from: *Naja haje* (Egyptian cobra, Uganda), *Naja naja* (Indian cobra, captive bred origin), *Naja kaouthia* (monocled cobra, captive bred, likely of Thai ancestry), *Bungarus caeruleus* (common krait, historical venom of Indian origin), *Dendroaspis viridis* (West African green mamba, Togo), *Micrurus fulvius* (eastern coral snake, historical venom of USA origin), and *Oxyuranus scutellatus* (coastal taipan, Australia). Crude venoms were lyophilized and stored at 4°C to ensure long-term stability. Before use, venoms were resuspended to 10 mg/ml in PBS (pH 7.4) and then further diluted to 1 mg/ml stock solutions (with PBS) for the described experiments.

Transcriptomics and Molecular Data

We constructed venom gland transcriptomes from single individuals for *N. haje* ($n = 1$, Uganda, wild-caught), *N. naja* ($n = 1$, captive bred of Indian origin), and *N. kaouthia* ($n = 1$, captive bred of Thai origin), from glands dissected 3 days post-venom extraction, using methods previously described by our group (Pla et al., 2017; Ainsworth et al., 2018a; Whiteley et al., 2018). The venom of the animals used for transcriptomics was either used for direct comparison for the *N. kaouthia* specimen or contributed to the venom pools used in this study for *N. haje* (the venom of six snakes from Uganda) or *N. naja* (historical venom pool of an unknown number of donor snakes of Indian ancestry). Briefly, the snakes were euthanized using an overdose of pentabarbitone, and the venom glands were excised and immediately flash frozen in liquid nitrogen. The venom gland tissue was homogenized under liquid nitrogen using a pestle and mortar and a TissueRuptor (QIAGEN), and total RNA was extracted using the TRIzol Plus RNA Purification System (Thermo Fisher) protocol. Resulting RNA samples were DNAse treated (On-Column PureLink DNase; Life Technologies) and total RNA eluted in 30 µl nuclease-free water (Qiagen). The RNA then underwent two rounds of poly(A) selection using the Dynabeads mRNA DIRECT purification kit (Life Technologies) and was eluted in nuclease-free water before the quality and quantity of isolated RNA was assessed using a Bioanalyzer (Agilent). Subsequently, the sequencing library was prepared using 50 ng of enriched RNA using the Script-Seq v2 RNA-Seq Library Preparation Kit (epicenter), following 12 cycles of amplification. The sequencing library was then purified using AMPure XP beads (Agencourt), quantified using the Qubit dsDNA HS Assay kit (Life Technologies), and the size distribution assessed using a Bioanalyzer (Agilent). Sequencing libraries were multiplexed with others not reported in this study, and sequencing was performed on an Illumina MiSeq platform using 250 bp paired-end read technology (Centre for Genomics Research, University of Liverpool). Each of the three samples represented one-sixth of a sequencing lane. The ensuing read data were quality processed as previously described (Ainsworth et al., 2018a), resulting in the removal of adapter sequences (Cutadapt; https://code.google.com/p/cutadapt/) and low-quality bases (Sickle; https://github.com/najoshi/sickle). Paired-end read data were then assembled into contigs using VTBuilder (Archer et al., 2014) with the following parameters: minimum transcript length, 150 bp; minimum read length, 150 bp; and minimum isoform similarity, 96%. Assembled contigs were then annotated using BLAST2GO Pro v3 (Conesa et al., 2005) using the blastx-fast algorithm with a significance threshold of 1e−5 against NCBI's nonredundant (NR) protein database (41 volumes, Nov 2015). Following annotation, contigs were assigned to one of the following three categories: toxins (contigs with blast annotations to sequences

previously described as pathogenic toxins), nontoxins (contigs matching other sequences, such as housekeeping genes), and unidentified (those with no matches assigned or hits <1e−5). Toxin contigs were then manually analyzed using sequence alignments generated by the MUSCLE algorithm (Edgar, 2004) embedded within MEGA v7 (Kumar et al., 2016) for quality control purposes, including the merging of contigs that exhibited 100% identity to one another in overlapping regions >50 bp long (indicative of underclustering during assembly), the identification of open reading frames, and the removal of contigs containing stop codons within the coding region. Finally, the toxin encoding contigs were translated using MEGA v7 and ExPASy Translate (https://web.expasy.org/translate/) to generate species-specific toxin databases for proteomic analyses (see below). Thus, for the cobras and *D. viridis*, we used translations of venom gland transcriptomic data generated in this study or previously published by our group (Ainsworth et al., 2018a). For *N. kaouthia*, we only used translations of the venom gland transcriptome generated in this study (and not other previously published studies), as venom from this same specimen was used in our AChBP pulldowns. For *M. fulvius* and *O. s. scutellatus* we used existing sequence resources available on Uniprot (accessed July 2018) (Herrera et al., 2012; Vergara et al., 2014). Lastly, for *B. caeruleus*, we extracted all proteomic data present in Uniprot (Oh et al., 2017) and supplemented it with translations of toxins from a venom gland transcriptome of its congener, *B. multicintus* (Jiang et al., 2011), to increase coverage and breadth of 3FTxs. A supplementary fasta file containing all of the translated toxins encoding sequences, and all of the protein sequences sourced from Uniprot, that together were used for our proteomic identifications, is available as **Supplementary Data Sheet 2**. Raw sequencing reads and resulting *de novo* assemblies generated for the *N. haje*, *N. naja*, and *N. kaouthia* venom gland transcriptomes have been deposited in the NCBI Sequence Read Archive (SRA) and Transcriptome Shotgun Assembly (TSA) databases, respectively, and are linked to the BioProject identifier PRJNA506018.

Capture and Purification of Venom Toxins Using Magnetic Beads

Ligand-fishing using AChBP was adapted from a previously published method (Pochet et al., 2011). Briefly, 20 µg of venom and 20 µg of recombinant α7-AChBP were brought up in binding buffer (1 mM KH_2PO_4, 3 mM Na_2HPO_4, 0.16 mM NaCl, 20 mM Tris–Cl, pH 7.5) to a final volume of 200 µl and incubated for 2 h at room temperature with gentle agitation. Another sample containing 10 µg of venom and 4.8 µg of α7-AChBP was also incubated alongside these samples but did not undergo separation using magnetic beads. Dynabeads (His-Tag isolation and Pulldown, Thermo Fisher Scientific, cat. No.: 10103D) were washed three times in binding buffer and resuspended at a final concentration of 20 mg/ml. Thirty microliters of Dynabeads were then added to each sample and incubated for another 15 min with gentle agitation. The beads were next separated using a magnetic stand, and the flow-through was recovered as the "unbound" fraction. The beads were washed four times with 200 µl wash buffer (50 mM sodium phosphate buffer pH 8.0, 300 mM NaCl, 0.01% Tween-20), allowing 2 min for magnetic separation. The bound AChBP and toxin-AChBP complexes were eluted in 12 µl of His elution buffer (300 mM imidazole, 50 mM sodium phosphate buffer pH 8.0, 300 mM NaCl, 0.01% Tween-20) and resuspended 1:1 in 2× SDS-PAGE gel loading dye under reducing or nonreducing conditions and loaded onto 15% SDS-PAGE gels. The unbound and control sample were concentrated up to ~15 µl using a speedvac, after which they were resuspended 1:1 in 2× SDS-PAGE loading buffer. For the Ls-AChBP, the conditions were the same, with the exception that 50 µl of 40 mg/ml Dynabeads was used to capture the AChBP and the elution volume was 30 µl.

One-Dimensional SDS-PAGE Gel Electrophoresis

We used SDS-PAGE gel electrophoresis to evaluate the bound and unbound fractions in each of our profiled venoms following the ligand-fishing assay. For each venom, we ran SDS-PAGE gels containing the following five lanes: 10 µg of venom, 2.5 µg of AChBP, a mixture containing 10 µg of AChBP + 4.8 µg venom, and the entire bound and unbound fractions. Samples were diluted 1:1 with a reducing or nonreducing loading buffer. Samples were then loaded onto 15% hand-cast SDS-PAGE gels alongside a protein marker (Broad Range Molecular Marker, Promega) and run at 120 V for 90–100 min using a Mini-PROTEAN Tetra System (Bio-Rad). The resulting gels were stained with Coomassie brilliant blue for 2 h and then destained (4.5:1:4.5 methanol/acetic acid/H_2O) for visualization.

Two-Dimensional SDS-PAGE Gel Electrophoresis

We used our previously described method (Ainsworth et al., 2018b; Calvete et al., 2018) to perform two-dimensional (2D) SDS-PAGE gel electrophoresis experiments using *N. haje* venom. Ligand fishing was scaled up appropriately using 100 µg of α7-AChBP and 100 µg of *N. haje* venom. The AChBP and venom were incubated for 30 min at room temperature, after which the purification was carried out as described above. The bound and unbound fractions were prepared for 2D gel electrophoresis using the ReadyPrep™ 2-D Cleanup Kit for isoelectric focusing (IEF) (Bio-Rad) as per the manufacturer's instructions. Cleaned-up venom samples were then applied to 7 cm, pH 3–10, nonlinear IPG strips (Bio-Rad) using the ReadyPrep™ 2-D starter kit (Bio-Rad), as per manufacturer's instructions and rehydrated overnight at room temperature. After rehydration, IEF was performed using a PROTEAN® IEF Cell (Bio-Rad) with the manufacturer's standard electrophoresis protocol for 7 cm IPG strips (default cell temperature = 20°C; maximum current 50 µA/strip; voltage = 250 V with linear ramp for 20 min; 4,000 V with linear ramp for 2 h; 4,000 V with rapid ramp for 10,000 V-h). After IEF, IPG strips were equilibrated (as per the ReadyPrep™ 2-D starter kit) and loaded onto Mini-PROTEAN TGX AnyKd precast gels (Bio-Rad) and run at 200 V for 35 min. Gels were then rinsed in water and stained with G-250 Coomassie blue stain (Bio-Rad) for 2 h to visualize the proteins.

In-Gel Tryptic Digestion of Proteins

All visible protein bands under ~20 kDa were excised from the 1D nonreducing and 2D gels for both the bound and unbound fractions (**Supplementary Figure 1**) and prepared for mass spectrometry. Gel slices were cut into small pieces and washed twice in washing buffer 1 [100 mM ammonium bicarbonate, 50% acetonitrile (ACN)], followed by three ACN washes and centrifuged at top speed in a microfuge to pellet the gel particles. The samples were then incubated in 40 µl reduction buffer (25 mM ammonium bicarbonate, 0.5% β-mercaptoethanol) for 40 min at 56°C to reduce the disulfide bridges and alkylated with 55 mM iodoacetamide for 20 min in the dark. Next, the gel slices were alternatively washed with washing buffer and ACN until they turned white (no residual dye left), after which they were dried in a vacuum centrifuge. Samples were trypsinized overnight at 37°C with 0.6 µg of trypsin (Sigma, cat. no.: T6567) per sample, after which 1 µl of 5% formic acid (FA) was added to the tubes to quench the digestion. The samples were sequentially extracted in 0.1% FA, 0.1% FA and 50% ACN, and finally 100% ACN, and moved to autosampler vials with glass inserts.

NanoLC-MS/MS of Tryptic Digests and Data Analysis

The NanoLC separation of the tryptic digests was performed using an UltiMate 3000 RSLCnano system (Thermo Fisher Scientific). The autosampler was run in full-loop injection mode. The autosampler was set to a 1-µl injection volume, and after injection, the samples were separated on an analytical capillary column (150 mm × 75 µm) with Aqua C18 particles, packed in-house (3 µm particle size and 200 Å pore diameter; Phenomenex). The mobile phases comprised eluent A (98% H_2O, 2% ACN, 0.1% FA) and eluent B (98% ACN, 2% H_2O, 0.1% FA). The gradient program used for the separation was as follows: 2 min isocratic separation at 5% B, linear increase to 80% B in 15 min, 3 min isocratic separation at 80% B, down to 5% B in 0.5 min, and equilibration for 9 min. The column was kept at 30°C in the column oven. Detection was performed by a variable wavelength detector set at 254 nm followed by a Bruker Maxis q-TOF mass spectrometer (Bruker). The mass spectrometer was operated in positive-ion mode and had an electrospray ionization (ESI) source. The ESI source parameters for the MS instrument consisted of the following: source temperature, 200°C; capillary voltage, 4.5 kV; and gas flow, 10 l/min. Spectra were obtained at 1 spectrum/s in the 50–3,000 m/z range. MS/MS spectra were obtained in data-dependent mode using 35-eV collision energy in the CID collision cell. Bruker Compass software was used for instrument control and data analysis.

Mascot (Matrix Science) searches against our custom databases (see above, **Supplementary Data Sheet 2**) were used for protein identification of the analyzed tryptic digests. The following search parameters were used: ESI-QUAD-TOF as the instrument type, semiTrypsin as the digestion enzyme allowing for one missed cleavage, carbamidomethyl on cysteine as a fixed modification, amidation (Protein C-term) and oxidation on methionine as variable modifications, ± 0.05 Da fragment mass tolerance, and ±0.2 Da peptide mass tolerance.

In addition to providing details on the resulting toxin coverage derived from the recovered peptides (see **Supplementary Tables 1** and **2**), we transformed the resulting data to provide an overview of peptide matching by extracting the unique peptides identified in our Mascot searches and then calculating a score for each identified toxin as the number of unique peptides per protein divided by the number of amino acids in that protein.

Molecular Analysis of 3FTxs

The bound and unbound 3FTxs from the various snake species were aligned in MEGA v7 using MUSCLE and then manually curated and validated. The resulting alignments were then exported and annotated in Jalview (http://www.jalview.org) for figure production.

Assessing the Efficacy of AChBP *in vivo*

Animal experiments were conducted using protocols approved by the Animal Welfare and Ethical Review Boards of the Liverpool School of Tropical Medicine and the University of Liverpool, and they were performed in specific pathogen-free conditions under licensed approval of the UK Home Office and in accordance with the Animal (Scientific Procedures) Act 1986 and institutional guidance on animal care. Experimental design was based upon refined WHO-recommended protocols (Harrison et al., 2017), and the investigators conducting the experiment were blinded to the treatment each group of mice would receive.

The median lethal dose (venom lethal dose 50 [LD_{50}]) of *N. haje* venom (0.43 µg/g body weight) used in this experiment was previously determined (Harrison et al., 2017). Similarly, the median effective dose (effective dose 50 [ED_{50}]) of SAIMR polyvalent against 5 × LD_{50} *N. haje* venom was previously determined to be 71 µl (Harrison et al., 2017). Owing to limited amounts of AChBP, we used 2.5 × LD_{50} doses of *N. haje* venom (20.4 µg) in a modified version of the antivenom ED_{50} neutralization experiments (Ainsworth et al., 2018b). Groups of five male 18–22 g CD-1 mice (Charles River, UK) received experimental doses, which comprised either a) venom only (2.5 × LD_{50}, 20.4 µg); b) venom and SAIMR polyvalent antivenom [either the "suboptimal" dose of 0.25 × ED_{50} (17.75 µl) or the "protective" dose of 0.75 × ED_{50} (53.25 µl)], both previously determined against 5 × LD_{50} venom doses; c) venom and "suboptimal" dose of antivenom and α7-AChBP (102 µg); d) "suboptimal" dose of antivenom only; or e) α7-AChBP (102 µg) only. All experimental doses were prepared to a volume of 200 µl in PBS and incubated at 37°C for 30 min before their intravenous injection *via* the tail vein. The mice were monitored for 6 h and euthanized upon observation of humane endpoints (seizure, pulmonary distress, paralysis). Deaths, time of death, and survivors were recorded, where "deaths/time of death" actually represents the implementation of euthanasia based on the defined humane endpoints.

For statistical analysis, we performed a one-way ANOVA with Tukey's *post hoc* test on the means of the five independent measurements in GraphPad Prism7, using default parameters. It is worth noting that this model utilizes the intravenous delivery of venom in order to cause venom-induced lethality within an

acceptable experimental time frame and to reduce unnecessary suffering in experimental animals. However, the intravenous delivery of venom does not accurately reflect a human snakebite, and thus, the therapeutic doses used in this study cannot be easily extrapolated to anticipate the therapeutic doses that might be required clinically.

RESULTS

Ligand Fishing with Ls- and α7-AChBP Captures Low Molecular Weight Toxins

To characterize the binding specificity of toxins from various neurotoxic elapid venoms to nAChRs, we used a ligand-fishing approach adapted from a previously published method (Pochet et al., 2011). Elapid venoms (*N. haje*, *N. naja*, *N. kaouthia*, *D. viridis*, *B. caeruleus, M. fulvius*, and *O. s. scutellatus*) were incubated with recombinant His-tagged nAChR mimics (α7-AChBP or Ls-AChBP), after which the toxin-bound fraction was purified using magnetic beads. The venom, AChBP, and bead amounts, as well as the incubation times, were optimized with *N. haje* venom (**Supplementary Figure 2**), a representative venom rich in 3FTxs (Malih et al., 2014). The bound and unbound fractions were then separated on SDS-PAGE gels under reducing and nonreducing conditions (**Figures 1A, B** and **Supplementary Figure 3**). The monomeric α7- or Ls-AChBPs were observed at ~25 kDa, and some AChBP dimers and pentamers were noted under nonreducing conditions, which dissociated in the presence of a

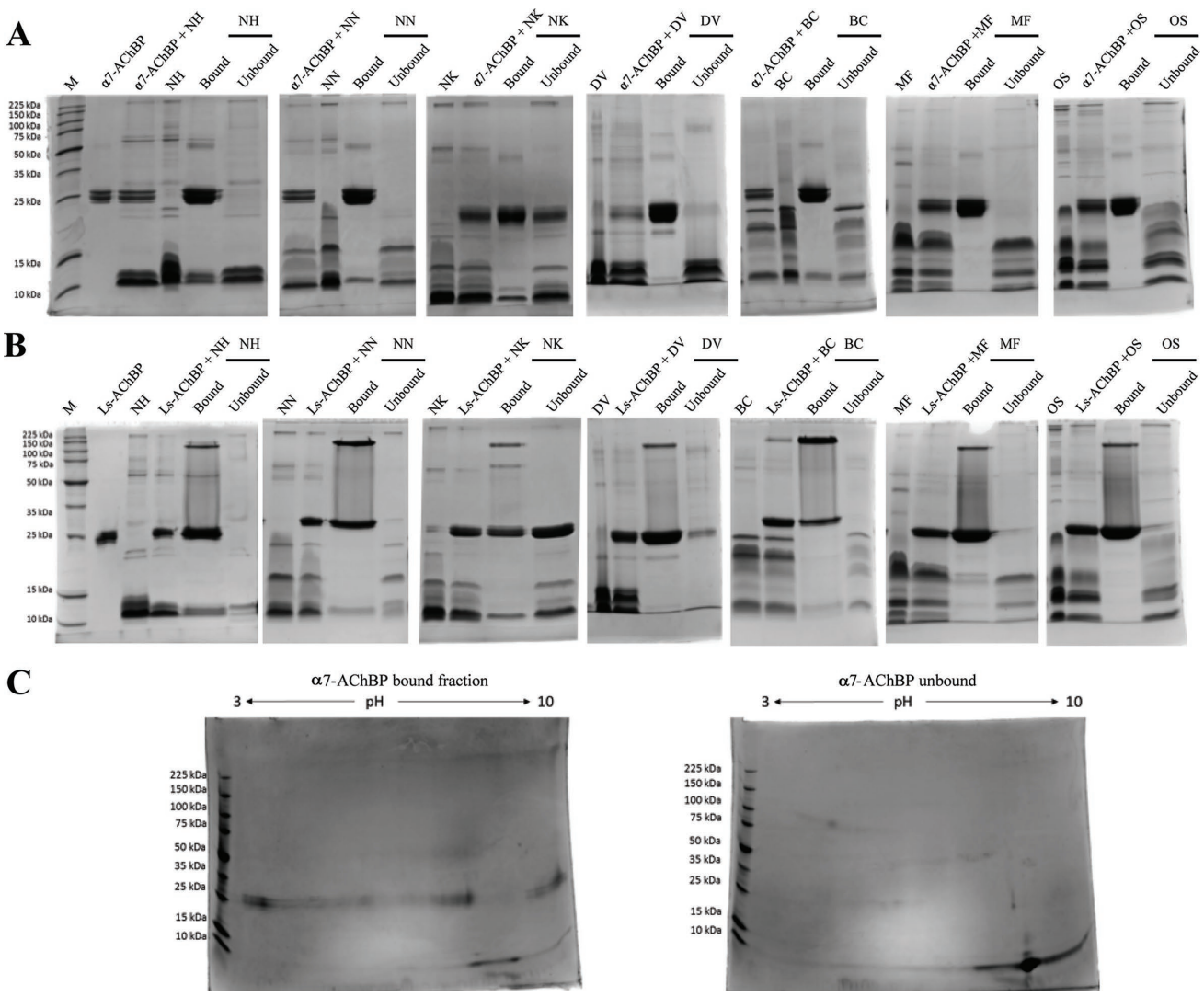

FIGURE 1 | Toxins captured using the AChBP ligand-fishing assay. Nonreducing 1D and 2D SDS-PAGE gels showing the bound and unbound fractions from *N. haje* (NH), *N. naja* (NN), *N. kaouthia* (NK), *D. viridis* (DV), *B. caeruleus* (BC), *M. fulvius* (MF), and *O. s. scutellatus* (OS) venoms. The gels display the bound and unbound (FT) fractions from purifications using the α7-AChBP **(A)** and *Lymnaea stagnalis* AChBP (Ls-AChBP) **(B)** binding proteins. Venom alone and a mixture of both the venom and binding protein are also presented as controls. **(C)** 2D SDS-PAGE gels for the bound (left) and unbound fractions (right) collected from *N. haje* venom incubated with α7-AChBP.

reducing agent. Moreover, while proteins in the 3FTx molecular weight range (~7–12 kDa) were recovered in both the bound and unbound fractions, the patterns of these bands differed, suggesting that specific toxins may be differentially captured by these AChBPs. In addition, these patterns were not markedly different between the humanized α7-AChBP and the *Lymnaea* Ls-AChBP, suggesting that these two types of nAChR mimics may be capturing similar toxins. To better resolve the captured fraction from the flow-through (i.e., to test for the potential of multiple captured toxins being present in single protein bands), we chose the humanized α7-AChBP and *N. haje* venom and performed 2D gel electrophoresis. However, this approach did not additionally distinguish between the protein bands in the 3FTx molecular weight range (~7–12 kDa), suggesting that our 1D-gel approach was appropriate for identifying toxins that bind to AChBPs (**Figure 1C**).

Notably, some AChBP leakage into the unbound fraction was observed with *N. kaouthia* venom (**Figure 1**). This may be due to components in the venom denaturing the binding protein or masking the His-tag, thus hindering the binding of the AChBP to the beads, as this phenomenon was apparent when using both α7-AChBP and Ls-AChBP for ligand fishing. To a lesser extent, this was also observed with venom from *D. viridis* (Ls fractionation). Importantly though, the leakage of these AChBPs into the supernatant does not appear to markedly affect the patterns of the captured toxins. Overall, our results suggest that the α7- and Ls-AChBPs differentially bind proteins in the 3FTx molecular weight range.

Long-Chain 3FTxs Bind With High Affinity to AChBPs

To elucidate the differences between the bound and unbound toxin fractions, the relevant protein bands were isolated from SDS-PAGE gels and subjected to tryptic digestion and mass spectrometry. To identify the resulting peptides, we initially performed a Mascot search using the SwissProt database. However, as snake venom proteins are not extensively represented in this database, the quality of the recovered matches was suboptimal, with very few matches obtained for our venoms of interest, and typically assigned to toxins identified from related snake species. To resolve this identification bottleneck, we utilized translations of transcriptomic data sourced from the venom glands of our species of interest as custom databases for MS/MS Mascot searches (see **Supplementary Data Sheet 2**). To this end, we generated and analyzed venom gland transcriptomes and their translations for *N. haje*, *N. naja*, and *N. kaouthia,* whose venoms were either utilized directly in this study (*N. kaouthia*) or contributed to the venom pool employed in the AChBP experiments (*N. haje* and *N. naja*). Existing, transcriptomic [*D. viridis* (Ainsworth et al., 2018a)] or proteomic resources [*M. fulvius* (Vergara et al., 2014), *B. caeruleus* (Oh et al., 2017), and *O. s. scutellatus* (Herrera et al., 2012)] were used for the remaining species under investigation.

In line with previous findings (Servent et al., 1997; Antil-Delbeke et al., 2000), our MS/MS identifications revealed that long-chain 3FTxs (long-chain α-neurotoxins) were consistently captured by both AChBPs when incubated with the three cobra venoms (*Naja* spp). and that of the common krait (*B. caeruleus*) (**Figure 2**, **Supplementary Tables 1**–**3**). Moreover, the protein IDs identified with both these AChBPs were largely consistent. In the cobra venoms, the detected peptides amounted to ~60% sequence coverage for long-chain 3FTxs, while α-δ-bungarotoxin 4 was the top binder in *B. caeruleus* venom. In contrast, the highly similar short-chain 3FTxs (short-chain α-neurotoxins) were almost exclusively observed in the unbound fraction, or a similar number of peptides were identified in both the bound and unbound fractions (**Supplementary Table 3**), suggesting a rapid exchange between the on- and off-bead fractions. Thus, if these short-chain 3FTx isoforms are being captured, they are not tightly associated with AChBPs, suggesting either weak binding to the receptor or background noise. Bearing in mind the presence of AChBP in the flow-through when incubating with *N. kaouthia* venom, we observed a relatively equal distribution of long-chain 3FTxs between the bound and unbound fractions (e.g., 17 vs. 19 peptides for Ls-AChBP and 10 vs. 8 peptides for α7-AChBP recovered for long-chain 3FTx T1411, **Supplementary Table 3**), likely due to the association of some long-chain 3FTxs with an AChBP that cannot interact with the magnetic beads; however, this data nevertheless suggest that long-chain 3FTxs are still being captured in this venom.

In contrast to our results with venom from *Naja* spp. and *B. caeruleus*, no long-chain 3FTxs were recovered from the bound fractions following the incubation of the two AChBPs with *D. viridis* venom. We did detect one short-chain 3FTx bound to the AChBPs, but this toxin was also recovered in the unbound fraction (**Figure 2**). However, a previous analysis of the *D. viridis* venom gland transcriptome (Ainsworth et al., 2018a) demonstrated that while this species contains three long-chain 3FTx transcripts, all have very low expression (<0.1% of all venom toxins in the transcriptome). It is therefore unsurprising that these toxins were not detected *via* our approach. Furthermore, the short-chain 3FTx recovered from the bound fraction is the most highly expressed toxin in the *D. viridis* transcriptome (19.4% of all venom toxins) and represents 40.1% of the *D. viridis* proteome (Ainsworth et al., 2018a). The abundance of this short-chain 3FTx likely explains its transitory binding to AChBPs at high concentrations.

We did not observe any 3FTxs in the bound fractions from *M. fulvius* venom, and only one peptide from a short-chain 3FTx was recovered in the unbound fraction. Several PLA_2 isoforms in this venom bound weakly to Ls-AChBP, but with one exception; we only recovered a few peptides for these toxins, while several PLA_2 isoforms were observed in the flow-through. This low level of binding is potentially due to the high abundance of these toxins in the venom, as the *M. fulvius* venom gland transcriptome is dominated by PLA_2s (~65% of toxin expression), with only 21% of transcripts encoding 3FTxs (Margres et al., 2013). While the *M. fulvius* venom proteome was previously shown to contain 6–7 kDa nAChR-binding toxins, which made up 24.9% of the venom toxins, these toxins typically exhibited only weak and reversible binding to the muscle-type nAChR in a cell-based assay (Vergara et al., 2014). In the current study, we employed two types of α7-neuronal receptor mimics that appear to only be effectively binding long-chain, but not short-chain, 3FTxs across

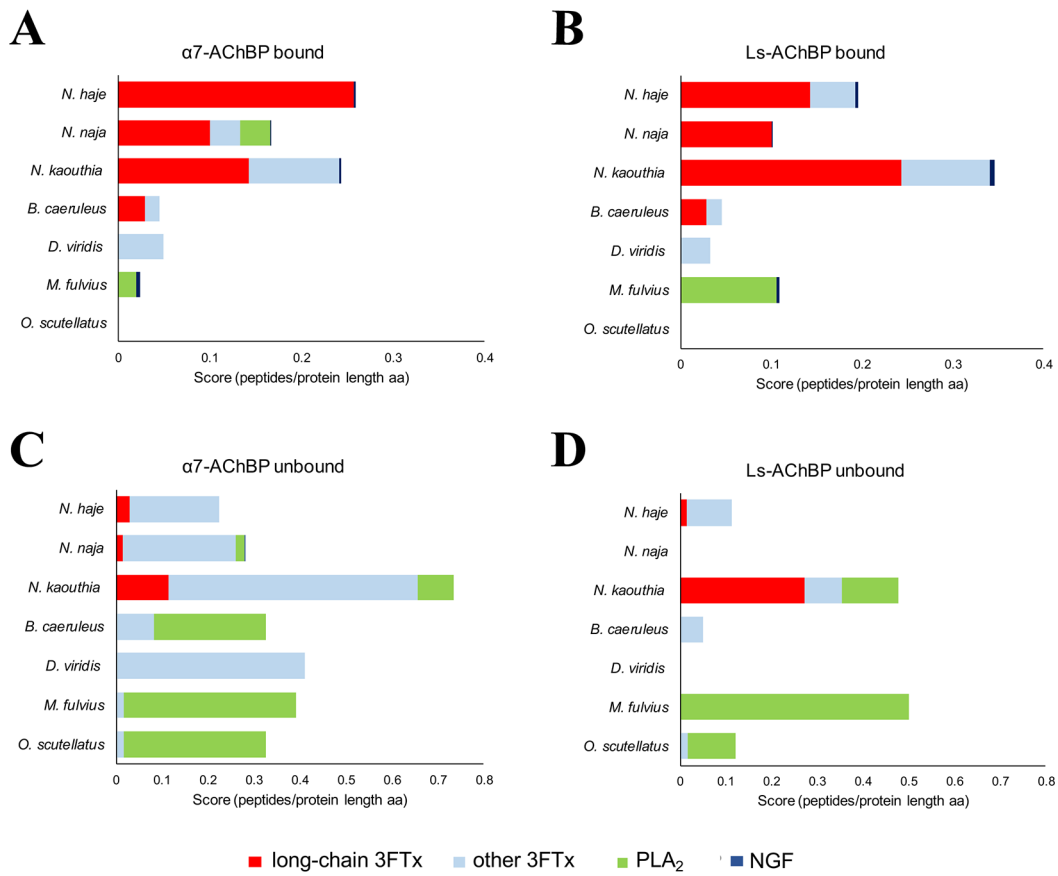

FIGURE 2 | Identification of the toxins captured by α7- and Ls-AChBP. The mass spectrometry data were expressed as the number of unique peptides recovered per protein divided by the protein length (in amino acids) for all proteins in each of the bound and unbound fractions. Scores (number of peptides per protein length in aa) are displayed for the different classes of toxins captured from *N. haje*, *N. naja*, *N. kaouthia*, *D. viridis*, *B. caeruleus*, *M. fulvius*, and *O. s. scutellatus* venoms or recovered in the unbound fraction. Classes of toxins bound by α7-AChBP **(A)** or Ls-AChBP **(B)** are categorized into long-chain three-finger toxins (3FTxs), other 3FTxs, PLA_2s, and NGF. Toxins recovered in the unbound fraction are presented in **(C)** (α7-AChBP) and **(D)** (Ls-AChBP). Please note that the axes have different lengths driven by the number of unique sequences recovered in each fraction.

the species tested. Analysis of a sequence alignment of *M. fulvius* 3FTxs sourced from the venom gland transcriptome (Margres et al., 2013) revealed an absence of canonical long-chain 3FTxs (**Supplementary Figure 4**) and thus may explain these observations. Given that we only detect PLA_2s from *M. fulvius* venom being weakly captured by the AChBPs, we conclude that these may be binding to Ls-AChBP at background levels, in a similar manner to previously reported interactions between viper or elapid PLA_2s and this AChBP, which occur in the micromolar range (Vulfius et al., 2014; Slagboom et al., 2018).

Similarly, no 3FTx bands were recovered in the bound fraction of *O. s. scutellatus* venom, which is unsurprising as the *O. s. scutellatus* venom proteome consists of only 1.5% 3FTxs, while PLA_2s represent 79.4% of all venom toxins (Herrera et al., 2012). In addition, the high neurotoxicity of this venom is driven by presynaptic neurotoxins (Kornhauser et al., 2010), among which taipoxin, a PLA_2 heterotrimer, is the most toxic component isolated from snake venom to date. Upon visual inspection of all aligned 3FTxs in our dataset (**Supplementary Figure 5**), we did not identify any canonical long-chain 3FTxs. While long-chain 3FTxs (e.g., LNTX-1) have been proteomically annotated from *O. s. scutellatus* venom (Herrera et al., 2012), our analysis shows that this isoform does not contain the additional cysteines required to make the extra fifth disulfide bond characteristic of long-chain 3FTxs and, therefore, may have been misannotated based on its protein length. As with *M. fulvius*, our data imply that long-chain 3FTxs are not being captured from *O. s. scutellatus* because they may not be present in the venom.

Interestingly, we also identified venom nerve growth factor (vNGF) as an AChBP binder in several of the venoms surveyed. The toxic role of vNGF remains unclear, and it represents a minor venom component in almost all snake venoms from which it has been recovered (Tasoulis and Isbister, 2017). vNGF was effectively captured by both α7- and Ls-AChBP from the venoms of *N. haje*, *N. kaouthia*, and *M. fulvius*, while vNGF from *N. naja* venom only appeared to interact with Ls-AChBP. These results hint at the potential of vNGF to interact with nAChRs, although this requires future experimental validation.

Bound 3FTxs Harbor Canonical Long-Chain 3FTx Features

Our results suggest that AChBPs effectively capture long-chain 3FTxs and only weakly interact with other toxin classes, such as short-chain 3FTxs and PLA_2s. To uncover the relevant features underlying the interaction of long-chain 3FTxs with AChBPs, we generated a sequence alignment of the 3FTxs recovered in the bound and unbound fractions of our ligand-fishing experiment, using the transcriptomic data (**Figure 3**). All bound toxins, with the exception of the *D. viridis* short-chain 3FTx described earlier, were confirmed as canonical long-chain 3FTxs, as they displayed high conservation throughout the second 3FTx loop and contained the two additional cysteine residues involved in the formation of the fifth disulfide bond (**Figure 3**). In contrast, all 3FTxs recovered in the unbound fraction were either short-chain 3FTxs, weak neurotoxins, or cardiotoxins.

AChBPs as Therapeutics in a Murine Model of Envenoming

Our transcriptomic analysis (**Figure 4**) predicts *N. haje* venom to be highly enriched in long-chain 3FTxs, as the expression of these toxins constitutes ~41% of that of all toxin-encoding genes expressed in the venom gland of this species. Since AChBPs effectively capture long-chain 3FTxs, we used *N. haje* venom as our model to test whether AChBPs could be used as a novel therapeutic approach for treating snake envenoming. To this end, we employed the gold-standard preclinical assay

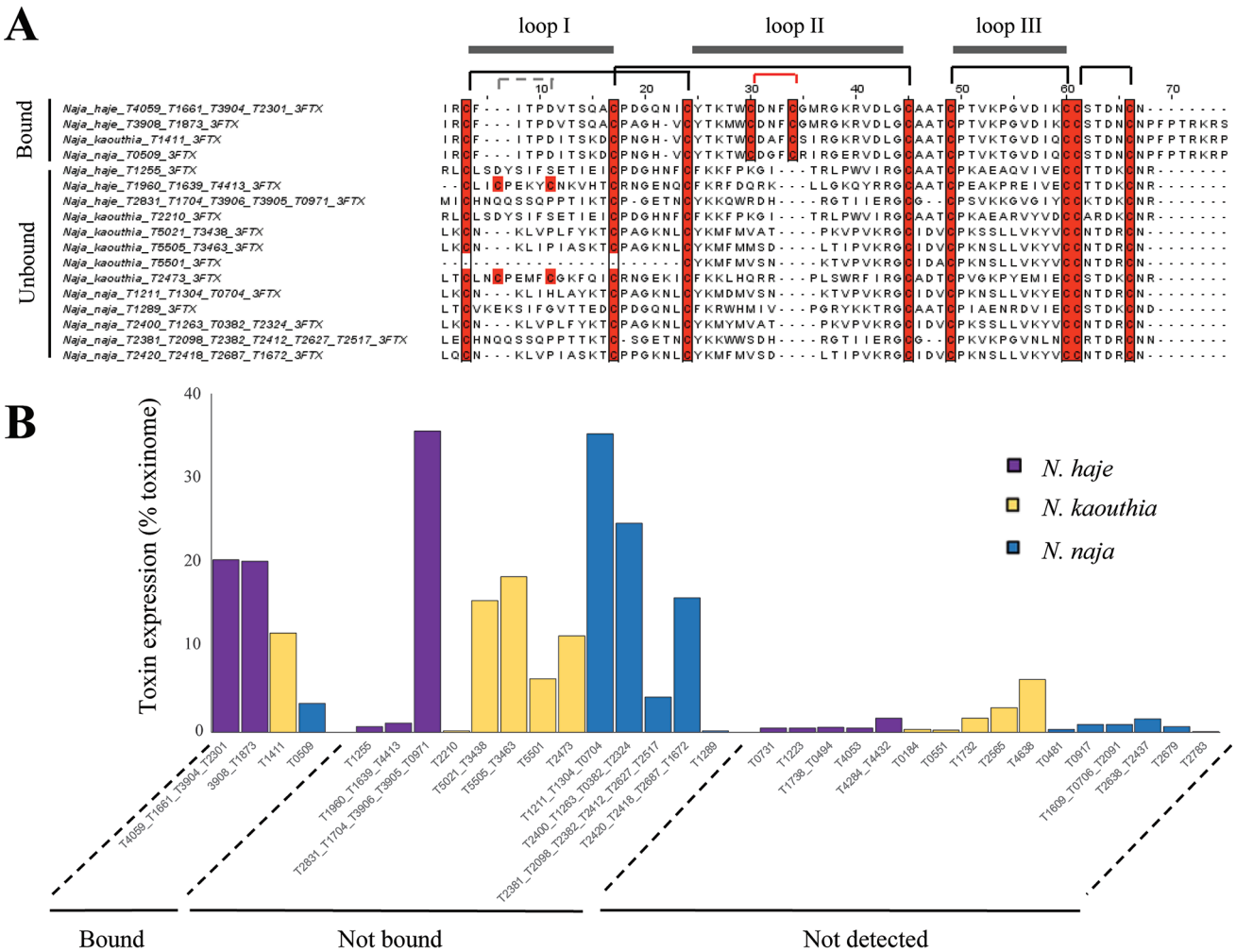

FIGURE 3 | AChBPs capture available canonical long-chain 3FTxs. **(A)** Sequence alignment displaying 3FTxs captured (bound) and not captured (unbound) by AChBPs in the three *Naja* venoms. Cysteines are highlighted in red. The canonical disulfide bridges present in all 3FTxs are indicated by the black lines linking cysteines, while the gray lines highlight an additional disulfide bridge in loop I for two of the unbound toxins. The red lines indicate the additional cysteine residues that characterize long-chain 3FTxs as being distinct from other types of 3FTx. The three 3FTx loops are displayed above the alignment. **(B)** Comparisons of the transcriptomic expression of *Naja* toxins that were detected (both AChBP bound and unbound) or were not detected by mass spectrometry. Undetected toxins consistently had lower transcriptomic expression compared to those detected (whether in the bound or unbound fractions).

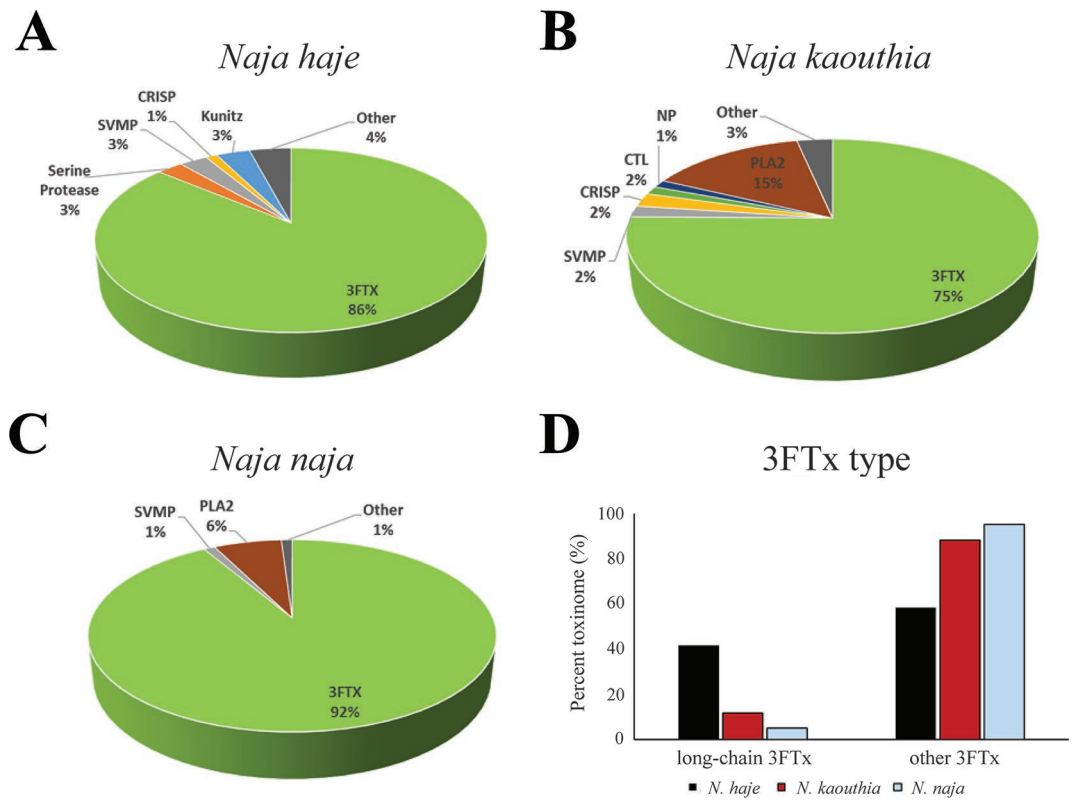

FIGURE 4 | The relative expression of toxin families in the *Naja haje*, *N. naja,* and *N. kaouthia* venom gland transcriptomes. Breakdown of the expression levels of the toxins (toxinome) present in the *N. haje* **(A)**, *N. kaouthia* **(B)**, and *N. naja* **(C)** venom gland transcriptomes. **(D)** Comparisons of the relative expression of long-chain 3FTxs versus other 3FTxs in the venom gland transcriptomes (toxinome). 3FTx, three-finger toxins; SVMP, snake venom metalloproteinases; NP, natriuretic peptides; CTL, C-type lectins; PLA2, phospholipases A_2; CRISP, cysteine-rich secretory proteins; Other, other minor expressed venom toxins.

recommended by the World Health Organization (WHO, 2018) for assessing the efficacy of snakebite treatments (antivenoms) *in vivo*. We first challenged groups of mice (n = 5) with 2.5 × LD_{50s} of *N. haje* venom *via* the intravenous route and compared survival times with the same dose of venom preincubated with 102 μg of α7-AChBP (venom/AChBP = 1:5 ratio). We also administered the same dose of AChBP in the absence of venom, as a control. The absence of detectable adverse effects in the latter demonstrated that α7-AChBP is not acutely toxic to mice at this dose. However, we observed no difference in the mean survival times of the experimental animals that received venom alone and those that received venom preincubated with AChBP (6 vs. 6.2 min, respectively) (**Figure 5**). Given that AChBPs only captured long-chain 3FTxs in our ligand-fishing assays, these data suggest that either other toxic components present in the venom (e.g., short-chain 3FTxs, etc.) are also capable of causing lethality or that binding by AChBP does not result in the neutralization of long-chain 3FTxs.

To explore this further, we challenged mice with venom preincubated with an antivenom known to neutralize *N. haje* venom (SAIMR polyvalent antivenom) (Harrison et al., 2017). We incubated the same dose of venom with a "suboptimal" dose of antivenom (17.75 μl) unable to confer protection on its own and a "protective dose" predicted to prevent lethality (53.25 μl). In comparison with the venom-only control, the "protective" dose of antivenom provided complete protection against the lethal effects of the venom until the end of the experiment (360 min), while the "suboptimal" dose of antivenom prolonged survival by 51.6 min (**Figure 5**). The coincubation of *N. haje* venom with the "suboptimal" dose of antivenom and 102 μg of α7-AChBP prolonged the survival of the experimental animals for an additional 93.4 min, therefore resulting in increased survival for 145 min when compared to the venom-only control (**Figure 5**). These results demonstrate that the humanized α7-AChBP does confer some protection against venom toxins and thus is likely neutralizing at least some of the neurotoxicity caused by long-chain 3FTxs *in vivo*. It therefore seems likely that other toxic components found in the venom of *N. haje*, which do not interact with AChBPs, are responsible for causing the delayed lethality observed in this model.

DISCUSSION

Using a ligand-fishing approach to probe nAChR receptor mimics with a range of elapid snake venoms, we demonstrate herein that AChBPs interact with and capture long-chain 3FTxs but fail to bind to highly related 3FTxs, such as short-chain

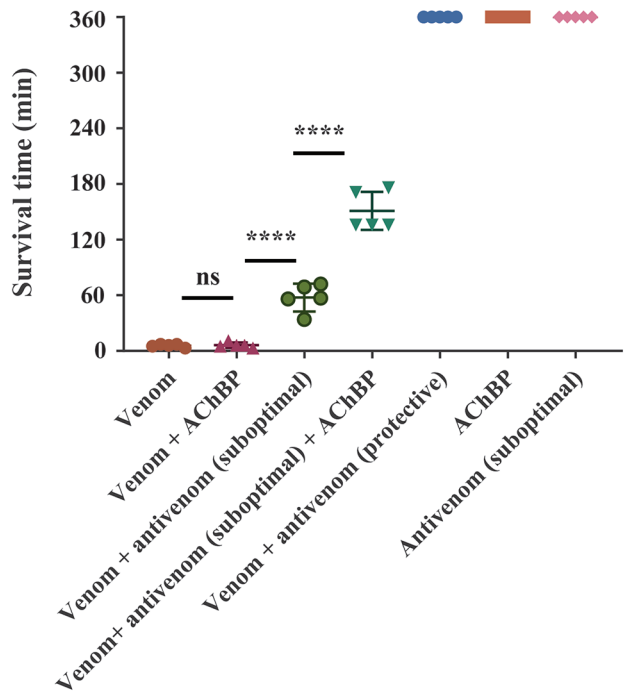

FIGURE 5 | α7-AChBPs prolong survival *in vivo* when coadministered with antivenom. Groups of five mice were intravenously administered with either 2.5 × LD_{50s} of *N. haje* venom alone, AChBP alone, venom preincubated with AChBP (1:5 venom/AChBP ratio), a protective dose (53.25 µl) of SAIMR polyvalent antivenom alone, or venom preincubated with a protective dose of SAIMR polyvalent antivenom. A suboptimal dose (17.75 µl) of antivenom, which did not extend the survival of the experimental animals for more than 1 h, was also preincubated with 2.5 × LD_{50s} of venom and AChBP (1:5 venom/AChBP weight ratio) and delivered intravenously. Experimental animals were observed for the duration of the experiment (360 min) and survival times monitored. AChBP enhances the effect of antivenom when administered in combination with a suboptimal antivenom dose. Data points represent mean survival times and error bars represent SDs (n = 5). Ns, not significant, **** $P < 0.0001$, using a one-way ANOVA with Tukey's test.

α-neurotoxins. Long-chain 3FTxs were recovered when using both the Ls-AChBP and the humanized α7-AChBP, which exhibit 24 and 64% identity with the human α7-receptor, respectively (Li et al., 2011); interestingly, these molecules specifically bound long-chain 3FTxs in a comparable manner. Our findings are consistent with prior studies that used purified long-chain 3FTxs and demonstrated that they interact with high affinity (K_d in the nanomolar range) with neuronal nAChR receptors, whereas short-chain 3FTxs only bind weakly (K_d in the micromolar range) (Servent et al., 1997).

Previous studies have highlighted the importance of the tip of the second 3FTx loop containing the fifth disulfide bridge (Servent et al., 1997; Bourne et al., 2005), and that of specific key residues in this loop (Antil-Delbeke et al., 2000), for the interaction between 3FTxs and the interface created between any two subunits of the Ls-AChBP. The reduction in this fifth disulfide bond in α-cobratoxin followed by dithiopyridylation lowered the affinity of this long-chain 3FTx for the α7-nAChR to a comparable level to that of short-chain neurotoxins (Servent et al., 1997), while a chimeric construct containing the fifth disulfide bond of long-chain neurotoxin 1 from *Naja oxiana* inserted into short-chain neurotoxin 2 from the same species was sufficient to increase the affinity of this toxin for the α7-nAChR to that of long-chain neurotoxins (Lyukmanova et al., 2007). Importantly, all 3FTxs that bound to the Ls- or α7-AChBP in the present study contained the fifth disulfide bond (**Figure 3**) and conserved Phe29 and Arg33 residues, which have previously been shown to interact with the Ls binding pocket (Bourne et al., 2005). In contrast, Phe29 was absent, and Arg33 was not conserved among the other 3FTxs recovered in the unbound fractions, nor did they contain the additional fifth disulfide bridge due to the absence of the two cysteine residues harbored by long-chain 3FTxs. Mutagenesis studies (Antil et al., 1999; Antil-Delbeke et al., 2000; Fruchart-Gaillard et al., 2002) have demonstrated that Trp25, Asp27, and Arg33 are also important residues for the binding of 3FTxs to both the neuronal and muscle-type receptors, while Ala28, Lys35, and the two cysteines involved in the fifth disulfide bond (Cys26 and Cys30) selectively bind to the α7-nAChR. Trp25, Asp27, and Arg33 were conserved across the captured long-chain 3FTxs identified here but not among the unbound 3FTxs recovered. In contrast, a neutral charge, but not the Ala28 residue itself, was conserved among the bound long-chain 3FTxs, while Lys35 was retained by all binders with the exception of the *N. naja* long-chain 3FTx. Moreover, α-δ-bungarotoxin 4 was the top AChBP binder from *B. caeruleus* venom, which is consistent with a recent report showing that α-δ-bungarotoxins interact with the α7-nAChR (Utkin et al., 2019).

Nonconventional 3FTxs can also bind to the neuronal α7-nAChR. One such example is candoxin (Nirthanan et al., 2002), a 66-amino-acid 3FTx neurotoxin from *B. candidus* that binds with high affinity to the α7-nAChR (IC_{50} = 50 nM) *via* a fifth disulfide bond present in loop I. This is in contrast to other weak neurotoxins from *N. kaouthia* (WTX) (Utkin et al., 2001) and *Naja sputatrix* (Wtn-5) (Poh et al., 2002) that bind only weakly (micromolar affinity) to this receptor, suggesting that other residues beside the fifth disulfide bond located in loop I dictate the binding affinity of these toxins to the neuronal receptor. Moreover, haditoxin (Roy et al., 2010), a homodimeric 3FTx from the venom of the king cobra, *Ophiophagus hannah*, was the first reported dimeric toxin to bind to α7-nAChR (IC_{50} = 180 nM). Given that haditoxin does not possess a fifth disulfide bond or residues important for contacting the α7-nAChR (e.g., Ala28, Lys35), it remains unclear how this dimer interacts with the neuronal receptor. These observations do suggest that while the fifth disulfide bond and specific residues that protrude into the binding pocket of the AChBP represent strong binding determinants, other contacts could drive the interaction of atypical 3FTxs with the α7-nAChR. However, in the present study, we did not detect the binding of any nonconventional toxins to AChBPs, likely because our ligand-fishing approach may only pull out the most abundant of binders. Toxin abundance clearly influences binding in our assay (**Figure 3**), as a highly abundant short-chain 3FTx from *D. viridis* venom was found to bind weakly to both the α7- and Ls-AChBPs, while PLA_2s, which dominate the venom of *M. fulvius*, were also found to bind to the nAChR mimics.

Since nAChR mimics bind long-chain 3FTxs, which are some of the most potent neurotoxins found in elapid venoms [with LD_{50}s ranging from 0.04 to 0.3 mg/kg (Nirthanan and Gwee, 2004)], we were interested in assessing the potential value of AChBPs as novel snakebite therapeutics for neurotoxic envenoming. We selected *N. haje* as our model for these studies, as this snake is considered to have a highly neurotoxic venom (Malih et al., 2014), and our transcriptomic analysis demonstrated that long-chain 3FTxs are the major venom components (~41% of all toxins; **Figure 4**). While our *in vivo* data showed that the intravenous delivery of α7-AChBP was unable to protect mice from the lethal effects of *N. haje* venom, we demonstrated that these nAChR mimics are likely neutralizing long-chain 3FTxs, as increased survival times ($P < 0.0001$) were observed in envenomed mice treated with both α7-AChBP and a "suboptimal" dose of antivenom, when compared with the "suboptimal" dose of antivenom alone, which only briefly prolonged survival (**Figure 5**). Thus, the ability of α7-nAChR mimics to potentially neutralize a class of 3FTxs *in vivo* represents an encouraging prospect to build upon in the context of developing future treatments with the goal of generically targeting neurotoxicity in envenomed victims.

Given that the binding specificity of this molecule is directed predominately towards long-chain 3FTxs, broad-spectrum AChBPs capable of capturing a large variety of different 3FTx, or a mixture of AChBPs able to neutralize both short- and long-chain 3FTxs, would likely be needed to effect cure in envenomed victims. One advantage of the humanized α7-AChBP used in this study is its similarity (~71%) with the human α7-nAChR, which may result in reduced immunogenic effects if administered to patients. The engineering of broad-spectrum AChBPs would ideally also use this humanized molecular backbone while taking advantage of the increased affinity (Nirthanan and Gwee, 2004) and pharmacological properties of other nAChR mimics, such as the *Torpedo* nAChR. Finally, while we explored the toxin capturing potential of AChBPs against a number of geographically diverse elapid snakes, such optimized broad-spectrum AChBPs would require testing against an increased breadth of venoms, including additional species within the elapid genera studied here and perhaps also members of the Hydrophiinae (marine elapids), whose venoms often contain abundant and highly potent α-neurotoxins that are typically not effectively neutralized by existing antivenoms (Tan et al., 2015; Tan et al., 2018).

Irrespective of whether a single broad-spectrum nAChR mimic or multiple mimics with different specificities would be required, such approaches could prove highly advantageous for circumventing venom variation—a major limitation with current antivenoms, which are typically only effective against a single, or a limited number of, snake venom/s. By neutralizing a whole class of toxins, a successful receptor mimic would thus represent a significant step forward compared to existing polyclonal antivenoms, which, given their low economies of scale due to restricted geographical usage, result in high costs to impoverished snakebite victims (Gutiérrez et al., 2017). Conceptually, this approach is analogous to recent studies exploring other non-antibody therapeutics, such as enzyme inhibitors and metal chelators (Ainsworth et al., 2018b; Bulfone et al., 2018), to target whole classes of snake venom toxins that cause pathologies such as hemorrhage and coagulopathy. Ideally, these AChBP mimics would bind rapidly and with high affinity to venom toxins, thus precluding their binding to nAChRs in the victim. Strong and rapid binding is a highly desirable characteristic for new therapeutics, as delays in treatment in resource-poor settings inevitably allow 3FTxs to access nAChR receptors before treatment administration. Therefore, investigating whether AChBPs can effectively displace already bound toxins should be a key focus of future research. Nonetheless, our present *in vivo* results show the promise of AChBPs to delay lethality caused by neurotoxic snake venom and thus advocate exploring such characteristics in future work.

As an alternative to the use of AChBPs as solo therapeutics, the coadministration of these molecules alongside traditional antivenom therapy may prove to be of greatest value. Prolonged survival was observed in our mouse model of envenoming when AChBP was administered alongside a suboptimal dose of polyvalent antivenom. These findings suggest that AChBPs might facilitate reducing clinical doses of antivenom in the future, as only 10–15% of antivenom immunoglobulins are typically specific to venom toxins and only a proportion of those antibodies will be specific to highly pathogenic toxins (e.g., 3FTx neurotoxins in this case) found in any particular venom (Gutiérrez et al., 2017). As many antivenoms require large therapeutic doses to effect cure, the further development of a highly specific yet generically acting (e.g., irrespective of snake species) inhibitor capable of reducing antivenom doses should result in a decreased incidence of adverse effects associated with antivenom administration and, most importantly, reduce treatment costs.

In an analogous manner, a recent study has demonstrated the value of the PLA_2 inhibitor varespladib, alone or in combination with antivenom, in preventing the onset of neurotoxicity after the administration of the neurotoxic *O. s. scutellatus* venom in experimental animals (Lewin et al., 2018). While our model venom (*N. haje*) contains only trace amounts of PLA_2s (< 0.05% of toxins in the venom gland transcriptome), this class of enzymes has been found to be more abundant in other cobra species (**Figure 4**) (Tan et al., 2019) and indeed other elapid snakes, such as *O. s. scutellatus* and *M. fulvius* (Herrera et al., 2012; Vergara et al., 2014). PLA_2s may enable and accelerate the spread of the venom after a bite *via* their cytolytic effects (Gutiérrez and Ownby, 2003), thus enhancing the access of other venom components to their targets. In the case of elapid snakes, PLA_2s have also been demonstrated to potentiate the cytotoxic effect of specific 3FTxs (Suzuki-Matsubara et al., 2016) and may facilitate the rapid action of 3FTxs on their muscular and neuronal targets, leading to the onset of paralysis. Therefore, combination treatments using AChBPs, enzyme inhibitors such as varespladib, and/or antivenom should be extensively explored by the scientific community to address current therapeutic limitations associated with this lethal neglected tropical disease.

In summary, our study demonstrates a proof of principle that AChBP-type proteins can effectively capture entire classes of lethal toxins, irrespective of variation in venom composition among snake species, and that they may possess therapeutic potential when administered in combination with antivenom. Further work is required to determine if broad-spectrum AChBPs can be

engineered or whether combinations of different AChBPs offer a viable strategy to combat neurotoxicity in envenomed snakebite victims. Further studies are also required to define the likely effective dose of these optimized molecules and whether they are likely to be well tolerated by humans. Despite saving thousands of lives annually, the numerous limitations associated with existing snakebite treatments (e.g., species specificity, limited cross-reactivity, severe adverse reactions, high cost) strongly advocate for research into alternative or adjunct treatments that could be used to treat snakebite caused by a wide variety of medically important snake species. AChBPs are promising in this regard, and their subsequent development and validation may lead to them becoming a welcome addition to the snakebite treatment portfolio.

ETHICS STATEMENT

All animal experiments were conducted using protocols approved by the Animal Welfare and Ethical Review Boards of the Liverpool School of Tropical Medicine and the University of Liverpool, and they were performed in specific pathogen free conditions under licensed approval of the UK Home Office and in accordance with the Animal [Scientific Procedures] Act 1986 and institutional guidance on animal care. Experimental design was based upon refined WHO-recommended protocols.

AUTHOR CONTRIBUTIONS

L-OA, CU, JK, and NRC devised the study. CU expressed and purified the AChBP proteins. L-OA performed the AChBP ligand-fishing experiments and prepared the samples for mass spectrometry. JS and BB performed mass spectrometry experiments. L-OA, JS, BB, JK, and NRC analyzed the resulting data. TK, GW, SCW, and NRC generated and analyzed the transcriptomes. SA, JA, RAH, and NRC performed the *in vivo* experiments. L-OA wrote the manuscript, with assistance from CU, JK, and NRC, and input from all other authors.

FUNDING

This work was supported by a UK Medical Research Council grant (MR/L01839X/1) to RAH and NRC, a Leverhulme Trust research grant (RPG-2012-627) to RAH, a KU Leuven C3-project (C32/16/035) to CU and a Wellcome Trust and Royal Society Sir Henry Dale Fellowship (200517/Z/16/Z) to NRC.

ACKNOWLEDGMENTS

We thank Paul Rowley for maintenance and husbandry of the snake collection at LSTM and for performing venom extractions and Mark Wilkinson for critically reading the manuscript. We thank Marijke Brams for contributing to AChBP purifications.

SUPPLEMENTARY MATERIAL

The Supplementary Material for this article can be found online at: https://www.frontiersin.org/articles/10.3389/fphar.2019.00848/full#supplementary-material

REFERENCES

Ainsworth, S., Petras, D., Engmark, M., Süssmuth, R. D., Whiteley, G., Albulescu, L.-O. O., et al. (2018a). The medical threat of mamba envenoming in sub-Saharan Africa revealed by genus-wide analysis of venom composition, toxicity and antivenomics profiling of available antivenoms. *J. Proteomics* 172, 173–189. doi: 10.1016/j.jprot.2017.08.016

Ainsworth, S., Slagboom, J., Alomran, N., Pla, D., Alhamdi, Y., King, S. I., et al. (2018b). The paraspecific neutralisation of snake venom induced coagulopathy by antivenoms. *Commun. Biol.* 1, 34. doi: 10.1038/s42003-018-0039-1

Antil-Delbeke, S., Gaillard, C., Tamiya, T., Corringer, P.-J., Changeux, J.-P., Servent, D., et al. (2000). Molecular determinants by which a long chain toxin from snake venom interacts with the neuronal α7-nicotinic acetylcholine receptor. *J. Biol. Chem.* 275, 29594–29601. doi: 10.1074/jbc.M909746199

Antil, S., Servent, D., and Ménez, A. (1999). Variability among the sites by which curaremimetic toxins bind to Torpedo acetylcholine receptor, as revealed by identification of the functional residues of α-cobratoxin. *J. Biol. Chem.* 274, 34851–34858. doi: 10.1074/jbc.274.49.34851

Archer, J., Whiteley, G., Casewell, N. R., Harrison, R. A., and Wagstaff, S. C. (2014). VTBuilder: a tool for the assembly of multi isoform transcriptomes. *BMC Bioinformatics* 15, 389. doi: 10.1186/s12859-014-0389-8

Bourne, Y., Talley, T. T., Hansen, S. B., Taylor, P., and Marchot, P. (2005). Crystal structure of a Cbtx-AChBP complex reveals essential interactions between snake α-neurotoxins and nicotinic receptors. *EMBO J.* 24, 1512–1522. doi: 10.1038/sj.emboj.7600620

Brams, M., Pandya, A., Kuzmin, D., van Elk, R., Krijnen, L., Yakel, J. L., et al. (2011). A Structural and mutagenic blueprint for molecular recognition of strychnine and d-tubocurarine by different cys-loop receptors. *PLoS Biol.* 9, e1001034. doi: 10.1371/journal.pbio.1001034

Brejc, K., van Dijk, W. J., Klaassen, R. V., Schuurmans, M., van Der Oost, J., Smit, A. B., et al. (2001). Crystal structure of an ACh-binding protein reveals the ligand-binding domain of nicotinic receptors. *Nature* 411, 269–76. doi: 10.1038/35077011

Bulfone, T. C., Samuel, S. P., Bickler, P. E., and Lewin, M. R. (2018). Developing small molecule therapeutics for the initial and adjunctive treatment of snakebite. *J. Trop. Med.* 2018, 1–14. doi: 10.1155/2018/4320175

Calvete, J. J., Casewell, N. R., Hernández-Guzmán, U., Quesada-Bernat, S., Sanz, L., Rokyta, D. R., et al. (2018). Venom complexity in a pitviper produced by facultative parthenogenesis. *Sci. Rep.* 8, 11539. doi: 10.1038/s41598-018-29791-y

Casewell, N. R., Cook, D. A. N., Wagstaff, S. C., Nasidi, A., Durfa, N., Wüster, W., et al. (2010). Pre-clinical assays predict Pan-African Echis viper efficacy for a species-specific antivenom. *PLoS Negl. Trop. Dis.* 4, e851. doi: 10.1371/journal.pntd.0000851

Casewell, N. R., Wagstaff, S. C., Wuster, W., Cook, D. A. N., Bolton, F. M. S., King, S. I., et al. (2014). Medically important differences in snake venom composition are dictated by distinct postgenomic mechanisms. *Proc. Natl. Acad. Sci.* 111, 9205–9210. doi: 10.1073/pnas.1405484111

Casewell, N. R., Wüster, W., Vonk, F. J., Harrison, R. A., and Fry, B. G. (2013). Complex cocktails: the evolutionary novelty of venoms. *Trends Ecol. Evol.* 28, 219–229. doi: 10.1016/j.tree.2012.10.020

Chang, C. C. (1979). *The action of snake venoms on nerve and muscle BT—snake venoms*. Lee C-Y, editor. Berlin, Heidelberg: Springer Berlin Heidelberg, 309–376. doi: 10.1007/978-3-642-66913-2_10

Chippaux, J. P., Williams, V., and White, J. (1991). Snake venom variability: methods of study, results and interpretation. *Toxicon* 29, 1279–303. doi: 10.1016/0041-0101(91)90116-9

Conesa, A., Gotz, S., Garcia-Gomez, J. M., Terol, J., Talon, M., and Robles, M. (2005). Blast2GO: a universal tool for annotation, visualization and analysis

in functional genomics research. *Bioinformatics* 21, 3674–3676. doi: 10.1093/bioinformatics/bti610

de Silva, H. A., Ryan, N. M., and de Silva, H. J. (2016). Adverse reactions to snake antivenom, and their prevention and treatment. *Br. J. Clin. Pharmacol.* 81, 446–452. doi: 10.1111/bcp.12739

Edgar, R. C. (2004). MUSCLE: multiple sequence alignment with high accuracy and high throughput. *Nucleic Acids Res.* 32, 1792–1797. doi: 10.1093/nar/gkh340

Fruchart-Gaillard, C., Gilquin, B., Antil-Delbeke, S., Le Novere, N., Tamiya, T., Corringer, P.-J., et al. (2002). Experimentally based model of a complex between a snake toxin and the 7 nicotinic receptor. *Proc. Natl. Acad. Sci.* 99, 3216–3221. doi: 10.1073/pnas.042699899

Gutiérrez, J. M., Calvete, J. J., Habib, A. G., Harrison, R. A., Williams, D. J., and Warrell, D. A. (2017). Snakebite envenoming. *Nat. Rev. Dis. Prim.* 3, 17063. doi: 10.1038/nrdp.2017.63

Gutiérrez, J. M., and Ownby, C. L. (2003). Skeletal muscle degeneration induced by venom phospholipases A2: insights into the mechanisms of local and systemic myotoxicity. *Toxicon* 42, 915–931. doi: 10.1016/j.toxicon.2003.11.005

Harrison, R. A., Oluoch, G. O., Ainsworth, S., Alsolaiss, J., Bolton, F., Arias, A.-S., et al. (2017). Preclinical antivenom-efficacy testing reveals potentially disturbing deficiencies of snakebite treatment capability in East Africa. *PLoS Negl. Trop. Dis.* 11, e0005969. doi: 10.1371/journal.pntd.0005969

Herrera, M., Fernández, J., Vargas, M., Villalta, M., Segura, Á., León, G., et al. (2012). Comparative proteomic analysis of the venom of the Taipan snake, *Oxyuranus scutellatus*, from Papua New Guinea and Australia: role of neurotoxic and procoagulant effects in venom toxicity. *J. Proteomics* 75, 2128–2140. doi: 10.1016/j.jprot.2012.01.006

Hibbs, R. E., Sulzenbacher, G., Shi, J., Talley, T. T., Conrod, S., Kem, W. R., et al. (2009). Structural determinants for interaction of partial agonists with acetylcholine binding protein and neuronal alpha7 nicotinic acetylcholine receptor. *EMBO J.* 28, 3040–51. doi: 10.1038/emboj.2009.227

Huang, S., Li, S.-X., Bren, N., Cheng, K., Gomoto, R., Chen, L., et al. (2013). Complex between α-bungarotoxin and an α7 nicotinic receptor ligand-binding domain chimaera. *Biochem. J.* 454, 303–310. doi: 10.1042/BJ20130636

Jiang, Y., Li, Y., Lee, W., Xu, X., Zhang, Y., Zhao, R., et al. (2011). Venom gland transcriptomes of two elapid snakes (*Bungarus multicinctus* and *Naja atra*) and evolution of toxin genes. *BMC Genomics* 12, 1. doi: 10.1186/1471-2164-12-1

Kessler, P., Marchot, P., Silva, M., and Servent, D. (2017). The three-finger toxin fold: a multifunctional structural scaffold able to modulate cholinergic functions. *J. Neurochem.* 142, 7–18. doi: 10.1111/jnc.13975

Kornhauser, R., Hart, A. J., Reeve, S., Smith, A. I., Fry, B. G., and Hodgson, W. C. (2010). Variations in the pharmacological profile of post-synaptic neurotoxins isolated from the venoms of the Papuan (*Oxyuranus scutellatus canni*) and coastal (*Oxyuranus scutellatus scutellatus*) taipans. *Neurotoxicology* 31, 239–243. doi: 10.1016/j.neuro.2009.12.009

Kumar, S., Stecher, G., and Tamura, K. (2016). MEGA7: Molecular Evolutionary Genetics Analysis Version 7.0 for bigger datasets. *Mol. Biol. Evol.* 33, 1870–1874. doi: 10.1093/molbev/msw054

Lewin, M., Gutiérrez, J., Samuel, S., Herrera, M., Bryan-Quirós, W., Lomonte, B., et al. (2018). Delayed oral LY333013 rescues mice from highly neurotoxic, lethal doses of Papuan Taipan (*Oxyuranus scutellatus*) venom. *Toxins (Basel)* 10, 380. doi: 10.3390/toxins10100380

Li, S. X., Huang, S., Bren, N., Noridomi, K., Dellisanti, C. D., Sine, S. M., et al. (2011). Ligand-binding domain of an α7-nicotinic receptor chimera and its complex with agonist. *Nat. Neurosci.* 14, 1253–1259. doi: 10.1038/nn.2908

Lyukmanova, E. N., Shenkarev, Z. O., Schulga, A. A., Ermolyuk, Y. S., Mordvintsev, D. Y., Utkin, Y. N., et al. (2007). Bacterial expression, NMR, and electrophysiology analysis of chimeric short/long-chain alpha-neurotoxins acting on neuronal nicotinic receptors. *J. Biol. Chem.* 282, 24784–91. doi: 10.1074/jbc.M611263200

Malih, I., Ahmad rusmili, M. R., Tee, T. Y., Saile, R., Ghalim, N., and Othman, I. (2014). Proteomic analysis of Moroccan cobra *Naja haje legionis* venom using tandem mass spectrometry. *J. Proteomics* 96, 240–252. doi: 10.1016/j.jprot.2013.11.012

Margres, M. J., Aronow, K., Loyacano, J., and Rokyta, D. R. (2013). The venom-gland transcriptome of the eastern coral snake (*Micrurus fulvius*) reveals high venom complexity in the intragenomic evolution of venoms. *BMC Genomics* 14, 531. doi: 10.1186/1471-2164-14-531

Miyazawa, A., Fujiyoshi, Y., and Unwin, N. (2003). Structure and gating mechanism of the acetylcholine receptor pore. *Nature* 423, 949–955. doi: 10.1038/nature01748

Nirthanan, S., Charpantier, E., Gopalakrishnakone, P., Gwee, M. C. E., Khoo, H.-E., Cheah, L.-S., et al. (2002). Candoxin, a novel toxin from *Bungarus candidus*, is a reversible antagonist of muscle (αβγδ) but a poorly reversible antagonist of neuronal α7 nicotinic acetylcholine receptors. *J. Biol. Chem.* 277, 17811–17820. doi: 10.1074/jbc.M111152200

Nirthanan, S., and Gwee, M. C. E. (2004). Three-finger alpha-neurotoxins and the nicotinic acetylcholine receptor, forty years on. *J. Pharmacol. Sci.* 94, 1–17. doi: 10.1254/jphs.94.1

Oh, A. M. F., Tan, C. H., Ariaranee, G. C., Quraishi, N., and Tan, N. H. (2017). Venomics of *Bungarus caeruleus* (Indian krait): comparable venom profiles, variable immunoreactivities among specimens from Sri Lanka, India and Pakistan. *J. Proteomics* 164, 1–18. doi: 10.1016/j.jprot.2017.04.018

Oh, A. M. F., Tan, C. H., Tan, K. Y., Quraishi, N. H., and Tan, N. H. (2019). Venom proteome of Bungarus sindanus (Sind krait) from Pakistan and *in vivo* cross-neutralization of toxicity using an Indian polyvalent antivenom. *J. Proteomics* 193, 243–254. doi: 10.1016/j.jprot.2018.10.016

Pla, D., Sanz, L., Whiteley, G., Wagstaff, S. C., Harrison, R. A., Casewell, N. R., et al. (2017). What killed Karl Patterson Schmidt? Combined venom gland transcriptomic, venomic and antivenomic analysis of the South African green tree snake (the boomslang), *Dispholidus typus*. *Biochim. Biophys. Acta Gen. Subj.* 1861, 814–823. doi: 10.1016/j.bbagen.2017.01.020

Pochet, L., Heus, F., Jonker, N., Lingeman, H., Smit, A. B., Niessen, W. M. A., et al. (2011). Online magnetic bead based dynamic protein affinity selection coupled to LC-MS for the screening of acetylcholine binding protein ligands. *J. Chromatogr. B Anal. Technol. Biomed. Life Sci.* 879, 1781–1788. doi: 10.1016/j.jchromb.2011.04.023

Poh, S. L., Mourier, G., Thai, R., Armugam, A., Molgó, J., Servent, D., et al. (2002). A synthetic weak neurotoxin binds with low affinity to Torpedo and chicken alpha7 nicotinic acetylcholine receptors. *Eur. J. Biochem.* 269, 4247–56. doi: 10.1046/j.1432-1033.2002.03113.x

Ratanabanangkoon, K., Simsiriwong, P., Pruksaphon, K., Tan, K. Y., Chantrathonkul, B., Eursakun, S., et al. (2018). An *in vitro* potency assay using nicotinic acetylcholine receptor binding works well with antivenoms against *Bungarus candidus* and *Naja naja*. *Sci. Rep.* 8, 1–9. doi: 10.1038/s41598-018-27794-3

Ratanabanangkoon, K., Simsiriwong, P., Pruksaphon, K., Tan, K. Y., Eursakun, S., Tan, C. H., et al. (2017). A novel *in vitro* potency assay of antisera against Thai *Naja kaouthia* based on nicotinic acetylcholine receptor binding. *Sci. Rep.* 7, 1–8. doi: 10.1038/s41598-017-08962-3

Roy, A., Zhou, X., Chong, M. Z., D'Hoedt, D., Foo, C. S., Rajagopalan, N., et al. (2010). Structural and functional characterization of a novel homodimeric three-finger neurotoxin from the venom of *Ophiophagus hannah* (King cobra). *J. Biol. Chem.* 285, 8302–8315. doi: 10.1074/jbc.M109.074161

Servent, D., Antil-Delbeke, S., Gaillard, C., Corringer, P. J., Changeux, J. P., and Ménez, A. (2000). Molecular characterization of the specificity of interactions of various neurotoxins on two distinct nicotinic acetylcholine receptors. *Eur. J. Pharmacol.* 393, 197–204. doi: 10.1016/S0014-2999(00)00095-9

Servent, D., Winckler-Dietrich, V., Hu, H. Y., Kessler, P., Drevet, P., Bertrand, D., et al. (1997). Only snake curaremimetic toxins with a fifth disulfide bond have high affinity for the neuronal alpha7 nicotinic receptor. *J. Biol. Chem.* 272, 24279–86. doi: 10.1074/jbc.272.39.24279

Slagboom, J., Otvos, R. A., Cardoso, F. C., Iyer, J., Visser, J. C., van Doodewaerd, B. R., et al. (2018). Neurotoxicity fingerprinting of venoms using on-line microfluidic AChBP profiling. *Toxicon* 148, 213–222. doi: 10.1016/j.toxicon.2018.04.022

Smit, A. B., Syed, N. I., Schaap, D., van Minnen, J., Klumperman, J., Kits, K. S., et al. (2001). A glia-derived acetylcholine-binding protein that modulates synaptic transmission. *Nature* 411, 261–8. doi: 10.1038/35077000

Spurny, R., Debaveye, S., Farinha, A., Veys, K., Vos, A. M., Gossas, T., et al. (2015). Molecular blueprint of allosteric binding sites in a homologue of the agonist-binding domain of the α7 nicotinic acetylcholine receptor. *Proc. Natl. Acad. Sci.* 112, E2543–E2552. doi: 10.1073/pnas.1418289112

Suzuki-Matsubara, M., Athauda, S. B. P., Suzuki, Y., Matsubara, K., and Moriyama, A. (2016). Comparison of the primary structures, cytotoxicities, and affinities to phospholipids of five kinds of cytotoxins from the venom of Indian cobra, *Naja*

naja. *Comp. Biochem. Physiol. Part C Toxicol. Pharmacol.* 179, 158–164. doi: 10.1016/j.cbpc.2015.09.015

Tan, C. H., Liew, J. L., Tan, K. Y., and Tan, N. H. (2016a). Assessing SABU (Serum Anti Bisa Ular), the sole Indonesian antivenom: a proteomic analysis and neutralization efficacy study. *Sci. Rep.* 6, 37299. doi: 10.1038/srep37299

Tan, C. H., Tan, K. Y., Lim, S. E., and Tan, N. H. (2015). Venomics of the beaked sea snake, *Hydrophis schistosus*: a minimalist toxin arsenal and its cross-neutralization by heterologous antivenoms. *J. Proteomics* 126, 121–130. doi: 10.1016/j.jprot.2015.05.035

Tan, C., Tan, K., Ng, T., Sim, S., Tan, N., Tan, C. H., et al. (2018). Venom proteome of spine-bellied sea snake (*Hydrophis curtus*) from Penang, Malaysia: toxicity correlation, immunoprofiling and cross-neutralization by sea snake antivenom. *Toxins (Basel)* 11, 3. doi: 10.3390/toxins11010003

Tan, C., Wong, K., Tan, N., Ng, T., and Tan, K. (2019). Distinctive distribution of secretory phospholipases A2 in the venoms of Afro-Asian cobras (Subgenus: Naja, Afronaja, Boulengerina and Uraeus). *Toxins (Basel)* 11, 116. doi: 10.3390/toxins11020116

Tan, K., Tan, C., Fung, S., and Tan, N. (2016b). Neutralization of the principal toxins from the venoms of Thai *Naja kaouthia* and Malaysian *Hydrophis schistosus*: insights into toxin-specific neutralization by two different antivenoms. *Toxins (Basel)* 8, 86. doi: 10.3390/toxins8040086

Tasoulis, T., and Isbister, G. K. (2017). A review and database of snake venom proteomes. *Toxins (Basel)* 9, 290. doi: 10.3390/toxins9090290

Unwin, N. (2005). Refined structure of the nicotinic acetylcholine receptor at 4 Å resolution. *J. Mol. Biol.* 346, 967–989. doi: 10.1016/j.jmb.2004.12.031

Utkin, Y. N., Kuch, U., Kasheverov, I. E., Lebedev, D. S., Cederlund, E., Molles, B. E., et al. (2019). Novel long-chain neurotoxins from Bungarus candidus distinguish the two binding sites in muscle-type nicotinic acetylcholine receptors. *Biochem. J.* 476, 1285–1302. doi: 10.1042/BCJ20180909

Utkin, Y. N., Kukhtina, V. V., Kryukova, E. V., Chiodini, F., Bertrand, D., Methfessel, C., et al. (2001). "Weak toxin" from *Naja kaouthia* is a nontoxic antagonist of α7 and muscle-type nicotinic acetylcholine receptors. *J. Biol. Chem.* 276, 15810–15815. doi: 10.1074/jbc.M100788200

Vergara, I., Pedraza-Escalona, M., Paniagua, D., Restano-Cassulini, R., Zamudio, F., Batista, C. V. F., et al. (2014). Eastern coral snake *Micrurus fulvius* venom toxicity in mice is mainly determined by neurotoxic phospholipases A2. *J. Proteomics* 105, 295–306. doi: 10.1016/j.jprot.2014.02.027

Vulfius, C. A., Kasheverov, I. E., Starkov, V. G., Osipov, A. V., Andreeva, T. V., Filkin, S. Y., et al. (2014). Inhibition of nicotinic acetylcholine receptors, a novel facet in the pleiotropic activities of snake venom phospholipases A2. *PLoS One* 9. doi: 10.1371/journal.pone.0115428

Whiteley, G., Casewell, N. R., Pla, D., Quesada-Bernat, S., Logan, R. A. E., Bolton, F. M. S., et al. (2018). Defining the pathogenic threat of envenoming by South African shield-nosed and coral snakes (genus *Aspidelaps*), and revealing the likely efficacy of available antivenom. *J. Proteomics*. 198, 186–198. doi: 10.1016/j.jprot.2018.09.019

WHO. (2018). WHO Guidelines for the Production, Control and Regulation of Snake Antivenom Immunoglobulins. Geneva, Switzerland: World Health Organization. Available at: https://www.who.int/bloodproducts/snake_antivenoms/snakeantivenomguide/en/ [Accessed January 24, 2019].

Williams, D. J., Gutiérrez, J.-M., Calvete, J. J., Wüster, W., Ratanabanangkoon, K., Paiva, O., et al. (2011). Ending the drought: new strategies for improving the flow of affordable, effective antivenoms in Asia and Africa. *J. Proteomics* 74, 1735–1767. doi: 10.1016/j.jprot.2011.05.027

Wong, K. Y., Tan, C. H., and Tan, N. H. (2016). Venom and purified toxins of the spectacled cobra (*Naja naja*) from Pakistan: insights into toxicity and antivenom neutralization. *Am. J. Trop. Med. Hyg.* 94, 1392–1399. doi: 10.4269/ajtmh.15-0871

Conflict of Interest Statement: The authors declare that the research was conducted in the absence of any commercial or financial relationships that could be construed as a potential conflict of interest.

The handling editor is currently editing/co-organizing a Research Topic with one of the authors, CU, and confirms the absence of any other collaboration.

Advantages of publishing in Frontiers

OPEN ACCESS
Articles are free to read for greatest visibility and readership

FAST PUBLICATION
Around 90 days from submission to decision

HIGH QUALITY PEER-REVIEW
Rigorous, collaborative, and constructive peer-review

TRANSPARENT PEER-REVIEW
Editors and reviewers acknowledged by name on published articles

Frontiers
Avenue du Tribunal-Fédéral 34
1005 Lausanne | Switzerland

Visit us: www.frontiersin.org
Contact us: info@frontiersin.org | +41 21 510 17 00

REPRODUCIBILITY OF RESEARCH
Support open data and methods to enhance research reproducibility

DIGITAL PUBLISHING
Articles designed for optimal readership across devices

FOLLOW US
@frontiersin

IMPACT METRICS
Advanced article metrics track visibility across digital media

EXTENSIVE PROMOTION
Marketing and promotion of impactful research

LOOP RESEARCH NETWORK
Our network increases your article's readership